Instabilities and Transport in Magnetized Plasmas

Mark Saul Rosin

Darwin College

For my mother, father and sister.

"Astrophysics is too important to be left in the hands of astrophysicists."

– Hannes Alfvén

Acknowledgments

Declaration

This dissertation is the result of my own work and includes nothing which is the outcome of work done in collaboration except where specifically indicated in the text. It is based on research done at the DAMTP, Cambridge from October 2006 to July 2010. No part of this thesis has been or is being submitted for any qualification other than the degree of Doctor of Philosophy at Cambridge. The main collaborative parts of my thesis are the result of work with my supervisor Dr. Alex Schekochihin. However, Jon Mestel, François Rincon and Steve Cowley have also contributed to the publications that came out of this work:

- M. S. Rosin, A. A. Schekochihin, F. Rincon, & S. C. Cowley, *"A nonlinear theory of the parallel firehose and gyrothermal instabilities in a weakly collisional plasma"*, *MNRAS*, (Submitted, 2010). [e-print:arXiv.org/pdf/1002.4017].

- M. S. Rosin, A. J. Mestel, & A. A. Schekochihin, *"The global MRI with Braginskii viscosity"*, *MNRAS*, (In Preparation, 2010).

Chapter 2 is largely based on the latter of these and chapter 3 on the former. I have also contributed to the following publications as part of my Ph.D:

- A. A. Schekochihin, S. C. Cowley, F. Rincon, & M. S. Rosin, *"Magnetofluid dynamics of magnetized cosmic plasma: firehose and gyrothermal instabilities"*, *MNRAS*. 405, 291 (2010) [e-print arXiv:0912.1359]

- A. A. Schekochihin, S. C. Cowley, R. M. Kulsrud, M. S. Rosin, & T. Heinemann, *"Nonlinear growth of firehose and mirror fluctuations in astrophysical plasmas"*, *Phys. Rev. Lett.*, **100**, 081301, (2008). [e-print:arxiv.org/pdf/0709.3828].

Work done in the former appears in several places in chapters 1 and 3, and work done in the latter appears in chapter 3. They are cited respectively as Schekochihin *et al.* (2010) and Schekochihin *et al.* (2008).

- M. Rosin, 18th October, 2010

Abstract

In a magnetized plasma, naturally occurring pressure anisotropies facilitate instabilities that are expected to modify the transport properties of the system. In this thesis we examine two such instabilities and, where appropriate, their effects on transport.

First we consider the collisional (fluid) magnetized magnetorotational instability (MRI) in the presence of the Braginskii viscosity. We conduct a global linear analysis of the instability in a galactic rotation profile for three magnetic field configurations: purely azimuthal, purely vertical and slightly pitched. Our analysis, numerical and asymptotic, shows that the first two represent singular configurations where the Braginskii viscosity's primary role is dissipative and the maximum growth rate is proportional to the Reynolds number when this is small. For a weak pitched field, the Braginskii viscosity is destabilising and when its effects dominate over the Lorentz force, the growth rate of the MRI can be up to $2\sqrt{2}$ times faster than the inviscid limit. If the field is strong, an over-stability develops and both the real and imaginary parts of the frequency increase with the coefficient of the viscosity.

Second, in the context of the ICM of galaxy clusters, we consider the pressure-anisotropy-driven firehose instability. The linear instability is fast ($\sim$ ion cyclotron period) and small-scale (ion Larmor radius ρ_i) and so fluid theory is inapplicable. We determine its nonlinear evolution in an *ab initio* kinetic calculation (for parallel gradients only). We use a particular physical asymptotic ordering to derive a closed nonlinear equation for the firehose turbulence, which we solve. We find secular ($\propto t$) growth of magnetic fluctuations and a $k_\parallel^{-3}$ spectrum, starting at scales $\gtrsim \rho_i$. When a parallel ion heat flux is present, the parallel firehose instability mutates into the new *gyrothermal instability*. Its nonlinear evolution also involves secular magnetic energy growth, but its spectrum is eventually dominated by modes with a maximal scale $\sim \rho_i l_T/\lambda_{mfp}$, ($l_T$ is the parallel temperature gradient scale). Throughout we discuss implications for modelling, transport and other areas of magnetized plasma physics.

Contents

Part I

Introduction

Chapter 1

Introduction

"If reading Chapman and Cowling is like chewing glass, then reading Braginskii is like chewing fibre-glass."

P.J.Dellar, Oxford, 2010

1.1   Setting the stage

Neutral fluid theory relies on the asymptotic smallness of the inter-particle mean free path λ_{mfp} to formally close the moment hierarchy of the underlying kinetic equation (Chapman & Cowling, 1970)[1]. In a plasma another potentially asymptotically small parameter exists that allows the kinetic equation to be simplified considerably. This parameter is the Larmor radius ρ_s.

In a plasma with a sufficiently strong magnetic field, charged particles execute Larmor orbits about the field lines with a radius ρ_s and (cyclotron) frequency Ω_s. When the mean free path of the plasma is greater than the Larmor radius $\lambda_{\mathrm{mfp}} \gg \rho_s$ and the collision frequencies less than the cyclotron frequency $\nu_s \ll \Omega_s$, the plasma is said to be *magnetized*. The smallness of ρ_s restricts motion across magnetic field lines (but not along them) and the largeness of Ω_s renders the position of the charged particle about its Larmor orbit irrelevant to lowest order

---

[1]A profile of Sydney Chapman published in the *Observer*, July 2, 1957 and reprinted in Brush (1976) quotes him as saying his book was very heavy going, "like chewing glass". The comments at the start of this chapter are in reference to this.
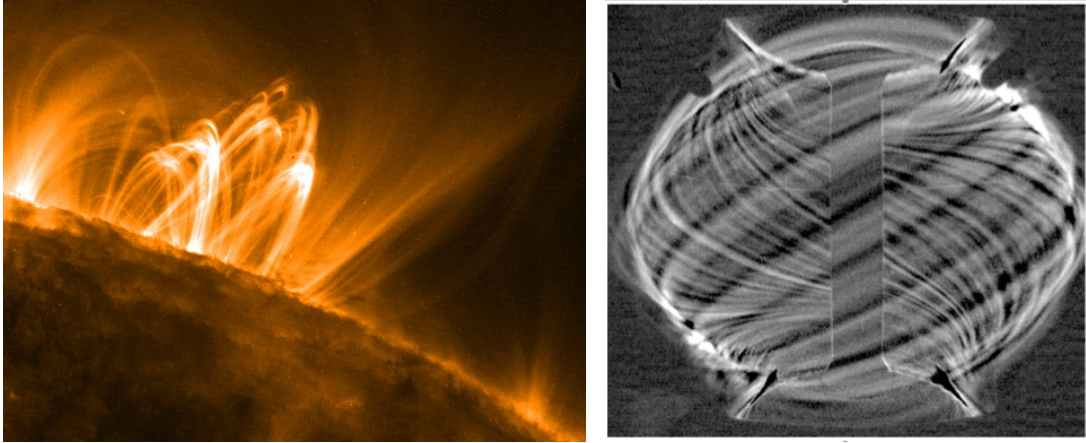
Figure 1.1: In a magnetized plasma, charged particles are constrained to travel along, but not across strong magnetic field lines. The ensuing flows and temperature profiles are anisotropic with respect to the direction of the magnetic field, and lead to highly filamentary structures. Left Panel: X-ray emission image of solar coronal loops taken by the Transition Region and Coronal Explorer (TRACE) (Reale & Peres, 2000; Reale *et al.*, 2000; TRACE, 2000). Right Panel: D_α emission images (visible light) from Edge Localised Modes (ELMS) on the Mega Ampere Spherical Tokomak (MAST) (Kirk *et al.*, 2005; Dudson *et al.*, 2008).

in an asymptotic expansion of the plasma distribution function. As a result the number of independent variables necessary to fully describe a kinetic plasma can be reduced by one (Kulsrud, 1962, 1983). Furthermore, the component of the particle velocity perpendicular to the magnetic field is controlled by a constant of motion, the first adiabatic invariant. The physics of such plasma differs considerably from a neutral fluid (and indeed a collisionally dominated plasma, e.g. one described by magnetohydrodynamics (MHD)) in three important ways.

First, on *macroscopic* scales (greater than λ_{mfp} in a collisional plasma), the transport of momentum, heat and current become highly anisotropic with respect to the direction of the local magnetic field. Cross-field diffusion is limited by a random walk of step size ρ_s, whilst the along-field transport is often either unconstrained or limited by $\lambda_{\mathrm{mfp}} \gg \rho_s$. The effects of this can be clearly seen in the elongated filamentary structures of the Sun's magnetic coronal loops and the guide fields of a terrestrial tokomak, Figure 1.1.

Second, the manner in which free energy gradients, angular velocity and temperature are relaxed can change. Well known instabilities like the magnetorotational instability (MRI) are modified considerably (Balbus & Hawley, 1998; Quataert *et al.*, 2002; Sharma *et al.*, 2003; Islam & Balbus, 2005), and new instabilities appear: the magnetothermal instability (MTI), the heat flux buoyancy instability (HBI) and the magnetoviscous instability (MVI) (Balbus, 2000, 2001, 2004; Quataert, 2008).

Third, changing magnetic fields and heat fluxes arising from, say, an instability or macroscopic transport, create pressure anisotropies with respect to the local direction of the magnetic field, (see e.g. Chew *et al.*, 1956; Kulsrud, 1983). In turn, these drive fast growing instabilities on *microscopic* scales (between ρ_s and λ_{mfp}) whose effect on the instabilities and macroscopic transport processes from which the anisotropy arose is unknown (Schekochihin *et al.*, 2005).

Understanding the rich interplay between these three realisations of magnetized plasma phenomena constitutes an important and, as of yet, unsolved issue in astrophysics; specifically in galaxy clusters, galaxies and accretion discs. Without delving into the details too deeply (we will do so later) let us consider a sample of questions whose answers fundamentally depend on a complete understanding of the magnetized plasma physics referenced above:

- In galaxy clusters, to what extent does anisotropic transport help/hinder proposed solutions to the cooling flow problem (Fabian, 1994; Peterson & Fabian, 2006)? What effect do magnetized instabilities that feed off the temperature gradient have? What is the resultant effective viscosity and conductivity relative to the Spitzer values? Does this depend on the magnetic field configuration and strength (Balbus & Reynolds, 2008; Parrish & Quataert, 2008; Bogdanović *et al.*, 2009; Parrish *et al.*, 2010; Kunz *et al.*, 2010)?

- What is the nature of the fluid turbulence arising from magnetized instabilities in the galaxy and accretion discs (Schekochihin & Cowley, 2006)? What is its effective α-parameter (Shakura & Sunyaev, 1973)? Is this the same in a collisionless or weakly collisional plasma (Sharma *et al.*, 2006,

2007)? Do global effects have a role to play (Rosin *et al.*, 2010*a*)? Again, to what extent does the strength and configuration of the magnetic field matter (Quataert *et al.*, 2002; Sharma *et al.*, 2003; Balbus, 2004)?

- How does small-scale dynamo action proceed in a magnetized plasma (Shukurov *et al.*, 2006; Brandenburg & Nordlund, 2009)? Does the presence of microscale instabilities categorically change, or merely modify, the rate of field amplification (Malyshkin & Kulsrud, 2002; Schekochihin & Cowley, 2006)? What is the structure of the field and how does it affect the macroscopic dynamics?

- How precisely do microscale instabilities affect all of the above (Schekochihin & Cowley, 2006; Lyutikov, 2007; Schekochihin & Cowley, 2007; Kunz *et al.*, 2010)? Can they be parameterised or is a full microphysical theory necessary? In either case, in what way will they appear in the equations governing the macroscopic plasma evolution (Schekochihin *et al.*, 2008; Rosin *et al.*, 2010*b*)?

The existing literature (some of which is cited above) addresses some of these questions, but an all-encompassing description is far from complete and even existing work is open to reassessment[2]. The overall picture is a deeply interconnected one and the types of questions outlined above are probably pertinent, to some degree, to most magnetized astrophysical processes. In Figure 1.2 we present a grossly simplified, but nevertheless useful, framework for considering these processes.

It is the purpose of the research presented here to answer two sub-questions from the list above. In chapter 2 we consider the global nature of a magnetized shear instability, locally identifiable as the MRI in the presence of Braginskii viscosity, and its dependence on the magnetic field configuration, plasma beta, rotation rate and ion collision frequency (Balbus, 2004; Islam & Balbus, 2005).

---

[2]For example, Sharma *et al.* (2006, 2007) have investigated the turbulent state of a collisionless magnetized accretion disc. In doing so, they assumed micro-instabilities relax the pressure anisotropy towards the marginal stability boundary via an effective collision process. In chapter 3 we show that this method of maintaining marginal stability is not the only possibility and, instead, the pressure anisotropy can be regulated by the growth of microscale magnetic fields.

In particular, we focus on its role in the historic Interstellar Medium (ISM) of spiral galaxies. In chapter 3 we consider the nonlinear evolution of the pressure-anisotropy-driven firehose instability and the newly discovered heat flux driven gyrothermal instability (GTI) and their effect on transport (Schekochihin *et al.*, 2010). In this case we focus on the Intracluster Medium (ICM) of galaxy clusters. Throughout, we attempt to draw together the implications of our results for those issues we do not directly address. Because the two problems considered in this thesis are quite different, we attempt to keep the content of this introduction as broad as possible.

We start in section 1.2 by introducing the fundamental equations of plasma physics before, in section 1.3, reducing them to a hierarchy of moment equations. Because of the complicated nature of the pressure tensor we do not immediately close the hierarchy and instead, in section 1.4, we examine its general form assuming only that the plasma is highly magnetized. However, in section 1.5 we make use of the asymptotic smallness of ρ_s (largeness of Ω_s) to derive, and provide an physical interpretation of, the modified CGL equations which we then use to close the moment hierarchy (neglecting heat fluxes). These equations, along with the lower order moments provide the conceptual starting point from which the rest of our work proceeds. In section 1.6 we summarise and lay out our plan for the remainder of this dissertation.

1.2   Basic plasma theory

1.2.1   Fundamental equations

At the most basic super-quantum level a plasma is simply a statistically large collection of ionized particles whose macroscopic evolution is fundamentally governed by gravity (which we shall omit until chapter 2) and the electromagnetic force at both short and long ranges.

The plasma is described by the evolution of the number density distribution function $f_s(t, \boldsymbol{r}, \boldsymbol{w})$ where the subscript $s = i, e$ indicates the species type: ions
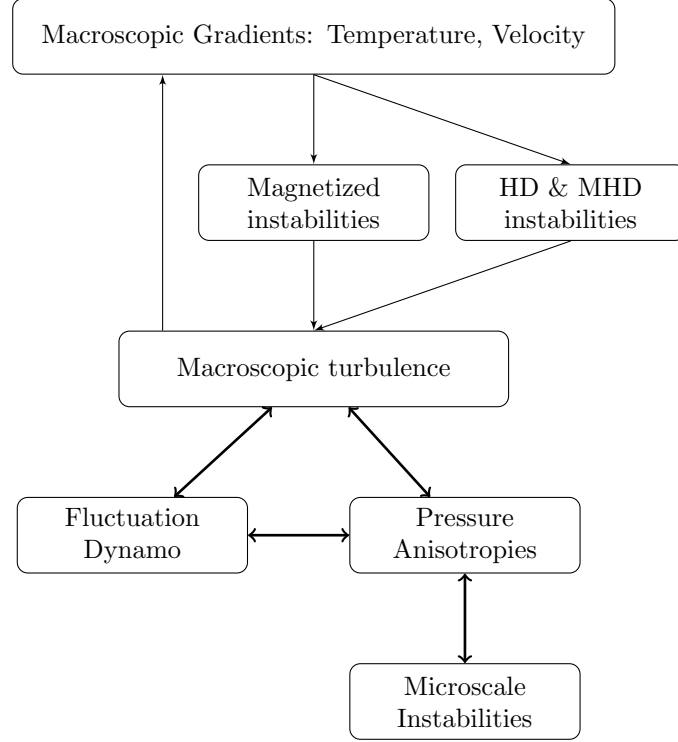
Figure 1.2: Schematic representation of the salient astrophysical magnetized plasma processes in, for example, a galaxy cluster, galaxy or accretion disc. Free energy gradients sustained by active galactic nuclei (AGN), supernovae or the differential rotation of a disc or galaxy can be unstable to both MHD, HD (hydrodynamic) and magnetized instabilities. In the nonlinear stages these instabilities leads to turbulence. The turbulent scale flows induce rapidly changing magnetic fields and therefore fluctuation dynamos and pressure anisotropies. The pressure anisotropy leads to micro-instabilities that changes both the pressure anisotropy itself and, possibly, the fluctuation dynamo. One would expect these processes to then feed back onto the macroscale turbulence which, in turn, affects the macroscopic gradients by changing the macroscopic transport properties of the system, e.g. an enhanced viscosity or reduced conductivity.

or electrons. The equation governing the evolution of f_s is the kinetic equation,

$$\frac{\mathrm{D}f_s}{\mathrm{D}t} \equiv \frac{\partial f_s}{\partial t} + \boldsymbol{w} \cdot \nabla f_s + \frac{Z_s e}{m_s} \left(\boldsymbol{E} + \frac{\boldsymbol{w} \times \boldsymbol{B}}{c} \right) \cdot \frac{\partial f_s}{\partial \boldsymbol{w}} = C[f_s], \tag{1.1}$$

where $\mathrm{D}/\mathrm{D}t$ is the full convective derivative in time t, position $\boldsymbol{r}$ and particle velocity $\boldsymbol{w}$ phase-space and $C[f_s]$ represents the combined effect of all collisions on species s, including like-like collisions between particles of the same species. The remaining undefined terms are, Z_s the charge (Z_i is unspecified, $Z_e = -1$) in units of e the unit of elementary charge, $\boldsymbol{E}$ the electric field, $\boldsymbol{B}$ the magnetic field and c the speed of light. The term in parentheses is the total force acting on the particles, which in this case is simply the Lorentz force.

It is convenient for what follows to make a change of variables and calculate the distribution function in terms of peculiar (also known as random) velocities $\boldsymbol{v} = \boldsymbol{w} - \boldsymbol{u}(t, \boldsymbol{r})$ where $\boldsymbol{u}$ is the mean "fluid" (not particle) velocity. Under this change $(t, \boldsymbol{r}, \boldsymbol{w}) \rightarrow (t, \boldsymbol{r}, \boldsymbol{v})$, the kinetic equation (1.1) becomes

$$\frac{\mathrm{d}f_s}{\mathrm{d}t} + \boldsymbol{v} \cdot \boldsymbol{\nabla} f_s + \left(\boldsymbol{a} + \frac{Z_s e}{m_s} \frac{\boldsymbol{v} \times \boldsymbol{B}}{c} - \boldsymbol{v} \cdot \nabla \boldsymbol{u}_s \right) \cdot \frac{\partial f_s}{\partial \boldsymbol{v}} = C[f_s], \tag{1.2}$$

where $d/dt = \partial/\partial t + \boldsymbol{u}_s \cdot \nabla$ is the fluid convective derivative and $\boldsymbol{a} = (Z_s e/m)(\boldsymbol{E} + \boldsymbol{u}_s \times \boldsymbol{B}/c) - d\boldsymbol{u}_s/dt$ represents the fluid Lorentz force and acceleration terms.

To self-consistently determine the electromagnetic fields in this equation, we must also consider Maxwell's equations

$$\frac{\partial \boldsymbol{B}}{\partial t} = -c\nabla \times \boldsymbol{E}, \tag{1.3}$$

$$\sum_s Z_s e\boldsymbol{u}_s = \boldsymbol{j} = \frac{c}{4\pi}\nabla \times \boldsymbol{B}, \tag{1.4}$$

$$\sum_s Z_s n_s e \simeq 0, \tag{1.5}$$

$$\nabla \cdot \boldsymbol{B} = 0, \tag{1.6}$$

where n_s is the number density and $\boldsymbol{j}$ the current.

These differ from the standard set in that the plasma is quasi-neutral (equation (1.5)) and the displacement current $(\partial \boldsymbol{E}/\partial t)/4\pi$ has been neglected from Am-

pere's Law in equation (1.4). The first modification is valid if the typical length scales of the problem are greater than $\lambda_{Ds} = \omega_{D,s}\sqrt{T_s/m_s}$ where ω_D is the plasma frequency. In this case the ion and electron densities are approximately equal. The second modifications holds for relativistically slow flows, as the ratio of the displacement current to $c\nabla \times \boldsymbol{B}$ scales as $(u_s/c)^2$. Both conditions are readily met in the plasmas we consider here.

Equations (1.2)-(1.6) provide a complete description of the plasma. However, in all but the simplest of cases, such a treatment is entirely impractical. Not only are the equations highly nonlinear, but f_s is seven dimensional (and it describes multiple species). Instead, the general approach is to simplify this set of equations by taking moments and invoking some appropriate small parameter to close or truncate the ensuing hierarchy. As we now see, the resultant "fluid" equations are considerably simpler to solve.

1.3   Moment equations

1.3.1   Moments

The zeroth, first and second moments of the distribution function (in peculiar variables) are defined as follows

$$n_s = \int \mathrm{d}^3\boldsymbol{v} f_s, \tag{1.7}$$

$$0 = \int \mathrm{d}^3\boldsymbol{v}\boldsymbol{v} f_s, \tag{1.8}$$

$$\mathbf{P}_s = m_s \int \mathrm{d}^3\boldsymbol{v}\boldsymbol{v}\boldsymbol{v} f_s, \tag{1.9}$$

where $\mathbf{P}_s$ is the pressure tensor for species s. By our change of variables $\boldsymbol{w} \to \boldsymbol{v}$ we have removed the mean flow dependence from f_s and it is now explicit in equation (1.2). From the kinetic point of view however,

$$n_s\boldsymbol{u}_s = \int d^3\boldsymbol{w}\boldsymbol{w} f_s. \tag{1.10}$$

As an aside, it is traditional in fluid dynamics to divide $\mathbf{P}_s$ into two parts. The first

is its trace, the isotropic pressure $p_s \equiv \mathrm{Trace}(\mathbf{P}_s)/3 = m_s/3 \int \mathrm{d}^3\boldsymbol{v}\,\mathrm{Trace}(\boldsymbol{v}\boldsymbol{v})f_s = (1/2)m_s n_s v_{\mathrm{th},s}^2$ where $v_{\mathrm{th},s} = \sqrt{2T_s/m_s}$ is the particle thermal speed, T_s its temperature and from which it follows $p_s = n_s T_s$. The second part is the traceless deviatoric, or viscous, stress tensor $\mathbf{D} = \mathbf{P} - p\mathbf{I}$. Where appropriate, primarily in chapter 2, we will make use of this notation.

Returning to the moments of f_s, their evolution is governed by the corresponding moment of the kinetic equation (in which $\boldsymbol{u}_s$ is now explicit). The zeroth and first moments of equation (1.2) are

$$\frac{\mathrm{d}n_s}{\mathrm{d}t} = -n_s \nabla \cdot \boldsymbol{u}_s, \tag{1.11}$$

$$n_s m_s \frac{\mathrm{d}\boldsymbol{u}_s}{\mathrm{d}t} = -\nabla \cdot \mathbf{P}_s + Z_s e\, n_s \left(\boldsymbol{E} + \frac{\boldsymbol{u}_s \times \boldsymbol{B}}{c} \right) + \boldsymbol{R}_s, \tag{1.12}$$

where $\boldsymbol{R}_s = m_s \int \mathrm{d}^3\boldsymbol{v}\,\boldsymbol{v}\,C[f_s]$ is the mean inter-species collisional transfer of momentum (friction force) between particles of species s and all other species.

As we shall see later in this chapter, determining $\mathbf{P}_s$ is non-trivial in a magnetized plasma, but possible by virtue of the largeness of Ω_s. In a frame oriented along the magnetic field, its diagonal elements are governed by not just one, but rather two equations, one for the parallel and one for the perpendicular pressure (equivalently, one equation for the scalar pressure p and one for the pressure anisotropy). Therefore we momentarily postpone taking the second moment of the kinetic equation and instead examine the first moment. In doing so, it is convenient to re-write the ion and the electron versions as two equations: the induction equation which does not explicitly depend on $\mathbf{P}_i$ and $\mathbf{P}_e$ and the "total" momentum equation, which depends on both. (Because $\boldsymbol{u}_i$ appears on the left hand side, we sometimes refer to it as the "ion momentum" equation.)

1.3.2 Electrons & ions: Induction and momentum equations

Considering the electron version of equation (1.12) first, we can eliminate the flow $\boldsymbol{u}_e = \boldsymbol{u}_i - \boldsymbol{j}/en_e$ in favour of the ion velocity and the current using equation

(1.4). Doing so and rearranging yields

$$en_e \left(\boldsymbol{E} + \frac{\boldsymbol{u}_i \times \boldsymbol{B}}{c} \right) = \frac{\boldsymbol{j} \times \boldsymbol{B}}{c} - \nabla \cdot \mathbf{P}_e - \boldsymbol{R}_e - n_e m_e \frac{\mathrm{d}}{\mathrm{d}t_e} \left(\boldsymbol{u}_i - \frac{\boldsymbol{j}}{en_e} \right), \quad (1.13)$$

where $d/dt_e = \partial/\partial t + \boldsymbol{u}_e \cdot \nabla = \partial/\partial t + (\boldsymbol{u}_i - \boldsymbol{j}/en_e) \cdot \nabla$ is the electron convective derivative. Equation (1.13) is known as the generalised Ohm's Law (Spitzer, 1962). Depending on the regime, some, if not all, of the terms on the right hand side can be neglected as small.

Let us assume for the purposes of this thesis that:

$$T_i \sim T_e, \qquad \boldsymbol{u}_i \sim \boldsymbol{u}_e, \qquad m_i/m_e \gg 1. \qquad (1.14)$$

The first assumption is conditional on the ions and electrons having been in collisional contact long enough to equilibrate; the second, that the friction force $\boldsymbol{R}_e$ is sufficient to keep electrons at a similar velocity to ions; and the third is self evident since the proton mass is approximately 1800 times that of the electron mass. For the time being we also assume that $k\rho_i \gg \mathcal{M}$ where $k \sim \nabla$ is one over the typical gradient scale length and $\mathcal{M} = u_i/v_{\mathrm{th},i}$ is the Mach number (although in chapter 3 we will consider a case where this does not hold, but proves to be irrelevant).

Under this set of assumptions, the dominant force balance for electrons is given by the ideal Ohm's Law,

$$\boldsymbol{E} + \frac{\boldsymbol{u}_i \times \boldsymbol{B}}{c} = 0. \qquad (1.15)$$

Now combining it with Faraday's Law, equation (1.3), yields an evolution equation for the magnetic field

$$\frac{\partial \boldsymbol{B}}{\partial t} = \nabla \times (\boldsymbol{u}_i \times \boldsymbol{B}), \qquad (1.16)$$

which is the familiar ideal induction equation. The many non-ideal versions of this are simply the non-gradient terms from equation (1.13) that survive the ordering elimination. For example, $\boldsymbol{R}_e$ is responsible for resistivity whilst $\boldsymbol{j} \times \boldsymbol{B}/c$ is the Hall term (which we ordered out by assuming $k\rho_i \gg \mathcal{M}$).

The induction equation readily couples to the ion version of the momentum equation (1.12) once we write the Lorentz force in terms of the current. To do so we must either add the electron momentum equation to it (thereby eliminating the electric field) or simply replace the ion Lorentz force by the appropriate Ohm's Law. Both processes are equivalent but the latter requires us to go to an order at which the Lorentz force does not vanish (as it does in the ideal case, equation (1.15)).

Adopting the former approach, we sum the ion and electron versions of equation (1.12). Neglecting electron contributions to the momentum since $m_i u_i \gg m_e u_e$ and noting that inter-species friction forces R_s are equal and opposite (by momentum conservation), as are the particle electric forces on each species $Z_s n_s \boldsymbol{E}$, we find

$$n_i m_i \frac{\mathrm{d}\boldsymbol{u}_i}{\mathrm{d}t} = -\nabla \cdot (\mathbf{P}_i + \mathbf{P}_e) + \frac{\boldsymbol{B} \times (\nabla \times \boldsymbol{B})}{4\pi},\tag{1.17}$$

where we have used Ampere's Law equation (1.4) to eliminate $\boldsymbol{j}$ in favour of $\boldsymbol{B}$.

As they stand, equations (1.11), (1.16) and (1.17) are not a closed set because we do not yet have an expression for $\mathbf{P}_s$. Depending on the particular problem there are many ways to find it.

In the highly collisional (neutral) regime $\mathbf{P}_s$ is described by the theory of Chapman and Enskog (Chapman & Cowling, 1970) and in the highly collisional, magnetized regime by its generalisation due to Braginskii (1965). Braginskii's work lays the foundations for much of collisional magnetized transport theory. However, because it is limited to $\mathcal{M} \sim 1$, contributions from heat fluxes are omitted from $\mathbf{P}$. Later works rectified this by allowing for $\mathcal{M} \ll 1$ and thereby included heat fluxes (see Mikhailovskii & Tsypin, 1971, 1984; Catto & Simakov, 2004). Outside the collisional regime other descriptions have also been developed. In the long-wavelength collisionless regime, double adiabatic theory, or CGL theory, and its modifications to include Landau damping are applicable (Chew *et al.*, 1956; Snyder *et al.*, 1997). Anisotropic gradient-scale-length theories also exist in the form of gyrokinetics (Howes *et al.*, 2006) as well as the Kinetic MHD simplification to the kinetic equation (Kulsrud, 1962, 1983). Many other theories exist and in chapter 3 we develop one specifically tailored to the problem of pressure
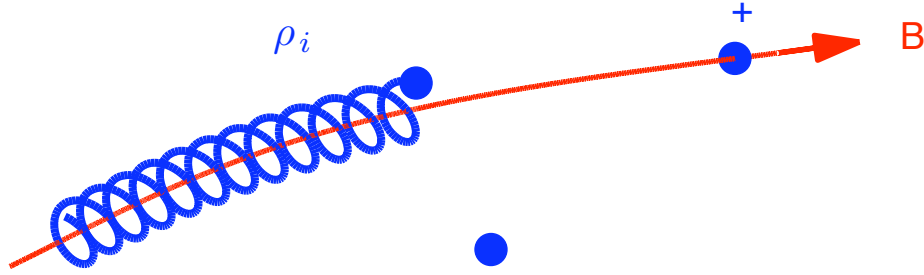
Figure 1.3: In a magnetized plasma, a positively charged ion executes Larmor orbits of radius ρ_i and frequency Ω_i about the magnetic field $\boldsymbol{B}$. Transport becomes highly anisotropic as particles are constrained to move along, but not across, field lines and the pressure tensor becomes anisotropic with respect to the direction of the local field (Dellar, 2010)

anisotropy driven micro-instabilities. However, for now we do not wish to concentrate on the particulars of any one theory. Instead we restrict ourselves to simply considering the general structure of the pressure tensor.

1.4   The pressure tensor

1.4.1   Asymptotic expansion

In a highly magnetized plasma the lowest order contribution to the distribution function (expanded as a series in the large ratio of the gyrofrequency $\Omega_s = Z_s eB/m_s c = \rho_s v_{\mathrm{th},s}$ to the remaining frequencies in the system) is *gyrotropic*, i.e. independent of the local phase angle along the Larmor orbit. This means that the zeroth order contribution of f_s to $\mathbf{P}_s$ is gyrotropic too and one must go to higher orders in the expansion to recover any gyrophase dependency. Doing so, one finds the finite Larmor radius (FLR) terms associated with the gyrophase dependency of the distribution function at first order. It is relatively easy to show the form of $\mathbf{P}$ under these rather general conditions and we do so now.

We formally assume that the frequencies associated with equation (1.2) can be

ordered to be less than Ω_s:

$$kv_{\text{th},s} \;\sim\; k\,u_s \;\sim\; \gamma \;\sim\; \gamma_e \;\sim\; \nu_s \;\sim\; \delta\,\Omega_s, \qquad \delta \ll 1 \tag{1.18}$$

where $\gamma \sim d/dt$ is the typical response frequency, γ_e is the typical electric field time scale and $\nu_s = \lambda_{\text{mfp}} v_{\text{th},s}$ is the typical collision frequency with which $C[f_s]$ scales.

Now using δ as an expansion parameter we write f_s as a series in increasing powers,

$$f_s = f_s^{(0)} + \delta f_s^{(1)} + \delta^2 f_s^{(2)} + \ldots, \tag{1.19}$$

where all terms $f_s^{(n)}$ (n an integer) are of the same order. Substituting equation (1.18) and equation (1.19) into equation (1.2) and grouping terms of the same order in δ leads to a set of coupled differential equations. To lowest order we find

$$\Omega_s \frac{\partial f_s^{(0)}}{\partial \vartheta} = 0, \tag{1.20}$$

where ϑ is the gyrophase coordinate about a Larmor orbit, defined in Cartesian velocity space by $\boldsymbol{v} = v_\parallel \boldsymbol{b} + \boldsymbol{v}_\perp = v_\parallel \boldsymbol{b} + v_\perp (\cos\vartheta\,\hat{\boldsymbol{e}}_x + \sin\vartheta\,\hat{\boldsymbol{e}}_y)$ so that $(\boldsymbol{v} \times \boldsymbol{b}) \cdot \partial/\partial\boldsymbol{v} = -\partial/\partial\vartheta$. Here $v_\parallel$ and $v_\perp$ are the particle's velocities parallel and perpendicular to the direction of the magnetic field, $\boldsymbol{b}$. As promised, $f_s^{(0)}$ is gyrotropic. Now proceeding to next order we find

$$\Omega_s \frac{\partial f_s^{(1)}}{\partial \vartheta} = \frac{\mathrm{d}f_s^{(0)}}{\mathrm{d}t} + \boldsymbol{v} \cdot \boldsymbol{\nabla} f_s^{(0)} + (\boldsymbol{a}_s - \boldsymbol{v} \cdot \nabla \boldsymbol{u}_s) \cdot \frac{\partial f_s^{(0)}}{\partial \boldsymbol{v}} - C[f_s^{(0)}], \tag{1.21}$$

where only the gyrotropic $f_s^{(0)}$ appears on the right hand side. It follows that any gyrophase dependency on the right hand side is in the coefficients of $f_s^{(0)}$ and the derivative operators acting on it. This, and the fact that we do not need to explicitly solve equations (1.20) and (1.21) for $f_s^{(0)}$ and $f_s^{(1)}$ is key to obtaining the form of the $\mathbf{P}_s$. Instead we can simply take velocity moments of the various orders of the distribution function.

1.4.2   Structure of the pressure tensor

Under an algebraic decomposition, the tensor $\boldsymbol{vv}$ can be written in terms of gyrophase-independent (first and second terms) and gyrophase dependent (final term) parts:

$$\boldsymbol{vv} = \frac{v_\perp^2}{2}(\mathbf{I} - \boldsymbol{bb}) + v_\parallel^2 \boldsymbol{bb} + \frac{\partial \mathbf{T}}{\partial \vartheta}, \tag{1.22}$$

where

$$\mathbf{T} = \left(v_\parallel \boldsymbol{b} + \frac{\boldsymbol{v}_\perp}{4}\right)(\boldsymbol{v}_\perp \times \boldsymbol{b}) + (\boldsymbol{v}_\perp \times \boldsymbol{b})\left(v_\parallel \boldsymbol{b} + \frac{\boldsymbol{v}_\perp}{4}\right). \tag{1.23}$$

Using this decomposition we can take the second moments of $f_s^{(0)}$ and $f_s^{(1)}$ to determine $\mathbf{P} = \mathbf{P}_s^{(0)} + \mathbf{P}_s^{(1)} + \dots$. The lowest order contribution to the pressure tensor is therefore given by

$$\mathbf{P}_s^{(0)} = m_s \int \mathrm{d}^3 \boldsymbol{v} \, \boldsymbol{vv} f_s^{(0)} = p_{\perp,s}^{(0)} \mathbf{I} - \left(p_{\perp,s}^{(0)} - p_{\parallel,s}^{(0)}\right) \boldsymbol{bb}, \tag{1.24}$$

where

$$p_{\perp,s}^{(0)} = \int \mathrm{d}^3 \boldsymbol{v} \frac{v_\perp^2}{2} f_s^{(0)}, \tag{1.25}$$

$$p_{\parallel,s}^{(0)} = \int \mathrm{d}^3 \boldsymbol{v} \, v_\parallel^2 f_s^{(0)}, \tag{1.26}$$

are the perpendicular and parallel pressures to zeroth order (similar expressions exist for the first order perpendicular and parallel pressures), and $\int \mathrm{d}^3 \boldsymbol{v} \, \partial \mathbf{T} / \partial \vartheta \, f_s^{(0)}$ vanishes upon integrating by parts and recalling $f_s^{(0)}$ is gyrotropic. In a frame oriented along the direction of the magnetic field $\boldsymbol{b}$, equation (1.24) is diagonal. Proceeding to first order in δ we find,

$$\mathbf{P}_s^{(1)} = m_s \int \mathrm{d}^3 \boldsymbol{v} \, \boldsymbol{vv} f_s^{(1)} = p_{\perp,s}^{(1)} \mathbf{I} - \left(p_{\perp,s}^{(1)} - p_{\parallel,s}^{(1)}\right) \boldsymbol{bb} + \mathbf{G}, \tag{1.27}$$

where, as detailed in Appendix A,

$$\mathbf{G}_s = \int \mathrm{d}^3\boldsymbol{v} f_s^{(1)} \frac{\partial \mathbf{T}}{\partial \vartheta}, \tag{1.28}$$

$$= \frac{1}{4\Omega_s} \left[\boldsymbol{b} \times \mathbf{H}_s \cdot (\mathbf{I} + 3\boldsymbol{bb}) - (\mathbf{I} + 3\boldsymbol{bb}) \cdot \mathbf{H}_s \times \boldsymbol{b} \right] + \frac{1}{\Omega_s} \left[\boldsymbol{bh}_s \times \boldsymbol{b}) + (\boldsymbol{h}_s \times \boldsymbol{b})\boldsymbol{b} \right],$$

and the tensor $\mathbf{H}_s$ and the vector $\boldsymbol{h}_s$ are given by,

$$\mathbf{H}_s = \left(p_{\perp,s}^{(0)} \nabla \boldsymbol{u}_s + \nabla \boldsymbol{q}_{\perp,s}^{(0)} \right) + \left(p_{\perp,s}^{(0)} \nabla \boldsymbol{u}_s + \nabla \boldsymbol{q}_{\perp,s}^{(0)} \right)^{\mathrm{T}}, \tag{1.29}$$

$$\boldsymbol{h}_s = \left(p_{\perp,s}^{(0)} - p_{\parallel,s}^{(0)} \right) \left(\frac{\mathrm{d}\boldsymbol{b}}{\mathrm{d}t} + \boldsymbol{b} \cdot \nabla \boldsymbol{u}_s \right) + \left(3q_{\perp,s}^{(0)} - q_{\parallel,s}^{(0)} \right) \boldsymbol{b} \cdot \nabla \boldsymbol{b}, \tag{1.30}$$

and the superscript T denotes the transpose.

Here we have introduced the zeroth order parallel fluxes of the perpendicular and parallel heat

$$\boldsymbol{q}_{\perp,s}^{(0)} = \boldsymbol{b}\, m_s \int \mathrm{d}^3\boldsymbol{v} v_\parallel \frac{v_\perp^2}{2} f_s^{(0)}, \tag{1.31}$$

$$\boldsymbol{q}_{\parallel,s}^{(0)} = \boldsymbol{b}\, m_s \int \mathrm{d}^3\boldsymbol{v} v_\parallel^3 f_s^{(0)}. \tag{1.32}$$

Combining equations (1.24) and (1.27), the total pressure tensor is given by

$$\mathbf{P}_s = \mathbf{P}_s^{(0)} + \mathbf{P}_s^{(1)}$$

$$= p_{\perp,s}\mathbf{I} - \left(p_{\perp,s} - p_{\parallel,s} \right) \boldsymbol{bb} + \mathbf{G}_s, \tag{1.33}$$

where $p_{\perp,s} = p_{\perp,s}^{(0)} + p_{\perp,s}^{(1)}$ and $p_{\parallel,s} = p_{\parallel,s}^{(0)} + p_{\parallel,s}^{(1)}$. Alternatively, splitting $\mathbf{P}_s$ into an isotropic pressure p_s and deviatoric stress $\mathbf{D}_s = [\ldots]$,

$$\mathbf{P}_s = p_s\mathbf{I} + \mathbf{D}_s \tag{1.34}$$

$$= p_s\, \mathbf{I} + \left[\frac{1}{3}(p_{\perp,s} - p_{\parallel,s})(\mathbf{I} - 3\boldsymbol{bb}) + \mathbf{G}_s \right] \tag{1.35}$$

where $p_s = (p_{\parallel,s} + 2p_{\perp,s})/3$ and, because it is traceless, $\mathbf{G}_s$ contributes only to $\mathbf{D}$. It is also important to emphasize that $\mathbf{G}$ is a factor δ smaller than the gyrotropic component of the pressure and so its significance is felt primarily at small scales where k is large.

Both equations (1.33) and (1.35) are accurate up to and including first order in δ. However, as it stands neither helps close the kinetic hierarchy because we do not yet have expressions for the pressures or heat fluxes. (In fact we shall not be overly concerned with determining the heat fluxes in this thesis and, except in the second half of chapter 3, we neglect them). Therefore, in the absence of such expressions, one might ask what was to be gained by casting the pressure tensor in this form. The answer to this question is twofold as we now explain.

1.4.3   Implications of the pressure tensor

Let us assume $p_{\perp,s} - p_{\parallel,s} \neq 0$, an assumption we will later show to be true under a wide range of circumstances. Firstly, it is immediately obvious from $\mathbf{D}_s$ that $\mathbf{P}_s$, and therefore the momentum equation, is anisotropic, as per our initial discussion. We therefore expect the dynamics of a magnetized plasma to differ from those of an unmagnetized plasma.

In chapter 2 we consider exactly such a case using a collisional closure. The anisotropy modifies the global linear behaviour of the collisional magnetized MRI leading to an enhanced growth rate for some configurations of the magnetic field, and viscous damping for others. Although no numerical simulations are yet published in this regime analogous studies have been made in the local, collisionless case by Sharma *et al.* (2006, 2007). They found, compared to an unmagnetized plasma, that there is an additional anisotropic pressure stress which is well in excess of the Reynolds stress, and comparable to the Maxwell stress. They go on to suggest that this may moderately enhance the angular momentum transport. Such differences, as well as many others, between a magnetized and unmagnetized plasma count as sufficient motivation to determine under what general conditions $\mathbf{P}_s$ is anisotropic.

The second reason for determining the general form of $\mathbf{P}_s$ is as follows, and in chapter 3 we explore this in greater detail (including nonlinearly). Pressure anisotropy driven instabilities, for example the firehose, can be shown to exist *independently* of an expression for the anisotropy, provided that $(p_{\perp} - p_{\parallel})/p < -2/\beta$ where $\beta = 8\pi nT/B^2$ is the plasma beta[3] (Schekochihin *et al.*, 2005). Similarly,

---

[3]The mirror instability may also be shown to exist when $p_{\perp} - p_{\parallel} > 1/\beta$. Correctly capturing

when $2q_{\perp,i} - q_{\parallel,i} \neq 0$ heat fluxes are a destabilising influence and the newly discovered gyrothermal instability can emerge (Schekochihin *et al.*, 2010).

For both instabilities, the term $\mathbf{G}_s$ plays a crucial role, and so any less sophisticated description of $\mathbf{P}_s$ that excludes it, for example double adiabatic theory or lowest order Braginskii theory, is inadequate. Although $\mathbf{G}_s$ is negligible in the long wavelength limit, on small scales it is crucial. For the firehose this is because, in its absence, the dispersion relation is ill-posed and predicts an ultraviolet catastrophe (infinite growth at infinitesimal wavelengths). Its effect is to regularise the instability and this much can be shown simply from the form of equation (1.35) (see Schekochihin *et al.*, 2010). For the gyrothermal instability the role of $\mathbf{G}$ is even more fundamental because it (the GTI) turns out to be an FLR instability. That is, in its absence, the GTI is not captured *at all*.

In short, equation (1.35) is a minimal description for $\mathbf{P}_s$ that both captures the pressure anisotropies inherent in a magnetized plasma whilst remaining well posed in the face of some of the microscale instabilities that they drive[4]. It is also the minimal description that captures the unstable interactions between heat fluxes and FLR terms. It is still necessary to determine the functional forms of the pressure anisotropy (we do so now) but at least we have some very crude idea of its role. (For a fully self-consistent theory it is also necessary to determine the form of the heat fluxes, but we side step that challenge here.)

1.5 Determining the pressure anisotropy

1.5.1 The CGL equations

The earliest expressions for anisotropic pressures are the CGL or double adiabatic equations of Chew *et al.* (1956). Although their equations are limited (they are for a collisionless plasma that neglects parallel Landau damping and does not include heat fluxes) they remain a good conceptual guide to the physical processes

---

the growth rates of these two pressure anisotropy driven instabilities requires closures of varying degrees of sophistication. For the firehose, a fluid closure is sufficient, whereas for the mirror, the importance of resonant particles makes a kinetic approach necessary (Kulsrud, 1983).

[4]It is not clear yet whether the mirror instability is regularised by the gyroviscous correction given by equation (1.28) and we neglect detailed discussion of this issue in this work.

at work (Kulsrud, 1983; Snyder *et al.*, 1997; Sharma *et al.*, 2006). Since it is not particularly difficult to modify these equations to include the heat fluxes and an approximate form for collisions, we now use them to explain the origin and form of the pressure anisotropy that is so important for what is to follow.

Determining the modified CGL equations is easiest to do by taking moments of the Kinetic-MHD equation (Kulsrud, 1962, 1983). This equation is entirely equivalent to taking the gyroaverage, $(1/2\pi)\int_0^{2\pi}d\vartheta$, of equation (1.21) and noting that the left hand side vanishes and, therefore, the gyroaverage of the right hand side must be zero (this is effectively a solvability condition that enforces the gyrophase periodicity of the left hand side).

The resultant equation, as given by Schekochihin *et al.* (2010), is

$$\frac{\mathrm{d}f_s^{(0)}}{\mathrm{d}t} + v_\parallel \boldsymbol{b}_0 \cdot \nabla f_s^{(0)} + \frac{v_\perp^2}{2}(\nabla \cdot \boldsymbol{b})\frac{\partial f_s^{(0)}}{\partial v_\parallel} + \boldsymbol{b} \cdot \boldsymbol{a}_s \left(\frac{v_\parallel}{v}\frac{\partial f_s^{(0)}}{\partial v} + \frac{\partial f_s^{(0)}}{\partial v_\parallel} \right) +$$

$$\boldsymbol{b}\boldsymbol{b} : \nabla \boldsymbol{u}_s \left[\left(\frac{v_\perp^2}{2} - v_\parallel^2 \right) \frac{1}{v}\frac{\partial f_s^{(0)}}{\partial v} - v_\parallel \frac{\partial f_s^{(0)}}{\partial v_\parallel} \right] - \nabla \cdot \boldsymbol{u}_s \frac{v_\perp^2}{2}\frac{1}{v}\frac{\partial f_s^{(0)}}{\partial v} = C[f_s^{(0)}],$$

$$(1.36)$$

where, because $v_\parallel = \boldsymbol{v} \cdot \boldsymbol{b}(t, \boldsymbol{r})$ is a function of space and time, we have used the following identities to obtain equation (1.36):

$$\left(\frac{\mathrm{d}f_s^{(0)}}{\mathrm{d}t} \right)_{\boldsymbol{v}} = \left(\frac{\mathrm{d}f_s^{(0)}}{\mathrm{d}t} \right)_{v,v_\parallel} + \frac{\mathrm{d}\boldsymbol{b}}{\mathrm{d}t} \cdot \boldsymbol{v} \left(\frac{\partial f_s^{(0)}}{\partial v_\parallel} \right)_v, \tag{1.37}$$

$$(\nabla f_s^{(0)})_{\boldsymbol{v}} = (\nabla f_s^{(0)})_{v,v_\parallel} + (\nabla \boldsymbol{b}) \cdot \boldsymbol{v} \left(\frac{\partial f_s^{(0)}}{\partial v_\parallel} \right)_v. \tag{1.38}$$

To obtain evolution equations for the parallel and perpendicular pressures it is not actually necessary to solve equation (1.36). Rather, as for equations (1.24) and (1.27), it is simply a matter of taking its $\int\mathrm{d}^3\boldsymbol{v}v_\parallel^2$ and $\int\mathrm{d}^3\boldsymbol{v}v_\perp^2/2$ moments.

Doing so yields,

$$\frac{\mathrm{d}p_{\perp,s}}{\mathrm{d}t} = -\nabla\cdot\boldsymbol{q}_{\perp,s} - q_{\perp,s}\nabla\cdot\boldsymbol{b} + p_{\perp,s}\left(\boldsymbol{bb}:\nabla\boldsymbol{u}_s - 2\nabla\cdot\boldsymbol{u}_s\right) - \nu_s(p_{\perp,s} - p_{\parallel,s}),$$
(1.39)

$$\frac{\mathrm{d}p_{\parallel,s}}{\mathrm{d}t} = -\nabla\cdot\boldsymbol{q}_{\parallel,s} + 2q_{\perp,s}\nabla\cdot\boldsymbol{b} - 2p_{\parallel,s}\left(\boldsymbol{bb}:\nabla\boldsymbol{u}_s + \nabla\cdot\boldsymbol{u}_s\right) - 2\nu_s(p_{\parallel,s} - p_{\perp,s}),$$
(1.40)

where we have neglected inter-species collisional heating and approximated the full Landau collision operator by the Lorentz pitch-angle scattering operator $C[f_s] = \nu_s\partial/\partial\xi((1-\xi^2)/2)\partial f_s/\partial\xi$ where $\xi = v_\parallel/v$ (see e.g. Helander & Sigmar, 2002; Rosin *et al.*, 2010*b*).

Writing the shear and divergence of the flow in terms of n_s and $\boldsymbol{B}$[5], equations (1.11) and (1.16), yields the modified version of the CGL equations:

$$p_{\perp,s}\frac{\mathrm{d}}{\mathrm{d}t}\ln\frac{p_{\perp,s}}{n_s B} = -\nabla\cdot\boldsymbol{q}_{\perp,s} - q_{\perp,s}\nabla\cdot\boldsymbol{b} - \nu_s(p_\perp - p_\parallel),$$
(1.41)

$$p_{\parallel,s}\frac{\mathrm{d}}{\mathrm{d}t}\ln\frac{p_{\parallel,s}B^2}{n_s^3} = -\nabla\cdot\boldsymbol{q}_{\parallel,s} + 2q_{\perp,s}\nabla\cdot\boldsymbol{b} - 2\nu_s(p_\parallel - p_\perp).$$
(1.42)

These are the two equations for the components of the pressure we referred to in section 1.3.

For the purposes of considering a collisionally dominated plasma, it is also useful to recast them in terms of p_s,

$$\frac{3}{2}\frac{\mathrm{d}p_s}{\mathrm{d}t} = (p_{\perp,s} - p_\parallel)\boldsymbol{bb}:\nabla\boldsymbol{u}_s + \frac{1}{2}(4p_{\parallel,s} + p_{\perp,s})\nabla\cdot\boldsymbol{u}_s - \nabla\cdot(\boldsymbol{q}_{\perp,s} + \boldsymbol{q}_{\parallel,s}), \quad (1.43)$$

and the pressure anisotropy,

$$\frac{\mathrm{d}}{\mathrm{d}t}\left(p_{\perp,s} - p_{\parallel,s}\right) = (p_{\perp,s} + 2p_{\parallel,s})\frac{\mathrm{d}\ln B}{\mathrm{d}t} - (3p_{\parallel,s} - p_{\perp,s})\frac{\mathrm{d}\ln n_s}{\mathrm{d}t}$$
$$- \nabla\cdot(\boldsymbol{q}_{\perp,s} - \boldsymbol{q}_{\parallel,s}) - 3q_{\perp,s}\nabla\cdot\boldsymbol{b} - 3\nu_s(p_{\perp,s} - p_{\parallel,s}). \quad (1.44)$$

In this form, the source terms for evolution of p_s are almost recognisable from

---

[5]Equation (1.16) describes the evolution of $\boldsymbol{B}$ in terms $\boldsymbol{u}_i$ not $\boldsymbol{u}_e$. However, recalling that electron Lorentz force is the only term that appears at lowest order in the electron force balance, equations (1.13) and (1.15), an identical electron version of equation (1.16) readily follows.

neutral fluid theory as, from left to right, viscous heating, compressive heating and the heat flux.

With the mathematical expressions for the evolution of the pressure anisotropy in place, it is worthwhile considering the associated physical mechanisms.

1.5.2   Physical origins

It is a fundamental property of a Hamiltonian system that the action, defined as $\oint \mathrm{d}\hat{q}\,\hat{p}$ around a loop, is adiabatically invariant. Here $\hat{p}$ and $\hat{q}$ are the canonical momentum and position variables (not to be confused with the p the pressure).

Neglecting collisions and heat fluxes, and assuming slowly varying fields in space and time, equation (1.18), the first adiabatic invariant of a charged particle executing Larmor orbits in a magnetic field is given by its magnetic moment $J_1 = m_s v_\perp^2 / 2B$. Here $\hat{p} = m_s v_\perp \rho_s$ is its angular momentum and $\hat{q} = \vartheta$ its gyrophase angle. Since J_1 is conserved for each particle individually, multiplying the distribution function by J_1 and carrying out a weighted average over velocity space yields the macroscopically conserved quantity,

$$\frac{\int \mathrm{d}^3\boldsymbol{v}\,J_1 f_s}{\int \mathrm{d}^3\boldsymbol{v}\,f_s} = \frac{p_{\perp,s}}{n_s B} \qquad \text{(Conserved)}. \tag{1.45}$$

It follows that if B changes (at constant n_s) then to conserve J_1, $p_{\perp,s}$ must change too, and one can even cast the equation for the magnetic moment density, $p_{\perp,s}/B$ in conservative form (Sharma *et al.*, 2006).

Similarly, if the magnetic field exhibits a local well, there is a second adiabatic invariant associated with the particle motion, the bounce frequency $J_2 = m_s v_\parallel l_M$ where l_M is the distance between mirror points at which charged particles are reflected. In this case $\hat{p} = m_s v_\parallel + e/cA_\parallel$ where $A_\parallel$ is the parallel component of the vector potential and $\hat{q}$ is a coordinate measuring the distance along the magnetic field. By conservation of fluid mass and magnetic flux $l_M \propto B/(m_s n_s)$ and so, multiplying the distribution function by $m_s J_2^2$ and, again, integrating

over velocity space yields

$$\frac{m_s \int \mathrm{d}^3\boldsymbol{v} J_2^2 f_s}{\int \mathrm{d}^3\boldsymbol{v} f_s} = \frac{p_{\parallel,s} B^2}{n_s^3} \qquad \text{(Conserved)}, \qquad (1.46)$$

which is also a macroscopically conserved quantity. Here, changes in $\boldsymbol{B}$ at constant n_s cause changes in $p_{\parallel,s}$ and the rate at which $p_{\perp,s}$ and $p_{\parallel,s}$ change with respect to $\boldsymbol{B}$ differ, leading to pressure anisotropies (see e.g. Hazeltine & Meiss, 2003; Gurnett & Bhattacharjee, 2005).

The left hand sides of equations (1.41) and (1.42) simply represent the conservation of these two constants of particle motion, and the right hand sides, departures from them.

The heat flux contributions $\boldsymbol{q}_{\perp,s}$ and $\boldsymbol{q}_{\parallel,s}$ may be simply understood as the parallel fluxes of the perpendicular and parallel pressures, $p_{\perp,s}$ and $p_{\parallel,s}$. Because we have restricted ourselves to the case where ρ_s is much less than all other length scales, the heat fluxes perpendicular to the magnetic field are suppressed from our equation. For example, in a collisionally dominated plasma, the coefficient of perpendicular thermal conductivity is a factor $(\nu_s/\Omega_s)^2 = (\rho_s/\lambda_{\mathrm{mfp},s})^2$ smaller than the parallel component (Braginskii, 1965).

As well as the heat fluxes, collisions affect the pressure anisotropy and, because of the important role they will play in this work, they require a little more discussion.

Let us consider the simple case where the heat fluxes are set to zero and the density is constant. In this case, equation (1.41) can be written as,

$$\frac{1}{B}\frac{\mathrm{d}B}{\mathrm{d}t} = \frac{\mathrm{d}p_{\perp,s}}{\mathrm{d}t} + \nu_s \Delta_s, \qquad (1.47)$$

where

$$\Delta_s \equiv \frac{p_{\perp,s} - p_{\parallel,s}}{p_{\perp,s}}, \qquad (1.48)$$

is a dimensionless measure of the pressure anisotropy. Treating the left hand side of equation (1.47) as a prescribed drive for the right hand side, it is clear that as $p_{\perp,s}$ changes, the size of the collisional term changes too. Taking the heuristic view that $p_{\parallel,s}$ is constant (of course it in fact changes, but in the "right" way for

this argument to hold), the steady state must be given by

$$\frac{1}{B}\frac{\mathrm{d}B}{\mathrm{d}t} = \nu_s \Delta_s. \tag{1.49}$$

The implication of equation (1.49) is that for a given drive, it is collisions that set the level of the anisotropy. This is true whether the source of the anisotropy is flows, heat fluxes, compression or some combination of the three.

The role of collisions is to isotropise the pressure. In their complete absence, the changing magnetic field will increase the magnitude of the anisotropy without bound (or, actually, until other processes come into play). The velocity-space dependency of a kinetic plasma makes the role of collisions especially important, relative to a fluid. For example, both kinetic and fluid systems exhibit a turbulent cascade of energy from some injection scale to a smaller, *phase-space* dissipation scale where it is irreversibly turned into heat. In both cases this relies on the existence of a non-vanishing dissipation mechanism, e.g. viscosity, resistivity, collisions, but what makes collisions especially important in a kinetic plasma, and therefore here, is their role in relaxing velocity-space structures as well as real-space structures (Abel *et al.*, 2008; Schekochihin *et al.*, 2009). This is because, fundamentally, pressure anisotropies are velocity space structures in the distribution function.

The effect of collisions on pressure anisotropies can be formalised rigourously using Boltzmann's H-theorem (briefly explored in Appendix B.0.3 and see Boltzmann, 1872; Chapman & Cowling, 1970; Hazeltine & Meiss, 2003). The upshot of the theorem is that the presence of collisions, even weak ones, irreversibly drives the distribution function towards an isotropic Maxwellian in velocity space (the state of maximum entropy)

$$f_s = \frac{n_s}{\left(\pi v_{\mathrm{th},s}^2\right)^{3/2}} e^{-v^2/v_{\mathrm{th},s}^2}. \tag{1.50}$$

Since the pressure associated with a Maxwellian is always isotropic, i.e. $p_{\perp,s} - p_{\parallel,s} = 0$, this explains why collisions limit the size of the anisotropy for a given

drive as shown in equation (1.49).

This, and the other processes described in this section, account for the form of the CGL equations (1.41) and (1.42), or alternatively equations (1.43) and (1.44). Along with the FLR corrections given by equation (1.28), these expressions represent the conceptual basis for much of the remainder of our work. Although we will not always work with them directly, the alternatives we employ (the Braginskii equations in chapter 2 and a set of specifically tailored kinetically-derived equations in chapter 3) can always be understood physically by reference to them. We have derived the CGL equations and the FLR correction to the pressure tensor here to give the reader a feel for the type of calculation which, later, we will either reference or relegate to an appendix so as not to interrupt the flow of the thesis.

1.6   Summary

In the introduction to this dissertation we have argued that understanding the behaviour of astrophysical magnetized plasmas constitutes an interesting and, as of yet, largely unsolved challenge.

Starting from the kinetic equation and Maxwell's equations we have shown that the pressure tensor is naturally anisotropic by assuming only that the magnetic field is strong, We have shown its general form, including the effect of FLR terms, and in the final section we showed how magnetic fields, heat fluxes, density variations and collisions affect it through the CGL equations, (1.41) and (1.42). These equations, along with equations for the evolution of the density (1.11), magnetic field (1.16) and momentum (1.17), (1.28) and (1.33), are the closed set (neglecting heat fluxes) from which we start our next chapter.

In chapter 2 we consider the global (retaining full radial derivatives) linear behaviour of a magnetized plasma in the presence of the shear flow of an isothermal accretion disc (specifically the galactic disc) and a time independent background magnetic field. We find an instability analogous to the MRI which, instead of being mediated by the Maxwell stress, is controlled by the anisotropic pressure stress. We work in the long wavelength limit ($k\lambda_{\mathrm{mfp}} \ll 1$) so our equations are

those of Braginskii MHD and, locally, the instability is the MVI of Balbus (2004); Islam & Balbus (2005).

We treat the system as a two parameter problem in the magnetic field strength B and and the dimensionless combination $S_B = \beta \hat{\Omega} / \nu_i$ where $\hat{\Omega}$ is the rotation rate of the disc and ν_i is the ion collision frequency. For certain isolated field configurations we show the local approximation yields incorrect results and for more general configurations show the maximum growth rate of the instability exceeds that of its unmagnetized counterpart by a factor $2\sqrt{2}$ for the galactic rotation profile. In several regimes we derive the asymptotic scaling of the maximum growth rate and Alfvén frequency at which the growth occurs with respect to B and S_B.

In chapter 3 we tackle a separate, but related problem. Working in the short wavelength limit ($k\lambda_{\mathrm{mfp}} \gg 1$) we show that the pressure anisotropies due to a decreasing magnetic field lead to the fast growing firehose instability. Initially we argue heuristically that its nonlinear evolution is expected to drive pressure anisotropies towards marginal stability values, controlled by β.

This evolution is then worked out formally in an *ab initio* kinetic calculation for the simplest analytically tractable case, that of the parallel firehose ($k_\perp = 0$) instability. The detailed results from this are presented in Appendices B and C. We use a particular physical asymptotic ordering that leads to the same expression for pressure tensor and anisotropy that we found in this chapter (but could not be assumed to hold *a priori*). The result of the kinetic calculation is a closed nonlinear equation for the firehose turbulence, which we solve numerically. We find secular ($\propto t$) growth of magnetic fluctuations and a $k_\parallel^{-3}$ spectrum, starting at scales greater than ρ_i. When a parallel ion heat flux is present, the parallel firehose instability mutates into the FLR gyrothermal instability. Its nonlinear evolution also involves secular magnetic energy growth, but its spectrum is eventually dominated by modes with a maximal scale $\sim \rho_i l_T / \lambda_{mfp}$, ($l_T$ is the parallel temperature gradient scale).

Finally, in chapter 4, we conclude with some thoughts on how our two sets of results tie together and what further questions they prompt. We present an example where the both the magnetized MRI and pressure anisotropy-driven-

instabilities may interact in an interesting way and offer some suggestions for avenues of future work.

Part II

Magnetized MRI

Chapter 2

Magnetized MRI

2.1 Introduction

The formation of compact objects such as stars, planets and black holes from accretion discs requires angular momentum transport. Turbulence driven by the magnetorotational instability (MRI), and possibly the magnetoviscous instability (MVI), offers a promising mechanism for this transport (Velikhov, 1959; Chandrasekhar, 1960; Balbus & Hawley, 1991)[1]. It has also been suggested that the observed velocity fluctuations $\sim 6\,\mathrm{km\,s^{-1}}$ in the warm HI (neutral hydrogen) parts of the interstellar medium (ISM) with low star formation rates may, in part, arise from this process (Sellwood & Balbus, 1999; Tamburro *et al.*, 2009). The evidence for this comes primarily from numerical simulations and a wide range of studies agree that weak magnetic fields and outwardly decreasing angular velocity profiles are an unstable combination (Balbus & Hawley, 1998; Balbus, 2003).

The most illuminating explanation for this comes from a shearing sheet analysis in which the mean azimuthal flow of the differentially rotating disc is locally approximated by a constant angular velocity rotation plus a linear velocity shear (Goldreich & Lynden-Bell, 1965; Umurhan & Regev, 2004). In the simplest pos-

---

[1]Careful reading of Velikhov (1959) reveals the following acknowledgement: "The author is deeply grateful to S.I. Braginskii for assigning the problem and for valuable suggestions during the course of its solution." This is well over forty years before Braginskii's work on anisotropic viscosity was being evoked in connection with the MRI.

sible setup, incompressible, isothermal, dissipationless, axisymmetric linear perturbations to a magnetic field with a weak vertical component, i.e. parallel to the rotation axis of the disc, are unstable when the angular velocity decreases away from the disc's centre. Azimuthal velocity perturbations to fluid elements at different heights, tethered to each other by the magnetic field, increase (decrease) their angular momentum. This causes them to move to larger (smaller) radii as dictated by the gravitational field which sets the mean flow. In the frame rotating at constant angular velocity, this motion deforms the tethering magnetic field, provided it is not too strong, and this induces a prograde (retrograde) Lorentz force on the outer (inner) element thus destabilising the system as it moves to yet larger (smaller) radii. This mechanism is at the heart of the MRI.

This model and description captures much of the essential physics, but to fully understand the MRI, or at least the framework in which the shearing sheet should exist, a more nuanced approach is needed. In part this is because the shearing sheet is formulated in a Cartesian coordinate system, where curvature terms that arise naturally from the cylindrical geometry of an accretion disc are neglected. Indeed, in the local approximation, the over-stabilising effects of hoop tension (a curvature effect) associated with the azimuthal magnetic field are totally ignored. Furthermore, the model predicts that the fastest growing, and therefore most physically relevant, MRI modes have a homogeneous radial structure on the scale of the shearing sheet in which the local approximation is made. This means that the global disc structure, including boundary conditions, not captured by the local approximation may have a significant effect on these large scale modes in a way that cannot be determined locally. There are other limitations to this method but they are beyond the scope of this thesis (Regev & Umurhan, 2008).

The extents to which these limitations matter have been investigated linearly by ideal global analyses that take into account the full radial structure of the disc and its boundaries (Dubrulle & Knobloch, 1993; Curry *et al.*, 1994; Curry & Pudritz, 1995; Ogilvie & Pringle, 1996; Pino & Mahajan, 2008; Mahajan & Krishan, 2008), and specifically for the galaxy, Kitchatinov & Rüdiger (2004). The conclusions of these investigations largely confirm the local picture of a large radial scale instability driven by the differential rotation of the disc. In the nonlinear regime,

a recent local investigation by Guan *et al.* (2009) used two-point correlation functions to study turbulent MRI motions in ideal MHD. Their results, for zero net magnetic flux and mean azimuthal magnetic field configurations, indicate that density, velocity and magnetic fields decorrelate on local scales $\sim$ the disc scale height (which is of order the shearing sheet simulation box size) in all directions[2]. This combination of studies suggest that a local MRI analysis is generally correct (especially in the nonlinear regime where modes are well confined to the shearing sheet). Nevertheless, at least linearly, the regime of validity for these results must be checked globally. It is the purpose of this work to do just that for the MRI operating in a collisional, magnetized plasma (like the ISM).

As we have seen in chapter 1, the deviatoric stress tensor of such a plasma is naturally anisotropic. In the collisional regime, the pressure anisotropy is equal to the parallel gradient of the parallel component component of the rate of strain tensor times a coefficient μ_B and so the stress tensor can be formulated as an anisotropic viscosity (Braginskii, 1965). Although we do not consider it here, thermal conduction also becomes anisotropic in a magnetized plasma, leading to different values for the perpendicular and parallel heat fluxes. This last fact is responsible for both the magnetothermal instability (MTI) and the heat flux buoyancy instability (HBI) that arise in the presence of temperature gradients (Balbus, 2000, 2001; Quataert, 2008). Ignoring these instabilities (our system is isothermal), we concentrate on the interaction between the magnetic field and the Braginskii viscosity in the presence of a (galactic) shear flow (Balbus, 2004; Islam & Balbus, 2005).

We conduct a global linear stability analysis for three separate, galactically relevant, background magnetic field orientations: purely azimuthal, purely toroidal and pitched (magnetic field lines follow helical paths on cylinders of constant radius). In agreement with earlier local studies, we find that when the field has both a vertical and an azimuthal component, a linear instability with a real part up to $2\sqrt{2}$ times faster than the MRI emerges (Balbus, 2004; Islam & Balbus, 2005). In contrast to local studies we also find that it has a travelling wave

---

[2]Guan *et al.* (2009) also find that the largest correlation lengths exist between rotationally modified sound waves excited by MHD turbulence. Such motions are filtered out under the assumption of incompressibility, thereby 'localising' the MRI yet further.

component and this varies with the size of the viscous coefficient.

In the presence of a vertical field, we also recover the standard inviscid MRI. Upon introducing the Braginskii viscosity we find its growth rate is always reduced, and significantly so when Re $\lesssim$ 1. A similar effect is found for a purely azimuthal field where we find that the Braginskii viscosity damps modes that are, inviscidly, neutrally stable. In the case of vertical and pitched fields, the instability we find is the Braginskii-modified-MRI, or MVI in the limit of vanishing Lorentz force, (closely related to the collisionless MRI of Quataert *et al.* (2002); Sharma *et al.* (2003)).

The structure of this chapter is as follows. In section 2.2 we summarise the conditions in our physical example, the ISM, and introduce the model and governing equations we use to describe it. (For the reader primarily interested in our mathematical treatment of the instability, rather than an astrophysical example where it is relevant, we suggest skipping directly to section 2.2.3.) In section 2.3, we introduce and perturb a series of equilibrium solutions which form the basis of our global stability analysis. We combine the perturbed equations into a single ODE which we analyse in the following sections. In sections 2.4 – 2.6 we consider the stability of a purely azimuthal field, a purely vertical field, and a slightly pitched field, respectively. For each case we compare and contrast the inviscid behaviour to the behaviour in the presence of the Braginskii viscosity. In section 2.7 we provide a physical explanation of the instability and its dependence on the magnetic field orientation. We also examine the similarities and differences between the global and local results. After this we discuss some potential issues in modelling the magnetized MRI within the uniform disc approximation and fluid regimes. Finally, in section 2.8, we summarise our findings.

2.2   Galactic discs

2.2.1   Conditions in the ISM

The study of magnetized accretion discs has attracted increasing attention in recent years in both the collisionless (Quataert *et al.*, 2002; Sharma *et al.*, 2003,

2006, 2007) and collisional regimes (Balbus, 2004; Islam & Balbus, 2005; Ferraro, 2007; Mikhailovskii *et al.*, 2008; Devlen & Pekünlü, 2010). However, a number of fundamental questions, like those mentioned in section 1.1, remain unanswered. Primarily, what is the non-linear fate of the MRI in a collisional magnetized plasma, i.e. one where the pressure anisotropy is described by the Braginskii viscosity? Does it transport angular momentum and if so, is the transporting stress primarily viscous, Maxwell or Reynolds[3] (Balbus & Hawley, 1998)? On what scales do the most unstable modes emerge and how does this vary with the system parameters (Curry & Pudritz, 1995; Sharma *et al.*, 2003; Islam & Balbus, 2005)? In what regime will local analysis become untenable and global effects (either radial or vertical) become important (Gammie & Balbus, 1994; Guan *et al.*, 2009)? What effect does the presence, or absence, of a net vertical field have given Cowling's anti-dynamo theorem and the dissipative properties of the Braginskii viscosity (Moffatt, 1978; Balbus & Hawley, 1998; Lyutikov, 2007)? Could viscous heating from the Braginskii viscosity lead to secondary magnetized or unmagnetized thermal instabilities (Balbus, 2001; Piontek & Ostriker, 2005, 2007; Quataert, 2008; Kunz *et al.*, 2010)? Do channel solutions, or something approaching them, emerge (Goodman & Xu, 1994)? If they do, the associated field growth will generate pressure anisotropies that could feed new parasitic instabilities such as the mirror. What would their effects be at this stage and in the inevitable turbulence where the firehose instability will also arise (see chapter 3)?

Addressing these questions will require a two-pronged approach involving both numerical and analytic studies. It may transpire that much of the existing work on the unmagnetized MRI is directly applicable, but determining this requires a rigorous treatment and as such, the subject of this work is a global stability analysis for the magnetized MRI. The mathematical results in this chapter should be applicable to any magnetized accretion disc with a radially decreasing angular velocity profile. However, it is helpful to provide a physical example where our results are expected to hold.

---

[3]Simulations in the collisionless regime by Sharma *et al.* (2006) shows that there is angular momentum transport and the anisotropic pressure constitutes a significant portion of the total stress ($\sim$ Maxwell and $\gg$ Reynolds).

We consider the ISM of a spiral galaxy, a system for which a range of analytic and numerical unmagnetized MRI studies already exist (Kim *et al.*, 2003; Kitchatinov & Rüdiger, 2004; Dziourkevitch *et al.*, 2004; Piontek & Ostriker, 2005, 2007; Wang & Abel, 2009). This choice is motivated by the fact that our theory is developed for a disc with an angular velocity profile that varies inversely with radius, and this closely resembles a galactic rotation profile. Further motivation comes from Sellwood & Balbus (1999) who have argued that in the H I region outside the optical disc of a spiral galaxy, the velocity dispersion measurements of $\sim 5-7$ km s^{-1} may be driven by the differential rotation of the disc, mediated by the MRI. (Inside the optical disc, supernovae and other processes drive the same velocity dispersions.) Since the ISM is a varied multiphase system (cold atomic and molecular clouds, warm atomic and ionized gas, and hot ionized gas) both their study and ours does not pertain to much, $\gtrsim 1/2$ by mass, of the medium. Whether this should be rectified (to include the remaining phases) seems unnecessary, at least for the magnetized MRI, since the interstellar clouds are too cold to be magnetized and the hot ionized gas too buoyantly unstable for the MRI to have any obviously significant effect (Ferrière, 2001).

On this basis, we concentrate on the warm ISM in the quiescent regions of a typical spiral galaxy where the plasma is subject to a weak magnetic field and an outwardly decreasing angular velocity profile. Generally it is magnetized and so, on large scales, the naturally occurring pressure anisotropy can be described in terms of the Braginskii viscosity. In order to show this and to determine the equations that govern the system, we must set the ion parameters. We adopt the set of fiducial values found in (Binney & Tremaine, 1988; Beck *et al.*, 1996; Ferrière, 2001). Our numbers are similar to those of NGC1058, the well studied face-on disc galaxy considered by Sellwood & Balbus (1999). These are:

- Particle number density (the same for ion and electron)

$$n \sim 0.3 \text{ cm}^{-3}. \tag{2.1}$$

- Assuming ions and electrons are in thermal equilibrium viz. equation (1.14),

the temperature is

$$T \sim 5 \times 10^4 \text{ K}, \tag{2.2}$$

and consequently the ion thermal speed is

$$v_{\text{th},i} = \left(\frac{2T_i}{m_i} \right)^{1/2} \sim 3 \times 10^6 \text{ cm s}^{-1}, \tag{2.3}$$

where m_i is the mass of hydrogen and T_i is in erg. The ion Debye length is

$$\lambda_{Di} = \frac{v_{\text{th},i}}{\omega_{Di}} = v_{\text{th},i} \left(\frac{4\pi e^2 n_i}{m_i} \right)^{-1/2} \sim 4 \times 10^4 \text{ cm}. \tag{2.4}$$

- The ion collision frequency (in seconds, assuming n_i in cm^{-3}, T_i in K and the Coulomb logarithm $C_l = 25$) is[4]

$$\nu_i \sim 1.5 n T_i^{-3/2} \sim 4 \times 10^{-8} \text{ s}^{-1}, \tag{2.5}$$

and consequently, the mean free path is

$$\lambda_{\text{mfp}} = \frac{v_{\text{th},i}}{\nu_i} \sim 7 \times 10^{13} \text{ cm}. \tag{2.6}$$

- The observed mean magnetic field strengths vary between galaxies but on the lower end of the scale are at the present time (Beck *et al.*, 1996),

$$B \sim 2 \times 10^{-6} \text{ G} \qquad \text{(present)}. \tag{2.7}$$

However, if the MRI is the dominant turbulence generating mechanism in the ISM, this figure must represent the saturated state of the magnetic field. One must assume that present field strengths have been amplified over time; it follows that at some earlier time they were weaker (e.g. Malyshkin & Kulsrud, 2002; Kitchatinov & Rüdiger, 2004).

To ensure our theory is fluid-like (see section 2.2.2) the most unstable modes

---

[4]In a thermalised plasma ν_i is dominated by the ion-ion collision frequency (ion-electron collisions are sub-dominant) and the full expression for this is given by $\nu_i = 4\sqrt{\pi} n e^4 C_l / 3 m_i^2 T^{3/2}$ where e is the elementary charge and T is in erg (Spitzer, 1962).

must exist above λ_{mfp}. Accordingly, we adopt the following value for the historical "initial" field strength:

$$B \sim 2 \times 10^{-10} \text{ G} \qquad \text{(initial)}. \tag{2.8}$$

The origin of this initial value is beyond the scope of this thesis but see the following for interesting discussion: Kulsrud (1999); Brandenburg & Subramanian (2005).

For a plasma in this "initial" era, or the ISM in a galaxy where the magnetic field is not saturated, the ion plasma beta is

$$\beta_i = \frac{8\pi n_i T_i}{B^2} \sim 1.3 \times 10^9, \tag{2.9}$$

the ion cyclotron frequency is

$$\Omega_i = \frac{eB}{m_i c} \sim 2 \times 10^{-6} \text{ s}^{-1}, \tag{2.10}$$

the ion Larmor radius is

$$\rho_i = \frac{v_{\mathrm{th},i}}{\Omega_i} \sim 1.5 \times 10^{12} \text{ cm}, \tag{2.11}$$

and the plasma is magnetized $\Omega_i \gg \nu_i$ (and will become even more so if the magnetic field becomes stronger).

- The typical rotation rate of a spiral galaxy is

$$\hat{\Omega} \sim 5 \times 10^{-16} \text{ s}^{-1}. \tag{2.12}$$

A typical radius for the outer edge of the optical disc, or indeed the corotation radius between spiral arms where magnetized shear instabilities may be important (private correspondence: Shukurov, 2010), is

$$r \sim 3 \times 10^{22} \text{ cm}. \tag{2.13}$$

Outside the optical disc the vertical scale-height is

$$H \sim 10^{21} \text{ cm,} \tag{2.14}$$

and so the disc is thin. The measured system-scale rotation (not turbulent) velocity is

$$U \sim 2 \times 10^7 \text{ cm s}^{-1}. \tag{2.15}$$

- The magnetic Prandtl number P_m, the ratio of the viscous coefficient (in this case μ_{B} for the Braginskii viscosity) and the resistivity η, is[5]

$$P_m = \frac{\mu_{\text{B}}}{\eta} \simeq 7.5 \times 10^{-6} \frac{T^4}{n} \sim 7.5 \times 10^{13}, \tag{2.16}$$

where T is in K.

- The dimensionless parameter S_B that characterises the relative effectiveness of kinetic magnetization and dynamic magnetic fields will be important for what follows[6]. It can be estimated as

$$S_B = \frac{\mu_{\text{B}}\hat{\Omega}}{B^2} = \frac{\beta_i\hat{\Omega}}{2.88\,\nu_i} \sim 2.3 \times 10^{-15} \frac{\hat{\Omega}T^{5/2}}{B^2} \sim 15, \tag{2.17}$$

for the conditions above (although we consider larger values later).

2.2.2 Model assumptions

On the basis of the parameters given in section 2.2.1, our galactic disc model is as follows. Working in cylindrical polar coordinates (r, ϕ, z) we consider a thin, gravitationally constrained, differentially rotating disc made up of an isothermal,

---

[5]The coefficient of the Braginskii viscosity is given by $\mu_{\text{B}} = 2.88\,p_i/m_i n\nu_i$. The expression for the Spitzer resistivity is given by $\eta = 3\sqrt{2m_e/\pi}c^2C_le^2T^{-3/2}$, where m_e is the electron mass and T is in erg (Spitzer, 1962; Braginskii, 1965).

[6]In the collisionless regime, the dependency of the MRI growth rate on the relative importance of kinetic magnetization and dynamic magnetic fields was first noted by Quataert *et al.* (2002) and Sharma *et al.* (2003). Amongst other things they showed the transition between the collisionless and collisional MRI in a local setting as a function of this parameter. We recover their results in the local limit, see Figures 3 and 4 of Quataert *et al.* (2002) and Figure 2 of Sharma *et al.* (2003).

incompressible, magnetized plasma fluid whose motion is restricted by an inner boundary at some finite radius r_0. We treat the structure in the plane of the disc globally but ignore the vertical structure perpendicular to the plane by considering scales much less than the vertical scale height of the disc $H \sim c_s/\hat{\Omega} \sim$ where c_s is the isothermal sound speed (see Gammie & Balbus (1994) for global-in-z analysis). Throughout we treat the ion mass density $n_i m_i$ as constant and absorb it into our definitions of the thermal pressure and magnetic field $B/\sqrt{4\pi n m_i} \to B$ so the latter is now equivalent to the Alfvén speed. On the basis of equation (2.16), we neglect η and take the Braginskii viscosity to be the only dissipative process in our system.

Within this framework we allow for a steady equilibrium state which varies on spatial scales of order r_0 and perturbations to it that vary with a vertical wavenumber k. Physically, we expect the growth rate $\gamma \sim \hat{\Omega}$ and this will be justified by our subsequent results. Formally these model assumptions can be expressed as a hierarchy of time-scales which are well satisfied for our set of parameters,

$$\frac{1}{\Omega_i} \ll \frac{1}{\nu_i} \ll \frac{1}{kc_s} \ll \frac{1}{\hat{\Omega}} \ll \frac{1}{\hat{\Omega}}\frac{r_0}{H}. \tag{2.18}$$

From left to right, these inequalities correspond to: the plasma being magnetized, the plasma being collisional (i.e., a fluid), the disc being uniform in the vertical direction, and, finally, the disc being thin. The first two inequalities are illustrated in Figure 2.1.

Whilst the uniformity-in-z ordering in equation (2.18) gives a lower bound on the order of k we must look to the physics of the MRI to find an upper bound. First we split the magnetic field into a vertical and azimuthal component (so as to construct a time independent equilibrium, we neglect radial magnetic fields[7]). That is, $\boldsymbol{B} = B_z \hat{\boldsymbol{e}}_z + B_\phi \hat{\boldsymbol{e}}_\phi = B(\sin\theta \hat{\boldsymbol{e}}_z + \cos\theta \hat{\boldsymbol{e}}_\phi)$ where $\theta = \arctan(B_z/B_\phi)$ is the pitch angle of the magnetic field. The vertical Alfvén frequency is $\sigma = kB_z =$

---

[7]Although magnetic field configurations vary from galaxy to galaxy, they are commonly found tracing the spiral arms and therefore, in the plane of the disc, predominantly azimuthal. Beck *et al.* (1996) gives values for the mean in-plane field $B_r/B_\phi \sim 0.25$ thereby justifying, to some degree, our neglect of the radial field.
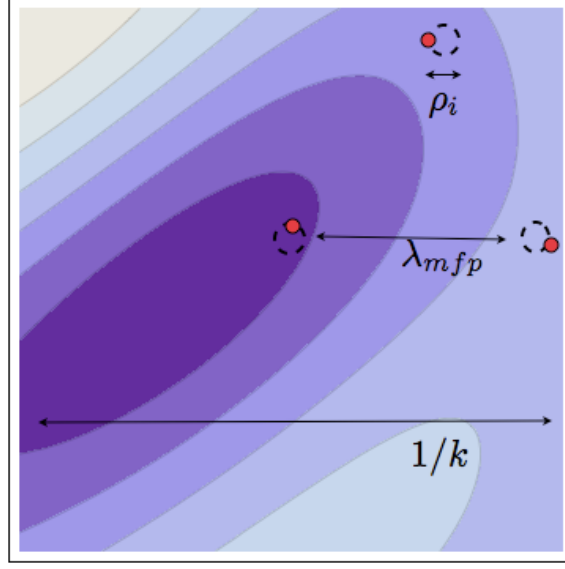
Figure 2.1: In the long wavelength (collisional) regime plasma, $1/k \gg \lambda_{\mathrm{mfp}} \gg \rho_i$ (or equivalently $1/kc_s \gg 1/\nu_i \gg 1/\Omega_i$), the pressure anisotropies that occur naturally in a magnetized plasma can be directly related to the rate of strain tensor, viz. equations (2.24) and (2.27).

$kB\sin\theta$, and locally we have

$$\sigma_{n,\mathrm{m}}^2 = -\frac{1}{4}\frac{\mathrm{d}\hat{\Omega}^2}{\mathrm{d}\ln r}\left(1 + \frac{\kappa^2}{4\hat{\Omega}^2}\right), \qquad \sigma_{\mathrm{c}}^2 = -\frac{\mathrm{d}\hat{\Omega}^2}{\mathrm{d}\ln r}. \tag{2.19}$$

The growth rate of the vertical field instability peaks for the maximizing Alfvén frequency $\sigma_{n,\mathrm{m}}$ and is suppressed for the critical Alfvén frequency σ_{c}. Here, $\kappa^2 = 2\hat{\Omega}(2\hat{\Omega} + \mathrm{d}\hat{\Omega}/\mathrm{d}\ln r)$ is the square of the epicyclic frequency.

This implies that for fixed $\hat{\Omega}$, as B decreases, the range of unstable wavenumbers increases. It follows that at some critically weak field, there will be an unstable wavenumber such that $k\lambda_{\mathrm{mfp}} \gtrsim 1$ which would invalidate the fluid approximation. Therefore our theory describes unstable modes only in the regime where

$$\frac{\hat{\Omega}}{c_s} \ll k < \frac{\hat{\Omega}}{B\sin\theta} \text{ and } \frac{1}{\lambda_{\mathrm{mfp}}}. \tag{2.20}$$

This assumption will be justified later when we show the scalings between σ_c and

Ω also hold globally.

Similarly, for small values of B and S_B, the scaling of maximizing wavenumber with B, holds globally and later we make use of this to guide our asymptotic ordering.

2.2.3 Governing equations

In the long wavelength regime ($k\lambda_{\mathrm{mfp}} \ll 1$), the set of closed equations found in chapter 1 can be further simplified; in particular the pressure tensor $\mathbf{P}$ given by equation (1.35). Its gyrophase-dependent component $\mathbf{G}$ can be neglected as a factor ku_s/Ω_s smaller than the remaining terms (see section 1.4.2) and so:

$$
\begin{aligned}
\mathbf{P}_s &= p_s\mathbf{I} + \mathbf{D}, \\
&= p_s\mathbf{I} + \frac{1}{3}p_{\perp,s}\Delta_s(\mathbf{I} - 3\boldsymbol{bb}),
\end{aligned}
\tag{2.21}
$$

and the pressure anisotropy Δ_s itself can be related to the ion rate of strain tensor as we now demonstrate.

The fact that all the frequencies, barring Ω_i, are small compared to ν_i in the long wavelength regime has two consequences (which are also true for electrons). First, as shown by equation (1.49), collisions are strong enough to bring the system into steady state faster than the changing magnetic field can bring it away. Second, the size of the anisotropy $\Delta_s \ll 1$ will be "small" (although as we will see later, large enough to have dramatic effects).

In this case the ion pressure anisotropy, as given by equation (1.44) (or equation (1.49)) yields the expression[8]

$$
\Delta_i = \frac{1}{\nu_i}\frac{\mathrm{d}\ln B}{\mathrm{d}t} = \frac{1}{\nu_i}\boldsymbol{bb} : \nabla\boldsymbol{u}_i \simeq 3\frac{\mu_{\mathrm{B}}}{p_i}\boldsymbol{bb} : \nabla\boldsymbol{u}_i,
\tag{2.22}
$$

where we have used equation (1.16) to re-write the evolution of $\boldsymbol{B}$ in terms of the strain and the factor of 3 in the definition of μ_{B} comes from the full kinetic calculation (Braginskii, 1965). A similar equation exists for electrons.

---

[8]Working in the slow-flow regime $\mathcal{M} \ll 1$ Mikhailovskii & Tsypin (1971, 1984) have calculated, kinetically, the analogous equation including the contribution from heat fluxes.

Now, recall that $T_i \sim T_e$, $\boldsymbol{u}_i \sim \boldsymbol{u}_e$ and $m_i \gg m_e$, viz. equation (1.14). From this it follows that $\nu_i \sim (m_i/m_e)^{1/2}\nu_e$ and so the electron pressure anisotropy is massively sub-dominant to the ion equivalent, i.e. $|\Delta_i| \gg |\Delta_e|$, but the isotropic pressures are comparable, i.e. $p_i \sim p_e$, (Spitzer, 1962; Helander & Sigmar, 2002). As a a result, the total pressure tensor is given by

$$\begin{aligned} \mathsf{P} &= \sum_{s=i,e} p_s \mathsf{I} + \frac{1}{3}p_{\perp,s}\Delta_s(\mathsf{I} - 3\boldsymbol{bb}), \\ &= (p_i + p_e)\,\mathsf{I} + \mu_{\mathrm{B}}\,(\mathsf{I} - 3\boldsymbol{bb})\,\boldsymbol{bb} : \nabla\boldsymbol{u}_i. \end{aligned} \tag{2.23}$$

This expression for the deviatoric component of the pressure tensor is simply the lowest order contribution (in the small parameter $\nu_i/\Omega_i \ll 1$) of the ion Braginskii viscosity (Braginskii, 1965). Substituting this into the momentum equation (1.17) the equations describing the system are those of ideal MHD with the Braginskii viscosity (e.g. Lifshitz *et al.*, 1984; Schekochihin *et al.*, 2005). Explicitly they are the momentum equation (1.17) including the Braginskii stress tensor and, for the first time, gravity; the induction equation (1.16); the continuity equation in the incompressible limit, equation (1.11); and the viscous stress tensor itself. Collecting them together, we have:

$$\frac{\partial \boldsymbol{u}_i}{\partial t} + \boldsymbol{u}_i \cdot \nabla \boldsymbol{u}_i = -\nabla\Pi + \boldsymbol{B} \cdot \nabla\boldsymbol{B} - \nabla\Phi_{\mathrm{D}} - \nabla \cdot \mathsf{D}, \tag{2.24}$$

$$\frac{\partial \boldsymbol{B}}{\partial t} + \boldsymbol{u}_i \cdot \nabla\boldsymbol{B} = \boldsymbol{B} \cdot \nabla\boldsymbol{u}_i, \tag{2.25}$$

$$\nabla \cdot \boldsymbol{u}_i = 0\,, \tag{2.26}$$

$$\mathsf{D} = \mu_{\mathrm{B}}\,(\mathsf{I} - 3\boldsymbol{bb})\,\boldsymbol{bb} : \nabla\boldsymbol{u}_i. \tag{2.27}$$

Recall that the mass density is constant and has been absorbed into our definitions. Here, $\Pi = p_i + p_e + B^2/2$ is the total gas plus magnetic pressure and Φ_{D} is the gravitational potential we now use to set the equilibrium flow in our global stability analysis.

2.3   Global stability analysis

2.3.1   Equilibrium solutions

In this section we introduce equilibrium solutions to equations (2.24)-(2.27) that
describe a differentially rotating global shear flow constrained by gravity and
threaded by a magnetic field that lies on cylinders of constant radius. In these
solutions, by virtue of the scalings given in equation (2.18), it is gravity $\nabla \Phi_\mathrm{D}$
that dictates the rotation profile of the equilibrium flow $\hat{\Omega} = \hat{\Omega}_0 (r/r_0)^{-q}$. $\hat{\Omega}_0$ is
the rotation frequency at the inner boundary and q is a dimensionless measure of
the shear. We are interested in the case of $q = 1$, which is analytically treatable.
Physically, this corresponds to a galactic disc where, unlike the Keplerian case
of $q = 3/2$, the gravitational potential of the *dark matter halo* sets the rotation
profile (Rubin & Ford, 1970; Sofue & Rubin, 2001). In modelling this we set
the dark matter mass distribution (whose sole purpose is to ultimately set the
rotation profile) to be inversely proportional to r and, via Poisson's equation,
the potential to be $\Phi_\mathrm{D} \propto r(\ln r - 1)$ (Mestel, 1963). In this case, the flow
$\boldsymbol{u}_i = \hat{\Omega}(r) r \hat{\boldsymbol{e}}_\phi = \hat{\Omega}_0 r_0 \hat{\boldsymbol{e}}_\phi$ does not vary with radius.

At this stage we do not specify the pitch angle θ at which the magnetic field
lies. However, for mathematical simplicity, we demand that both B_ϕ and B_z
are independent of radius so θ remains constant. Whilst this implies a vertical
current $\propto 1/r$ is associated with B_ϕ, a simple super-galactic magnetic field can
account for B_z. If the B_z is also bound by equation (2.20), we can ensure the
system will be unstable to the inviscid MRI (but only treatable by fluid theory if
the λ_mfp condition holds too). Our equilibrium flow and magnetic fields therefore
take the form

$$\boldsymbol{u}_i = \Omega_0 r_0 \hat{\boldsymbol{e}}_\phi, \qquad \boldsymbol{B} = B_z \hat{\boldsymbol{e}}_z + B_\phi \hat{\boldsymbol{e}}_\phi, \tag{2.28}$$

and are constant in space in and time.

It is a mathematically convenient feature of our equilibrium solutions that there is
no evolution of the magnetic field strength and therefore no pressure anisotropy.
This means that pressure anisotropy driven instabilities such as the mirror are

not present (Schekochihin *et al.*, 2005). Additionally, this implies that the viscous stress tensor **D** is zero, and equations (2.24)-(2.27) admit an ideal MHD solution. This is in contrast to the case where Laplacian viscosity (or indeed resistivity) is present, and hence we can construct an ideal MHD solution independent of any radial flows (Kersalé *et al.*, 2004).

2.3.2   Perturbed equations

To determine the stability of this system we introduce small axisymmetric perturbations to our equilibrium solutions to equations (2.24)-(2.27). We allow the velocity to vary as $\delta \boldsymbol{u}_i = \delta \boldsymbol{u}_i(r) \exp[\mathrm{i}kz + \gamma t]$ and similarly for the magnetic and pressure fields. As before k is the wavenumber in the z direction and γ the growth rate. We retain curvilinear terms arising from the cylindrical geometry but neglect self-gravity and terms quadratic in the perturbed quantities. This leads to a set of coupled equations for the components of the flow and magnetic field. Substituting in our equilibrium plus perturbed solutions, non-dimensionalising with respect to time-scales $\hat{\Omega}_0$ and length-scales r_0, and writing $\mu_{\mathrm{B}} = S_B B^2$ from equation (2.17), the components are as follows

$$\gamma \delta u_{r,i} = 2\frac{\delta u_{\phi,i}}{r} - \frac{\mathrm{d}\delta\Pi}{\mathrm{d}r} + \mathrm{i}\sigma\delta B_r - 2\frac{B\cos\theta\delta B_\phi}{r} - \frac{\mathrm{d}\delta Z}{\mathrm{d}r} - 3\frac{\cos^2\theta}{r}\delta Z, \quad (2.29)$$

$$\gamma \delta u_{\phi,i} = -\frac{\delta u_{r,i}}{r} + \frac{B\cos\theta\delta B_r}{r} + \mathrm{i}\sigma\delta B_\phi + 3\mathrm{i}k\frac{\sin 2\theta}{2}\delta Z, \quad (2.30)$$

$$\gamma \delta u_{z,i} = -\mathrm{i}k\delta\Pi + \mathrm{i}\sigma\delta B_z - \mathrm{i}k(1 - 3\sin^2\theta)\delta Z, \quad (2.31)$$

$$\gamma \delta B_r = \mathrm{i}\sigma\delta u_{r,i}, \quad (2.32)$$

$$\gamma \delta B_\phi = \mathrm{i}\sigma\delta u_{\phi,i} - \frac{\delta B_r}{r} + \frac{B\cos\theta\delta u_{r,i}}{r}, \quad (2.33)$$

$$\gamma \delta B_z = \mathrm{i}\sigma\delta u_{z,i}, \quad (2.34)$$

$$\mathrm{i}k\delta u_{z,i} = -\frac{1}{r}\frac{\mathrm{d}(r\delta u_{r,i})}{\mathrm{d}r}, \quad (2.35)$$

$$\delta Z = S_B B^2 \left[\left(\cos^2\theta - \mathrm{i}\frac{k}{\gamma}\frac{\sin 2\theta}{2}\right)\frac{\delta u_{r,i}}{r} + \right.$$

$$\left. \mathrm{i}k\sin^2\theta\delta u_{z,i} + \mathrm{i}k\frac{\sin 2\theta}{2}\delta u_{\phi,i} \right], \quad (2.36)$$

where, once again, $\sigma = kB \sin \theta$ is the Alfvén frequency that measures the tension of the vertical field (it is always zero for $\theta = 0$) and we have written $Z = S_B B^2 \boldsymbol{bb} : \nabla \boldsymbol{u}_i$. Equations (2.29)-(2.36) form a closed set which we can combine into a single differential equation.

Eliminating the perturbed magnetic fields, stress, pressure and the vertical component of the velocity field yields two coupled ordinary differential equations for $\delta u_{r,i}$ and $\delta u_{\phi,i}$,

$$C_0 \frac{\mathrm{d}\delta u_{\phi,i}}{\mathrm{d}r} + C_1 \delta u_{\phi,i} = C_2 \frac{\mathrm{d}^2 \delta u_{r,i}}{\mathrm{d}r^2} C_3 \frac{\mathrm{d}\delta u_{r,i}}{\mathrm{d}r} + C_4 \delta u_{r,i}, \tag{2.37}$$

$$D_0 \delta u_{\phi,i} = D_1 \frac{\mathrm{d}\delta u_{r,i}}{\mathrm{d}r} + D_2 \delta u_{r,i}, \tag{2.38}$$

where

$$C_0 = \frac{1}{r}k^2 \left(2 - 2\mathrm{i}\frac{\gamma}{\sigma}B\cos\theta \right) - 3\mathrm{i}kS_B\sigma^2 \cos^2\theta \cot\theta,$$

$$C_1 = -3\mathrm{i}kS_B\sigma^2 \frac{\sin^2\theta}{2},$$

$$C_2 = -\frac{1}{\gamma}(\gamma^2 + \sigma^2) - 3S_B\sigma^2 \sin^2\theta,$$

$$C_3 = \frac{1}{r}\left[-\frac{1}{\gamma}(\gamma^2 + \sigma^2) + 3S_B\sigma^2(E_0 - \cot^2\theta) \right],$$

$$C_4 = \frac{1}{\gamma}(\gamma^2 + \sigma^2)\left(k^2 + \frac{1}{r^2} \right) +$$
$$\frac{1}{r^2}\left[\frac{2k^2}{\gamma}B\cos\theta\left(B\cos\theta - \mathrm{i}\frac{\sigma}{\gamma} \right) + 3S_B\sigma^2 E_0(\cot^2\theta - 1) \right],$$

and

$$D_0 = \gamma^2 + \sigma^2 + 3\gamma S_B\sigma^2 \cos^2\theta,$$

$$D_1 = -\frac{\mathrm{i}}{k}3S_B\gamma\sigma^2 \cos\theta \sin\theta,$$

$$D_2 = \frac{1}{r}\left[\sigma\left(2\mathrm{i}B\cos\theta + \frac{\sigma}{\gamma} - \frac{\gamma}{\sigma} \right) + \frac{i}{k}3S_B\gamma\sigma^2 \cot\theta E_0 \right],$$

$$E_0 = -\mathrm{i}\frac{k}{\gamma}\frac{\sin(2\theta)}{2} + \cos^2\theta - \sin^2\theta.$$

2.3.3   Bessel's equation and its solutions

Equations (2.37) and (2.38) can then readily be combined into a single *complex* second order ordinary differential equation for $\delta u_{r,i}$, the modified Bessel equation,

$$\frac{\mathrm{d}^2 \delta u_{r,i}}{\mathrm{d}r^2} + \frac{\mathrm{d}\delta u_{r,i}}{\mathrm{d}r} - \left(w^2 - \frac{v^2}{r^2} \right) \delta u_{r,i} = 0, \tag{2.39}$$

where

$$w^2 \equiv \frac{k^2}{E_1}(\sigma^2 + \gamma^2)(\sigma^2 + \gamma^2 + 3S_B \sigma^2 \gamma \cos^2 \theta), \tag{2.40}$$

$$v^2 \equiv -\frac{1}{E_1}(\gamma^4 + a_3 \gamma^3 + a_2 \gamma^2 + a_1 \gamma + a_0), \tag{2.41}$$

and

$$E_1 = (\sigma^2 + \gamma^2)(\sigma^2 + \gamma^2 + 3S_B \gamma \sigma^2),$$

$$a_3 = 3S_B \sigma^2 [\cos^2 \theta (\cot^2 \theta - 1) + \sin^2 \theta],$$

$$a_2 = 2[\sigma^2(1 + \cot^2 \theta) + k^2] + 6\mathrm{i}S_B \sigma^2 \sin 2\theta k(1 - \cot^2 \theta),$$

$$a_1 = 3S_B \sigma^4 \left[\cos^2 \theta \left(3 - 2\frac{k^2}{\sigma^2} \right) + 1 - \cot^2 \theta \right] - 8\mathrm{i}\sigma^2 k \cot \theta$$

$$a_0 = \sigma^2 [\sigma^2(1 - 2\cot^2 \theta) - 2k^2].$$

To obtain solutions to equation (2.39), we choose boundary conditions: an impenetrable wall at r_0 so $\delta u_{r,i}(r_0) = 0$, and the requirement that $r^{\frac{1}{2}}\delta u_{r,i}$ decays at infinity (see Furukawa *et al.* (2007) for an inviscid treatment that includes the shear singularity at the origin). In this case, its eigenfunctions are the modified Bessel functions of the second kind $\mathrm{K}_{\mathrm{i}v}(wr)$, of argument wr and order v, (Watson, 1944; Abramowitz & Stegun, 1964). The spectrum of solutions is discrete and we index v (and the corresponding γ) with n: v_n and γ_n[9]. In the special case when w (or γ_n from equation (2.40)) is real (in general it is complex) the problem is Sturm-Liouville and v_n is an infinite ordered set of eigenvalues

---

[9]For notational simplicity we retain the notation γ_n for the growth rate even in the degenerate limits where there is no dependence on n.

$v_0 < v_1 < v_2 \ldots < v_\infty$. To determine v_n and therefore γ_n, it is necessary to solve,

$$\mathrm{K}_{\mathrm{i}v_n}(w) = 0. \tag{2.42}$$

From solutions to this and equations (2.53) and (2.54), the full set of flow, magnetic and pressure fields can be constructed. Although they can easily be found from equations (2.29)-(2.36) we list the functional form of these fields here for completeness,

$$\delta u_{r,i} = \mathrm{K}_{\mathrm{i}v_n}(wr) \exp[\mathrm{i}kz + \gamma_n t], \tag{2.43}$$

$$\delta u_{\phi,i} = \frac{D_1}{D_0} \frac{\mathrm{d}\delta u_{r,i}}{\mathrm{d}r} + \frac{D_2}{D_0} \delta u_{r,i}, \tag{2.44}$$

$$\delta u_{z,i} = \frac{\mathrm{i}}{k} \frac{1}{r} \frac{\mathrm{d}(r\delta u_{r,i})}{\mathrm{d}r}, \tag{2.45}$$

$$\delta B_r = \mathrm{i}\frac{\sigma}{\gamma_n} \delta u_{r,i}, \tag{2.46}$$

$$\delta B_\phi = \mathrm{i}\frac{\sigma}{\gamma} \frac{D_1}{D_0} \frac{\mathrm{d}\delta u_{r,i}}{\mathrm{d}r} + \left[\mathrm{i}\frac{\sigma}{\gamma} \frac{D_2}{D_0} + \frac{1}{r}\left(\frac{B\cos\theta}{\gamma} - \mathrm{i}\frac{\sigma}{\gamma^2} \right) \right] \delta u_{r,i}, \tag{2.47}$$

$$\delta B_z = -\frac{\sigma}{\gamma_n} \frac{1}{kr} \frac{\mathrm{d}(r\delta u_{r,i})}{\mathrm{d}r}, \tag{2.48}$$

$$\delta\Pi = \frac{(\gamma^2 + \sigma^2)}{k^2\gamma} \frac{1}{r} \frac{\mathrm{d}(r\delta u_{r,i})}{\mathrm{d}r} - S_B \frac{\sigma^2}{k^2}(\csc^2\theta - 3)\times$$
$$\left[\left(\frac{D_2}{D_0} - \sin^2\theta \right) \frac{\mathrm{d}\delta u_{r,i}}{\mathrm{d}r} + \left(\frac{E_0}{r} + \mathrm{i}k\frac{\sin 2\theta}{2} \frac{D_1}{D_0} \right) \delta u_{r,i} \right]. \tag{2.49}$$

In Figure 2.2 we consider the case $\theta = \pi/2$ for which γ_n, and therefore v_n, is real and show three particular $\mathrm{K}_{\mathrm{i}v_n}(wr)$ which satisfy equation (2.42).

2.3.4 Specific configurations

Equations (2.40)-(2.42) provide a complete description for γ_n as a function of k and the system parameters S_B and σ, B, θ. (Although one of these three quantities is redundant, it is both notationally and conceptually convenient to retain them all.) Whilst it is entirely possible to determine γ_n for any set of parameters, in general it must be done numerically.

However, for the most physically relevant magnetic field configurations, the prob-

$K_{iv_n}(wr)$
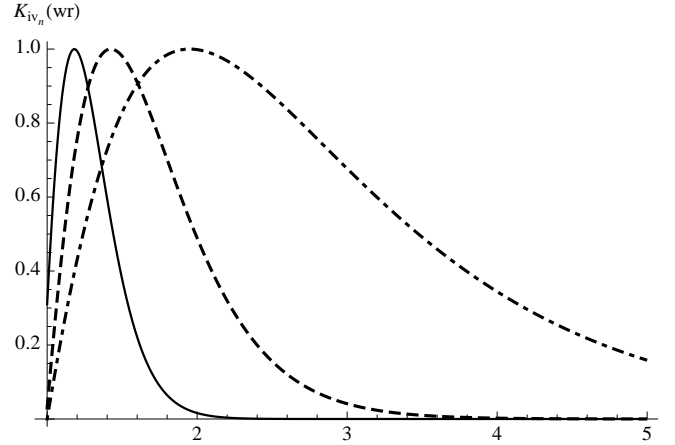
Figure 2.2: Radial component of the flow, equation (2.43), for the fastest grow-ing $n = 0$ branch MRI modes with $\theta = \pi/2, B = 0.02$ and $S_B = 10$, (solid), 100 (dashes), 1000 (dots/dashes). The associated (purely real) growth rates are $\gamma_{0,m} = 0.36, 0.26, 0.14$ and the Alfvén frequency at which they occur are $\sigma_{n,m} = 0.67, 0.52, 0.32$. The mode width is of order $1/w$, so as S_B increases, so does the mode width, viz. equation (2.40).

lem becomes, in part, analytically tractable. These cases, a purely azimuthal field $\theta = 0$ (in the galactic plane), a purely vertical field $\theta = \pi/2$ (a super-galactic field) and a slightly pitched field, $\theta \ll 1$ (very slightly out of the galactic plane), exhibit categorically different behaviour because $\theta \to 0, \pi/2$ are singular limits. In the first case, linear perturbations are damped. In the second, the system is unstable to the MRI but the Braginskii viscosity can reduce the maximum growth rate $\gamma_{n,m}$ below the Oort-A value maximum $(|\mathrm{d}\ln\hat{\Omega}/\mathrm{d}\ln r|)/2 = 1/2$ (Balbus & Hawley, 1992). In the third case, the system is unstable to the MVI with a growth rate approaching $\gamma_{n,m} = \sqrt{|\mathrm{d}\ln\hat{\Omega}^2/\mathrm{d}\ln r|} = \sqrt{2}$, even for *asymptotically small θ* (Balbus, 2004).

To show this in the azimuthal case we use a variational energy principle à la Chandrasekhar (1961), whereas in the vertical field case we make use the asymp-totic properties of $K_{iv_n}(w)$. In the pitched field case we make use of the smallness of the pitch angle to order the system parameters and variables and by doing so, we reduce equations (2.40) and (2.41) to a form that can be treated in the same manner as the vertical case. We present the details of these calculations now.

2.4 Azimuthal field, $\theta = 0$

The stability of inviscid axisymmetric perturbations to a purely azimuthal magnetic field in the presence of a shear flow are well known. When the shear flow has $q < 2$ and a magnetic field of the form $\boldsymbol{B} = Br^{-d}\hat{\boldsymbol{e}}_\phi$ with $d > -1$ the system is always stable (as ours is). When only one criterion is met (depending on the form of the fields) the system may still remain stable by the modified Rayleigh criterion (Rayleigh, 1916; Michael, 1954; Chandrasekhar, 1961; Coppins, 1988). (It is worth noting however that global non-axisymmetric perturbations are unstable, Ogilvie & Pringle (1996).) Do these results for our inviscidly stable system, $\mathcal{R}(\gamma_n) = 0$, persist in the presence of the Braginskii viscosity? The answer is no. Setting $\theta = 0$ in equations (2.39)-(2.41), whereby $\sigma = 0$, and making a change of variables, $\delta u_{r,i} \to r^{-1/2}\delta u_{r,i}$, we obtain the simple expression,

$$\gamma_n^2 \frac{\mathrm{d}^2\delta u_{r,i}}{\mathrm{d}r^2} - \left(\gamma_n^2 Q_1 + \gamma_n Q_2 + Q_3\right)\delta u_{r,i} = 0 \tag{2.50}$$

where

$$Q_1 = \frac{3}{4}\frac{1}{r^2} + k^2, \ Q_2 = 3S_B \frac{B^2 k^2}{r^2}, \ Q_3 = \frac{2k^2}{r^2}(1 + B^2). \tag{2.51}$$

We now multiply equation (2.50) by the complex conjugate of the perturbed radial velocity $\delta u_{r,i}^\dagger$ and integrate between the inner boundary r_0 and infinity. Noting that the first term in equation (2.50) can be integrated by parts and that boundary terms vanish, we find

$$\gamma_n^2 \left(\overline{\left(\frac{\mathrm{d}\delta u_{r,i}}{\mathrm{d}r}\right)^2} + Q_1\overline{|\delta u_{r,i}|^2} \right) + \gamma_n Q_2 \overline{|\delta u_{r,i}|^2} + Q_3\overline{|\delta u_{r,i}|^2} = 0, \tag{2.52}$$

where $\overline{|\delta u_{r,i}|^2} = \int_{r_0}^\infty \mathrm{d}r\, \delta u_{r,i}\delta u_{r,i}^\dagger > 0$ is positive definite (and similarly with $\overline{(\mathrm{d}\delta u_{r,i}/\mathrm{d}r)^2}$).

Equation (2.52) is a quadratic in γ_n whose roots depend crucially on S_B. When $S_B = 0$ (the inviscid limit), γ_n is purely imaginary (neutrally stable, travelling waves), whereas when $S_B > 0$ the result is quite different. In this case $\mathcal{R}(\gamma) < 0 \ \forall \ S_B$ and the only question is whether perturbations are purely damped, or

damped and travelling.

It follows that if the system is stable in the absence of the Braginskii viscosity, it remains so in its presence. From a modelling perspective this suggests that any axisymmetric simulation of a magnetized accretion disc in the presence of a purely azimuthal field will remain laminar and therefore not accrete. We will now show the same is not true for a vertical field.

2.5 Vertical field, $\theta = \pi/2$

We now consider the case of a purely vertical magnetic field, $\boldsymbol{B} = B_z \hat{\boldsymbol{e}}_z$ i.e. $\theta = \pi/2$. Equations (2.40) and (2.41) again reduce to a relatively simple form[10]:

$$w^2 \equiv k^2 \frac{\gamma_n^2 + \sigma^2}{\gamma_n^2 + \sigma^2 + 3S_B \gamma_n \sigma^2}, \tag{2.53}$$

$$v_n^2 \equiv - \left[\frac{2k^2}{\gamma_n^2 + \sigma^2 + 3S_B \gamma_n \sigma^2} \frac{(\gamma_n^2 - \sigma^2)}{(\gamma_n^2 + \sigma^2)} + 1 \right]. \tag{2.54}$$

In section 2.5.2 we determine the values of γ_n that satisfy our boundary conditions. We find that for each n there are four branches, one of which is a purely growing mode with a growth rate proportional to the shear of the disc. This is the MRI in the presence of Braginskii viscosity (two of the other roots are complex and describe damped Alfvén waves whilst the final root is a purely damped mode). However, before we detail these results, let us first consider the inviscid case.

In this case and for the subsequent configurations we adopt the following format. After stating the governing equations we first present our numerical result, and then, our analytic results in three asymptotic limits: the weak field limit, the highly oscillatory limit and, where relevant, the highly viscous limit.
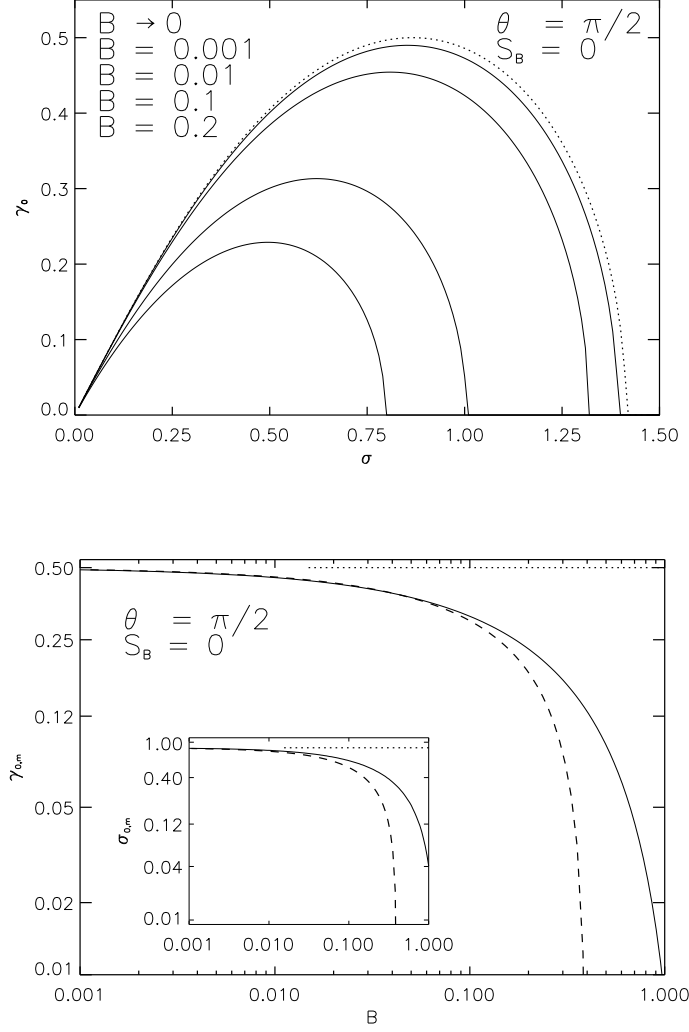
Figure 2.3: *Top panel:* The fastest growing mode γ_0 of the inviscid global MRI as a function of σ for a several values of B (recall, length-scales and time-scales are non-dimensionalised with respect to the radius of the inner boundary r_0 and the frequency at it $\hat{\Omega}_0$). In the weak field limit, we recover the behaviour of the local MRI (dotted line). *Bottom panel:* Maximum growth rate $\gamma_{0,m}$ as a function of B. As $B \to 0$ the fastest accessible growth rate asymptotes to the local Oort-A maximum $= 1/2$ (dotted line) in a galactic rotation profile. The dashed line is the weak B asymptotic solution for the fastest growing mode, as given by equation (2.63). Inset: The Alfvén frequency $\sigma_{0,m}$ at which $\gamma_{0,m}$ occurs as a function of B; its maximum $\sqrt{3/4}$ (dotted line) and its asymptotic scaling (dashed line and equation (2.63)). Note: In the weak field limit, any magnetic field with $\theta \neq 0$ is unstable to perturbations with the same γ_n as perturbations to a vertical field with the same strength as the vertical component of the pitched field, see section 2.6.3

2.5.1 Vertical inviscid MRI

The case of the inviscid global MRI with a vertical magnetic field has been examined in earlier works and our results are in agreement with these studies e.g. (Dubrulle & Knobloch, 1993; Curry *et al.*, 1994).

When $S_B = 0$, equation (2.53) simplifies to $w = k$ and therefore equation (2.54), which also simplifies, becomes real too. The problem is reduced to[11]

$$\mathrm{K}_{\mathrm{i}v_n}(k) = 0 \tag{2.55}$$

with

$$v_n^2 \equiv -\left[\frac{2k^2}{\gamma_n^2 + \sigma^2} \frac{(\gamma_n^2 - \sigma^2)}{(\gamma_n^2 + \sigma^2)} + 1 \right]. \tag{2.56}$$

For $v_n^2 < 0$ we note that $\mathrm{K}_{\mathrm{i}v_n}(k)$ is a sign definite function of monotonically decreasing magnitude with respect to k and therefore it has no nontrivial zeros. For equation (2.55) to be satisfied it follows that $v_n^2 > 0$; thus explaining our sign convention for v_n^2 in equation (2.39). A simple examination of equation (2.56) then reveals that γ_n^2 is bounded from above by σ^2. Further detail requires a more in depth investigation.

Numerical results

We use Newton's method (implemented through Mathematica's root finding algorithm) to determine v_n, and therefore γ_n. We find a real instability, the global MRI, with $\gamma_n \sim$ the shear rate. Its fastest growing branch of unstable modes γ_0, shown in Figure 2.3, are those that correspond to the lowest eigenvalue v_0, i.e.

---

[10]Although we do not show it here, the entire analysis that follows can be reproduced if compressive effects, i.e. sound waves, are included. In the limit of infinite sound speed the incompressible results we present here are recovered.

[11]Equations (2.39) and (2.56) correspond to equations (3.4) and (3.5) of Curry *et al.* (1994) with $a = 1$ and equations (30) and (31) of Dubrulle & Knobloch (1993).

$n = 0$, the first zero of $K_{iv_n}(k)$. This branch peaks at

$$\gamma_{0,m} = \frac{1}{2} \tag{2.57}$$

$$\sigma_{0,m} = \sqrt{\frac{3}{4}}. \tag{2.58}$$

Even for strong magnetic fields we find, in agreement with equation (2.19), that $\sigma_{0,m} \sim 1$ and so, when $B \lesssim 1$, unstable wavenumbers are of order $k \sim 1/B \gtrsim 1$ (physically, smaller scale modes are suppressed by magnetic tension). Since the mode width is of order $1/k$ (see Figure 2.2), curvature effects in this regime that occur on this scale become pronounced. The result is that the maximum occurs for $k \gg 1$ when the mode is localised on the inner boundary (Curry *et al.*, 1994). By making use of the asymptotic properties of the modified Bessel function it is relatively easy to recover this result for $B \ll 1$ analytically and we do so now.

Weak field limit

The fastest growing MRI mode has a wavenumber $k \sim 1/B$ and so we find, $k \gg 1$ in the weak field limit. It has been shown by Cochran (1965) and Ferreira & Sesma (1970, 2008) and references therein, that in this asymptotic limit, $|k| \gg 1$, the zeros of $K_{iv_n}(k)$ are given by

$$v_n \sim k + a_n 2^{-\frac{1}{3}} k^{\frac{1}{3}} + \dots, \tag{2.59}$$

where a_n is the modulus of the nth real negative zero of the Airy function Ai (Abramowitz & Stegun, 1964) and omitted terms are of the form k^b with $b < 1/3$. This result can be used to find the asymptotic-in-k form of γ_n by inverting equation (2.56) to form a bi-quadratic

$$\gamma_n^4 + 2 \left(\sigma^2 + \frac{k^2}{1 + v_n^2} \right) \gamma_n^2 + \sigma^2 \left(\sigma^2 - 2 \frac{k^2}{1 + v_n^2} \right) = 0, \tag{2.60}$$

into which we substitute equation (2.59). Retaining the first two terms of the large k limit of v_n yields

$$\gamma_n^4 + 2 \left(\sigma^2 + 1 - s_n k^{-\frac{2}{3}} \right) \gamma_n^2 + \sigma^2 \left(\sigma^2 - 2 \left(1 - s s_n k^{-\frac{2}{3}} \right) \right) = 0, \tag{2.61}$$

where $s_n = a_n 2^{\frac{2}{3}}$. To draw an analogy with the local approximation, the n that indexes the number of zeros in the domain is somewhat like a radial wavenumber, section 2.7.2.

Solving equation (2.61) for the fastest growing mode and its associated Alfvén frequency $\sigma_{n,\mathrm{m}}$, we find

$$\gamma_{n,\mathrm{m}} = 1/2 \left(1 - s_n k^{-\frac{2}{3}}/2 \right), \tag{2.62}$$

$$\sigma_{n,\mathrm{m}} = \sqrt{3/4} \left(1 - s_n k^{-\frac{2}{3}}/2 \right), \tag{2.63}$$

which is valid for $s_n k^{-\frac{2}{3}} \ll 1$ and, as expected, peaks at $\gamma_{0,\mathrm{m}} = 1/2$. For $k \sim 1/B > 10$, there is excellent agreement between these results and the full numerical solution for $n = 0$, Figure 2.3.

For fixed k, increasing n decreases $\gamma_{n,m}$, confirming the numerical results of the previous section. The mode with the least radial structure – the $n = 0$ mode– is the most unstable. Extrapolating from this, we would expect $\gamma_{n,\mathrm{m}}$ to always decrease with n. However, the results of this section are limited to values of $s_n k^{-\frac{2}{3}} \ll 1$. To determine $\gamma_{n,\mathrm{m}}$ outside this regime, it is appropriate to take the large n limit of the governing ODE.

Highly oscillatory limit

Let us consider solutions to the governing ODE, equation (2.39), in the limit $v_n \gg kr = x$ (corresponding to large n since v_n is an unbounded monotonically increasing series in n). Here we have introduced the scaled coordinate x (this is effectively a WKB approach to solving equation (2.39) using the small parameter x/v_n, (Dubrulle & Knobloch, 1993; Ogilvie, 1998)). In this case, the expansion given by equation (2.59) no longer applies (n is large and so higher order terms must be included). However, values of v_n satisfying our boundary conditions do still exist. In this limit, the equation governing these solutions is

$$\frac{\mathrm{d}^2 \delta u_{r,i}(x)}{\mathrm{d}x^2} + \frac{v_n^2}{x^2} \delta u_{r,i}(x) = 0. \tag{2.64}$$

Demanding that $\delta u_{r,i}$ is real, this has solutions

$$\delta u_{r,i} = \sqrt{x}\cos(v_n \ln x), \tag{2.65}$$

and to ensure $\cos(v_n \ln x) = 0$ at $r = 1$, it must satisfy the boundary condition

$$v_n \ln k = \left(n + \frac{1}{2}\right)\pi. \tag{2.66}$$

This constraint on v_n determines the spectrum of solutions just as equations (2.42) and (2.59) do. Neglecting the factor of $1/2$ since n is large, this can be inverted to yield a dispersion relation,

$$\gamma_n^4 + 2\left[\sigma^2 + \left(\frac{k\ln k}{n\pi}\right)^2\right]\gamma_n^2 + \sigma^2\left[\sigma^2 - 2\left(\frac{k\ln k}{n\pi}\right)^2\right] = 0, \tag{2.67}$$

valid in the limit $v_n \gg kr$. The maximum growth rate associated with this equation decreases as n increases, and the Alfvén frequency at which it occurs are given by

$$\gamma_{n,\mathrm{m}} = k/2v_n = k\ln k/2n\pi, \tag{2.68}$$
$$\sigma_{n,\mathrm{m}} = \sqrt{3/4}\,k/v_n, \tag{2.69}$$

so modes with more radial structure are less unstable.

In the large n limit, on small enough scales, the mode structure given by equation (2.65) is especially simple. Reverting to r as our radial coordinate, we consider a small region at some radius r_1 of order 1 and departures from it such that $|r - r_1| < \delta r$ where $\delta r \ll 1$. In this limit we can expand equation (2.65) about $r = r_1$ and retaining the leading order terms in δr we find,

$$\delta u_{r,i} = \mathcal{A}\left(1 + \frac{1}{2}\frac{r}{r_1}\right)\cos\left(\frac{v_n}{r_1}r + \xi\right), \tag{2.70}$$

where $\mathcal{A} = \sqrt{kr_1}$ and $\xi = v_n \ln kr_1$.

Since $v_n \gg kr_1$ (our initial assumption) equation (2.70) describes rapidly oscillating modes with frequency v_n and a slowly varying amplitude $\propto \mathcal{A}$. For

sufficiently large v_n, the variation in amplitude can be neglected and equation (2.70) describes plane wave solutions whose growth rate decreases with n. In section 2.7.2 we contrast these results with a local plane wave analysis. We find that there are subtle differences associated with the spectrum of modes permitted by our boundary conditions.

Before we do so, let us first consider the behaviour of the vertical MRI in the presence of Braginskii viscosity.

2.5.2 Vertical MRI with Braginskii Viscosity

In the case of the Braginskii viscosity and a vertical field, our system is now governed by equations (2.42), (2.53) and (2.54). Unlike the inviscid case, we can no longer *guarantee* the reality of w as γ_n can, and indeed sometimes does, take complex values. This is because the problem is generally not of Sturm-Liouville form and so the roots of $\mathrm{K}_{iv_n}(w)$ are complex. However for the modes of interest to us, this turns out to be irrelevant. We find, both numerically (next section) and analytically (in section 2.5.2) that the only solutions with $\mathcal{R}(\gamma_n) > 0$ are purely real.

Numerical results

Again making use of Newton's method we start from the solutions to the inviscid problem found in section 2.5.1 and proceed to map out the two-dimensional (B and S_B) parameter space of γ_n for moderate w.

There are four mode branches of which three are stable and one is unstable. Considering only the unstable branch, which can be traced from the inviscid MRI, we again find that the growth rate is maximised for the modes the minimum number of zeros (i.e. radial structure), γ_0. Considering only these fastest growing modes, in the limit $S_B \ll 1$ the effect of the Braginskii viscosity is negligible and γ_0 approaches values of the inviscid MRI. However, in the opposite limit where $S_B \gg 1$, the maximum accessible γ_0 is significantly reduced and the value of σ at which it occurs is shifted to smaller values, as shown in Figure 2.2 and 2.6.

We find, as in the inviscid case, the characteristic radial scale of the modes is $1/w$.
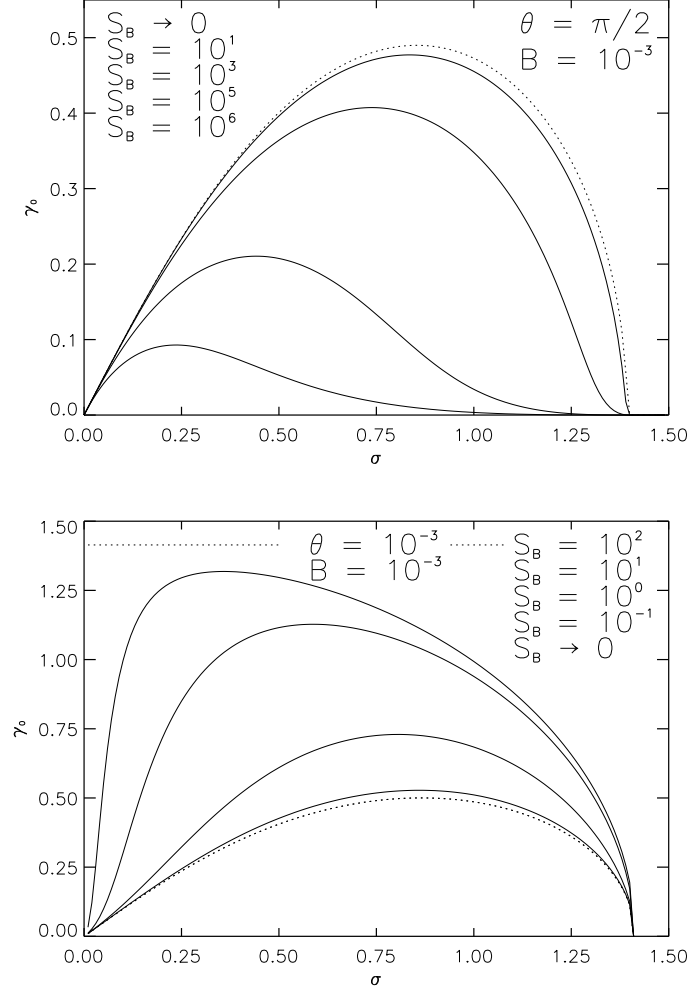
Figure 2.4: The fastest growing mode γ_0 of the global MRI with Braginskii viscosity for a two different weak, $B = 1/1000$, field configurations and a range of S_B: *Top panel:* Vertical Field: For a given σ the growth rate is always less than the inviscid case (dotted) which is recovered as $S_B \to 0$. For $S_B \to \infty$, both the peak growth rate and tension at which it occurs, $\gamma_{0,m}, \sigma_{0,m} \to 0$. However, the critical Alfvén frequency σ_c remains unaltered. *Bottom panel:* Slightly pitched field: In contrast to the purely vertical case, for a given σ the growth rate is always greater than the inviscid case (dotted) and less than the $\sqrt{2}$ maximum of the Lorentz force free limit (Balbus, 2004). When $S_B \to 0$, as expected, γ_0 approaches the inviscid growth rates. In the opposite limit when $S_B \to \infty$, like the vertical case, $\sigma_{0,m} \to 0$. However, unlike the vertical case, the corresponding $\gamma_{0,m} \to \sqrt{2}$. In this case σ_c is imperceptibly modified by the effects of magnetic hoop tension. In the formal limit that this can be neglected, $B \to 0$, σ_c remains unaltered.

In the limit where $S_B B^2 \gtrsim 1$, modes that would be extremely well localised to the inner boundary r_0, were they inviscid, can exhibit significant radial structure. This is shown in Figures 2.2 and 2.5.

Contrasting the viscous and inviscid results, we find the fastest growing inviscid modes for weak magnetic fields with $\theta = \pi/2$ can be summarised by

$$S_B \to 0, \qquad B \to 0 \qquad \gamma_{n,\mathrm{m}} \to 1/2, \qquad \sigma_{n,\mathrm{m}} \to \sqrt{3/4}, \qquad (2.71)$$

whereas the highly (Braginskii) viscous modes have,

$$S_B \to \infty, \qquad B \to 0 \qquad \gamma_{n,\mathrm{m}} \to 0, \qquad \sigma_{n,\mathrm{m}} \to 0. \qquad (2.72)$$

As we now show, these results can be recovered analytically.

Weak field limit

As in section 2.5.1, if $B \ll 1$ the typical wavenumber at which the γ_n peaks is $k \sim 1/B \gg 1$. Assuming momentarily that in this limit we also have $|w| \gg 1$, we can investigate the behaviour of v_n. Fortunately, this is relatively easy to do since the results of Cochran (1965) and Ferreira & Sesma (2008) also hold for large complex w:

$$v_n \sim w + a_n 2^{-\frac{1}{3}} w^{\frac{1}{3}} + \dots, \quad w \in \mathbb{C}, \qquad (2.73)$$

and so we proceed without assuming anything about the reality of w or, therefore, γ_n. Here a_n and the terms omitted are of the same form as in equation (2.59).

As before, we invert equation (2.54) to obtain an expression for γ_n that takes the form

$$\gamma_n^4 + 3S_B \sigma^2 \left(\gamma_n^3 + \sigma^2 \gamma_n \right) + 2 \left(\sigma^2 + \frac{k^2}{1 + v_n^2} \right) \gamma_n^2 + \sigma^2 \left(\sigma^2 - 2\frac{k^2}{1 + v_n^2} \right) = 0, \; (2.74)$$

where $v_n(w)$ is given by equation (2.73) and w is given by equation (2.53). The solutions to the ensuing polynomial must be consistent with our earlier assumption, namely that $k \gg 1$ implies $w \gg 1$.

When $S_B \ll k^2$ it is simple to show that this requirement is met. Retaining only the leading order term in equation (2.73) and substituting this into equation (2.74) we find, neglecting factors of order unity compared to k^2,

$$\gamma_n^4 + 3\frac{S_B}{k^2}\sigma^2\left(\gamma_n^3 + \sigma^2\gamma_n\right) + 2\left(\sigma^2 + 1\right)\gamma_n^2 + \sigma^2\left(\sigma^2 - 2\right) = 0. \tag{2.75}$$

The terms proportional to S_B are small corrections to the inviscid result and so $\gamma_{n,\mathrm{m}} \sim \sigma_{n,\mathrm{m}} \sim 1$ by equation (2.63). Therefore $w^2 \sim k^2/(1 + S_B)$ from which it follows, as necessary, $w \gg 1$.

A more restrictive assumption on the size of S_B allows us to analytically recover radial structure in equation (2.74). Retaining the two leading terms in equation (2.73) and expanding w as a Taylor series in small S_B we can write

$$v_n^2 \sim k^2\left(1 - \chi + \dots\right) + s_n k^{\frac{4}{3}}\left(1 - \frac{4}{3}\chi + \dots\right) + \dots, \tag{2.76}$$

where

$$\chi = \frac{3S_B\sigma^2\gamma_n}{\gamma_n^2 + \sigma^2} \ll 1. \tag{2.77}$$

Assuming that $\chi \sim S_B \sim s_n k^{-\frac{2}{3}} \ll 1$ we can neglect all terms not shown in the first set of brackets and all but the first term in the second set. This is the minimum needed to incorporate the radial structure into our system in the weak field limit.

Substituting this approximation to equation (2.76) into equation (2.74) and rearranging yields

$$\gamma_n^4 + 3S_B\sigma^2 s_n k^{-\frac{2}{3}}(\sigma^2 + \gamma_n^2)\gamma_n + 2\left(\sigma^2 + 1 - s_n k^{-\frac{2}{3}}\right)\gamma_n^2 + $$
$$\sigma^2\left(\sigma^2 - 2\left(1 - s_n k^{-\frac{2}{3}}\right)\right) = 0. \tag{2.78}$$

Considering the γ_n solutions to this confirms the results of the numerical investigation of section 2.5.2. There are four branches to γ_n; two purely real (the unstable one corresponding to the MRI in the presence of Braginskii viscosity) and two complex ones with $\mathcal{R}(\gamma_n) < 0$ corresponding to damped Alfvén waves.

To determine the variation of $\gamma_{0,\mathrm{m}}$ with n and S_B we differentiate equation (2.78) with respect to σ and set this to zero to obtain an equation constraining the turning points of γ_n. Combining this with the equation (2.78) and assuming a series solution for $\gamma_{n,\mathrm{m}}$ and $\sigma_{n,\mathrm{m}}$ in the small parameter $k^{-\frac{2}{3}}$, yields a series of simple algebraic equations for the coefficients of the series expansion. These coefficients can be obtained order by order and in section 2.6.3 we present a worked example of this procedure. However, for now we simply state the result for the maximum growth rate and Alfvén frequency:

$$\gamma_{n,\mathrm{m}} = \frac{1}{2}\left(1 - s_n k^{-\frac{2}{3}}\left(\frac{1}{2} + \frac{9}{16}S_B\right)\right), \tag{2.79}$$

$$\sigma_{n,\mathrm{m}} = \sqrt{\frac{3}{4}\left(1 - s_n k^{-\frac{2}{3}}\left(\frac{1}{2} + \frac{33}{48}S_B\right)\right)}. \tag{2.80}$$

Neglecting radial structure (sufficiently large k), we can also determine σ_{c} by solving equation (2.78) and setting $\gamma_n = 0$. Because dissipative terms containing S_B are proportional to some non-zero power of γ_n, like the case of a *local* Laplacian viscosity, $\sigma_{\mathrm{c}}^2 = \mathrm{d}\ln\hat{\Omega}^2/\mathrm{d}\ln r$ (as in the inviscid case), thereby justifying the assumptions in equation (2.20) (Pessah & Chan, 2008). These results are in complete agreement with the numerical analysis preceding this.

In expanding equation (2.74) we assumed $S_B \ll k^2$ initially (and then $S_B \sim s_n k^{-\frac{2}{3}}$ when we introduced radial structure). What happens when $S_B \gtrsim k^2$ is less clear because $k \gg 1$ no longer necessarily implies $w \gg 1$ and so equation (2.73) need not hold. In fact, as we now show, assuming it does hold leads to a scaling of $\sigma_{n,\mathrm{m}}$ with S_B that does not match the full numerical solution (although the scaling we find for $\gamma_{n,\mathrm{m}}$ does).

Large S_B limit

Assuming that $v_n \sim w$, equation (2.75) governs the behaviour of γ_n. In the large S_B limit, the dominant balance for the unstable mode is between the γ_n and the constant terms so

$$\gamma_n = \frac{2 - \sigma^2}{3S_B B^2}, \qquad S_B \gg 1 \tag{2.81}$$
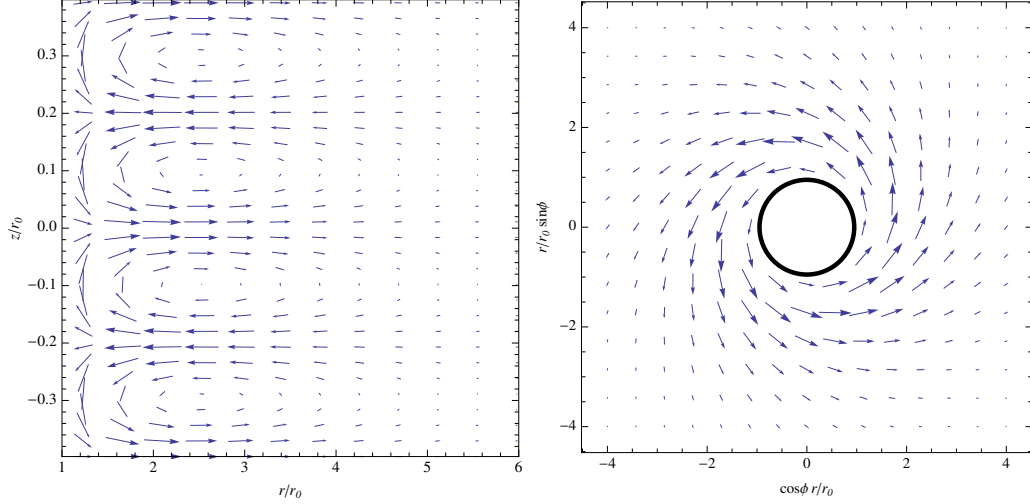
Figure 2.5: The flow fields associated with unstable Braginskii-MRI modes for a vertical magnetic field as given by equations (2.43)-(2.45) and the numerical results of section 2.5.2. The magnetic field is weak $B = 0.02$ and $S_B = 1000$ is large. The mode shown is the fastest growing mode for this set of parameters, it has $\gamma_{0,\mathrm{m}} = 0.14$ and $\sigma_{0,\mathrm{m}} = 0.32$ (significantly less than if the system were inviscid). *Left panel:* Spanning the disc midplane and projected onto the $r - z$ plane: As required by the impenetrable inner boundary condition at $r = 1$, the radial component of the flow becomes zero here. Relative to the flow field, the $r - z$ components of the magnetic field (not shown) are a factor $\sigma_{0,\mathrm{m}}/\gamma_{0,\mathrm{m}}$ larger and displaced vertically down by half a wavelength $= \pi/k$ but otherwise identical (see equations (2.46) and (2.48)). *Right panel:* Face-on view of the disc, $r - \phi$ plane, at the $z/r_0 = 0$ midplane: At the inner boundary (black ring) the radial component of the flow vanishes. Compared to the flow field, the ϕ component of the magnetic field (not shown) is a factor $1/2(\sigma_{0,\mathrm{m}}/\gamma_{0,\mathrm{m}} - \gamma_{0,\mathrm{m}}/\sigma_{0,\mathrm{m}})$ smaller and displaced vertically down by half a wavelength $= \pi/k$ (see equation (2.47)).

where we have written $k = \sigma/B$. This implies γ_n is maximised as $\sigma \to 0$. However, this limit is inconsistent with the assumption $k \gg 1$ implicit in $v_n \sim w$.

To determine the fastest growing mode we differentiate equation (2.75) with respect to σ and set this equal to zero, yielding an equation governing the turning points of γ_n. This equation is

$$\gamma_n^2 + \frac{3}{2} S_B B^2 \gamma_n + \sigma^2 - 1, \tag{2.82}$$

and eliminating σ between it and equation (2.75) gives a quadratic from which we determine:

$$\gamma_{n,\mathrm{m}} = \frac{2}{4 + 3 S_B B^2} = \frac{2}{4 + 3/\mathrm{Re}}, \tag{2.83}$$

$$\sigma_{n,\mathrm{m}} = \sqrt{\frac{12 \left(1 + S_B B^2\right)}{\left(4 + 32 S_B B^2\right)^2}} = \sqrt{\frac{12 \left(1 + 1/\mathrm{Re}\right)}{\left(4 + 3/\mathrm{Re}\right)^2}}. \tag{2.84}$$

where $S_B B^2 = 1/\mathrm{Re}$ is the inverse of the Reynolds number. For $S_B B^2 \ll 1$ the dominant contribution to $\gamma_{n,\mathrm{m}}$ and $\sigma_{n,\mathrm{m}}$ is the same as the inviscid case (ignoring $s_n k^{-\frac{2}{3}}$ as we have done here, see equation (2.63)). Furthermore, in full agreement with the numerical solution, it is only when $S_B B^2 \gtrsim 1$ that the damping effects of the Braginskii viscosity become pronounced. It is hardly surprising that significant damping only occurs when $\mathrm{Re} \lesssim 1$.

In Figure 2.7 the scalings given by equation (2.83) are plotted against the full numerical solutions. Our analytic expression for $\gamma_{n,\mathrm{m}}$ is in good agreement, but in the large $S_B B^2$ regime, the numerical solution for $\sigma_{n,\mathrm{m}}$ appears to decrease more like with $S_B^{-3/4}$ than the scaling of $S_B^{-1/2}$ predicted here. This discrepancy indicates that it was not correct to assume $v_n \sim w$ in the large $S_B B^2$ regime, despite the fact that γ_n is correctly captured. Unfortunately, as a result, we are unable to produce a better analytic estimate for $\sigma_{n,\mathrm{m}}$.

Leaving the large S_B limit aside for now (we return to it in section 2.6.3), let us again consider the highly oscillatory limit, his time with Braginskii viscosity.

Highly oscillatory limit

Our numerical results suggest that, like the inviscid case, as n increases the (real) growth rate of the MRI in the presence of the Braginskii viscosity and a vertical field, decreases. We investigate the large n limit here by following the methods developed for the inviscid case in Section 2.5.1. Here, however, we replace k by w and recall that v_n is now given by equation (2.54).

In the limit $S_B \ll 1$ (so equation (2.77) holds) we can write $w = k(1 - \chi/2 + \ldots)$ and the ensuing dispersion relation is

$$\gamma_n^4 + 3S_B\sigma^2(\sigma^2 + \gamma_n^2)\gamma_n + 2\left[\sigma^2 + \left(\frac{k\ln k}{n\pi}\right)^2\right]\gamma_n^2 +$$

$$\sigma^2\left[\sigma^2 - 2\left(\frac{k\ln k}{n\pi}\right)^2\right] = 0, \quad (2.85)$$

valid in the limit $v_n \gg kr \gg 1$. As in section 2.5.2 (and detailed in 2.6.3), we can obtain a series solution for $\gamma_{n,\mathrm{m}}$ and $\sigma_{n,\mathrm{m}}$, this time using the small expansion parameter $k/v_n = k\ln k/n\pi$. The result of such an expansion is

$$\gamma_{n,\mathrm{m}} = \frac{1}{2}\frac{k}{v_n}\left(1 - \frac{9}{16}S_B\right), \tag{2.86}$$

$$\sigma_{n,\mathrm{m}} = \sqrt{\frac{3}{4}}\frac{k}{v_n}\left(1 - \frac{33}{48}S_B\right), \tag{2.87}$$

and in the limit $S_B \to 0$, we recover the inviscid results of section 2.5.1.

That is, in the highly oscillatory limit, the effect of S_B is to decrease both $\gamma_{n,\mathrm{m}}$ and $\sigma_{n,\mathrm{m}}$ (as is the effect of increasing n). Furthermore, in a small enough region about r_1, $\delta u_{r,i}$ the modes take on the same sinusoidally varying form as the inviscid modes (as do all the other field and flow components; the pressure, however, does not).

2.5.3 Vertical field summary

For a vertical magnetic field, the inviscid and weakly (Braginskii) viscous MRI are very similar. In both cases a real instability bounded by the Oort-A value of

1/2 emerges. Its growth rate is maximised for the $n = 0$, and the mode structure (apart from the pressure) is the same.

Outside this regime, where $S_B B^2 \equiv 1/\text{Re} \gtrsim 1$, the damping effects of the Braginskii viscosity become pronounced. We found that in this regime $\gamma_{n,\text{m}}, \sigma_{n,\text{m}} \to 0$ as $S_B \to \infty$. Although this is not surprising, since ultimately the Braginskii viscosity is a dissipative process, it is somewhat novel since in the unperturbed state, the system behaves ideally *for all values of S_B*. That is, there is no direct Laplacian viscosity equivalent. We discuss this further in section 2.7.

The overall picture is of a large (radial) scale instability whose growth rate is maximised when B is weak and reduced when B or $S_B B^2$ is strong. For the ISM parameters of section 2.2.1 this reduction is unlikely to be particularly important. However, at an earlier, hotter epoch when the collision frequency, and therefore Re, was less, this effect may have been more significant.

From the numerical modelling perspective, one should certainly be aware of the damping effects of the Braginskii viscosity for the vertical field MRI since, in the linear stages, the growth rate of the instability will be reduced. Of course, after the initial stages the instability will deform the background field so it acquires an azimuthal component. In this case, as we now show, the behaviour of the instability is categorically different.

2.6   Pitched field, $\boldsymbol{\theta} \ll 1$

When the magnetic field has both a vertical and an azimuthal component, the perturbed Braginskii stress tensor (equation (2.36)) exerts an azimuthal "tension" force on separating plasma elements, equation (2.44). For arbitrary θ, the system is neither Sturm-Liouville (equation (2.39) is complex) nor amenable to the kind of polynomial inversion used in sections 2.5.1 and 2.5.2. If we assume that $\theta \ll 1$, matters simplify considerably. Physically, this choice of pitch angle represents the most realistic non-isolated galactic magnetic field configuration (Beck *et al.*, 1996). Mathematically, as we now show, it is a singular limit that constitutes the stability threshold between actively damped modes (section 2.4) and an unstable configuration that grows even faster than the inviscid global MRI (to which the

following stability threshold also applies):

$$\text{Damped}: \ \theta = 0, \qquad\qquad \text{Unstable}: \ \theta \sim \epsilon. \qquad\qquad (2.88)$$

Here $\epsilon \ll 1$ is a small parameter with respect to which we order the pitch angle and the remaining quantities in equation (2.39): $\gamma, k, \mathrm{d}/\mathrm{d}r, B$ and S_B.

There are many different, self-consistent ways of ordering the parameters of the system, each corresponding to a different physical regime. In this work we concentrate on the order 1 magnetic field limit but, so as to compare our results with the vertical field case, restrict its values to $B \leq 0.2$ which we took to be the maximum field strength consistent with our uniform disc assumption (equation (2.18)).

In this section, we first introduce our small angle orderings and equations before examining, first the pitched inviscid MRI and then the pitched MRI in the presence of the Braginskii viscosity.

2.6.1   Ordering assumptions

Letting $\theta \sim \epsilon$ we can retain only the first few terms in a series expansion of our trigonometric functions,

$$\cos\theta = 1 - \frac{\theta^2}{2} + \mathcal{O}(\theta^4), \qquad \sin\theta = \theta - \frac{\theta^3}{6} + \mathcal{O}(\theta^5), \qquad\qquad (2.89)$$

and we assume the magnetic field strength $B \sim 1$ which allows us to include the effects of magnetic tension. Similarly, we order $S_B \sim 1$ to incorporate the effects of kinetic magnetization (the Braginskii viscosity).

To retain the effects of magnetic tensions $\sigma = kB\sin\theta$ to lowest order (failing to do would remove the high wavenumber cutoff and leave the equations ill-posed), we set $k \sim 1/\epsilon$. Then, in anticipation of unstable modes that grow at the shear rate, we order $\gamma \sim 1$ too.

It now simply remains to order the radial scale of variations $\mathrm{d}/\mathrm{d}r$. Examination of equation (2.40), in conjunction with the orderings given above, indicates that w (the boundary layer width of an unstable mode) is dominated by k. This

implies that the scale of the radial derivative must be comparable, and so we order $\mathrm{d}/\mathrm{d}r \sim k \sim 1/\epsilon$.

In all, the relevant scalings are,

$$\theta \sim \epsilon, \qquad \gamma \sim \sigma \sim B \sim S_B \sim 1, \qquad k \sim \frac{\mathrm{d}}{\mathrm{d}r} \sim \epsilon^{-1}. \tag{2.90}$$

Applying these scalings to equations (2.39)-(2.41) and retaining only the lowest order terms in ϵ, we find $\delta u_{r,i}$ is still governed by Bessel's equation and γ_n is determined by

$$w^2 \equiv k^2 \tag{2.91}$$

$$v^2 \equiv -\frac{1}{E_1}(\gamma^4 + b_3 \gamma^3 + b_2 \gamma^2 + b_1 \gamma + b_0), \tag{2.92}$$

where now

$$E_1 = (\sigma^2 + \gamma^2)(\sigma^2 + \gamma^2 + 3S_B \gamma \sigma^2),$$

$$b_3 = 3S_B \frac{\sigma^2}{\theta^2},$$

$$b_2 = 2\left(k^2 + \frac{\sigma^2}{\theta^2}\right) - 12\mathrm{i}S_B \sigma^2 \frac{k}{\theta},$$

$$b_1 = -3S_B \sigma^4 \left(2\frac{k^2}{\sigma^2} + \frac{1}{\theta^2}\right) - 8\mathrm{i}\sigma^2 \frac{k}{\theta},$$

$$b_0 = -2\sigma^4 \left(\frac{k^2}{\sigma^2} + \frac{1}{\theta^2}\right).$$

To determine the behaviour of the pitched field MRI in the presence of Braginskii viscosity, we solve equations (2.91) and (2.92) using a combination of basic numerics and further asymptotic analysis. To provide a basis for comparison we briefly consider the inviscid case first.

2.6.2   Pitched inviscid MRI

When $S_B = 0$ and $B \to 0$ (but $\sigma \sim 1$), equation (2.92) for v_n reduces exactly to that of the inviscid vertical field instability $\gamma_{n,\mathrm{m}} = 1/2 \in \Re$. In this case the magnetic field influences the growth rate, through its vertical component only, by

setting the range of k at which growth occurs. The radial length-scale is therefore also $\propto 1/k$.

The most unstable wavenumbers will inevitably be large $k \sim 1/B\theta$ and so the curvature effects, like those shown in figure 2.3, for $k \gtrsim 1$ will be precluded. For a vertical magnetic field of the same (necessarily weak) value as the *vertical component* of a weak pitched field, the systems (growth rates and mode structure) are identical. However, for a weak vertical field, an unstable perturbation that satisfies the fluid condition $k\lambda_{\mathrm{mfp}} \ll 1$ may fail to satisfy it if the same strength field becomes pitched (equation (2.20)) and so collisionless effects will come into play (Quataert *et al.*, 2002; Sharma *et al.*, 2003). This aside though, the growth rates of a weak vertical and a weak pitched magnetic field are the same, Figure 2.3.

If the magnetic field is not weak, inverting equation (2.92) and letting $w \sim k$, viz. equation (2.59), yields the complex quartic

$$\gamma_n^4 + 2\left[\sigma^2\left(1 + \frac{1}{k^2\theta^2}\right) + 1\right]\gamma_n^2 - 8\mathrm{i}\frac{\sigma^2}{k\theta} + \left[\sigma^2\left(1 - 2\frac{1}{k^2\theta^2}\right) - 2\right] = 0. \quad (2.93)$$

Solutions to this polynomial are considered in detail in Curry & Pudritz (1995) (and further discussion can be found in Knobloch (1992)). For our purposes, is is sufficient to consider solutions in the limit $B \ll 1$ but still finite. In this case we can expand γ_n as a power series in B. Substituting this into equation (2.93) and solving up to first order, we find

$$\gamma_n = 2\mathrm{i}\frac{B\sigma}{\sqrt{4\sigma^2 + 1}} + \sqrt{\left(\sqrt{4\sigma^2 + 1} - \sigma^2 - 1\right)}, \quad (2.94)$$

with a maximum value

$$\gamma_{n,\mathrm{m}} = \frac{1}{2} + \mathrm{i}\sqrt{\frac{3}{4}}B, \quad (2.95)$$

which occurs at $\sigma_{n,\mathrm{m}} = \sqrt{3/4}$. The imaginary part of γ_n is of order B and, as can be seen in the $S_B = 0$ limit of Figure 2.6, this is in excellent agreement with the full numerical solution for values of the magnetic field as large as $B = 0.2$. In the inviscid case, the MRI is an over-stability whose travelling wave component

arises from the finite azimuthal hoop tension ($\propto B$) absent in the vertical case.

This much is already well known. However, as we now show, both this strong field result and the weak field result change dramatically when the Braginskii viscosity is introduced. A new faster instability emerges whose behaviour we now describe.

2.6.3   Pitched MRI with Braginskii viscosity

When the Braginskii viscosity is not zero, the structure of v_n admits a complex instability whose real part and imaginary part exceeds that of the inviscid case.

To show this we invert equation (2.92) to form a polynomial for γ_n containing v_n. This takes the form

$$\gamma_n^4 + c_3\gamma_n^3 + c_2\gamma_n^2 + c_1\gamma_n + c_0 = 0, \tag{2.96}$$

where

$$c_3 = 3S_B\sigma^2\left(1 + \frac{1}{v_n^2\theta^2}\right),$$

$$c_2 = 2\left[\sigma^2 + \frac{1}{v_n^2}\left(k^2 + \frac{\sigma^2}{\theta^2}\right)\right] - 12\mathrm{i}S_B\sigma^2\frac{k}{\theta},$$

$$c_1 = 3S_B\sigma^4\left[1 - \frac{1}{v_n^2}\left(2\frac{k^2}{\sigma^2} + \frac{1}{\theta^2}\right)\right] - 8\mathrm{i}\frac{\sigma^2}{v_n^2}\frac{k}{\theta},$$

$$c_0 = \sigma^4\left[1 - 2\left(\frac{k^2}{\sigma^2} + \frac{1}{\theta^2}\right)\right].$$

In the weak field limit, this equation is very similar to equation (2.60) for the vertical Braginskii-MRI, but rather than solving equation (2.42) to determine v_n, we must now solve equation (2.55). The only other difference is the second term in c_1. This term constitutes the additional stress (proportional to the shear) that arises from the viscous stress tensor, equation (2.36), and is responsible for the enhanced growth rate we will find. When the finite magnetic field strength is not neglected, new terms appear, including the imaginary term in c_2 that, in the large S_B limit, enhances $\Im(\gamma_n)$. We investigate these effects now.
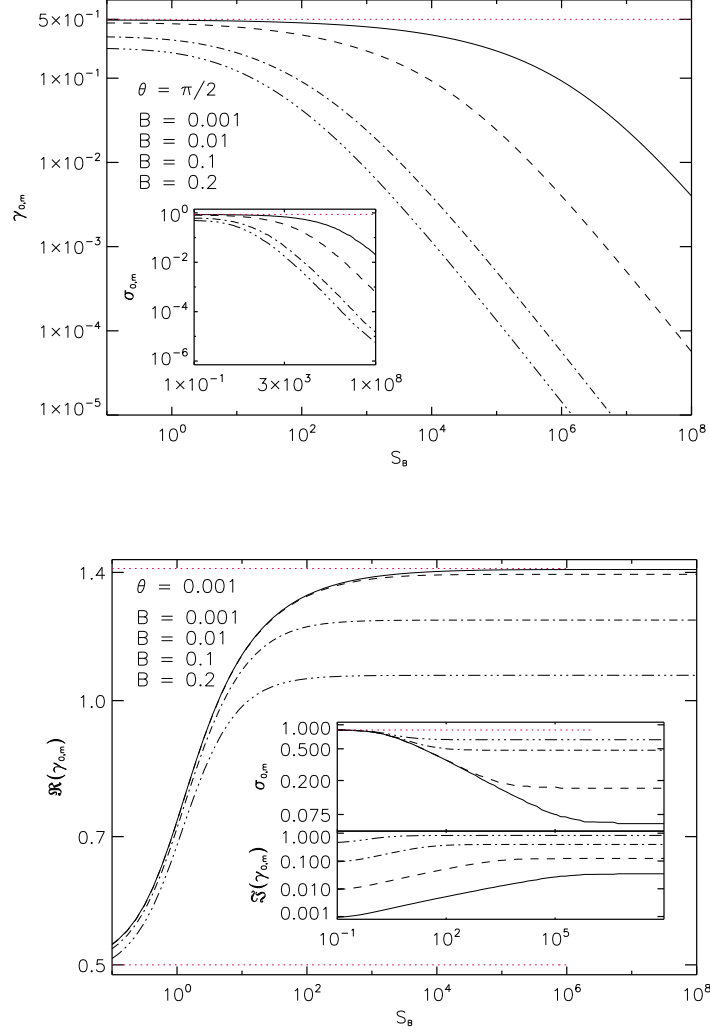
Figure 2.6: Maximum real, and when they exist, corresponding imaginary (inset) growth rates $\gamma_{0,m}$ as a function of S_B for two different field orientations and sets of magnetic field strengths, $B = 0.001$ (solid), $B = 0.01$ (dashed), $B = 0.1$ (dash-dot) and $B = 0.2$ (dash-dot-dot). Also shown, (inset) is the $\sigma_{0,m}$ at which they occur. *Top panel:* Vertical field: The maximum growth rates $\gamma_{0,m}$ (which are real) and the corresponding values of $\sigma_{0,m}$ are bounded from above by the weak field limits of $1/2$ and $\sqrt{3/4}$ (dotted lines) respectively. *Bottom Panel:* Slightly pitched case, $\theta = 0.001$: The maximum real part of the growth rate $\Re(\gamma_{0,m})$ (which is now complex) and the corresponding $\sigma_{0,m}$ (top inset) are bounded from above, respectively, by the weak field limit of $\sqrt{2}$ (main panel, top dotted line) and the inviscid limit $\sqrt{3/4}$ (top inset, dotted line). They are also bounded from below by, again respectively, the inviscid limit $1/2$ (main panel, bottom dotted line) and the maximised solutions to equation (2.111). The imaginary part of the growth rate $\Im(\gamma_{0,m})$ (bottom inset) is well described in the small and large S_B limits by equations (2.95) and (2.111). See Figure 2.7 for plots of the analytic asymptotic solutions.

Numerical results

As in the vertical case, v_n is determined by equation (2.55) and so $\delta u_{r,i}$ is the same. However, the other components of the flow, magnetic field and pressure differ, as shown in equations (2.44)-(2.49). We will now show γ_n does as well. To determine γ_n we have (trivially) adapted the root finding algorithm used in the inviscid case. We find a complex instability whose peak growth rate, $\Re(\gamma_n) = \sqrt{2\, \mathrm{d} \ln \hat{\Omega}/\mathrm{d} \ln r} = \sqrt{2}$ occurs when $B \to 0$ and, as before, $n = 0$.

If we concentrate on the limit where B can be neglected entirely, γ_n becomes real. Formally this requires us to re-order $k \sim \mathrm{d}/\mathrm{d}r \sim \epsilon^{-1}/B$, but this is a technicality and the results are the same as simply letting $B \propto \sigma/\theta \to 0$ in equation (2.96)). In this case is useful to contrast the variation of γ_n with σ for a discrete set of values of S_B, which we do in Figure 2.4. In the small S_B limit, γ_n approaches the inviscid growth rate so, for $\theta \ll 1$, we have,

$$S_B \to 0, \qquad B \to 0, \quad \gamma_{n,\mathrm{m}} \to 1/2, \quad \sigma_{n,\mathrm{m}} \to \sqrt{3/4}, \tag{2.97}$$

whilst in the opposite, large S_B limit (subsidiary to its ϵ ordering) we find,

$$S_B \to \infty, \qquad B \to 0, \quad \gamma_{n,\mathrm{m}} \to \sqrt{2}, \qquad \sigma_{n,\mathrm{m}} \to 0. \tag{2.98}$$

So, in the weak field regime, not only do the viscous and inviscid pitched cases differ categorically but, comparing equations (2.72) and (2.98), so do the viscous pitched and the viscous vertical cases. This is depicted in Figure 2.7.

If the magnetic field is allowed to be finite, growing modes become over-stable and both $\Re(\gamma_n)$ and $\Im(\gamma_n)$ increase above the inviscid values as seen in Figure 2.6.

As we now show, starting in the weak field limit, most of results of this section can be derived analytically in the appropriate asymptotic limits.

Weak field limit

The equations governing the viscous pitched field MRI, (2.91) and (2.92) are derived assuming $k \sim 1/\epsilon \gg 1$. In this case the asymptotic expansion for the

roots of the Bessel function v_n, equation (2.59), still holds. Taking the first two terms of this expansion, letting $B \to 0$ ($\sigma \sim 1$), and substituting into equation (2.96) yields

$$\gamma_n^4 + 3S_B\sigma^2\gamma_n^3 + 2\left(\sigma^2 + 1 - s_n k^{-\frac{2}{3}}\right)\gamma_n^2 +$$
$$3S_B\sigma^2\left[\sigma^2 - 2\left(1 - s_n k^{-\frac{2}{3}}\right)\right]\gamma_n + \sigma^2\left[\sigma^2 - 2\left(1 - s_n k^{-\frac{2}{3}}\right)\right] = 0. \quad (2.99)$$

If we also assume $S_B \sim s_n k^{-\frac{2}{3}}$, as in section 2.5.2, then to first order in this quantity we find

$$\gamma_{n,\mathrm{m}} = \frac{1}{2}\left(1 + \frac{9}{16}S_B - s_n\frac{k^{-\frac{2}{3}}}{2}\right), \quad (2.100)$$

$$\sigma_{n,\mathrm{m}} = \sqrt{\frac{3}{4}}\left(1 - \frac{S_B}{16} - s_n\frac{k^{-\frac{2}{3}}}{2}\right). \quad (2.101)$$

Unlike the vertical field case S_B now appears at first order (in equations (2.79) and (2.80) S_B terms arise at second order in the expansion parameter) and here its effect is to increase $\gamma_{n,\mathrm{m}}$, as shown in Figure 2.7. In both the weak and strong B regimes the maximum growth rate can only be determined in the large S_B limit which we turn to now.

Large (subsidiary) S_B limit

Starting from the dispersion relation of the weak field limit, equation (2.99), the fastest growing mode and Alfvén frequency in the large S_B limit can be determined as follows. Treating $(3S_B)^{-1} = \delta$ as small parameter and neglecting $k^{-\frac{2}{3}}$ terms, the governing dispersion relation is

$$\gamma_n^4 + \frac{\sigma^2}{\delta}\gamma_n^3 + 2(\sigma^2 + 1)\gamma_n^2 + \frac{\sigma^2}{\delta}(\sigma^2 - 2)\gamma_n + \sigma^2(\sigma^2 - 2) = 0. \quad (2.102)$$

Differentiating this with respect to σ and setting $\mathrm{d}\gamma_n/\mathrm{d}\sigma = 0$, the stationary points of γ_n obey the following constraint:

$$\gamma_n^3 + 2\delta\gamma_n^2 + 2(\sigma^2 - 1)\gamma_n + 2\delta(\sigma^2 - 1) = 0. \quad (2.103)$$
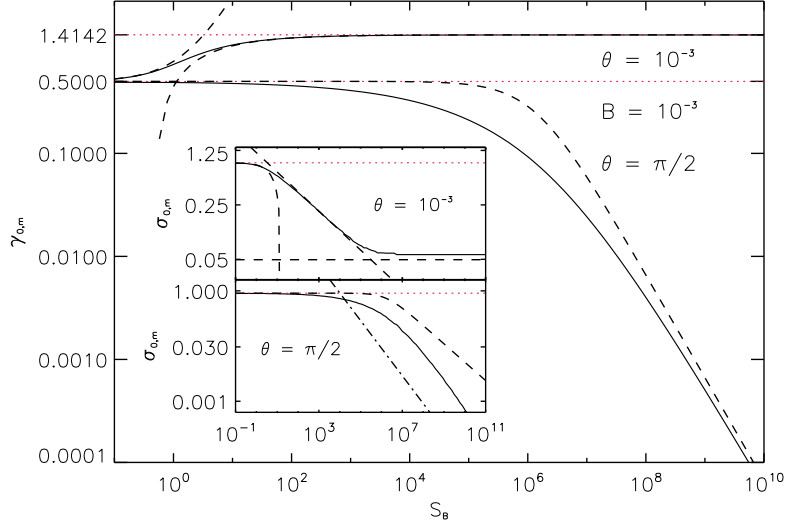
Figure 2.7: Direct comparison of $\gamma_{0,\mathrm{m}}$, $\sigma_{0,\mathrm{m}}$ behaviour of unstable modes for $\theta = 0.001$ (top solid line and inset) and $\theta = \pi/2$ (bottom solid line and inset) with S_B for a weak magnetic field, $B = 0.001$. The dotted lines represent the inviscid limits of $\gamma_{0,\mathrm{m}} = 1/2$ and $\sigma_{0,\mathrm{m}} = \sqrt{3/4}$. The dashed lines represent the various asymptotic solutions we have derived. For the main panel, these are equation (2.83) for the damped $\theta = \pi/2$ field, and equations (2.100) and (2.108) for the small and large S_B limit of the $\theta = 0.001$ field. In the top panel, equation (2.101), (2.109) and (2.111) give the small, intermediate and large S_B limits for $\sigma_{0,\mathrm{m}}$. In the bottom panel, the asymptotic result given by equation (2.83) is accurate only up to $S_B B^2 \sim 1$. Beyond this we have plotted a line of slope $S_B^{-3/4}$ (not derived) for comparison (dash-dot).

Considering the branch $\sigma = \sigma_{n,\mathrm{m}}$ that makes the stationary value of γ_n a maximum $\gamma_{n,\mathrm{m}}$ and introducing $\zeta_{n,\mathrm{m}} = \sigma_{n,\mathrm{m}}^2$, we find

$$\zeta_{n,\mathrm{m}} = \frac{\gamma_{n,\mathrm{m}}(2 - \gamma_{n,\mathrm{m}}^2) + 2\delta(1 - \gamma_{n,\mathrm{m}})}{2(\gamma_{n,\mathrm{m}} + \delta)}, \tag{2.104}$$

and upon substituting this into equation (2.102) we obtain a polynomial whose solutions describe the stationary points of γ_n including its maximum. This equation is

$$\gamma_{n,\mathrm{m}}^6 - 4\gamma_{n,\mathrm{m}}^4 - 20\delta\gamma_{n,\mathrm{m}}^3 + 4(1 - 4\delta^2)\gamma_{n,\mathrm{m}}^2 + 8\delta\gamma_{n,\mathrm{m}} + 4\delta = 0. \tag{2.105}$$

Because it is a sixth order polynomial, there is no general formula for its roots. However, the presence of the small parameter δ suggests that a series solution is appropriate. We assume that $\gamma_{n,\mathrm{m}}$ and $\zeta_{n,\mathrm{m}}$ can be written as

$$\gamma_{n,\mathrm{m}} = \gamma_{n,\mathrm{m},(0)} + \delta^{1/2}\gamma_{n,\mathrm{m},(1)} + \delta\gamma_{n,\mathrm{m},(2)} + \mathcal{O}(\delta^{3/2}), \tag{2.106}$$

$$\zeta_{n,\mathrm{m}} = \zeta_{n,\mathrm{m},(0)} + \delta^{1/2}\zeta_{n,\mathrm{m},(1)} + \delta\zeta_{n,\mathrm{m},(2)} + \mathcal{O}(\delta^{3/2}). \tag{2.107}$$

Substituting this expression for $\gamma_{n,\mathrm{m}}$ into equation (2.105), and solving order by order we can obtain the following set of solutions.

To lowest order we find that $\gamma_{n,\mathrm{m},(0)} = \pm\sqrt{2}, 0$ and we take the positive root, corresponding to the instability. At the next order we do not obtain any information about $\gamma_{n,\mathrm{m},(1)}$, but proceeding to second order in $\delta^{1/2}$, we find that $\gamma_{n,\mathrm{m},(1)} = \pm 2^{3/4}/3^{1/2}$. Guided by the full numerical solution (see Figure 2.7) we take the negative root, and so, to first order in δ, the maximum asymptotic growth rate is given by

$$\gamma_{n,\mathrm{m}} = \sqrt{2}\left(1 - \frac{2^{1/4}}{3}S_B^{-1/2}\right), \tag{2.108}$$

accurate up to and including terms of order $\delta^{1/2}$.

Now substituting our expression for $\gamma_{n,\mathrm{m}}$ into equation (2.107) and demanding that the equation is satisfied to each order in $\delta^{1/2}$, we find, to lowest order, that $\zeta_{n,\mathrm{m},(0)} = 0$. However, at next order we obtain a positive result, namely

that $\zeta_{n,\mathrm{m},(1)} = 2^{5/2}/3^{1/2}$. In anticipation of writing our final answer in terms of $\sigma_{n,\mathrm{m}} = \sqrt{\zeta_{n,\mathrm{m}}}$ we proceed to next order so that our solution for $\gamma_{n,\mathrm{m}}$ and $\sigma_{n,\mathrm{m}}$ are accurate to the same order. Doing so reveals that $\zeta_{n,\mathrm{m},(2)}$ is also zero. This means that we can write the magnetic tension associated with the fastest growing mode as

$$\sigma_{n,\mathrm{m}} = \frac{2^{5/8}}{\sqrt{3}} S_B^{-1/4}, \tag{2.109}$$

accurate up to and including terms of order $\delta^{1/2}$. This result and the result for $\gamma_{n,\mathrm{m}}$ in equation (2.108) are shown in Figure 2.7 and are in good agreement with the full numerical solution (although because of its weak dependence on S_B, the asymptotic expression for $\sigma_{n,\mathrm{m}}$ converges more slowly than $\gamma_{n,\mathrm{m}}$). These results confirm the findings of the previous sections, namely that $\gamma_{n,\mathrm{m}}$ increases with S_B.

If we now relax our weak field assumption so γ_n is given by equation (2.96), we recover the complex instability we found numerically. Assuming $|\gamma_n| \sim 1$ and writing $k = \sigma/B$, the leading order balance of terms $\propto S_B$ is

$$\gamma_n^2 \left(\sigma^2 + B^2 \right) - 4\mathrm{i}\sigma B \gamma_n + \sigma^2 (\sigma^2 - B^2 - 2) = 0, \tag{2.110}$$

and the resultant growth rate is

$$\gamma_n = \frac{2\mathrm{i}B\sigma + \sigma\sqrt{B^2 \left(B^2 - 2 \right) - \sigma^2 \left(\sigma^2 - 2 \right)}}{B^2 + \sigma^2}. \tag{2.111}$$

Although analytic expressions for $\gamma_{n,\mathrm{m}}$ and $\sigma_{n,\mathrm{m}}$ can be derived from this, they are not particularly enlightening. However, Figure 2.7 shows they agree well with the large S_B limit of $\sigma_{0,\mathrm{m}}$.

The results of this section confirm the destabilising properties of the Braginskii viscosity in both the weak and strong field regimes. Of particular interest is the difference in the $\Im(\gamma_n)$ between the inviscid and highly viscous regimes, equations (2.94) and (2.111); an effect not captured at all by local analysis and clearly visible in Figure 2.6.

Now, finally, to compare all the limits of the pitched and vertical cases we again consider the large v_n solutions to equation (2.96).

Highly oscillatory limit

The simplest regime in which to consider the highly oscillatory limit of the viscous MRI is $B \to 0$ so unstable modes will be purely real. In this case, the appropriate mathematical treatment is formally identical to the vertical inviscid case discussed in section 2.5.1, and so $\delta u_{r,i}$ will be the same (although the remaining components will not). The eigenvalue identity is given by equation (2.92) and so the dispersion relation found by inverting it is

$$\gamma_n^4 + 3 S_B \sigma^2 \gamma_n^3 + 2 \left[\sigma^2 + \left(\frac{k \ln k}{n\pi} \right)^2 \right] \gamma_n^2 +$$

$$3 S_B \sigma^2 \left[\sigma^2 - 2 \left(\frac{k \ln k}{n\pi} \right)^2 \right] \gamma_n + \sigma^2 \left[\sigma^2 - 2 \left(\frac{k \ln k}{n\pi} \right)^2 \right] = 0, \quad (2.112)$$

valid in the limit $v_n \gg kr \gg 1$ and $S_B \sim 1$.

Adopting a series solution approach as in the highly oscillatory limit of section 2.5.1 we can expand γ_n in the small parameter k/v_n. Substituting this into equation (2.112), differentiating and solving to determine the turning points of γ_n, we find

$$\gamma_{n,\mathrm{m}} = \frac{1}{2} \frac{k}{v_n} \left(1 + \frac{9}{16} \frac{k}{v_n} S_B \right), \quad (2.113)$$

$$\sigma_{n,\mathrm{m}} = \sqrt{\frac{3}{4} \frac{k}{v_n} \left(1 - \frac{1}{16} \frac{k}{v_n} S_B \right)}. \quad (2.114)$$

In this regime, the first order correction to $\gamma_{0,\mathrm{m}}$ increases, rather than decreases the growth rate viz. equation (2.86). On this, and all other counts, it appears that the effect of the viscous stress tensor on a tilted field otherwise unstable to the MRI, is to further destabilise it. We provide a physical explanation of this shortly and contrast it with that of the vertical field instability, but first let us summarise what we have found about the pitched field case.

2.6.4   Pitched field summary

For a pitched field, the inviscid and (Braginskii) viscous MRI have some simi-larities. As in the vertical case, when finite magnetic field effects are neglected ($B \to 0$, σ finite), both configurations support a purely real instability whose growth is maximised for $n = 0$ modes. When they are not neglected, these modes become over-stable and $\Re(\gamma_{n,\mathrm{m}})$ is reduced.

The wide applicability of the MRI as means of generating angular momentum transporting turbulence from magnetic fields and shear flows, in part, comes from the fact it only requires (and is most efficient for) weak fields. This does not change in the presence of the Braginskii viscosity.

However, some properties of the MRI do change in the presence of the Braginskii viscosity. In the weak field limit of the inviscid case, like the vertical equivalent, γ_n is bound by the Oort-A value $1/2$. The viscous solution is not. Its peak growth rate is $\sqrt{2}$ as $S_B \to \infty$, $B \to 0$ and its $n = 0$ mode is *always* faster than the corresponding inviscid mode. Retaining a finite magnetic field also leads to order of magnitude differences in $\Im(\gamma_n)$ when comparing the inviscid and highly viscous cases.

The azimuthal mode structures $\delta u_{\phi,i}$ and δB_ϕ of the viscous MRI also differ from their inviscid counterparts. However, because $k \gg 1$, in both cases the modes are highly localised on the inner boundary and so graphing them is largely uninformative.

The differences between the growth rates of the inviscid and viscous MRI are important. For weak magnetic fields in the historical ISM, amplification by the Braginskii viscous MRI to the current observed value could have occurred in just 0.5 G yrs, a factor ~ 3 faster in the viscous case. Potentially a significant difference, especially in earlier periods when accounting for the existence of the primordial galactic field is problematic (e.g. Kulsrud, 1999).

The difference between the tilted orientation and the singular vertical and az-imuthal limits where the Braginskii viscosity damps, rather than enhances, the growth rate of unstable modes may prove important in designing good numeri-cal models of the ISM or other magnetized accretion discs. As such, before we

conclude, let us discuss the physical processes that lead to such orientation dependent behaviour. Let us also discuss how what we have found relates to the local approximation, and under what conditions our model may run into difficulties.

2.7 Discussion

2.7.1 Physical mechanism

We have seen that depending on the orientation of an equilibrium magnetic field, the evolution of magnetized shear flow can differ categorically. How is this to be understood physically?

The most informative explanation comes in the weak field regime where the role of the magnetic field is twofold. Firstly it facilitates the generation of pressure anisotropies proportional to its rate of change, or equivalently (in the collisional regime) proportional to the parallel gradient of the parallel component of the rate-of-strain tensor. Because collisions are involved, this is a necessarily dissipative process (Boltzmann, 1872; Chapman & Cowling, 1970). Taking the dot product of the momentum equation, (2.24) with $\boldsymbol{u}_i$ and integrating over space shows that the energy contribution of the Braginskii viscosity is negative definite. That is, the Braginskii viscosity damps any motions that change the magnetic field strength. This is the first role of the magnetic field.

The second role of the magnetic field is a geometric one. Assuming anisotropies do arise (from changes in the magnetic field strength), the field's orientation dictates the projection of the anisotropic stress onto the fluid elements of the plasma, thereby affecting their dynamics. As we now explain, this fact is crucial in determining the stability, or lack thereof, and the role global effects have on a differentially rotating magnetized plasma.

When the field lines have both vertical and azimuthal components (i.e., the field is pitched), fluid elements at different heights can exert an azimuthal force on each other. The sign of this force can be either positive or negative. If the magnetic field is unstable, so its rate of change is positive, the anisotropic stress that leads to this force acts to oppose any azimuthal separation of the two elements. This

can be identified as the fluid version of the stress responsible for the microscopic mirror force. In this case, like the MRI, velocity perturbations to fluid elements at different heights increase (decrease) their angular momentum causing them to move to larger (smaller) radii. In a system with an outwardly decreasing angular velocity profile, this leads to an azimuthal separation of the fluid elements. The associated magnetic field growth ensures the stress is of the right sign to oppose this separation and this transfers angular momentum between them in a way that facilitates further (radial) separation; i.e. an instability (see Quataert *et al.* (2002) for a physical explanation including a spring analogy). However, unlike the Maxwell stress responsible for the MRI, the Braginskii stress does not exert a radial force that opposes the fluid elements' separation. As a result the growth rate of the viscous instability can exceed that of the inviscid MRI. In the limit where there is no Maxwell stress, there is no radial "tension" to limit the instability and the growth rate is maximised. This is the second role of the magnetic field.

In conjunction, the two roles explain our results. In isolated field geometries where there is no projection of the stress onto fluid elements at different heights, the Braginskii viscosity does not give rise to an instability; its only effect is dissipative (Kulsrud, 2005; Lyutikov, 2007; Kunz *et al.*, 2010). This accounts for the damping of perturbations in the azimuthal configuration and the reduced growth rate of the vertical MRI (that depends on the Maxwell, not the Braginskii, stress). When the field is pitched its dissipative effects persist, but the free energy contribution from the differential shear flow will *always* be greater, leading to an instability. The dissipative effects cannot change the stability boundary; they may only change the growth rate. Of course the total field energy (equilibrium plus perturbed) will decrease if viscosity is present and viscous heating is not. However, from the perspective of generating turbulence or transporting angular momentum, this is a secondary consequence.

Now considering finite magnetic field strengths (and therefore hoop tension and viscous curvature stresses) we find these modes become over-stable. The variation of the travelling wave component of the unstable mode is simply a combination of these two effects, to varying degrees.

So, with this explanation in mind, let us turn to the local description of the instability where we compare and contrast the similarities and differences between our global analysis and those from the shearing sheet.

2.7.2   Relation to the local approximation

The local approximation, or shearing sheet analysis, is an extremely useful model of an accretion flow. Therefore it is worth comparing how the results found using it compare to those found here. As we now explain, for the most part they are in agreement and any discrepancies that arise are the result of neglected curvature terms or different boundary conditions. The parts of the following discussion not specific to the Braginskii viscosity can be found in existing literature but, for completeness, we reproduce it (Dubrulle & Knobloch, 1993; Curry *et al.*, 1994; Curry & Pudritz, 1995).

In the local approximation, the coordinate system is Cartesian, the shear is modelled linearly, and the perturbed quantities are assumed to vary rapidly in the radial direction (with respect to the background variations) so they may be written as $\delta\boldsymbol{u}_i(r) = \delta\boldsymbol{u}_i \exp[\mathrm{i}lr]$, $lr \gg 1$. Under this assumption, a WKB-style analysis ignores terms proportional to $1/r$ and replaces $\mathrm{d}/\mathrm{d}r$ by $\mathrm{i}l$. This is, conceptually, the same as the highly-oscillatory approximation of sections 2.5.1, 2.5.2 and 2.6.3. As given by Islam & Balbus (2005); Ferraro (2007), the resultant dispersion relation is

$$\gamma^4 + d_1\gamma^3 + d_2\gamma^2 + d_3\gamma + d_4 = 0, \tag{2.115}$$

where

$$
\begin{aligned}
d_1 =&\, 3S_B\sigma^2 \frac{l^2 + k^2\cos^2\theta}{l^2 + k^2}, \\
d_2 =&\, 2\left(\sigma^2 + \frac{k^2}{l^2 + k^2}\right), \\
d_3 =&\, 3S_B\sigma^2\left(\sigma^2\frac{l^2 + k^2\cos^2\theta}{l^2 + k^2} - 2\cos^2\theta\frac{k^2}{l^2 + k^2}\right), \\
d_4 =&\, \sigma^2\left(\sigma^2 - 2\frac{k^2}{l^2 + k^2}\right).
\end{aligned}
$$

We now compare this with our global results in the relevant limits.

Similarities

Equation (2.115) supports both the inviscid MRI and, for $\theta \neq 0, \pi/2$, the Braginskii facilitated MRI. Taking the limit $k \gg l$, we can compare it to the weak field, large k limit of equations (2.60), (2.78) and (2.99), appropriate when the system is, respectively, vertical and inviscid; vertical and viscous; and pitched and viscous. We find the equations, and therefore the all-important growth rates, are identical.

For the same setups, the large l limit of equation (2.115) differs from the large n-limit of the highly oscillating solutions found in equations (2.67), (2.85) and (2.112). The local wavenumber takes continuous or, in the case of periodic boundary conditions, discrete values that are independent of k, whereas the global equivalent is given by $v_n = (n + 1/2)\pi / \ln w$ which is not independent of k. However, for sufficiently large values of l (and v_n) this difference is unimportant and when the values of l and v_n coincide, the growth rates are identical. Both analyses show that the presence of radial structure decreases the effect of the destabilising shear and increases the effect of viscous dissipation.

Discrepancies

In the strong, pitched magnetic field limit, the local and global results diverge. Whilst the local results predict unstable modes are always real, the global model finds that they are always complex. In the inviscid limit, $\Im(\gamma_n) \sim B$ and so this component can often be reasonably neglected when B is weak. In the very viscous limit $\Im(\gamma_n) \sim \sigma B/(\sigma^2 + B^2)$ and, as shown in Figure 2.6, this can be over an order of magnitude greater than the inviscid result. This difference may prove important (from a modelling perspective) for viscous systems which could have been treated locally, were they inviscid.

Another discrepancy occurs for isolated field configurations. It is easy to see that when $\theta = 0$ and $\theta = \pi/2$, $l = 0$ the terms $A_1, A_3 = 0$ and the local dispersion relation reduces to that of the inviscid case (i.e. the effects of the Braginskii

viscosity are absent). That is, axisymmetric perturbations are neutrally stable for $\theta = 0$ and lead to the MRI for $\theta = \pi/2$. This is in disagreement with sections 2.4 and 2.5. This discrepancy can be understood as follows.

In the azimuthal case, the relevant components of perturbed stress tensor $\boldsymbol{bb}$: $\nabla \boldsymbol{u}_i$ (associated with Braginskii viscosity, equation (2.27)) are given by

$$\delta(\boldsymbol{bb} : \nabla \boldsymbol{u}_i) = \hat{\boldsymbol{e}}_\phi \cdot (\hat{\boldsymbol{e}}_\phi \cdot \nabla(\delta u_{r,i} \hat{\boldsymbol{e}}_r)) = \frac{\delta u_{r,i}}{r} \quad \text{global,} \tag{2.116}$$

$$= 0 \qquad \text{local,} \tag{2.117}$$

and so locally there is no change in the magnetic field (equation (2.25)). This means that there is no Braginskii viscosity and therefore no dissipation, which thereby explains the different results.

In the vertical case there are two differences between the local and global analysis. The incompressibility condition, equation (2.26), is

$$\nabla \cdot \delta \boldsymbol{u}_i = ik\delta u_{z,i} + \frac{\mathrm{d}\delta u_{r,i}}{\mathrm{d}r} + \frac{\delta u_{r,i}}{r} \qquad \text{global,} \tag{2.118}$$

$$= ik\delta u_{z,i} + il\delta u_{r,i} \qquad \text{local,} \tag{2.119}$$

and so in the local case, assuming $l = 0$, we find $\delta u_{z,i} = 0$. However, in a global flow with an impenetrable inner boundary, radial derivatives cannot be ignored as $\mathrm{d}\delta u_{r,i}/\mathrm{d}r = 0$ implies $\delta u_{r,i} = 0$ (this is not true in a local flow with periodic boundary conditions). Because any radial structure reduces γ_n (be it $n \neq 0$ or a finite mode width; see Figure 2.2 and sections 2.5.1 and 2.5.1) the global MRI, both with and without the Braginskii viscosity, will always be slower than its local $l = 0$ counterpart.

A second difference, specific to the Braginskii viscosity, is related to the existence of vertical motions and their effect in a vertical field. Again, $l = 0$ locally implies $\delta(\boldsymbol{bb} : \nabla \boldsymbol{u}_i) \propto \delta u_{z,i} = 0$ whereas, globally, vertical motions are always allowed and so $\delta(\boldsymbol{bb} : \nabla \boldsymbol{u}_i) = ik\delta u_{z,i} \neq 0$. This means that the fastest growing local mode ($l = 0$) is not damped by the Braginskii viscosity, whereas the equivalent global mode is.

A final point is worth making. The local model predicts that the fastest growing

unstable modes ($\theta \neq 0$) occur as $l \to 0$. Formally this is inconsistent with the assumption $l \gg 1/r \neq 0$ that went into deriving equation (2.115). The local solutions obtained under the WKB-style approximation cannot be considered self-consistent and in fact should be described by the type of global solution we have constructed here. However, this fact turns out to be unimportant because, as we have found, it is indeed the modes with the least radial structure that grow the fastest and so the local approach turns out to be correct in this respect.

Overall, aside from the limitations of the local approximation in these two isolated field geometries, there is good agreement between it and our global model in the appropriate limits. Although it would be interesting to consider whether this similarity holds for arbitrary θ, this is outside the scope of the current study. Before we conclude let us consider a few modelling implications of our results.

2.7.3   Modelling implications

Uniform discs

In a magnetized accretion disc, the scale at which the fastest growing linear MRI modes emerge depends on the angle and strength of the background magnetic field. This much is known in the unmagnetized (or inviscid) case and the scaling we find here does not differ qualitatively when collisions are strong (viscosity is small), $k \sim 1/(B\theta)$. However, for a pitched field (the most generic configuration) and weak collisions (large viscosity) the scale of the fastest growing mode acquires an additional parametric dependence on the collision frequency so that $k \propto S_B^{-1/4} \propto \nu_i^{1/4}$. This implies that for a sufficiently collisionless plasma, but still one described by fluid theory, a local-in-z analysis is inappropriate (our choice of $\theta \ll 1$ renders this consideration unimportant for the choice of parameters we consider in section 2.2.1). Physically, density and temperature gradients in the background state will need to be considered as the mode extends over multiple disc scale heights. What this implies in a magnetized plasma is unclear but Gammie & Balbus (1994) have conducted such a study in the inviscid regime and found the presence of conducting boundaries to be important.

Finite pressure anisotropies and instabilities

The nonlinear fate of the MRI in the presence of Braginskii viscosity cannot be determined without a full numerical study and the emergence, or not, of channel modes has not been established here. However, if it is anything like the inviscid MRI, we can reasonably assume that on macroscopic scales far greater than λ_{mfp} coherent structures that grow at a rate $\sim \Omega$ will emerge. When these reach finite amplitudes they will give rise to pressure anisotropies which, as we discuss in detail in chapter 3, drive microscale instabilities. If modelled kinetically (as they should be) the peak growth rates of these instabilities are, in general, faster than the rate of change of the anisotropy generating magnetic fields and they occur on scales far less than λ_{mfp}. In this case the long wavelength description given by equation (2.24) should be used with care and one must ask: Under what conditions, if any, can pressure anisotropy driven micro-instabilities be neglected? In general they cannot be. However, in certain specific magnetized parameter regimes, like the one we consider here, they can. As such, let us briefly consider the mirror instability that occurs for $\Delta \propto \mathrm{d}B/\mathrm{d}t > 0$ (Hasegawa, 1969; Southwood & Kivelson, 1993).

It can been shown that for $\Delta > 1/\beta_i$ equations (2.24)-(2.27) support the slow wave polarised mirror instability. Although a full kinetic calculation is necessary to accurately capture its growth rate, its existence can be determined even in the long wavelength regime (Schekochihin *et al.*, 2005). In this regime modelling the mirror is potentially less problematic than one might expect because its growth rate asymptotes to a finite value[12] (Private correspondence: Kunz, 2010). The fluid version of the mirror instability is therefore not necessarily inconsistent, but it is not a true representation. This is because replacing equation (2.27) by the appropriate kinetic expression of the pressure anisotropy (as one must for $k\lambda_{\mathrm{mfp}} \gg 1$) yields a growth rate

$$\gamma \sim k v_{\mathrm{th},i} \left(\Delta - \frac{1}{\beta_i} \right) \qquad \text{(Mirror Instability)}, \qquad (2.120)$$

---

[12]We deliberately leave discussion of the firehose that can occur when $\mathrm{d}B/\mathrm{d}t < 0$ to the next chapter. Unlike the mirror, in the fluid regime its growth rate does not asymptote to a finite value and its description is therefore ill-posed even there.

so the fastest growing mode peaks, unphysically, at infinitesimal scales and the kinetic dispersion relation describing it is ill posed. This indicates that confining oneself to the fluid regime where the growth rate is finite, is missing something very important. This fact requires attention, or at the least acknowledgement, because fluid simulations that ignore this feature are missing what may turn out to be an important kinetic process. Although it remains an open question how to best incorporate its effects, *in lieu* of a microphysical transport theory, one possibility is to append to the governing equations, the finite Larmor radius corrections given by the hot plasma dispersion relation (Hellinger, 2007; Rincon *et al.*, 2010).

In the linear regime it is known that this regularises the mirror instability. So, for the historic values of the ISM we considered in section 2.2.1, the peak kinetic growth rate of the mirror is now given by

$$\gamma \sim |\Delta|^2 \, \Omega_i \sim 10^{-22} \text{ s}^{-1} \ll \hat{\Omega} \qquad \text{(Peak Mirror Instability)}, \qquad (2.121)$$

where $\Delta \propto \boldsymbol{bb} : \nabla \boldsymbol{u}_i \sim \hat{\Omega}$ for the MRI. So in this one case, the growth rate of the mirror is very slow compared to the MRI, and so its effect can be neglected. This is what we meant when we said that in certain parameter regimes microscale instabilities can be neglected. However, it is often the case (especially in a magnetized plasma) that microscale instabilities cannot be neglected. This cannot be stressed strongly enough. In the next chapter we will consider the firehose, the sister instability to the mirror that occurs when $\mathrm{d}B/\mathrm{d}t < 0$ and show, in the context of galaxy clusters, that its effects are significant and dramatic. However, before we do so let us summarise what we have learnt here.

2.8   Conclusion

Over time the nature of the ideal MRI has been well established but how it is modified in various non-ideal settings remains an active topic of research (Blaes & Balbus, 1994; Balbus & Terquem, 2001; Kunz & Balbus, 2004; Ferraro, 2007; Pessah & Chan, 2008; Devlen & Pekünlü, 2010). The subject of this study has been the global nature of the MRI in a collisional magnetized (Braginskii MHD)

plasma.

We found that for an azimuthal magnetic field with an asymptotically small vertical component, like the MRI, a singular linear instability emerges. The growth rate of this instability depends on S_B, a dimensionless combination of the temperature, shear rate and (mass density normalised) magnetic field strength and is up to a factor of $2\sqrt{2}$ faster than the MRI. We determined the scaling of the maximum growth rate $\gamma_{n,\mathrm{m}} = \sqrt{2}\left(1 - 2^{1/4}/3S_B^{-1/2}\right)$ and Alfvén frequency (or equivalently wavenumber) at which the growth occurs. We also found that the presence of a finite magnetic field strength causes the unstable mode to become over-stable with an imaginary component that can be over an order of magnitude greater than the equivalent over-stable inviscid mode.

In addition to the destabilising effects of the Braginskii viscosity we showed that dissipative effects are important in the isolated field geometries considered here: purely vertical or azimuthal fields. In contradiction to local theory we found that it damps all modes, even the fastest growing ones, and for these it does so significantly when $S_B B^2 \equiv 1/\mathrm{Re} \gtrsim 1$. We showed these effects occur without modifying the stability boundaries of the system.

Associated with both its dissipative and growth enhancing properties, we found the Braginskii viscosity pushes the fastest growing unstable mode towards longer vertical wavelengths as a function of its strength. This may have implications for the resolution and accessible parameter regime of any future numerical study that includes it.

Whilst we motivated our investigation by considering the historic conditions in the ISM, we expect our results to apply to magnetized accretion discs with non-galactic rotation profiles, e.g. Keplerian. In modelling all such magnetized systems, the effects of the Braginskii viscosity should be included. Since anisotropic stresses can now be included in the Athena MP code, it should be relatively easy to simulate the effects of the Braginskii viscosity locally, and hopefully soon, globally as well (Stone *et al.*, 2008; Skinner & Ostriker, 2010). Our results should be of help in benchmarking or at least constraining the appropriate parameter regime of such simulations.

Part III

Firehose instability

Chapter 3

Firehose instability

3.1 Introduction

It has recently been realised in various astrophysics and space physics contexts
that pressure anisotropies (with respect to the direction of the magnetic field)
occur naturally and ubiquitously in magnetized weakly collisional plasmas. They
lead to very fast microscale instabilities such as the firehose and mirror, whose
presence is likely to fundamentally affect the transport properties and, therefore,
both small- and large-scale dynamics of astrophysical plasmas — most interest-
ingly, the plasmas of galaxy clusters and accretion discs (Hall & Sciama, 1979;
Schekochihin & Cowley, 2006; Schekochihin *et al.*, 2008, 2005; Sharma *et al.*,
2006, 2007; Lyutikov, 2007). These instabilities occur even (and especially) in
high-beta plasmas and even when the magnetic field is dynamically weak. The
current state of theoretical understanding of this problem is such that we do not
in general even have a set of well-posed macroscopic equations that govern the
dynamics of such a plasma. This is because calculating the dynamics at long
spatial scales $l \gg \rho_i$ and slow time scales corresponding to frequencies $\omega \ll \Omega_i$
requires knowledge of the form of the pressure tensor and the heat fluxes, which
depend on the nonlinear evolution and saturation of the instabilities triggered by
the pressure anisotropies and temperature gradients. Since this is not currently
understood, we do not have an effective mean-field theory for the large-scale
dynamics.

In the absence of a microphysical theory, it is probably sensible to assume that the instabilities will return the pressure anisotropies to the marginal level and to model large-scale dynamics on this basis, via a suitable closure scheme (Sharma *et al.*, 2006, 2007; Schekochihin & Cowley, 2006; Lyutikov, 2007). This approach appears to be supported by the solar wind data (Gary *et al.*, 2001; Kasper *et al.*, 2002; Bale *et al.*, 2009)

However, a first-principles calculation of the nonlinear evolution of the instabilities remains a theoretical imperative, in order to construct the correct closure, we must understand the mechanism whereby the instabilities control the pressure anisotropy: do they scatter particles? do they modify the structure of the magnetic field? The calculation presented in this chapter will lead us to conclude that the latter mechanism is at work, at least in the simple case we are considering, and indeed a sea of microscale magnetic fluctuations excited by the plasma instabilities will act to pin the plasma to marginal stability.

In this chapter, we present a theory of the nonlinear evolution of the simplest of the pressure-anisotropy-driven instabilities, the parallel ($k_\perp = 0$) firehose instability and the gyrothermal instability (Schekochihin *et al.*, 2010). To be specific, we consider as our main application a plasma under physical conditions characteristic of galaxy clusters: weakly collisional, fully ionized, magnetized and approximately (locally) homogeneous. We will explain at the end the extent to which our results are likely to be useful in the context of the solar wind (section 3.7).

The plan of exposition is as follows. In section 3.2, we give an extended, qualitative, mostly low-analytical-intensity introduction to the problem, explain the relevant properties of the intracluster plasma (section 3.2.1), sketch the linear theory of the firehose instability (section 3.2.2), the main principle of its nonlinear evolution (section 3.2.3), and show that a more complicated theory is necessary to work out the spatial structure of the resulting "firehose turbulence" (section 3.2.4). In section 3.3, a systematic such theory is developed via asymptotic expansions of the electron and ion kinetics (the basic structure of the theory is outlined in the main part of the chapter, while the detailed derivation is relegated to Appendices B and C), culminating in a very simple one-dimensional equation for

the nonlinear evolution of the firehose fluctuations (section 3.4.1), the study of which is undertaken in section 3.4. The results are a theoretical prediction for the nonlinear evolution and spectrum of the firehose turbulence (section 3.4.3) and some tentative conclusions about its effect on the momentum transport (section 3.4.4). In section 3.5, we extend this study to include the effect of parallel ion heat flux on the firehose turbulence: in the presence of a parallel ion temperature gradient, a new instability emerges (the gyrothermal instabilty recently reported by Schekochihin *et al.* 2010 and recapitulated in section 3.5.2) — which, under some conditions, can take over from the firehose. For it as well, we develop a one-dimensional nonlinear equation (section 3.5.1), solve it to predict the nonlinear evolution and spatial structure of the gyrothermal turbulence (section 3.5.3) and discuss the implications for momentum transport (section 3.5.4). A discussion of differences from previous work on firehose instability in collisionless plasmas is given in section 3.6 and a brief survey of astrophysical implications in the solar wind and galaxy clusters in section 3.7. Finally, section 3.8 contains a very concise summary of our findings and of the outlook for future work.

A reader not interested in the technicalities of kinetic theory is advised to ignore section 3.3, and Appendices B and C. A reader only interested in the formal derivation may skip section 3.2, as section 3.3 (supplemented by Appendices B and C) and the sections that follow it can be read in a self-contained way.

3.2   Galaxy Clusters

3.2.1   Conditions in the ICM

Galaxy clusters have long attracted the interest of both theoreticians and observers both as dynamical systems in their own right and as cosmological probes (Bahcall, 2000; Peterson & Fabian, 2006). While gravitationally they are dominated by dark matter, most of their luminous matter is a hot, diffuse, fully ionized, X-ray emitting hydrogen plasma (Sarazin, 2003) known as the intracluster medium, or ICM (the galaxies themselves are negligible both in terms of their mass and the volume they occupy). Crudely, we can think of an observable galaxy cluster as an amorphous blob of ICM about 1 Mpc across, sitting in a gravita-

tional well, with a density profile peaking at the center and decaying outwards. Observationally, on the crudest level, we know what the overall density and temperature profiles in clusters are (e.g., Piffaretti *et al.*, 2005; Vikhlinin *et al.*, 2005). Recent highly resolved X-ray observations reveal the ICM to be a rich, complicated, multiscale structure displaying ripples, bubbles, filaments, waves, shocks, edges etc. (Fabian *et al.*, 2003*a*,*b*, 2006; Sanders & Fabian, 2008; Markevitch & Vikhlinin, 2007), temperature fluctuations (Markevitch *et al.*, 2003; Simionescu *et al.*, 2007; Million & Allen, 2009; Lagana *et al.*, 2009) and most probably also broad-band disordered turbulent motions (Churazov *et al.*, 2004; Schuecker *et al.*, 2004; Rebusco *et al.*, 2006, 2008; Sanders *et al.*, 2010*b*). Radio observations tell us that the ICM also hosts tangled magnetic fields, which are probably dynamically strong (Carilli & Taylor, 2002; Vogt & Enßlin, 2005; Govoni, 2006)

These and other observations motivate a number of questions about the ICM like the ones posed in chapter 1. Principally, can we explain the observed ICM temperature profiles, in particular the apparent lack of a cooling catastrophe at the cluster core predicted by fluid models (Fabian, 1994; Peterson & Fabian, 2006; Parrish & Quataert, 2008; Bogdanović *et al.*, 2009)? This requires modelling various heating processes involving conversion of the energy of plasma motions (turbulent or otherwise) into heat via some form of effective viscosity (e.g., Fabian *et al.*, 2005; Dennis & Chandran, 2005; Kunz *et al.*, 2010), the dynamical effect of thermal instabilities arising in the magnetized ICM (Parrish *et al.*, 2008; Sharma *et al.*, 2008, 2009; Bogdanović *et al.*, 2009; Parrish & Quataert, 2008; Parrish *et al.*, 2010), and the effective thermal conductivity of this medium with account taken of the tangled magnetic field (Chandran & Cowley, 1998; Narayan & Medvedev, 2001; Zakamska & Narayan, 2003). Which, if any, of these processes dominates and how are its effects best incorporated?

Addressing these questions requires a theoretically sound mean-field theory for the ICM dynamics, i.e., a set of prescriptions for its effective transport properties (viscosity, thermal conductivity), which depend on the unresolved microphysics. Without such a theory, all we have is numerical simulations based on fluid models (see references above). While they can often be tuned to produce results that are visually similar to what is observed, they are not entirely satisfactory because

they lack a solid plasma-physical basis. Additionally, refining the numerical resolution often breaks the agreement with observations and requires retuning. A satisfactory transport theory is lacking because any plasma motions in the ICM that change the strength of the magnetic field trigger microscale plasma instabilities (see section 3.2.2) and we do not know what happens next. The type of arguments employed in section 2.7 to neglect their effects must be seen as a special case rather than the norm.

How some of these instabilities arise and evolve is discussed in greater detail below. In order to make this discussion more quantitative, we need to fix a few physical parameters that characterise the ICM. In reality, these parameters vary considerably both between different clusters and within any individual cluster (as a function of radius: from the cooler, denser core to the hotter, more diffuse outer regions). However, for the purposes of this discussion, it is sufficient to adopt a set of fiducial values. Let us consider the plasma in the core of the Hydra A cluster where the parameters are (David *et al.*, 2001; Enßlin & Vogt, 2006)

- Particle (ion and electron) number density

$$n_i = n_e \sim 6 \times 10^{-2} \text{ cm}^{-3}. \tag{3.1}$$

- The measured electron temperature is

$$T_e \sim 3 \times 10^7 \text{ K}, \tag{3.2}$$

and although the ion temperature is unknown, it is assumed to be comparable, $T_i \sim T_e$. The ion thermal speed is then

$$v_{\text{th},i} = \left(\frac{2T_i}{m_i}\right)^{1/2} \sim 7 \times 10^7 \text{ cm s}^{-1}, \tag{3.3}$$

and the ion Debye length is

$$\lambda_{Di} = \frac{v_{\text{th},i}}{\omega_{Di}} = v_{\text{th},i} \left(\frac{4\pi e^2 n_i}{m_i}\right)^{-1/2} \sim 2 \times 10^5 \text{ cm}. \tag{3.4}$$

- The ion collision frequency (in seconds, assuming n_i in cm^{-3} and T_i in K)

is

$$\nu_i \sim 1.5 n_i T_i^{-3/2} \sim 5 \times 10^{-13} \text{ s}^{-1}, \tag{3.5}$$

and consequently the mean free path is

$$\lambda_{\mathrm{mfp}} = \frac{v_{\mathrm{th},i}}{\nu_i} \sim 1.3 \times 10^{20} \text{ cm}. \tag{3.6}$$

- The rms magnetic field strength is (Vogt & Enßlin, 2005)

$$B \sim 7 \times 10^{-6} \text{ G}, \tag{3.7}$$

and consequently the plasma (ion) beta is

$$\beta_i = \frac{8\pi n_i T_i}{B^2} \sim 130, \tag{3.8}$$

the ion cyclotron frequency is

$$\Omega_i = \frac{eB}{m_i c} \sim 0.07 \text{ s}^{-1}, \tag{3.9}$$

and the ion Larmor radius is

$$\rho_i = \frac{v_{\mathrm{th},i}}{\Omega_i} \sim 10^9 \text{ cm}. \tag{3.10}$$

Note that the magnetized-plasma condition $\rho_i \ll \lambda_{\mathrm{mfp}}$ is satisfied extremely well.

- The typical velocity of the plasma motions is (cf. Sanders *et al.*, 2010*a,b*, who place an upper bound on the velocities in a range of clusters including Hyrda A)

$$U \sim 2.5 \times 10^7 \text{ cm s}^{-1}, \tag{3.11}$$

while the typical length scale of these motions is

$$L \sim 2 \times 10^{22} \text{ cm}. \tag{3.12}$$

Consequently the Mach number is

$$M = \frac{U}{v_{\text{th},i}} \sim 0.3, \qquad (3.13)$$

(so the motions are subsonic, hence approximately incompressible on scales smaller than that of the mean density variation) and the Reynolds number based on collisional parallel viscosity is

$$\text{Re} = \frac{LU}{\lambda_{\text{mfp}} v_{\text{th},i}} \sim 60. \qquad (3.14)$$

Assuming Kolmogorov scalings for turbulence, the viscous cutoff scale is

$$l \sim L\text{Re}^{-3/4} \sim 10^{21} \text{ cm}, \qquad (3.15)$$

and the typical velocity at this scale is

$$u \sim U\text{Re}^{-1/4} \sim 10^7 \text{ cm s}^{-1}, \qquad (3.16)$$

so the approximate rms rate of strain (assuming a viscous cutoff for the motions) is

$$\gamma_0 \sim \frac{u}{l} \sim \frac{U}{L} \text{Re}^{1/2} \sim 10^{-14} \text{ s}^{-1}. \qquad (3.17)$$

3.2.2   Firehose instability

If we consider length scales greater than both ρ_i and λ_{mfp} and time scales longer than both Ω_i and ν_i then the moments governing the plasma evolution are those found in chapter 1, namely the ion momentum equation (1.16), and the induction equation (1.17). For clarity, these are

$$m_i n_i \frac{\mathrm{d}\boldsymbol{u}_i}{\mathrm{d}t} = -\boldsymbol{\nabla}\left(p_\perp + \frac{B^2}{8\pi}\right) + \boldsymbol{\nabla} \cdot \left[\boldsymbol{bb}\left(p_\perp - p_\parallel + \frac{B^2}{4\pi}\right)\right], \qquad (3.18)$$

$$\frac{\mathrm{d}\boldsymbol{B}}{\mathrm{d}t} = \boldsymbol{B} \cdot \boldsymbol{\nabla}\boldsymbol{u}_i - \boldsymbol{B}\boldsymbol{\nabla} \cdot \boldsymbol{u}_i. \qquad (3.19)$$

As in chapter 2, we have used equation (1.35) for the pressure tensor and neglected $\mathbf{G}_s$ at these long wavelengths and slow frequencies. As in our work on the MRI, we have restricted ourselves to collisional scales. This means the pressure anisotropy is

$$\Delta = \frac{1}{\nu_i}\frac{1}{B}\frac{\mathrm{d}B}{\mathrm{d}t} = \frac{1}{\nu_i}\boldsymbol{bb}:\nabla\boldsymbol{u}_i \sim \frac{\gamma_0}{\nu_i}, \tag{3.20}$$

where γ_0 is the typical rate of strain of the plasma motion and again we have dropped the subscript i from Δ because electrons contribute only small fraction of the anisotropy[1]. Thus, the pressure anisotropy is regulated by the ratio of the collision frequency to the typical rate of strain or, equivalently, the rate of change of the magnetic-field strength.

Substituting the numbers from section 3.2.1, we find that $|\Delta| \sim 0.02$ in the core of Hydra A. Is this a large number? It turns out that it is a huge number because such anisotropies will make the plasma motion violently unstable.

While the full description of the plasma instabilities triggered by pressure anisotropies requires kinetic treatment, it is extremely straightforward to deduce the presence of the firehose instability directly from equation (3.18).

Consider some "fluid" solution $(\boldsymbol{u}_{0,i}, \boldsymbol{B}_0, p_{0\perp}, p_{0\parallel})$ of equations (3.18) and (3.19) that varies on long time and spatial scales — that can be thought of as the turbulence and/or some regular magnetofluid motion caused by global dynamics. Let us now examine the linear stability of this solution with respect to high-frequency $(\omega \gg |\boldsymbol{\nabla}\boldsymbol{u}_{0,i}|)$, short-scale $(k \gg |\boldsymbol{\nabla}\boldsymbol{u}_{0,i}|/u_{0,i})$ perturbations $(\delta\boldsymbol{u}, \delta\boldsymbol{B}, \delta p_\perp, \delta p_\parallel)$. Mathematically, this is simply equivalent to perturbing a straight-magnetic-field

---

[1] If a Kolmogorov-style turbulence is assumed to exist in the ICM, the typical rate of strain γ_0 will be dominated by the motions at the viscous cutoff scale. However, as we saw in section 3.2.1, the Reynolds-number estimates for ICM do not give very large values and one might wonder whether calling these motions turbulence is justified (Fabian *et al.*, 2003*b*). However, for our purposes, it is not important whether the rate of strain is provided by the viscous cutoff of a turbulent cascade or by a single-scale motion because either can change the magnetic field and thus cause pressure anisotropy (Schekochihin & Cowley, 2006).

equilibrium of equations (3.18) and (3.19):

$$-m_i n_i \omega \delta \boldsymbol{u} = -\boldsymbol{k}_\perp \left(\delta p_\perp + \frac{B_0 \delta B_\parallel}{4\pi} \right) + k_\parallel \delta \boldsymbol{b} \left(p_{0\perp} - p_{0\parallel} + \frac{B_0^2}{4\pi} \right) -$$
$$k_\parallel \boldsymbol{b}_0 \left[\delta p_\parallel + \left(p_{0\perp} - p_{0\parallel} \right) \frac{\delta B_\parallel}{B_0} \right], \quad (3.21)$$

$$-\omega \frac{\delta \boldsymbol{B}}{B_0} = k_\parallel \delta \boldsymbol{u} - \boldsymbol{b}_0 \left(\boldsymbol{k} \cdot \delta \boldsymbol{u} \right), \quad (3.22)$$

where $\delta \boldsymbol{b} = \delta \boldsymbol{B}_\perp / B_0$, we have used $\boldsymbol{k} \cdot \delta \boldsymbol{b} = -k_\parallel \delta B_\parallel / B_0$ (from $\boldsymbol{\nabla} \cdot \boldsymbol{B} = 0$), and $\perp$ and $\parallel$ are with respect to the *unperturbed* magnetic field direction $\boldsymbol{b}_0$. Pressure perturbations can only be calculated from the linearised kinetic equation (see, e.g., Schekochihin *et al.*, 2005), but even without knowing them, we find that for the Alfvénically polarised modes, $\delta \boldsymbol{u} \propto \boldsymbol{b}_0 \times \boldsymbol{k}$, the dispersion relation is

$$\omega = \pm k_\parallel \left(\frac{p_{0\perp} - p_{0\parallel}}{m_i n_i} + v_A^2 \right)^{1/2} = \pm k_\parallel c_s \left(\Delta + \frac{2}{\beta} \right)^{1/2}, \quad (3.23)$$

here, $v_A = B_0 / \sqrt{4\pi m_i n_i}$, $c_s = (p_{0\perp} / m_i n_i)^{1/2}$, $\Delta = (p_{0\perp} - p_{0\parallel}) / p_{0\perp}$ and $\beta = 8\pi p_{0\perp} / B_0^2$. (This is the type of procedure one carries out to show the existence of the fluid mirror instability viz. section 2.7.3.)

Equation (3.23) is simply the dispersion relation for Alfvén waves with a phase speed modified by the pressure anisotropy. If the pressure anisotropy is negative, $\Delta < 0$, the associated stress opposes the Maxwell stress (the magnetic tension force), the magnetic-field lines become more easily deformable, the Alfvén wave slows down and, for $\Delta < -2/\beta$, turns into a nonpropagating unstable mode: the firehose instability (Chandrasekhar *et al.*, 1958; Parker, 1958; Rosenbluth, 1956; Vedenov & Sagdeev, 1958). Its growth rate can, in general, be almost as large as the ion cyclotron frequency as $k_\parallel \rho_i$ approaches finite values (see section 3.2.4). For the ICM parameters given in section 3.2.1, the instability is, therefore, many orders of magnitude faster than either the large-scale dynamics (typical turnover rate $\sim |\nabla \boldsymbol{u}_0| \sim \gamma_0$) or collisions (typical rate ν_i). Unlike the effects of the mirror in ISM, it cannot be ignored.

Thus, any large-scale motion that leads to a local decrease in the strength of

the magnetic field[2] gives rise to a negative pressure anisotropy, which, in turn
triggers the firehose instability. This produces Alfvénically polarised fluctuations
at small parallel scales unless the plasma beta is sufficiently low (magnetic field is
sufficiently strong) for the magnetic tension to stabilise these fluctuations. Using
the typical size of Δ estimated earlier in this section, we find that the typical
beta below which the firehose is stable is $\beta \sim 100$, which is quite close to the
measured value (see section 3.2.1) — perhaps not a coincidence?

Positive pressure anisotropies also lead to instabilities (most importantly, the mir-
ror that we discussed in section 2.7), but they involve resonant particles and are
mathematically harder to handle. We will not discuss them here (see Schekochi-
hin *et al.*, 2005, 2008; Rincon *et al.*, 2010).

3.2.3   Nonlinear evolution of the firehose instability

A nonlinear theory of the firehose instability can be constructed via a quasilin-
ear approach, in which the unstable small-scale (perpendicular) fluctuations of
the magnetic field on the average change the local magnetic-field strength and
effectively cancel the pressure anisotropy (Schekochihin *et al.*, 2008). In equation
(3.20), let us treat the changing magnetic field as the sum of the large-scale field
and the small-scale firehose fluctuations: $\boldsymbol{B} = \boldsymbol{B}_0 + \delta\boldsymbol{B}_\perp$. Then the field strength
averaged over small scales is

$$\overline{B} \sim B_0 \left(1 + \frac{1}{2} \frac{\overline{|\delta\boldsymbol{B}_\perp|^2}}{B_0^2} \right), \tag{3.24}$$

where the overbar denotes the average. The contribution from $\delta\boldsymbol{B}_\perp$ is small, but
for large enough $k_\parallel$, it is growing at a greater rate than the rate of change of the
large-scale field, so its time derivative can be comparable to the time derivative
of B_0. As B_0 is assumed to be decreasing, the growth of the fluctuations can
then cancel this decrease and drive the total average pressure anisotropy to the

---

[2]While turbulence on the average is expected to lead to the growth of the magnetic field
(the dynamo effec), locally there will always be regions where the field strength (temporarily)
decreases. Decrease of the field and, consequently, negative pressure anisotropy can also result
from expanding motion, which decreases the density of the plasma — as, e.g., in the solar wind.

marginal level, $\Delta = -2/\beta$. From equation (3.20), we get

$$\Delta \sim \frac{1}{\nu_i} \left(\frac{1}{B_0} \frac{\mathrm{d}B_0}{\mathrm{d}t} + \frac{1}{2} \frac{\mathrm{d}}{\mathrm{d}t} \frac{\overline{|\delta \boldsymbol{B}_\perp|^2}}{B_0^2} \right) = -\frac{2}{\beta}. \tag{3.25}$$

The rate of change of B_0 is the typical rate of strain of the (large-scale) motion, $(1/B_0)\mathrm{d}B_0/\mathrm{d}t \sim -|\gamma_0|$. The firehose growth rate $\gamma = -i\omega$ is given by equation (3.23). As long as the firehose fluctuations are smaller than the critical level

$$\frac{\overline{|\delta \boldsymbol{B}_\perp|^2}}{B_0^2} \sim \frac{|\gamma_0|}{\gamma}, \tag{3.26}$$

they cannot enforce the marginality condition expressed by equation (3.25) and will continue growing until they reach the required strength (which is still small compared to the large-scale field because $|\gamma_0|/\gamma \ll 1$ for sufficiently large $k_\parallel$). After that, their evolution becomes nonlinear and is determined by equation (3.25), whence we find that their energy has to grow secularly:

$$\frac{\overline{|\delta \boldsymbol{B}_\perp|^2}}{B_0^2} \sim \left(|\gamma_0| - \frac{2\nu_i}{\beta} \right) t. \tag{3.27}$$

As long as the large-scale field keeps decreasing, the small-scale fluctuation energy cannot saturate because if it did, its time derivative would vanish, the anisotropy would drop below marginal and the instability would come back.

The secular growth given by equation (3.27) leads to $\delta B_\perp/B_0 \sim 1$ after roughly one turnover time ($\sim |\gamma_0|^{-1}$) of the large-scale background motion that produces the anisotropy in the first place — thus, the magnetic field can develop order-unity fluctuations before this background motion decorrelates. What all this means for the large-scale dynamics on longer timescales, we do not know.

In what follows, we will be guided by the simple ideas outlined above in constructing a more rigorous kinetic theory of the nonlinear firehose instability.

3.2.4 Effect of finite Larmor radius

Although we have discussed it elsewhere, in this chapter we have so far carefully avoided discussing the magnitude of the wavenumber $k_\parallel$ of the firehose fluctu-

ations. We simply referred to them as "small-scale," with the implication that their scale would be smaller than that of the background fluid dynamics that cause the instability. Examining the dispersion relation (3.23), we see that the growth rate of the instability is proportional to $k_\parallel$, so the smaller the scale the faster the instability. This ultraviolet catastrophe cannot be resolved within the long-wavelength approximation (by which we mean $k\rho_i \ll 1$ as opposed to collisional) in which equation (3.18) is derived. Instead Finite-Larmor-radius (FLR) corrections like those encapsulated in $\mathbf{G}_s$, the gyrophase dependent component of the pressure tensor given by equation (1.28), must be brought in.

Introducing $\mathbf{G}$ to the momentum equation yields a well posed dispersion relation, (Davidson & Völk, 1968, this result will emerge in section 3.4.2) with a peak growth rate and scale

$$\gamma_{\max} \sim \left| \Delta + \frac{2}{\beta} \right| \Omega_i \sim 10^{-3} \ s^{-1} \gg \gamma_0, \tag{3.28}$$

$$k_\parallel \sim \left| \Delta + \frac{2}{\beta} \right|^{1/2} \rho_i^{-1} \sim 10^{-10} \ \text{cm}^{-1} \gg \lambda_{\mathrm{mfp}}^{-1}, \tag{3.29}$$

for the parallel ($k_\perp = 0$) firehose. The numerical values are based on the ICM parameters of section 3.2.1 and the estimate of Δ from section 3.2.2. We have also neglected the heat fluxes for simplicity. For the oblique firehose with $k_\perp \neq 0$ in general we find $\gamma_{\max} \sim |\Delta + 2/\beta|^{1/2}\Omega_i \sim 10^{-2} \ \text{s}^{-1}$ and $k \sim 1/\rho_i$ (Yoon *et al.*, 1993; Hellinger & Matsumoto, 2000).

There are two conclusions to be drawn from this. First, the linear instability is enormously fast compared with the large-scale dynamics that cause it, so its nonlinear behaviour must be fundamentally important at all times. Second, in order to understand the spatial structure of the firehose fluctuations, we need a theory that takes the FLR effects explicitly into account because it is the FLR that sets the scale and the growth rate of the fastest-growing mode as shown in Figure 3.1. We now proceed to construct such a theory for the simplest case — the parallel ($k_\perp = 0$) firehose instability.

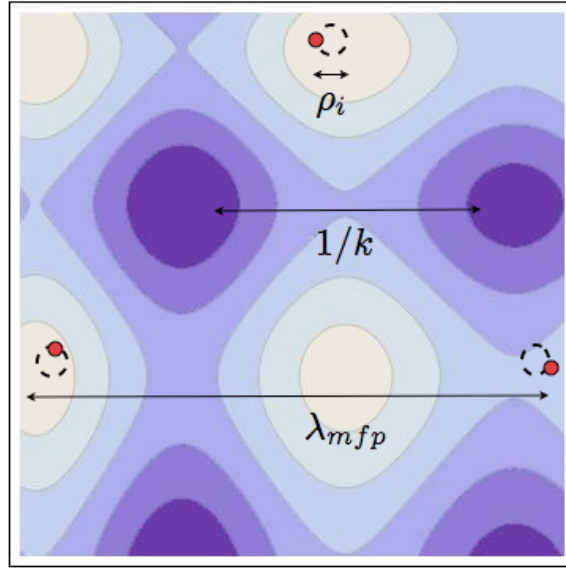Figure 3.1: Microscale firehose fluctuations in a magnetized plasma are regularised by FLR effects so the fastest growing modes occur on scales $\lambda_{\mathrm{mfp}} \gg 1/k \gtrsim \rho_i$, as given by equation (3.29). Macroscopic fluid motions on scales $\gg$ box size, induce changing magnetic fields and therefore pressure anisotropies which provide the free energy source to drive the growing modes.

3.3   Kinetic theory

3.3.1   Outline of the derivation

We start from the fundamental kinetic equation (1.2) and Maxwell's equations (1.3)-(1.6). The tactic is to expand them to obtain a series solution in much the same manner as in section 1.4.1, but in this case however our ordering is more sophisticated and differs for ions and electrons. To aid the reader, we start by quickly restating some key moment equations from the start of chapter 1. The procedure that follows can be thought of as an expansion tailored specifically to the problem of anisotropy driven instabilities.

Electron kinetics: Induction equation

The electron kinetic equation can be expanded in the square root of the electron-ion mass ratio $(m_e/m_i)^{1/2} \approx 0.02$, a natural small parameter for plasma. This expansion is carried out in Appendix B, where we also explain what assumptions have to be made in order for it to be valid. The outcome of the mass-ratio expansion is that electrons are Maxwellian, isothermal ($T_e = \text{const}$), and the electric field can be determined in terms of $\boldsymbol{u}_e$, $\boldsymbol{B}$ and n_e, again, via a generalised Ohm's law:

$$\boldsymbol{E} + \frac{\boldsymbol{u}_e \times \boldsymbol{B}}{c} = -\frac{\boldsymbol{\nabla} p_e}{en_e} = -\frac{T_e \boldsymbol{\nabla} n_e}{en_e}. \tag{3.30}$$

This can now be combined with Maxwell's equations to form the standard induction equation, this time with a Hall term:

$$\frac{\partial \boldsymbol{B}}{\partial t} = \boldsymbol{\nabla} \times \left[\left(\boldsymbol{u}_i - \frac{c}{4\pi Z e n_i} \boldsymbol{\nabla} \times \boldsymbol{B} \right) \times \boldsymbol{B} \right]. \tag{3.31}$$

Ion kinetics: continuity and momentum equations

To close this set of equations, we must determine n_i and $\boldsymbol{u}_i$. Taking moments of the kinetic equation (1.2) we find that n_i and $\boldsymbol{u}_i$ satisfy the continuity and

momentum equations

$$\frac{\partial n_i}{\partial t} = -n_i \boldsymbol{\nabla} \cdot \boldsymbol{u}_i, \tag{3.32}$$

$$\frac{\partial \boldsymbol{u}_i}{\partial t} = -\frac{\boldsymbol{\nabla} \cdot \mathbf{P}_i}{m_i n_i} - \frac{ZT_e \boldsymbol{\nabla} n_i}{m_i n_i} + \frac{(\boldsymbol{\nabla} \times \boldsymbol{B}) \times \boldsymbol{B}}{4\pi m_i n_i}, \tag{3.33}$$

$$\tag{3.34}$$

where the second term on the right-hand side is the electron pressure gradient and the ion pressure tensor is

$$\mathbf{P}_i = m_i \int \mathrm{d}^3 \boldsymbol{v} \, \boldsymbol{v}\boldsymbol{v} f_i. \tag{3.35}$$

We must solve the ion kinetic equation to calculate $\mathbf{P}_i$ in terms of $\boldsymbol{u}_i$ and $\boldsymbol{B}$. We do this by means of an asymptotic expansion in a physical small parameter.

3.3.2 Asymptotic ordering

The small parameter we will use to solve the ion kinetic equation is expressed in terms of the Mach and Reynolds numbers (Schekochihin *et al.*, 2008):[3]

$$\epsilon = \frac{M}{\mathrm{Re}^{1/4}} \sim 0.1, \tag{3.36}$$

where we used the ICM parameters of section 3.2.1. This is the natural small parameter for the plasma motions because, using equations (3.11)-(3.17), it is easy to see that

$$\frac{u}{v_{\mathrm{th},i}} \sim \frac{\lambda_{\mathrm{mfp}}}{l} \sim \epsilon, \tag{3.37}$$

where l is the viscous scale and u the typical flow velocity at this scale. The typical rate of strain $\gamma_0 \sim u/l$ is the relevant parameter for determining the size of the pressure anisotropy because, even though the viscous cutoff we are using is based on the parallel collisional viscosity and so motions can exist below this scale, these motions do not change the strength of the magnetic field (see

---

[3]As already pointed out in footnote 1, our considerations do not depend on Re being large. If a single-scale flow is considered, our expansion is simply an expansion in Mach number.

Schekochihin & Cowley, 2006).[4] Thus, the pressure anisotropy is (from equation (3.20))

$$\Delta \sim \frac{\gamma_0}{\nu_i} \sim \frac{u}{v_{\text{th},i}} \frac{\lambda_{\text{mfp}}}{l} \sim \epsilon^2. \tag{3.38}$$

We solve the ion kinetic equation by asymptotic expansion in ϵ. All ion quantities are expanded in ϵ, so

$$f_i = f_{0i} + f_{1i} + f_{2i} + f_{3i} + \cdots, \tag{3.39}$$

$$n_i = n_{0i} + n_{1i} + n_{2i} + n_{3i} + \cdots, \tag{3.40}$$

$$\boldsymbol{u}_i = \boldsymbol{u}_{0i} + \boldsymbol{u}_{1i} + \cdots, \tag{3.41}$$

$$\boldsymbol{B} = \boldsymbol{B}_0 + \boldsymbol{B}_1 + \cdots. \tag{3.42}$$

The lowest-order quantities n_{0i}, $\boldsymbol{u}_{0i}$, $\boldsymbol{B}_0$ are associated with the motions that produce the pressure anisotropy and have the length scale l and time scale γ_0, so we order

$$\boldsymbol{u}_{0i} \sim \epsilon v_{\text{th},i}, \quad \boldsymbol{\nabla} \boldsymbol{u}_{0i} \sim \gamma_0 \sim \epsilon^2 \nu_i. \tag{3.43}$$

Since the instability parameter is $\Delta + 2/\beta_i$, we must order $\boldsymbol{B}_0$ so that

$$\frac{2}{\beta_i} \sim \Delta \sim \epsilon^2 \quad \Rightarrow \quad \frac{B_0}{\sqrt{4\pi m_i n_{0i}}} \sim \epsilon v_{\text{th},i}. \tag{3.44}$$

The perturbations n_{1i}, $\boldsymbol{u}_{1i}$, $\boldsymbol{B}_1$ around this slow large-scale dynamics are assumed to be excited by the parallel ($k_\perp = 0$) firehose instability and have much shorter spatial and time scales. Their typical wavenumber is the one at which the instability's growth rate peaks and their time scale is set by this maximum growth

---

[4]This statement applies to macroscopic motions: for example, Alfvénic turbulence below the parallel viscous scale that can occupy a wide range of scales all the way down to the ion Larmor scale (e.g., Schekochihin *et al.*, 2009). The fast, microscale plasma fluctuations triggered by plasma instabilities, including the firehose fluctuations that will be considered in this chapter, will, on the average, change the field strength (see section 3.2.3). Accordingly, their ordering [equation (3.46)] will be arranged in precisely such a way that they are able to have an effect comparable to the macroscale motions that produce γ_0.

rate (see section 3.2.4):

$$k_\parallel \rho_i \sim \left| \Delta + \frac{2}{\beta_i} \right|^{1/2} \sim \epsilon, \quad \gamma \sim \left| \Delta + \frac{2}{\beta_i} \right| \Omega_i \sim \epsilon^2 \Omega_i. \tag{3.45}$$

In order to be able to proceed, we must order the time scales of the lowest-order ("equilibrium") fields and of the fluctuations with respect to each other. Physically, they depend on different things and are not intrinsically related. However, our *a priori* consideration of the nonlinear evolution of the instability (section 3.2.3) suggests that for the nonlinearity to become important, we must have (see equation (3.26))

$$\frac{\boldsymbol{B}_1}{B_0} \sim \left(\frac{\gamma_0}{\gamma} \right)^{1/2}. \tag{3.46}$$

Since $\boldsymbol{B}_1 \sim \epsilon \boldsymbol{B}_0$, this tells us that we must order

$$\gamma_0 \sim \epsilon^2 \gamma \sim \epsilon^4 \Omega_i \quad \Rightarrow \quad \nu_i \sim \epsilon^2 \Omega_i, \quad \rho_i \sim \epsilon^2 \lambda_{\mathrm{mfp}}. \tag{3.47}$$

These relations are, of course, not strictly right in the quantitative sense — the Larmor radius is grossly overestimated here if we take the value of ϵ for the ICM given by equation (3.36) and compare it with the observational value given by equation (3.10). However, ordering ρ_i this way allows us to capture all the important physics in our formal expansion. We will also argue in section 3.4.3 that this ordering of the finite Larmor radius physics gets quantitatively better as the nonlinear regime proceeds (see footnote 8).

Let us summarise our ordering of the relevant time and spatial scales compared to $k_\parallel v_{\mathrm{th},i}$ and $k_\parallel$, respectively: using equations (3.47) and (3.45), we have

$$\gamma_0 \sim \epsilon^3 k_\parallel v_{\mathrm{th},i}, \quad \gamma \sim \nu_i \sim \epsilon k_\parallel v_{\mathrm{th},i}, \quad \Omega_i \sim \epsilon^{-1} k_\parallel v_{\mathrm{th},i}, \tag{3.48}$$

$$l^{-1} \sim \epsilon^2 k_\parallel, \quad \lambda_{\mathrm{mfp}}^{-1} \sim \epsilon k_\parallel, \quad \rho_i^{-1} \sim \epsilon^{-1} k_\parallel. \tag{3.49}$$

3.3.3 Firehose fluctuations

The ordering we adopted, inasmuch as it concerns the properties of the firehose fluctuations, applies to the parallel firehose only, so we now explicitly restrict our consideration to the case of $\boldsymbol{\nabla}_\perp = 0$ for all first-order perturbations. Since $\boldsymbol{\nabla} \cdot \boldsymbol{B} = 0$, this immediately implies

$$B_1^\| = 0, \tag{3.50}$$

so $\boldsymbol{B}_1 = \boldsymbol{B}_1^\perp$. Here and in what follows, $\|$ and $\perp$ refer to directions with respect to the unperturbed field $\boldsymbol{B}_0$.

The induction equation (3.31), taken to the lowest order in ϵ, gives

$$\frac{\mathrm{d}}{\mathrm{d}t} \frac{\boldsymbol{B}_1^\perp}{B_0} = \nabla_\| \boldsymbol{u}_{1i}^\perp \tag{3.51}$$

(all terms here are order $\epsilon^2 k_\| v_{\mathrm{th},i}$; see section 3.3.2; note that the Hall term in equation (3.31) is subdominant by two orders of ϵ and so, as promised in section 1.3.2, irrelevant). Here $\mathrm{d}/\mathrm{d}t = \partial/\partial t + \boldsymbol{u}_0 \cdot \boldsymbol{\nabla}$ is the convective derivative, but, since $\boldsymbol{\nabla} \boldsymbol{u}_0 \sim \epsilon^3 k_\| v_{\mathrm{th},i}$, the shearing of the perturbed field due to the variation of $\boldsymbol{u}_0$ is negligible and we can replace $\mathrm{d}/\mathrm{d}t$ by $\partial/\partial t$ by transforming into the frame moving with velocity $\boldsymbol{u}_0$.

In the continuity equation (3.32) taken to the lowest order in ϵ, setting $\boldsymbol{\nabla}_\perp = 0$ gives

$$\frac{\mathrm{d}}{\mathrm{d}t} \frac{n_{1i}}{n_{0i}} = -\nabla_\| u_{1i}^\| \tag{3.52}$$

(all terms are order $\epsilon^2 k_\| v_{\mathrm{th},i}$). Anticipating the form of the unstable perturbation, we will set

$$n_{1i} = 0, \quad u_{1i}^\| = 0 \tag{3.53}$$

without loss of generality. In Appendix C.0.11, we will explicitly prove that $n_{1i} = 0$. In Appendix C.0.14, we will learn that $n_{2i} = 0$ as well.

Consider now the ion momentum equation (3.34). In the lowest order of the ϵ

expansion (terms of order $\epsilon k_\parallel v_{\text{th},i}^2$), it gives, upon using equation (3.53),

$$\boldsymbol{\nabla} \cdot \mathbf{P}_{1i} = 0. \tag{3.54}$$

We will learn in Appendix C.0.13 that this can be strengthened to set

$$\mathbf{P}_{1i} = 0. \tag{3.55}$$

In the next order ($\epsilon^2 k_\parallel v_{\text{th},i}$), we get (using $n_{2i} = 0$)

$$\boldsymbol{\nabla} \cdot \mathbf{P}_{0i} + \boldsymbol{\nabla} \cdot \mathbf{P}_{2i} + ZT_e\boldsymbol{\nabla} n_{0i} = 0. \tag{3.56}$$

Averaging this over small scales eliminates the perturbed quantities, so we learn[5]

$$\boldsymbol{\nabla} \cdot \mathbf{P}_{0i} + ZT_e\boldsymbol{\nabla} n_{0i} = 0 \tag{3.57}$$

and, therefore, from equation (3.56), also

$$\boldsymbol{\nabla} \cdot \mathbf{P}_{2i} = 0 \tag{3.58}$$

(confirmed in Appendix C.0.14). Finally, in the third order ($\epsilon^3 k_\parallel v_{\text{th},i}^2$), the perpendicular part of equation (3.34) determines the perturbed velocity field:

$$\frac{\mathrm{d}\boldsymbol{u}_{1i}^\perp}{\mathrm{d}t} = -\frac{(\boldsymbol{\nabla} \cdot \mathbf{P}_{3i})_\perp}{m_i n_{0i}} + v_A^2 \nabla_\parallel \frac{\boldsymbol{B}_1^\perp}{B_0}, \tag{3.59}$$

where $v_A = B_0^2/4\pi m_i n_{0i}$. There is no $ZT_e\boldsymbol{\nabla}_\perp n_{3i}$ term in equation (3.59) because we assume that the only small-scale spatial variations of all quantities are in the parallel direction. The ion pressure term $(\boldsymbol{\nabla} \cdot \mathbf{P}_{3i})_\perp$ is to be calculated by solving the ion kinetic equation (see section 3.3.5).

To summarise, we are looking for perturbations such that $\boldsymbol{\nabla}_\perp = 0$, $n_{1i} = 0$, $B_1^\parallel = 0$, $\boldsymbol{u}_{1i}^\parallel = 0$, while $\boldsymbol{B}_1^\perp$ and $\boldsymbol{u}_{1i}^\perp$ satisfy equations (3.51) and (3.59). Physically, this reflects the fact that the parallel ($k_\perp = 0$) firehose perturbations are

---

[5]This is simply the pressure balance for the large-scale dynamics, an expected outcome for a system with low Mach number. In Appendix C.0.10, we will show that the zeroth-order distribution is Maxwellian, so the pressure associated with it is a scalar, $p_{0i} = n_{0i}T_{0i}$, and equation (3.57) becomes $(T_{0i} + ZT_e)\boldsymbol{\nabla} n_{0i} + n_{0i}\boldsymbol{\nabla} T_{0i} = 0$. Further discussion of the role played by the ion temperature gradient can be found in section 3.5.

Alfvénic in nature (have no compressive part). That it is legitimate to consider such perturbations separately from other types of perturbations is not *a priori* obvious, but will be verified by our ability to obtain a self-consistent solution of the ion kinetic equation, which will satisfy equations (3.55), (3.57), and (3.58) (see Appendix C).

3.3.4   Large-scale dynamics

In section 3.3.3, equations for the first-order fields, $\boldsymbol{u}_{1i}^{\perp}$ and $\boldsymbol{B}_1^{\perp}$ emerged after expanding the induction equation (3.31) and the continuity equation (3.32) to lowest order in ϵ and the momentum equation (3.34) up to the third order. If, using the ordering of section 3.3.2, we go to the next order and average over small scales to eliminate small-scale perturbations, we recover the equations for the large-scale (unperturbed) fields: the induction equation

$$\frac{\mathrm{d}\boldsymbol{B}_0}{\mathrm{d}t} = \boldsymbol{B}_0 \cdot \boldsymbol{\nabla} \boldsymbol{u}_{0i} - \boldsymbol{B}_0 \boldsymbol{\nabla} \cdot \boldsymbol{u}_{0i} \tag{3.60}$$

(all terms are order $\epsilon^3 k_{\parallel} v_{\mathrm{th},i} B_0$), the continuity equation

$$\frac{\mathrm{d}n_{0i}}{\mathrm{d}t} = -n_{0i} \boldsymbol{\nabla} \cdot \boldsymbol{u}_{0i} \tag{3.61}$$

(all terms are order $\epsilon^3 k_{\parallel} v_{\mathrm{th},i} n_{0i}$), and the momentum equation

$$m_i n_{0i} \frac{\mathrm{d}\boldsymbol{u}_{0i}}{\mathrm{d}t} = -\boldsymbol{\nabla} \cdot \mathbf{P}_{2i} - \boldsymbol{\nabla}\frac{B_0^2}{8\pi} + \frac{\boldsymbol{B}_0 \cdot \boldsymbol{\nabla}\boldsymbol{B}_0}{4\pi} \tag{3.62}$$

(all terms are order $\epsilon^4 m_i n_{0i} k_{\parallel} v_{\mathrm{th},i}^2$). The divergence of the second-order ion pressure tensor here is with respect to the large-scale spatial variation (according to equation (3.58), it has no small-scale dependence). Again, $\mathbf{P}_{2i}$ is calculated from ion kinetics.

Equations (3.60)-(3.62) are precisely the kind of mean-field equations that are needed to calculate the large-scale dynamics of astrophysical plasmas. They look just like the usual fluid MHD equations, the only nontrivial element being the pressure term in the momentum equation (3.62). The goal of kinetic theory is to calculate this pressure, which depends on the microphysical fluctuations at

small scales. In this thesis, we only do this for the parallel ($k_\perp = 0$) firehose fluctuations. The implications of our results for the ion momentum transport will be discussed in section 3.4.4.

3.3.5 Solution of the ion kinetic equation

We now proceed to use the ordering established in section 3.3.2 to construct an asymptotic expansion of the ion kinetic equation. This procedure, while analytically straightforward, is fairly cumbersome and so its detailed exposition is exiled to Appendix C. The results are as follows.

In the expansion of the ion distribution function (equation (3.39)), f_{0i} is found to be a Maxwellian (Appendix C.0.10), with density n_{0i} and temperature T_{0i} that have to satisfy the equilibrium pressure balance constraint (see equation (3.57) and Appendix C.0.13).

The first-order perturbed distribution function, f_{1i}, is proportional to $\boldsymbol{b}_0 \cdot \boldsymbol{\nabla} T_{0i}$ and is responsible for the large-scale collisional ion heat fluxes (Appendix C.0.13).

The second-order perturbed distribution function f_{2i} contains the pressure anisotropy. The corresponding second-order pressure tensor is diagonal:

$$\mathbf{P}_{2i} = p_{2i}\mathbf{I} + (p_{2i}^\perp - p_{2i}^\parallel)\left(\frac{1}{3}\,\mathbf{I} - \boldsymbol{b}_0\boldsymbol{b}_0\right), \tag{3.63}$$

where p_{2i} is the perturbed isotropic pressure and $p_{2i}^\perp - p_{2i}^\parallel$ is the lowest-order pressure anisotropy. The isotropic part of the pressure is determined from the large-scale equations for density n_{0i}, temperature T_{0i} and velocity $\boldsymbol{u}_{0i}$ of the fluid — this is explained in detail in Appendix C.0.17, but here let us just assume for simplicity that the zeroth-order density and temperature are constant ($\boldsymbol{\nabla} n_{0i} = 0$, $\boldsymbol{\nabla} T_{0i} = 0$), in which case the continuity equation (3.61) reduces to $\boldsymbol{\nabla}\cdot\boldsymbol{u}_{0i} = 0$ and p_{2i} then follows from enforcing this incompressibility constraint on the momentum

equation (3.62). The pressure anisotropy is calculated in Appendix C.0.18:

$$\Delta(t) \equiv \frac{p_{2i}^{\perp} - p_{2i}^{\parallel}}{p_{0i}}$$

$$= \Delta_0 + \frac{3}{2} \int_0^t \mathrm{d}t' e^{-3\nu_i(t-t')} \frac{\partial}{\partial t'} \overline{\frac{|\boldsymbol{B}_1^{\perp}(t')|^2}{B_0^2}}, \qquad (3.64)$$

where $p_{0i} = n_{0i}T_{0i}$ is the equilibrium pressure, the overbar denotes the averaging over small scales of the nonlinear feedback on the anisotropy from the firehose fluctuations, and Δ_0 is the pressure anisotropy arising from the large-scale motions. In general, it contains contributions from changes in the magnetic field strength (because of the approximate conservation of the first adiabatic invariant, as discussed in section 1.5.2), compression and heat fluxes (see equation (C.57)). When n_{0i} and T_{0i} are constant, only the anisotropy induced by the changes in field strength survives,[6] which is the case we will consider here:

$$\Delta_0 = \frac{\boldsymbol{b}_0\boldsymbol{b}_0 : \boldsymbol{\nabla}\boldsymbol{u}_{0i}}{\nu_i} = \frac{1}{\nu_i}\frac{1}{B_0}\frac{\mathrm{d}B_0}{\mathrm{d}t} = \frac{\gamma_0}{\nu_i}. \qquad (3.65)$$

This is exactly what was anticipated qualitatively — see equation (3.20). Since we are interested in the firehose instability, we assume $\Delta_0 < 0$.

Finally, the third-order perturbed distribution function f_{3i} is responsible for the third-order pressure tensor that appears in the perturbed ion momentum equation (3.59). The relevant part of that tensor is calculated in Appendix C.0.20. Assuming constant density and temperature (otherwise, there is again a contribution from the heat fluxes; see Appendix 3.5), it may be written as follows

$$\frac{(\boldsymbol{\nabla} \cdot \boldsymbol{\mathsf{P}}_{3i})_{\perp}}{p_{0i}} = -\nabla_{\parallel}\left[\Delta(t)\frac{\boldsymbol{B}_1^{\perp}}{B_0} + \frac{\nabla_{\parallel}\boldsymbol{u}_{1i}^{\perp}}{\Omega_i} \times \boldsymbol{b}_0\right], \qquad (3.66)$$

where $\Delta(t)$ is given by equation (3.64).

Let us now use these results to study the firehose turbulence (sections 3.4.1–3.4.3) and its effect on the large-scale dynamics (section 3.4.4).

---

[6]The effect of heat fluxes on the firehose turbulence is considered in section 3.5.

3.4 Firehose turbulence

3.4.1 Firehose turbulence equation

Using the results derived in Appendix C and summarised in section 3.3.5, we find that the ion momentum equation (3.59), which describes the evolution of the perturbed ion velocity, is, in the reference frame moving with $\boldsymbol{u}_{0i}$,

$$\frac{\partial \boldsymbol{u}_{1i}^{\perp}}{\partial t} = \frac{v_{\mathrm{th},i}^2}{2} \nabla_{\parallel} \left[\left(\Delta(t) + \frac{2}{\beta_i} \right) \frac{\boldsymbol{B}_1^{\perp}}{B_0} + \frac{\nabla_{\parallel} \boldsymbol{u}_{1i}^{\perp}}{\Omega_i} \times \boldsymbol{b}_0 \right], \tag{3.67}$$

where we have used equation (3.66) for the pressure term in equation (3.59). Three forces appear on the right-hand side of this equation. First, there is the stress due to the anisotropy Δ of the ion distribution, given by equation (3.64). This is is the quantitative form of the expression for $\Delta(t)$ that we guessed in equation (3.25): the first term in equation (3.64) is due to the slow decrease of the large-scale magnetic field, the second to the average effect of the growing small-scale fluctuations, which strive to cancel that decrease. The second term in equation (3.67), proportional to $1/\beta_i = v_A^2/v_{\mathrm{th},i}^2$, is the magnetic tension force, which resists the perturbation of the magnetic-field lines and, therefore, acts against the pressure-anisotropy driven instability. The instability is marginal when $\Delta + 2/\beta_i \to -0$. Finally, the third term is the FLR effect, which, as was promised in section 3.2.4 and as will shortly be demonstrated, sets the scale of the most unstable perturbations.

Let us now combine equation (3.67) with the induction equation (3.51) for the perturbed magnetic field, also taken in the reference frame moving with $\boldsymbol{u}_0$. After differentiating equation (3.51) once with respect to time, we get

$$\frac{\partial^2 \boldsymbol{B}_1^{\perp}}{\partial t^2} = \frac{v_{\mathrm{th},i}^2}{2} \nabla_{\parallel}^2 \left[\left(\Delta + \frac{2}{\beta_i} \right) \boldsymbol{B}_1^{\perp} + \frac{1}{\Omega_i} \frac{\partial \boldsymbol{B}_1^{\perp}}{\partial t} \times \boldsymbol{b}_0 \right]. \tag{3.68}$$

In the second term on the right-hand side, we have used equation (3.51) to express $\nabla_{\parallel} \boldsymbol{u}_{1i}^{\perp}$ in terms of the time derivative of $\boldsymbol{B}_1^{\perp}$. Equation (3.68) with $\Delta(t)$ defined by equation (3.64) is a closed equation for the perturbed magnetic field with nonlinear feedback (last term in equation (3.64)). This is the equation for the
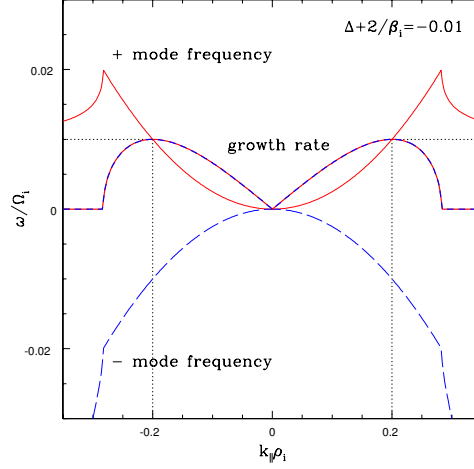
Figure 3.2: Frequencies (thin lines) and growth rates (bold lines) of the unstable firehose modes (red/solid: the "+" mode; blue/dashed: the "−" mode) given by equation (3.70). The instability parameter here is $\Delta + 2/\beta_i = -0.01$. Dotted vertical lines indicate the wavenumber of fastest growth $k_\mathrm{p} = 0.2$ (equation (3.72)) and the dotted horizontal lines the corresponding maximum growth rate $\gamma_\mathrm{max} = \mathrm{Im}\,\omega_\mathrm{p} = 0.01$ (equation (3.73)).

one-dimensional ($k_\perp = 0$) *firehose turbulence*. It represents the simplest nonlinear model for this kind of turbulence available to date.[7]

3.4.2   Linear theory

In the linear regime, we may neglect the second term in equation (3.64), so $\Delta = \Delta_0$. The linear dispersion relation for equation (3.68) is

$$\left[\omega^2 - \frac{k_\parallel^2 v_{\mathrm{th},i}^2}{2} \left(\Delta + \frac{2}{\beta_i} \right) \right]^2 = \frac{k_\parallel^4 v_{\mathrm{th},i}^4}{4} \frac{\omega^2}{\Omega_i^2}. \tag{3.69}$$

---

[7]The essential difference with the equation derived in Schekochihin *et al.* (2008) is the FLR term, which removes the ultraviolet catastrophe of the long-wavelength firehose and thus allows equation (3.68) to handle non-monochromatic (multiscale) solutions. In section 3.4.3, we will see that this produces a much more complex behaviour than was seen in Schekochihin *et al.* (2008), justifying the term "firehose turbulence."

This has four roots out of which two are unstable when $\Delta + 2/\beta_i < 0$:

$$\frac{\omega}{\Omega_i} = \pm\frac{k^2}{4} + i\,\frac{|k|}{\sqrt{2}}\,\left|\Delta + \frac{2}{\beta_i}\right|^{1/2}\sqrt{1 - \frac{k^2}{k_0^2}}, \tag{3.70}$$

where $k = k_\parallel \rho_i$ and

$$k_0 = 2\sqrt{2}\,\left|\Delta + \frac{2}{\beta_i}\right|^{1/2}. \tag{3.71}$$

Unlike in the long-wavelength limit ($k_\parallel \rho_i \to 0$), there is now a real frequency (so the firehose perturbation propagates while its amplitude grows exponentially and the vector $\boldsymbol{B}_1^\perp$ rotates; see section 3.4.3) and the growth rate has its peak at $k_\mathrm{p} = k_0/\sqrt{2}$, so

$$k_\mathrm{p} = 2\,\left|\Delta + \frac{2}{\beta_i}\right|^{1/2}, \tag{3.72}$$

$$\omega_\mathrm{p} = (\pm 1 + i)\,\left|\Delta + \frac{2}{\beta_i}\right|, \tag{3.73}$$

where the complex peak frequency ω_p is in units of Ω_i. At $k_\parallel \rho_i > k_0$, there is no growth and the firehose perturbations turn into purely propagating Alfveén waves (modified by pressure anisotropy and dispersive FLR corrections).

The dependence of the frequencies and growth rates of the two unstable modes on wavenumber is given by equation (3.70) and plotted in Figure 3.2 for a representative value of the instability parameter $\Delta + 2/\beta_i = -0.01$ (this is the value used in the numerical solution of section 3.4.3).

It should be pointed out here that in this theory, there is no dissipation of the magnetic fluctuations excited by the firehose. The most unstable wavenumber is set by dispersive effects; the stable modes are undamped.
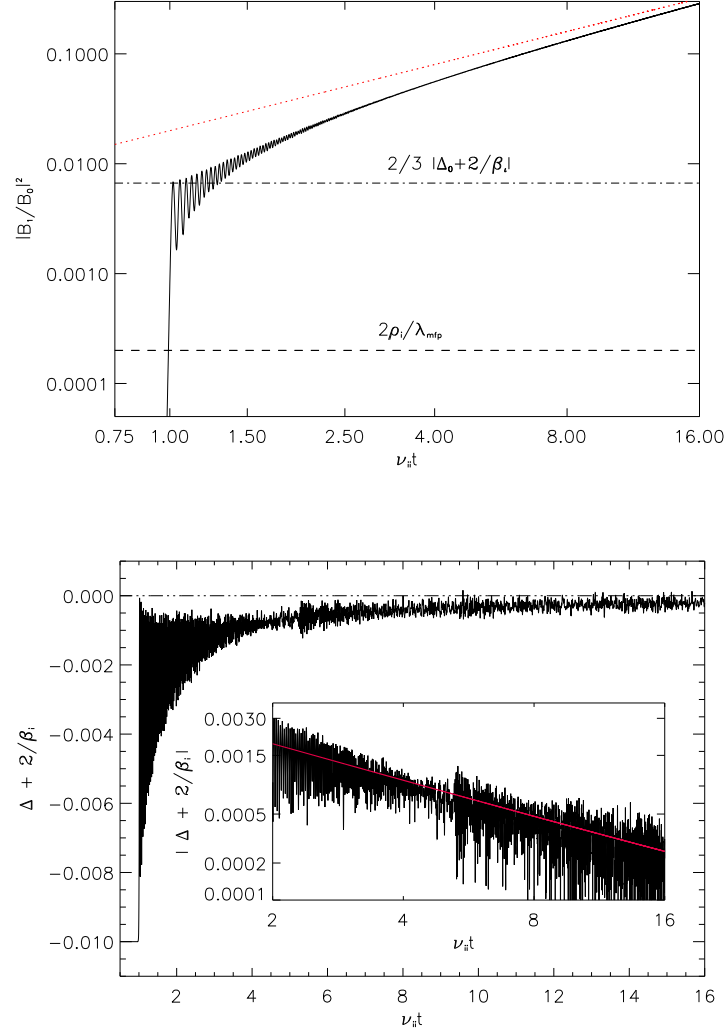
Figure 3.3: *Top panel:* evolution of the magnetic energy $\overline{|\boldsymbol{B}_1^\perp|^2}/B_0^2 = \sum_k |A_k|^2$ with time in a numerical solution of equations (3.77) and (3.78) with parameters (3.89); the time here is normalised using the collision frequency ν_i, not the cyclotron frequency Ω_i; the two horizontal lines show the "collisional" (lower line) and "collisionless" (upper line) estimates for the energy at which the nonlinear feedback turns on: equations (3.80) and (3.81), respectively; the red dotted line shows the nonlinear asymptotic given by equation (3.82). *Bottom panel:* evolution of the instability parameter (pressure anisotropy) $\Delta + 2/\beta_i$ in the same numerical solution. *Inset:* log-log plot of the evolution of $|\Delta + 2/\beta_i|$; the red line shows the slope corresponding to $1/t$ (see equation (3.86)).

3.4.3   Nonlinear evolution and spectrum

Firehose turbulence equation in scalar form

Since the nonlinearity involves the spatially averaged perturbed magnetic energy, the firehose turbulence is compactly described in Fourier space not just in the linear but also in the nonlinear regime: this amounts to replacing $\nabla_\parallel^2 \to -k_\parallel^2$ in equation (3.68) and $\overline{|\boldsymbol{B}_1^\perp|^2} = \sum_{k_\parallel} |\boldsymbol{B}_1^\perp(k_\parallel)|^2$ in equation (3.64). A simple ansatz can now be used to convert equation (3.68) into scalar form. Without confusing A_k with the vector potential, let

$$\frac{B_{1x}}{B_0} = A_k(t) \cos\left(\frac{k^2}{4} t + \phi_k\right), \tag{3.74}$$

$$\frac{B_{1y}}{B_0} = A_k(t) \sin\left(\frac{k^2}{4} t + \phi_k\right), \tag{3.75}$$

where the axes (x, y) in the plane perpendicular to $\boldsymbol{b}_0$ are chosen arbitrarily and we have non-dimensionalised wavenumbers and time:

$$k_\parallel \rho_i \to k, \quad \Omega_i t \to t. \tag{3.76}$$

This ansatz amounts to factoring out the rotation of the vector $\boldsymbol{B}_1^\perp(k)$ (the first term in equation (3.70)). The wavenumber-dependent but time-independent phase ϕ_k is determined by the initial condition. We assume $\phi_k = \phi_{-k}$, so $A_k^* = A_{-k}$ must be satisfied to respect the fact that $\boldsymbol{B}_1^\perp$ is a real field. The fluctuation amplitude $A_k(t)$ satisfies

$$\frac{\partial^2 A_k}{\partial t^2} = \frac{k^2}{2} \left[-\left(\Delta + \frac{2}{\beta_i}\right) - \frac{k^2}{8} \right] A_k, \tag{3.77}$$

$$\Delta(t) = \Delta_0 + \frac{3}{2} \int_0^t \mathrm{d}t' e^{-3\nu_*(t-t')} \frac{\partial}{\partial t'} \sum_k |A_k(t')|^2, \tag{3.78}$$

where $\nu_* = \nu_i/\Omega_i = \rho_i/\lambda_{\mathrm{mfp}}$ and we remind the reader that $\Delta_0 < 0$. It is manifest in the form of equation (3.77) how the dispersion relation (3.70) (without the first term) is recovered. Note that there is no coupling between different wavenumbers modes in the sense that if a mode is not initially excited, it is never excited. The only effect that modes have on each other is via the sum over k in equation (3.78),

to which they all contribute.

Qualitative picture

Using only linear theory and the qualitative considerations of section 3.2.3, we can construct a fairly clear picture of the evolution of the firehose turbulence. Assuming a broad-band infinitesimal initial perturbation in k space, at first, $\Delta = \Delta_0$ and all modes with $k < k_0$ (see equation (3.71)) will go unstable, with the fastest-growing one given by $k_{\mathrm{p}} = k_0/\sqrt{2}$. Eventually the amplitude in this mode reaches the level at which the back-reaction becomes important: approximating equation (3.78) by

$$\Delta(t) \simeq \Delta_0 + \frac{1}{2\nu_*} \frac{\partial}{\partial t} \sum_k |A_k|^2, \tag{3.79}$$

we find that the nonlinear contribution is comparable to $|\Delta_0 + 2/\beta_i|$ when (cf. equation (3.26)):

$$\sum_k |A_k|^2 \simeq 2 \left| \Delta_0 + \frac{2}{\beta_i} \right| \frac{\nu_*}{\gamma_{\mathrm{max}}} = \frac{2\nu_i}{\Omega_i} = \frac{2\rho_i}{\lambda_{\mathrm{mfp}}}, \tag{3.80}$$

where γ_{max} is the imaginary part of ω_{p} given by equation (3.73). Equation (3.80) only gives a good estimate of the critical amplitude if $3\nu_*$ is larger or not too much smaller than γ_{max} (collisions are sufficiently strong). If $\nu_* \ll \gamma_{\mathrm{max}}$ (as a subsidiary limit within our ϵ ordering), then a better approximation than equation (3.79) is to replace the collisional relaxation exponent in equation (3.78) by unity, which gives

$$\sum_k |A_k|^2 \simeq \frac{2}{3} \left| \Delta_0 + \frac{2}{\beta_i} \right|. \tag{3.81}$$

Once the nonlinear feedback becomes active, exponential growth must cease and secular growth starts because the anisotropy must be kept close to marginal: using equation (3.79), we find, to dominant order,

$$\Delta \simeq -\frac{2}{\beta_i} \quad \Rightarrow \quad \sum_k |A_k|^2 \simeq 2 \left| \Delta_0 + \frac{2}{\beta_i} \right| \nu_* t. \tag{3.82}$$

This is valid regardless of which of the two estimates (3.80) or (3.81) of the amplitude at the onset of nonlinearity was appropriate. This is because the effective growth rate associated with the secular growth decreases with time and so we will always eventually end up in the regime where the collisional relaxation exponent in equation (3.78) is faster than the magnetic energy growth and equation (3.79) gives a good approximation of equation (3.78).

The evolution of the fluctuation spectrum must be consistent with equation (3.82). As the magnitude of the total pressure anisotropy Δ approaches the marginal value, both the cutoff wavenumber $k_0(t)$ and the most unstable wavenumber $k_{\mathrm{p}}(t)$ decrease, as they can still be estimated by equations (3.71) and (3.72) with $\Delta = \Delta(t)$. The modes whose growth has been thus switched off become oscillatory: from equation (3.77), it is obvious that for $k \gg k_0(t)$,

$$A_k = c_1 e^{ik^2 t/4} + c_2 e^{-ik^2 t/4}, \tag{3.83}$$

where c_1 and c_2 are integration constants and $c_1^* = c_2$ because $A_k^* = A_{-k}$ (note that this oscillation of the amplitude is superimposed on the oscillation with the same frequency that was factored out in equations (3.74)-(3.75)). Since these modes oscillate in time at a rate that is much larger than the rate of change of the anisotropy, they no longer contribute to the feedback term in equation (3.78).

Thus, as the range of growing modes, peaked at $k_{\mathrm{p}}(t)$ and cut off at $k_0(t)$, sweeps from large to small wavenumbers, they leave behind a spectrum of effectively passive oscillations, whose amplitude no longer changes. Since there is no fixed special scale in the problem (except initial most unstable wavenumber), one expects the evolution to be self-similar and the spectrum a power law. It is not hard to determine its exponent. Let $|A_k|^2 \sim k^{-\alpha}$. Since the total energy must grow linearly (equation (3.82)), we have

$$\sum_k |A_k|^2 \sim k_{\mathrm{p}}^{1-\alpha} \sim t \quad \Rightarrow \quad k_{\mathrm{p}} \sim t^{-1/(\alpha-1)} \tag{3.84}$$

This is valid if $\alpha > 1$; the extra power of k comes from the integration over wavenumbers. On the other hand, for the fastest-growing mode, we must have,
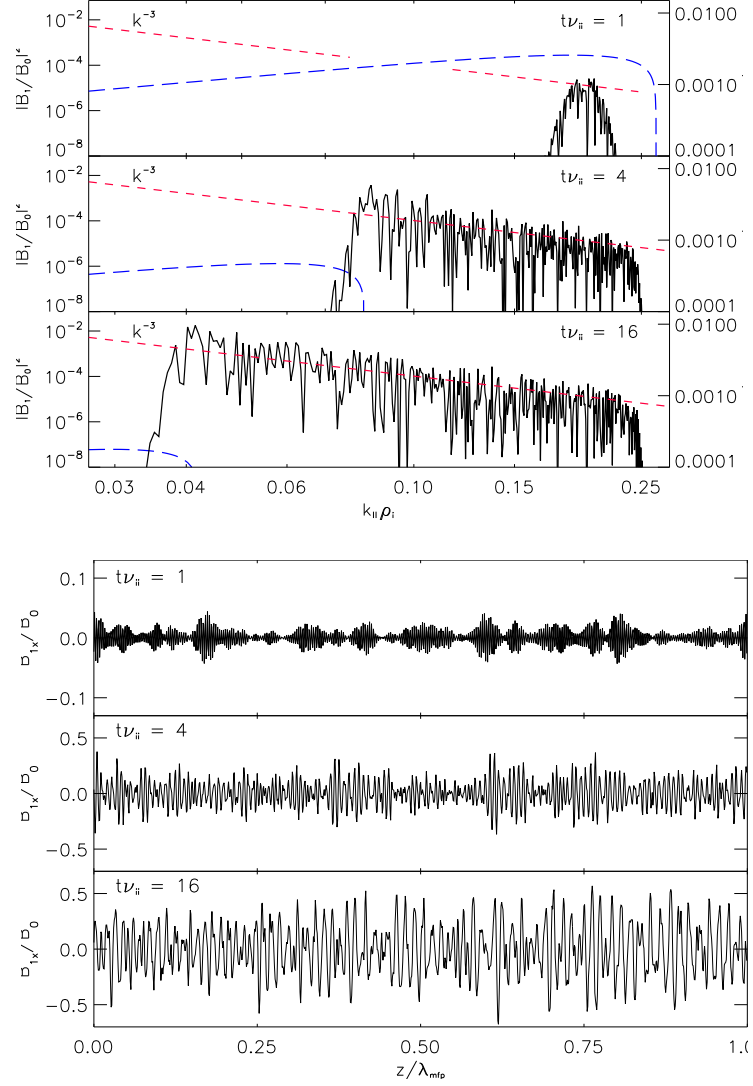
Figure 3.4: *Top panel:* spectrum of the magnetic fluctuation energy at three specific times ($t\nu_i = 1, 4, 16$) during the evolution shown in Figure 3.3; red short-dashed lines show the k^{-3} slope (equation (3.87)); blue long-dashed lines show the firehose growth rate (see equation (3.70)) for the instantaneous values of $\Delta + 2/\beta_i$ at the times the spectra are plotted. *Bottom panel:* magnetic fluctuations in real space (B_{1x}/B_0 vs. z) at the same times as the spectra in the left panel.

assuming secular growth,

$$\frac{1}{A_{k_\mathrm{p}}} \frac{\partial A_{k_\mathrm{p}}}{\partial t} \sim \frac{1}{t} \sim \gamma_\mathrm{max} \sim \left| \Delta + \frac{2}{\beta_i} \right|, \tag{3.85}$$

where the last relation follows from equation (3.73). This gives us a prediction for the time evolution of the residual pressure anisotropy and, via equation (3.72), of the most unstable wavenumber (the infrared cutoff of the spectrum):

$$\left| \Delta + \frac{2}{\beta_i} \right| \sim \frac{1}{t}, \quad k_\mathrm{p} \sim \frac{1}{\sqrt{t}}. \tag{3.86}$$

The only way to reconcile equations (3.84) and (3.86) is to set $\alpha = 3$. Thus, we expect the one-dimensional firehose turbulence spectrum to scale as

$$|A_k|^2 \sim k^{-3}. \tag{3.87}$$

The secular growth of the firehose fluctuations will continue until our asymptotic expansion becomes invalid, i.e., when the fluctuation amplitude is no longer small.[8] From equation (3.82), this happens at $t \sim (\nu_i |\Delta_0 + 2/\beta_i|)^{-1} \sim |\gamma_0|^{-1}$, where dimensions have been restored. This is the time scale of the large-scale dynamics. Thus, as we have already explained in section 3.2.3, there is no saturation of the firehose fluctuations on any faster time scale. Unsurprisingly, at the same time as the fluctuation amplitude becomes large enough to break our ordering, the scale of the fluctuations also breaks the ordering: substituting the above time scale into equation (3.86) gives $k_\parallel \rho_i \sim (|\gamma_0|/\Omega_i)^{1/2} \sim \epsilon^2$, or $k_\parallel \lambda_\mathrm{mfp} \sim 1$, while our original ordering assumption was $k_\parallel \rho_i \sim \epsilon$, or $k_\parallel \lambda_\mathrm{mfp} \sim 1/\epsilon$ (see equation (3.45)).

Numerical solution

The firehose turbulence equation (3.77) is one-dimensional, so it is very easy to solve numerically; equation (3.78) is most conveniently solved in a differential

---

[8] Note that while the amplitude grows and thus eventually breaks the ordering introduced in section 3.3.2, the stability parameter $|\Delta + 2/\beta_i|$ decreases, so the approximation of small Larmor radius gets quantitatively better with the growth of the firehose fluctuations moving to larger scales (equation (3.72)) — equivalently, our ordering of ρ_i introduced in section 3.3.2 (equation (3.47)) is quantitatively better satisfied.
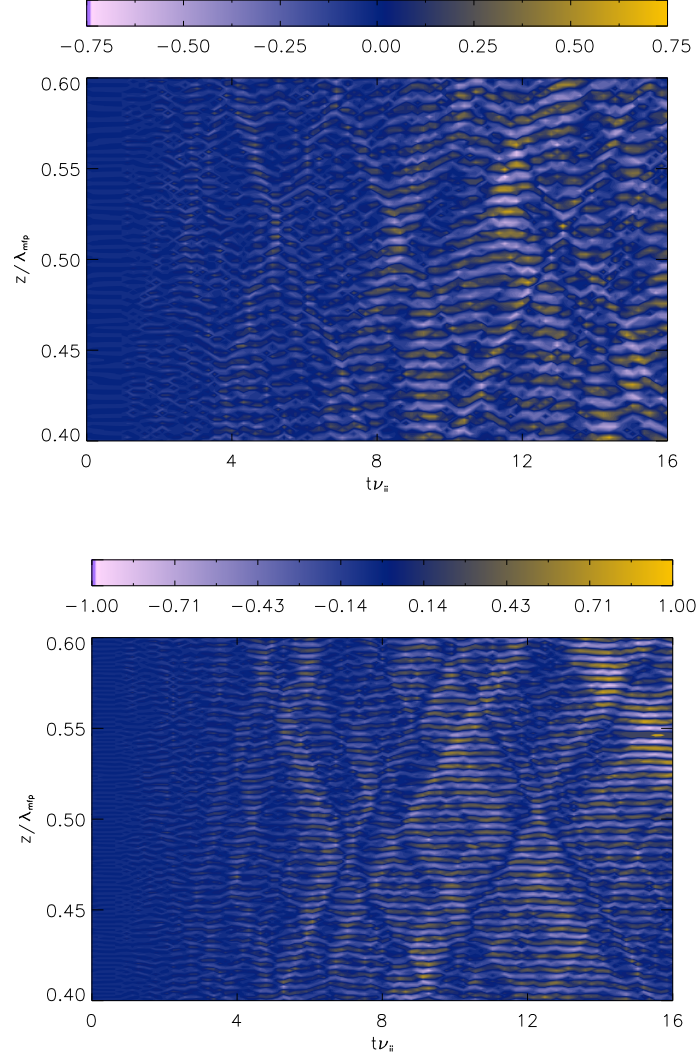
Figure 3.5: *Top panel:* contour plot of the time evolution of the firehose turbulence for the numerical solution discussed in section 3.4.3 — the vertical axis is space (the middle fifth of our entire periodic domain), horizontal axis is time, the colours respresent the value of B_{1x}/B_0. *Bottom panel:* the same plot for the gyrothermal turbulence discussed in section 3.5.3. Note that, as explained in the text, the firehose turbulence exhibits a gradual coarsening of the dominant structure with time, while the gyrothermal turbulence ends up dominated by a single scale.

form:

$$\frac{\partial}{\partial t}\left(\Delta - \frac{3}{2}\sum_k |A_k|^2\right) = -3\nu_*(\Delta - \Delta_0) \tag{3.88}$$

with the initial condition $\Delta(0) = \Delta_0$. Here we describe the results obtained from such a numerical calculation with the following parameters:

$$\Delta_0 = -0.02, \quad \frac{2}{\beta_i} = 0.01, \quad \nu_* = \frac{\rho_i}{\lambda_{\mathrm{mfp}}} = 0.0001. \tag{3.89}$$

This means that the maximum wavenumber at which firehose fluctuations can be excited is $k_0 \simeq 0.28$ (equation (3.71); see Figure 3.2). We solve equation (3.77) for 1024 wavenumbers in a periodic domain of size λ_{mfp}, so the smallest and the largest wavenumbers are (still normalised to ρ_i) $k_{\min} = 2\pi\rho_i/\lambda_{\mathrm{mfp}} \simeq 0.00063$ and $k_{\max} \simeq 0.32$. The initial conditions are random amplitudes in each wavenumber (satisfying the reality condition $A_{-k} = A_k^*$). Note that with the parameters (3.89), our ordering parameter is $\epsilon \sim 0.1$, so we have chosen a spatial scale separation between collisions and the Larmor motion that substantially exceeds $1/\epsilon^2$ formally mandated by our ordering (section 3.3.2). This does not break anything and is in fact more realistic for the physical parameters in weakly collisional plasmas of interest (section 3.2.1). It also widens the scale interval available to the firehose turbulence spectrum and ensures that even deep in the nonlinear regime, when the wavenumber of the firehose fluctuations drops substantially, there is still a healthy scale separation between them and the collisional dynamics.

The evolution of the total magnetic energy, $\overline{|\boldsymbol{B}_1^\perp|^2}/B_0^2 = \sum_k |A_k|^2$, is shown in Figure 3.3 (left panel). Initially it grows exponentially at the (normalised) rate $\gamma_{\max} = \mathrm{Im}\,\omega_{\mathrm{p}}$ (see equation (3.70); this part of the evolution is trivial and so not shown). The exponential growth is followed by a secular, linear in time, growth of the energy in accordance with equation (3.82). The energy at which this nonlinear regime starts is closer to the estimate given by equation (3.81) than by equation (3.80) because, as discussed above, we have taken a very small value of ν_*. Note that in this and all subsequent figures, we have normalised time using the collision frequency ν_i, not the cyclotron frequency Ω_i — this is indicated explicitly in the figures.

Figure 3.3 (bottom panel) shows the time evolution of the instability parameter $\Delta + 2/\beta_i$. As expected it is tending to the marginal stability value (zero). The inset shows that this approach to zero is consistent with the $1/t$ prediction (equation (3.86)).

The evolution of the spectrum of firehose fluctuations is illustrated by Figure 3.4 (top panel). As anticipated in section 3.4.3, the spectral peak moves to smaller wavenumbers in the nonlinear regime. The spectrum extending from this moving peak to the original wavenumber of the fastest linear growth ($k_\mathrm{p} = 0.2$; see equation (3.72)) is statistically stationary and consistent with the k^{-3} power law predicted by equation (3.87). The instantaneous firehose growth rate is overplotted on the spectra in Figure 3.4 (top panel) and confirms that the position of the spectral peak closely follows the wavenumber of the fastest instantaneous growth of the firehose instability.

Figure 3.4 (bottom panel) shows snapshots of one of the components (B_{1x}) of the perturbed magnetic field corresponding to the spectra in Figure 3.4 (top panel). The emergence of increasingly larger-scale fluctuations is manifest. Perhaps a better illustration of this real-space evolution of the firehose turbulence is Figure 3.5 (top panel), which is the space-time contour plot for the middle fifth of the domain.

3.4.4   Implications for momentum transport

Substituting the second-order pressure tensor calculated in section 3.3.5 into the large-scale momentum equation (3.62), we get

$$m_i n_{0i} \frac{\mathrm{d}\boldsymbol{u}_{0i}}{\mathrm{d}t} = -\boldsymbol{\nabla}\tilde{\Pi} + \boldsymbol{\nabla} \cdot \left[p_{0i}\boldsymbol{b}_0\boldsymbol{b}_0 \left(\Delta + \frac{2}{\beta_i} \right) \right], \qquad (3.90)$$

where, in the absence of density and temperature gradients, the total isotropic pressure $\tilde{\Pi} = p_{2i}^{\perp} + B_0^2/8\pi$ is set by the condition $\boldsymbol{\nabla} \cdot \boldsymbol{u}_{0i} = 0$,[9] while the pressure anisotropy Δ is given by equation (3.64). A remarkable feature of equation (3.90) is that all of the effects of the magnetic field appear in the term proportional

---

[9]More generally, $\tilde{\Pi}$ adjusts in such a way as to reconcile the pressure balance with the continuity and heat conduction equations; see Appendix C.0.17.

to $\Delta + 2/\beta_i$, which is precisely the instability parameter that the small-scale firehose turbulence described in section 3.4.3 contrives to make vanish. In the marginal state that results, the tension force (the $2/\beta_i$ term) is almost entirely cancelled by the combined pressure anisotropy due to large- and small-scale fields. This suggests that in regions of the plasma where the firehose is triggered (i.e., where the magnetic field is locally decreased by the plasma motion), the plasma motions become effectively hydrodynamic, with magnetic-field lines unable to resist bending by the flows.

Since the cancellation of the second term in equation (3.90) by the firehose turbulence also removes the (parallel) viscosity of the plasma, these hydrodynamic motions are not dissipated. In a turbulent situation, this should enable a cascade to ever smaller scales. Obviously, once this happens, the original motion that caused the negative pressure anisotropy to develop is supplanted by other, faster motions on smaller scales. The theory developed in this work eventually breaks down because the scale separation that formed the basis of our asymptotic expansion is compromised: while the fluid motions penetrate to smaller scales, the firehose fluctuations move to larger scales (see section 3.4.3).

Note also that the fluid motions produced by the turbulent cascade can give rise to both positive and negative pressure anisotropies — and to have a full description of their further evolution, we must know the effect on momentum transport not just of the firehose but also of the mirror and other instabilities triggered by positive pressure anisotropies (locally increasing magnetic field strength). This remains to be determined. Another important adjustment to the viscous-stress reduction argument above has to do with the modification of the firehose instability by the parallel ion heat fluxes — this we now proceed to investigate.

3.5   Gyrothermal turbulence

3.5.1   Firehose turbulence equation with heat fluxes

As we briefly mentioned in section 3.3.5, allowing a non-zero ion temperature gradient along the unperturbed magnetic field leads to substantial modifica-

tions. These are of two kinds. First, as shown in Appendix C.0.18, the pressure anisotropy Δ_0 caused by the large-scale dynamics contains contributions from the collisional parallel heat fluxes (proportional to $\boldsymbol{b}_0 \cdot \boldsymbol{\nabla} T_{0i}$) and from compressive motions (as we pointed out in footnote 5, the presence of a temperature gradient automatically implies a density gradient as well because of the requirement that pressure balance should be maintained; see equation (C.25) and Appendix C.0.17). Instead of equation (3.65), valid in the incompressible case, we must use the more general equation (C.57). This, however, does not change much: the unstable firehose fluctuations will grow in the manner described in section 3.4.3, first exponentially, then secularly, to compensate whatever pressure anisotropy is set up by the large-scale dynamics. The only change is the physical interpretation of the origin of the pressure anisotropy: as long as ion temperature gradients are present, the anisotropy is not tied exclusively to the change in the magnetic field. Physically, the heat-flux contributions to the anisotropy have to do with the fact that "parallel" and "perpendicular" heat flows along the magnetic-field lines somewhat differently and so imbalances between $p_\perp$ and $p_\parallel$ can occur — this can be seen already from the CGL equations (see Appendix C.0.19).

The second heat-flux-related modification of the theory developed thus far is more serious. It involves an additional contribution to the FLR term in the third-order pressure tensor (equation (3.66)) and, therefore, to the firehose turbulence equation (3.68). This contribution was derived in Appendix C.0.20, but suppressed in our previous discussion. It is given by equation (C.63) and consequently equation (3.68) now reads

$$\frac{\partial^2 \boldsymbol{B}_1^\perp}{\partial t^2} = \frac{v_{\text{th},i}^2}{2} \, \nabla_\parallel^2 \left[\left(\Delta + \frac{2}{\beta_i} \right) \boldsymbol{B}_1^\perp + \frac{1}{\Omega_i} \left(\frac{\partial \boldsymbol{B}_1^\perp}{\partial t} - \Gamma_T \frac{v_{\text{th},i} \nabla_\parallel \boldsymbol{B}_1^\perp}{B_0} \right) \times \boldsymbol{b}_0 \right] \; (3.91)$$

We have introduced a dimensionless parameter measuring the magnitude of the parallel heat flux:[10]

$$\Gamma_T = \frac{1}{2} \frac{v_{\text{th},i}}{\nu_i} \frac{\boldsymbol{b}_0 \cdot \boldsymbol{\nabla} T_{0i}}{T_{0i}} = \frac{1}{2} \frac{\lambda_{\text{mfp}}}{l_T}, \tag{3.92}$$

---

[10]We stress that we are discussing the effect of the *ion* heat flux as the electrons are assumed isothermal at the scales we are considering (see Appendix B). We also stress that these heat-flux effects enter through the FLR terms in the plasma pressure tensor and are absent in, e.g., the lowest-order Braginskii (1965) equations.

where l_T is the parallel length scale of the ion temperature variation. We see that the functional form of the firehose turbulence equation is changed. We now proceed to study the effect of this change.
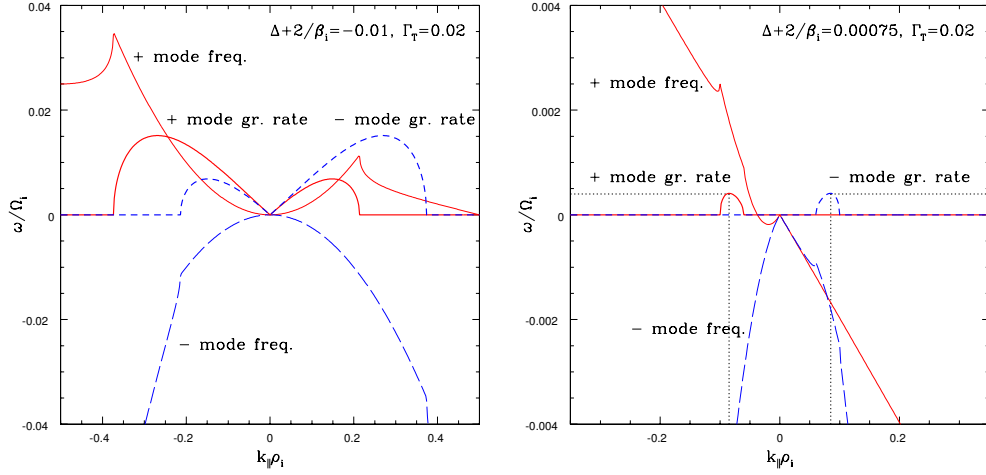
Figure 3.6: *Left panel:* frequencies (thin lines) and growth rates (bold lines) of the unstable firehose modes (red/solid: the "+" mode; blue/dashed: the "−" mode) given by equation (3.94); the parameters here are $\Delta + 2/\beta_i = -0.01$ and $\Gamma_T = 0.02$, so the instability parameter is $\Lambda = 0.0054$ (equation (3.95)). *Right panel:* same, but for $\Delta + 2/\beta_i = 0.00075$, so $\Lambda = 0.000025$ (close to marginal stability); dotted vertical lines indicate the wavenumber of fastest growth $k_p = 0.085$ (equation (3.100)) and the dotted horizontal lines the corresponding maximum growth rate $\gamma_{\max} = \operatorname{Im} \omega_p = 0.0004$ (equation (3.101)).

3.5.2   Linear theory: the gyrothermal instability

The linear dispersion relation for equation (3.91) is

$$\left[\omega^2 - \frac{k_\parallel^2 v_{\mathrm{th},i}^2}{2}\left(\Delta_0 + \frac{2}{\beta_i}\right)\right]^2 = \frac{k_\parallel^4 v_{\mathrm{th},i}^4}{4}\frac{\left(\omega + k_\parallel v_{\mathrm{th},i}\Gamma_T\right)^2}{\Omega_i^2}. \tag{3.93}$$

Like in the case of equation (3.69), there are four roots of which two are potentially unstable:

$$\frac{\omega}{\Omega_i} = \pm\frac{k^2}{4} + i\,\frac{|k|}{\sqrt{2}}\sqrt{-\left(\Delta + \frac{2}{\beta_i}\right)\mp k\Gamma_T - \frac{k^2}{8}}, \tag{3.94}$$

where $k = k_\parallel \rho_i$. Instability occurs at wavenumbers for which the expression under the square root is positive. There is an interval of such unstable wavenumbers if and only if

$$\Lambda \equiv \Gamma_T^2 - \frac{1}{2}\left(\Delta + \frac{2}{\beta_i}\right) > 0. \tag{3.95}$$

If this condition is satisfied, the "+" mode is unstable for

$$-4\left(\Gamma_T + \sqrt{\Lambda}\right) < k < -4\left(\Gamma_T - \sqrt{\Lambda}\right), \tag{3.96}$$

and the "−" mode for

$$4\left(\Gamma_T - \sqrt{\Lambda}\right) < k < 4\left(\Gamma_T + \sqrt{\Lambda}\right). \tag{3.97}$$

where we have assumed, without loss of generality, that $\Gamma_T > 0$. When $\Delta + 2/\beta_i < 0$, these two intervals intersect, so all modes with $|k| < k_0 = 4\left(\Gamma_T + \sqrt{\Lambda}\right)$ are unstable (others are pure propagating waves). When $\Delta + 2/\beta_i > 0$, the intervals are separated and there is an interval of stability at long wavelengths, viz., $|k| < 4\left(\Gamma_T - \sqrt{\Lambda}\right)$.

What is remarkable about all this is that not only the stability conditions and specific expressions for the firehose growth rate are modified by heat flux, but the presence of the heat flux allows for instability even when firehose is stable, $\Delta + 2/\beta_i > 0$ (but positive pressure anisotropy not too large and β_i not too small, subject to equation (3.95)). This *gyrothermal instability (GTI)*, leads to the growth of Alfvénically polarised fluctuations in the parameter regime in which they are otherwise stable (Schekochihin *et al.*, 2010).[11]

The formulae for the wavenumber of the fastest-growing mode and the maximum growth rate for the combined firehose-GTI are straightforward to write down. They are not particularly illuminating in the general case, but are interesting in various asymptotic limits. When the firehose instability parameter $\Delta + 2/\beta_i < 0$ and its magnitude is much larger than Γ_T^2, the effect of the heat flux is a small correction to the firehose instability already described in section 3.4.2. Conversely,

---

[11]Note that for $\Delta - 1/\beta_i > 0$, the mirror mode is unstable as well.

when $|\Delta + 2/\beta_i| \ll \Gamma_T^2$, the GTI is dominant and, for the fastest growing mode,

$$k_{\rm p} \simeq \mp 6\Gamma_T, \tag{3.98}$$

$$\omega_{\rm p} \simeq 9\Gamma_T^2 \left(\pm 1 + \frac{i}{\sqrt{3}} \right), \tag{3.99}$$

where $\omega_{\rm p}$ is normalised to Ω_i. Finally, close to the marginal state, $\Lambda \to +0$, we have

$$k_{\rm p} \simeq \mp 4\Gamma_T \left(1 + \frac{\Lambda}{\Gamma_T^2} \right), \tag{3.100}$$

$$\omega_{\rm p} \simeq 4\Gamma_T^2 \left(\pm 1 + \frac{i\sqrt{\Lambda}}{\Gamma_T} \right). \tag{3.101}$$

Note that, unlike the firehose, the GTI has a definite preferred wavenumber that does not change as marginal stability is approached.

Figure 3.6 (left panel) shows the dependence of the frequencies and growth rates of the two unstable modes on wavenumber for a set of parameters for which the instability is a hybrid of firehose and GTI (these are the parameters used in the numerical solution of section 3.5.3). Figure 3.6 (right panel) shows the same for the case in which the firehose is stable ($\Delta + 2/\beta_i > 0$) and that is very close to marginal stability: we see that the instability only exists in the immediate neighbourhood of the last unstable wavenumber given by equation (3.100).

3.5.3 Nonlinear evolution and spectrum

Firehose-GTI turbulence equation in scalar form

As happened in section 3.4.3, equation (3.91) can be reduced to one equation for a scalar field, although it is now a slightly more complicated transformation. Let us again non-dimensionalise time and space according to equation (3.76) and introduce new fields $A_k^\pm(t)$ (not to be confused with the vector potential) as follows:

$$\frac{B_{1x}}{B_0} \pm i \frac{B_{1y}}{B_0} = A_k^\pm \exp\left[\mp i \left(\frac{k^2}{4} t + \phi_k \right) \right]. \tag{3.102}$$
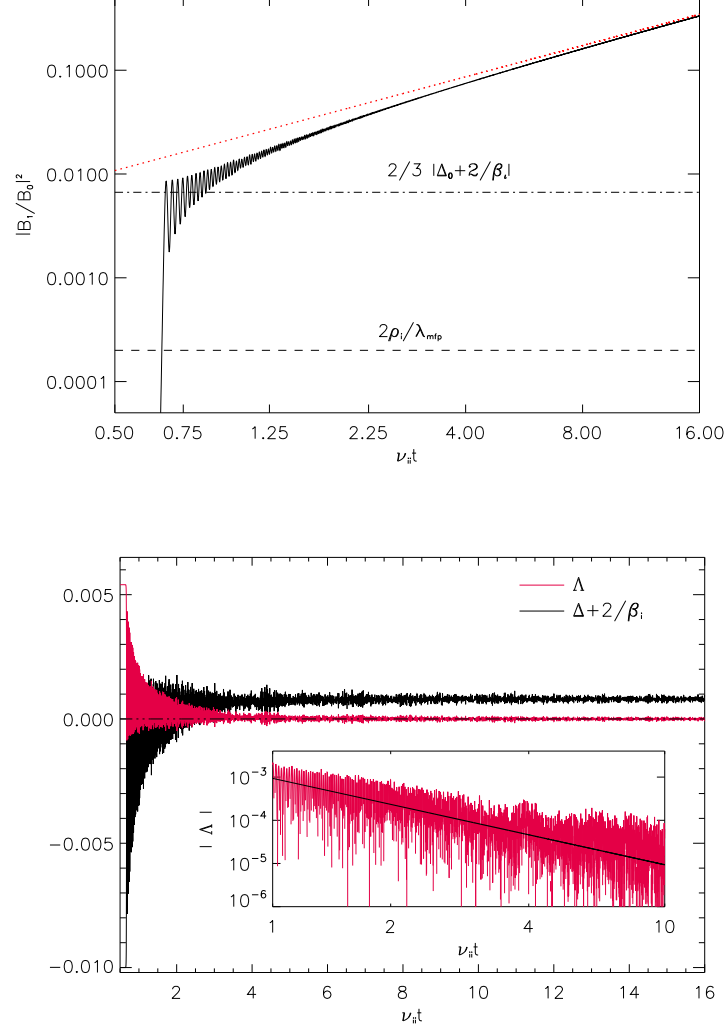
Figure 3.7: *Top panel:* evolution of the magnetic energy $\overline{|\boldsymbol{B}_1^\perp|^2}/B_0^2 = \sum_k |A_k|^2$ with time in a numerical solution of equations (3.103) and (3.104) with parameters (3.109); the red dotted line shows the nonlinear asymptotic given by equation (3.105); this figure is the GTI analog of Figure 3.3 (left panel). *Bottom panel:* evolution of the instability parameter Λ (pink) and the pressure anisotropy parameter $\Delta + 2/\beta_i$ (black) in the same numerical solution. *Inset:* log-log plot of the evolution of $|\Lambda|$; the black line shows the slope corresponding to $1/t^2$ (see equation (3.107)).

With the ansatz (3.102), equation (3.91) becomes

$$\frac{\partial^2 A_k^{\pm}}{\partial t^2} = \frac{k^2}{2}\left[-\left(\Delta + \frac{2}{\beta_i}\right) \mp k\Gamma_T - \frac{k^2}{8}\right]A_k^{\pm}, \tag{3.103}$$

$$\Delta(t) = \Delta_0 + \frac{3}{2}\int_0^t dt' e^{-3\nu_*(t-t')}\frac{\partial}{\partial t'}\sum_k \frac{|A_k^+(t')|^2 + |A_k^-(t')|^2}{2}. \tag{3.104}$$

It is now manifest how the dispersion relation (3.94) emerges from equation (3.103). Unlike in the case of pure firehose turbulence ($\Gamma_T = 0$), the evolution of the mode now depends on the sign of its real frequency — that is why we have two scalar equations. However, these equations have a symmetry: if we arrange initially that $A_k^+ = A_{-k}^-$ (which we can always do by an appropriate choice of the phases ϕ_k), then this relation will continue to be satisfied at later times. This also means that $A_k^{\pm}$ are real because, in order for $\boldsymbol{B}_1^{\perp}$ to be a real field, we must have (from equation (3.102)) $(A_k^+)^* = A_{-k}^-$ (we assume the phases satisfy $\phi_k = \phi_{-k}$). The conclusion is that it is enough to solve just one of the two equations (3.103) — either for the + or the − mode. The total energies of the two modes that enter equation (3.104) are equal.[12]

Qualitative picture

The evolution of the firehose-GTI turbulence is easy to predict arguing along the same lines as we did in section 3.4.3. Let us consider the case when initially the pressure anisotropy is negative and $-(\Delta_0 + 2/\beta_i) \gg 2\Gamma_T^2$, i.e., the instability parameter $\Lambda_0 > 0$ (given by equation (3.95) with $\Delta = \Delta_0$). In this regime, the heat flux does not matter and the evolution proceeds as in the case of the firehose turbulence: magnetic fluctuations grow and eventually the nonlinear feedback in equation (3.104) starts giving an appreciable positive contribution to the pressure anisotropy (estimates (3.80) and (3.81) for the fluctuation amplitude at which this happens are still valid). A k^{-3} spectrum will then form, with the infrared cutoff (wavenumber of maximum growth) moving to larger scales and $|\Delta + 2/\beta_i|$

---

[12]The same approach could have been taken in section 3.4.3: instead of solving equation (3.103) for a complex function A_k subject to $A_k^* = A_{-k}$, we could have solved for one of two real functions $A_k^{\pm}$ subject to $A_k^+ = A_{-k}^-$. The magnetic field is then recovered via equation (3.102).
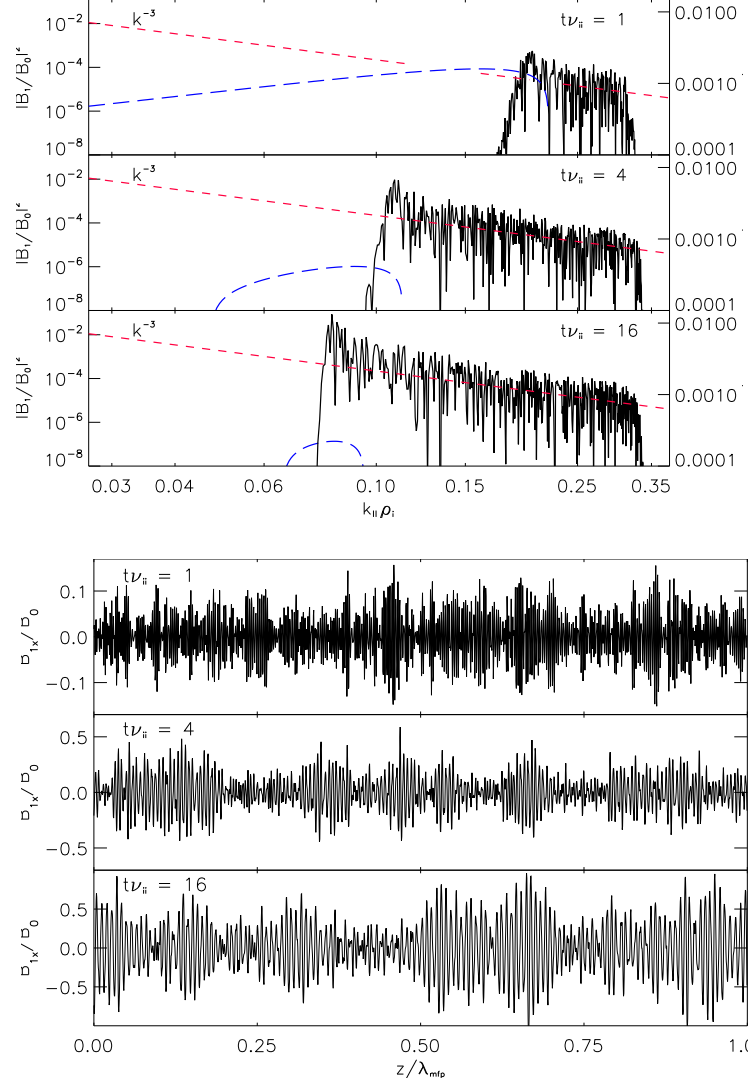
Figure 3.8: *Top panel:* spectrum of the magnetic fluctuation energy at three specific times ($t\nu_i = 1, 4, 16$) during the evolution shown in Figure 3.7; red short-dashed lines show the k^{-3} slope; blue long-dashed lines show the firehose/GTI growth rate (see section 3.5.2) for the instantaneous values of $\Delta + 2/\beta_i$ at the times the spectra are plotted. *Bottom panel:* magnetic fluctuations in real space (B_{1x}/B_0 vs. z) at the same times as the spectra in the left panel. This figure is the GTI analog of Figure 3.4.

decreasing (i.e., $\Delta + 2/\beta_i$ increasing and thus becoming less negative).

The evolution of the gyrothermal fluctuations starts to differ from the pure fire-hose case after $|\Delta + 2/\beta_i|$ becomes comparable to Γ_T^2. The GTI is now the dominant instability mechanism. Since the fluctuations continue growing, $\Delta + 2/\beta_i$ continues to increase and will become positive, tending eventually to $2\Gamma_T^2$, so as to push the instability parameter Λ (equation (3.95)) to zero and the GTI to its marginal state. As $\Lambda \to +0$, the growth is concentrated in a shrinking neighbourhood of the wavenumber $k_{\mathrm{p}} = 4\Gamma_T$ (see equation (3.100)). This means that the spectrum stops spreading towards lower wavenumbers and its infrared cutoff stabilises at k_{p}. All the growth of magnetic energy is now provided by the growth of the one mode associated with k_{p}, which will soon tower over the rest of the spectrum.

The growth is still secular: using equation (3.104) and the marginality condition $\Lambda = 0$, we find to dominant order, analogously to equation (3.82),

$$\Delta \simeq 2\Gamma_T^2 - \frac{2}{\beta_i} \quad \Rightarrow \quad \sum_k |A_k|^2 \simeq 4\Lambda_0 \nu_* t. \tag{3.105}$$

Finally, we can calculate the evolution of the residual Λ. Analogously to equation (3.85), the growing mode satisfies

$$\frac{1}{A_{k_{\mathrm{p}}}} \frac{\partial A_{k_{\mathrm{p}}}}{\partial t} \sim \frac{1}{t} \sim \gamma_{\max} \sim 4\Gamma_T \sqrt{\Lambda}, \tag{3.106}$$

where we used equation (3.101) for $\gamma_{\max}$. Therefore,

$$\Lambda \sim \frac{1}{t^2}. \tag{3.107}$$

As in the case of the firehose turbulence, the secular growth will continue until the fluctuation amplitude is no longer small: $t \sim (\nu_i \Lambda_0)^{-1} \sim |\gamma_0|^{-1}$ (time scale of the large-scale dynamics). The key difference from the pure firehose case is that the fluctuations are now stuck at a microscopic spatial scale given by equation (3.100): restoring dimensions and using equation (3.92), the corresponding wavenumber

is

$$k_\parallel \rho_i \sim \frac{\lambda_{\mathrm{mfp}}}{l_T} \tag{3.108}$$

(this scale is collisionless, $k_\parallel \lambda_{\mathrm{mfp}} \gg 1$, provided $l_T \ll \lambda_{\mathrm{mfp}}^2/\rho_i$; for galaxy clusters, this is always true as is easy to ascertain by using the numbers from section 3.2.1). Thus, the gyrothermal turbulence is essentially *one-scale*, in the sense that fluctuations at this one scale become energetically dominant as marginal stability is approached at late stages of the nonlinear evolution.

Numerical solution

We have solved equations (3.103) and (3.104) in a manner completely analogous to that described in section 3.4.3. The parameters we used are

$$\Delta_0 = -0.02, \quad \frac{2}{\beta_i} = 0.01, \quad \Gamma_T = 0.02, \quad \nu_* = \frac{\rho_i}{\lambda_{\mathrm{mfp}}} = 0.0001.$$

This implies that the instability parameter in the linear regime is $\Lambda = 0.0054$ (equation (3.95)) and so the maximum unstable wavenumber is $k_0 = 4(\Gamma_T + \sqrt{\Lambda}) \simeq 0.37$ (equations (3.96) and (3.97); see Figure 3.6 (left panel)). Our numerical solution now has 2048 wavenumbers, so $k_{\mathrm{min}} \simeq 0.00063$ and $k_{\mathrm{max}} \simeq 0.64$.

As expected, the evolution of the total magnetic energy is similar to the case of pure firehose turbulence discussed in section 3.4.3: exponential, then secular growth (see equation (3.105)) — this is shown in Figure 3.7 (left panel). The evolution of the instability parameter Λ (equation (3.95)) towards its zero marginal value is given in Figure 3.7 (right panel). The inset shows that this approach to zero is consistent with the $1/t^2$ prediction (equation (3.107)). Also shown in Figure 3.7 (right panel) is the evolution of the pressure anisotropy parameter $\Delta + 2/\beta_i$, which for the pure firehose used to be the instability parameter. Since $\Lambda \to 0$, it should tend to $2\Gamma_T^2 = 0.0008$ and it indeed does.

Finally, Figure 3.8 (left panel) illustrates the evolution of the spectrum of firehose/gyrothermal fluctuations. It follows the scenario outlined in section 3.5.3. At first it is similar to the firehose turbulence spectrum with the spectral peak moving towards larger scales leaving behind a k^{-3} spectrum. As the wavenum-

ber of fastest growth k_{p} approaches the value corresponding to the near-marginal GTI, $k_{\mathrm{p}} = 4\Gamma_T = 0.08$ (see equation (3.100)), the peak stays there and continues growing, eventually dominating all other modes. The emergence of a one-scale sea of gyrothermal fluctuations is further illustrated by Figure 3.5 (right panel), which shows what these fluctuations look like in real space as time progresses. The difference between them and the pure firehose fluctuations in Figure 3.5 (left panel) is manifest: the gyrothermal ones stay at the same scale while the firehose ones become larger-scale as time progresses.

3.5.4   Implications for momentum and heat transport

Let us now revisit the discussion of the effect of plasma instabilities on the momentum transport modification attempted for the pure firehose in section 3.4.4. As before, the combined large-scale viscous and Maxwell stress is contained in the second term on the right-hand side of equation (3.90). However, with parallel ion heat fluxes present, the nonlinear evolution of the GTI pushes the quantity $\Delta + 2/\beta_i$ not to zero but to a positive value $2\Gamma_T^2$, corresponding to the marginal state $\Lambda = 0$ (equation (3.105)). Since any smaller value of $\Delta + 2/\beta_i$ is GTI unstable, this leads to a curious conclusion that the momentum transport is now effectively determined by the ion heat flux:

$$m_i n_{0i} \frac{\mathrm{d}\boldsymbol{u}_{0i}}{\mathrm{d}t} = -\boldsymbol{\nabla}\tilde{\Pi} + \boldsymbol{\nabla}\cdot\left(p_{0i}\boldsymbol{b}_0\boldsymbol{b}_0 2\Gamma_T^2\right) = -\boldsymbol{\nabla}\tilde{\Pi} + \boldsymbol{\nabla}\cdot\left[\boldsymbol{b}_0\boldsymbol{b}_0\frac{n_{0i}\left(\boldsymbol{b}_0\cdot\boldsymbol{\nabla}T_{0i}\right)^2}{m_i\nu_i^2}\right],$$

where we used equation (3.92) for Γ_T. This equation has to be supplemented with the transport and pressure-balance equations for n_{0i}, T_{0i} and $\tilde{\Pi}$ as explained in Appendix C.0.17.

Equation (3.109) probably merits a careful study (which is a subject for future work), but we would like to accompany it with a very important caveat. Since pressure anisotropy in the nonlinear state of the GTI can be positive, other plasma instabilities may be triggered. Thus, if $\Delta > 1/\beta_i$, i.e., if $\Gamma_T^2 > 3/(2\beta_i)$, the plasma will be mirror unstable. The magnetic fluctuations that the mirror instability produces are different from the GTI both in polarization ($\delta B_\parallel$, not $\delta B_\perp$) and scale ($k_\perp \gg k_\parallel$, $k_\perp \rho_i \sim (\Delta - 1/\beta_i)^{1/2}$, $k_\parallel \rho_i \sim \Delta - 1/\beta_i$ for the mirror,

whereas for the GTI we had $k_\perp = 0$, $k_\parallel \rho_i \simeq 4\Gamma_T$). How they saturate and what they do to the effective pressure anisotropy is a matter under active current investigation (e.g. Rincon *et al.*, 2010) — and it is completely unknown how mirror and gyrothermal fluctuations might coexist.

The key question is whether the pressure anisotropy will be set by the GTI or the mirror marginal condition. If it is set by the latter ($\Delta = 1/\beta_i$, as, e.g., seems to be indicated by the solar wind data; see Bale *et al.* 2009), then one may ask whether a turbulent plasma has a way of suppressing the GTI by adjusting not the pressure anisotropy but the heat flux to the marginal condition: $\Gamma_T^2 = 3/(2\beta_i)$. This raises the possibility that not only the pressure anisotropy but also the (ion) heat fluxes are determined by the marginal stability conditions of the firehose/GTI and mirror. Thus, plasma instabilities may be the crucial factor in setting both the momentum and heat transport properties of a weakly collisional plasma. We stress, however, that under the assumptions adopted in this work, we have not produced a nonlinear mechanism for changing the ion heat flux and this remains a subject for future work.

3.6   Comparison with previous work and a collisionless plasma

The theory developed above is basically quasilinear in that the fluctuation amplitude is assumed small and it is found that such small fluctuations can drive the instability to a marginal state. There have been a number of previous quasilinear treatments of the firehose instability (Shapiro & Schevchenko, 1964; Kennel & Sagdeev, 1967; Davidson & Völk, 1968; Gary & Feldman, 1978; Quest & Shapiro, 1996), so it is perhaps useful to explain why they do not obtain similar results.

The approach in such theories is to consider a *collisionless* plasma with some initial distribution that has a negative pressure anisotropy (let us call it $\Delta_0 < 0$) and work out how it relaxes. The result is that a fluctuation level builds up,

with[13]

$$\frac{|\boldsymbol{B}_1^\perp|^2}{B_0^2} \sim \left| \Delta_0 + \frac{2}{\beta_i} \right|, \tag{3.109}$$

which is small when the instability parameter $\Delta_0 + 2/\beta_i$ is small. This saturated fluctuation level suffices to marginalize the instability. This result is easily recovered in our theory if we formally set $\nu_i = 0$ in equation (3.64). This gives

$$\Delta(t) = \Delta_0 + \frac{3}{2} \frac{\overline{|\boldsymbol{B}_1^\perp(t)|^2}}{B_0^2} \tag{3.110}$$

and assuming saturation in the marginal state $\Delta = -2/\beta_i$, we recover equation (3.109).

The difference in our approach is to include weak collisions and consider the case when the pressure anisotropy is constantly *driven* by the large-scale dynamics (which is physically how it appears). The steady level of the anisotropy is then set by the competition between collisions and the drive (equation (3.65)) and to offset this anisotropy and keep the instability marginal, the fluctuation level has to keep growing secularly (the earlier quasilinear theories can then be interpreted to describe correctly what happens before one collision time has elapsed).

It is interesting to inquire what would happen if the anisotropy were driven (rather than just initially imposed) but collisions were not strong enough to balance the drive and impose a steady anisotropy. Formally speaking, our theory breaks down in this case because the equilibrium distribution cannot be proved Maxwellian. However, that is a technical issue and one could, in fact, reformulate our theory as a near-marginal expansion in the instability parameter $|\Delta + 2/\beta_i|$. We expect that equation (C.52) (or, equivalently, equation (C.59)), with the collisional relaxation term removed, would still describe the evolution of the anisotropy:

$$\frac{\partial \Delta}{\partial t} = 3\gamma_0 + \frac{3}{2} \frac{\partial}{\partial t} \frac{\overline{|\boldsymbol{B}_1^\perp(t)|^2}}{B_0^2}, \tag{3.111}$$

---

[13]Hall (1981) argues qualitatively for a similar saturation level, but due to trapping of particles in firehose fluctuations. As the systematic kinetic calculation presented above shows, the trapping effect does not play a role at these amplitudes, at least not under the assumptions we adopted ($k_\perp = 0$ and relatively high collision frequency).

where γ_0 (assumed negative) is the drive — it contains all the terms in equation (C.52) due the large-scale dynamics. Under these conditions, the driven part of anisotropy is constantly increasing and so again the fluctuations will have to grow secularly in order to keep it at the marginal level:

$$\frac{3}{2}\frac{\overline{|\boldsymbol{B}_1^{\perp}(t)|^2}}{B_0^2} = \left|3\int_0^t \mathrm{d}t'\gamma_0(t') + \frac{2}{\beta_i}\right|. \tag{3.112}$$

This will, of course, break down once the fluctuation level is no longer small or collisions catch up.

There exist a number of numerical studies of the nonlinear evolution of the firehose instability (Quest & Shapiro, 1996; Gary *et al.*, 1998; Hellinger & Matsumoto, 2001; Horton *et al.*, 2004*a,b*; Matteini *et al.*, 2006). They mostly adopted the same relaxation-of-initial-anisotropy approach as the quasilinear theories discussed above and the results they report are broadly consistent in that the magnetic fluctuation energy saturates at a level scaling with the size of the initial anisotropy (see equation (3.109)). A notable exception is the recent work of Matteini *et al.* (2006) who consider the anisotropy driven by the expansion of the solar wind — the fluctuation levels they see are probably well described by equation (3.112).

The spectrum of the firehose fluctuations has not previously been addressed analytically. However, the results of section 3.4.3 are not in disagreement with some of the numerical evidence which does point to the growing predominance of smaller wavenumbers in the nonlinear regime (Quest & Shapiro, 1996; Matteini *et al.*, 2006).

Finally, to our knowledge, the effect of heat fluxes on the nonlinear behaviour of the firehose instability, studied in section 3.5, has not been specifically considered before. Note that although the heat fluxes are present in the numerical simulations of Sharma *et al.* (2006, 2007), their momentum equation does not have the gyroviscous and gyrothermal terms that regularise the firehose at small scales and give rise to the gyrothermal instability. The appropriate modification to the fluid equations suggested by Schekochihin *et al.* (2010) should in principle enable one to study the spectrum of the firehose and GTI fluctuations numeri-

cally (although, it is not clear whether it will provide the necessary regularisation for the mirror that one would also expect).

3.7 Astrophysical implications

3.7.1 Solar wind

Much of the observational evidence about the firehose instability comes from the measurements of pressure anisotropies and fluctuation levels in the solar wind. Since the wind is expanding, both the local density and the local magnetic-field strength are dropping, so one expects a negative pressure anisotropy to develop. This can be described by equation (3.111), where the drive is roughly $\gamma_0 \sim -V_{sw}/R$ (solar wind speed divided by the distance from the Sun) and the collisional relaxation is neglected. The evidence for this trend, negative pressure anisotropy developing with increasing distance from the Sun, is given by Matteini *et al.* (2007); a number of other papers also document the fact that the measured pressure anisotropies are bounded from below by the firehose marginal stability condition (Kasper *et al.*, 2002; Bale *et al.*, 2009).

Bale *et al.* (2009) found increased levels of ion-Larmor-scale magnetic fluctuations close to this stability boundary — presumably due to the firehose instability. There are also indications of an injection of energy into parallel wavenumbers just above the ion Larmor scale (Wicks *et al.*, 2010) — again, conceivably by the firehose instability. It is unclear how these firehose fluctuations coexist with the solar wind inertial- and dissipation-range turbulence. This is one of the contexts in which the absence of a complete microphysical theory of the firehose turbulence and its effect on the plasma motions is particularly acutely felt.

3.7.2 Galaxy clusters

In section 3.2, we discussed at length the basic properties of the galaxy cluster plasmas, the inevitability of pressure anisotropies and, therefore, plasma instabilities arising in a turbulent ICM, as well as the fundamental theoretical questions that this poses. We cannot answer these questions here as we have analysed only

one of several plasma instabilities that must be understood. However, just like in the case of the solar wind and the accretion flows, an impatient astrophysicist can conceivably glimpse the contours of the eventual theory by constraining pressure anisotropies and possibly also heat fluxes by the marginal stability conditions of the plasma instabilities — with all the same caveats and acknowledgments of uncertainty as discussed above.

Let us discuss how far this approach can take us in answering some of the problems posed in sections 1.1 and 3.2.1.

Regulation of cooling flows

The apparent refusal of the galaxy cluster cores to exhibit a cooling catastrophe (e.g., Peterson & Fabian, 2006) has long evaded a satisfactory theoretical explanation. A comprehensive review of the relevant literature is outside the scope of this brief discussion. It is probably fair to summarise the two main physical mechanisms invoked to explain the relatively weak drop in the ICM temperature between the bulk and the core as thermal conduction and some form of viscous conversion into heat of the mechanical energy injected into the ICM by the central active galactic nuclei (probably in a self-regulating way). It is clear that the latter mechanism cannot be ignored because the thermal conductivity of the ICM is unlikely to be sufficiently large (e.g., Voigt & Fabian, 2004) and at any rate, thermal conduction is a thermally unstable mechanism of balancing radiative cooling. Kunz *et al.* (2010) recently proposed that if a sufficient amount of turbulent power is assumed to be available, the viscous heating, regulated by the pressure anisotropy and, therefore, by the marginal stability of the mirror and/or firehose instabilities, can balance the cooling in a thermally stable way. They also found that assuming such a balance leads to reasonable predictions of the magnetic field strength, magnitude of the turbulent velocities and the outer scale of the turbulence in the ICM (interestingly, both for the cool-core and non-cool-core clusters).

Temperature fluctuations and the GTI

While detailed simulations of the turbulent ICM, bubble dynamics etc. similar to those of Sharma *et al.* (2006, 2007) for accretion flows have not been attempted, the marginal stability condition for the GTI (equation (3.95)) could perhaps be used to impose a lower bound on the typical scale of temperature fluctuations in the ICM (Schekochihin *et al.*, 2010). Indeed, *if* the magnitude of the ion heat flux is limited so as to prevent the GTI from being unstable (see section 3.5.4), then from equations (3.95) and (3.92), we get

$$l_T \gtrsim \beta_i^{1/2} \lambda_{\mathrm{mfp}} \sim 5 \times 10^{-4} \frac{T_i^{5/2}}{n_i^{1/2} B} \sim 1.4 \times 10^{21} \text{ cm}, \qquad (3.113)$$

where n_i is in cm^{-3}, T_i is in K, B is in G, and the numerical value has been computed for the plasma parameters in the core of Hydra A discussed in section 3.2.1 (see equations (3.6) and (3.8)). Interestingly, kpc-scale temperature fluctuations are indeed observed in cool-core clusters (e.g. Fabian *et al.*, 2006; Lagana *et al.*, 2009). Furthermore, if we use in equation (3.113) the physical parameters appropriate for the bulk of the cluster plasma, rather than the cores (say, $T_i \sim 10^8$ K and $n_i \sim 10^{-3}$ cm^{-3}) we would get much larger scales — in the 100 kpc range, which is also consistent with reported observational values for the cluster bulk (Markevitch *et al.*, 2003).

3.8   Conclusion

Let us recapitulate what we have discovered and how it relates to what was known previously. It has been appreciated for some time that macroscale turbulence of magnetized weakly collisional plasma (exemplified by the ICM) will naturally produce pressure anisotropies, which will in turn trigger firehose and mirror instabilities at spatial and temporal microscales (Schekochihin *et al.*, 2005, see sections 3.1 and 3.2). Since the pressure anisotropies are essentially due to local temporal change of the magnetic field strength, it is qualitatively intuitive that the nonlinear evolution of the instabilities is governed by the tendency to cancel this change on average; hence it follows that in a driven system (see dis-

cussion in section 3.6) the fluctuations must continue growing in the nonlinear regime, albeit secularly rather than exponentially (see Schekochihin *et al.*, 2008).

In this thesis, we have constructed a full *ab initio* (weakly) nonlinear kinetic theory of this process for the parallel ($k_\perp = 0$) firehose instability, which is the simplest analytically tractable case. Not only the evolution of the fluctuation energy but also of the full spectrum of the resulting firehose turbulence has been worked out, including the effect of gradual spreading of the fluctuations to ever larger scales as the nonlinearly compensated pressure anisotropy approaches its marginal-stability value (section 3.4.3). We have also extended our kinetic calculation to include the effect of ion temperature gradients parallel to the magnetic field (parallel heat fluxes). As was pointed out recently, they lead to a new instability, the GTI, of parallel Alfvénic fluctutions (Schekochihin *et al.*, 2010, see section 3.5.2). Here we have constructed a nonlinear theory of its evolution, featuring again a secular growth of magnetic fluctuations, but this time developing a spectrum heavily dominated by a particular scale (section 3.5.3).

While a speculative discussion of the implications of these results for transport in a general magnetized plasma (sections 3.4.4–3.5.4) and for particular astrophysical systems (section 3.7) is possible, a full transport theory has to await, at the very least, the completion of similar *ab initio* kinetic investigations of the nonlinear evolution of the mirror instability and of the oblique ($k_\perp \neq 0$) firehose. Only then can one attempt to devise an effective mean field theory for the macroscale dynamics of cosmic plasmas based on solid microphysical foundations. One goal of this research has been to set forth a template for building these microphysical foundations.

In the meanwhile, it appears sensible to rely on (or at least consider reasonable) the semiquantitative closure approach to the macroscale dynamics based on the assumption that average pressure anisotropies and, probably, also heat fluxes, are set by the marginal stability conditions of the microscale plasma instabilities. This approach has found strong observational support in the solar wind measurements (e.g. Bale *et al.*, 2009) and has already yielded nontrivial and possibly sensible physical predictions for the evolution of cosmic magnetism (Schekochihin & Cowley, 2006), accretion disk dynamics (Sharma *et al.*, 2006, 2007), and the

turbulence and heating in the intracluster medium (Kunz *et al.*, 2010).

Part IV

Conclusion

Chapter 4

Conclusions

4.1 Outlook

Before we summarise what we have found let us speculate on an example where both the types of magnetized processes considered in this thesis might come together.

Consider a laminar, isothermal, magnetized, differentially rotating disc with a decreasing angular velocity profile, perhaps the early ISM or the hot accretion flows of Quataert *et al.* (2002); Sharma *et al.* (2003). We saw in chapter 2 that in the collisional regime, even if the disc is initially laminar, it cannot remain so for long if the ambient magnetic field has a vertical component.

The magnetized MRI destabilises the flow leading, in the linear regime, to magnetic field amplification at a rate proportional to the disc's shear (and in excess of its unmagnetized counterpart). As the field increases in strength the Larmor radius decreases (so the plasma becomes more magnetized) and purely growing modes mutate into over-stabilities (provided the background field has an azimuthal component). Both of these factors will presumably affect the turbulence that eventually arises. However, even before fully developed turbulence has arisen, the growing magnetic field will generate pressure anisotropies. These will in turn generate micro-instabilities with growth rates that are, if properly treated, in general well in excess of the MRI. These must be accounted for.

The numerical models of Sharma *et al.* (2006, 2007) employ an *ad hoc* closure,

constraining the pressure anisotropy to lie within the marginal stability boundaries. They argue that this is justified if it can be shown microphysically that plasma instabilities (in their case, ion cyclotron and firehose) produce fluctuations at the ion Larmor scale, where pitch-angle scattering of particles off the fluctuation "foam" isotropizes pressure. (The same view was taken by Schekochihin & Cowley (2006) in their model of the dynamo action in a weakly collisional plasma.)

This is not the only possibility and our results for the parallel ($k_\perp = 0$) firehose do not support this picture as the fluctuations are not quite at the Larmor scale even in the linear regime and move to larger scales in the nonlinear stage. It is possible that the oblique firehose (which is much harder to treat analytically than the parallel one considered here) might produce fluctuations at the ion Larmor scale. However, it is not obvious that the validity of a closure based on the *average* pressure anisotropy being maintained at the marginal level must be predicated on the possibility of pitch-angle scattering. As we have shown above, a sea of secularly growing magnetic fluctuations far above the Larmor scale can produce the same effect.

What we do not know is the fate of these firehose fluctuations over long (transport) time scales and the eventual structure of the tangled magnetic field that results — a crucial question for accretion theories because they require knowledge of the Maxwell and Braginskii stresses in order to estimate the rate of the angular momentum transport (Shakura & Sunyaev, 1973). However, let us assume that somehow the firehose (and other microscale instabilities such as the mirror) pin the pressure anisotropy at the marginal value for the microscale instabilities. In this case the viscous stress generated by the Braginskii viscosity will proceed to heat the plasma at a rate $\propto \Delta^2$ (Kunz *et al.*, 2010).

Spatial inhomogeneities in the growth rate of the magnetic field, as one would expect in a turbulent system, will lead to inhomogeneities in the local pressure anisotropy, both in magnitude and sign. In regions of decreasing field strength the firehose will pin the anisotropy at $|\Delta| = 2/\beta$ and in regions of increasing field strength the mirror will pin it at $|\Delta| = 1/\beta$. The implication of this is that heating in regions of increasing and decreasing magnetic field strength could differ

by a factor of $\sim$ four. If differential heating of this nature does occur then one would expect temperature gradients and therefore, possibly, the GTI to develop.

It is difficult to even conjecture what happen next without numerical evidence, but a number of possibilities present themselves. The GTI could regulate the pressure anisotropy in a way that encouraged more evenly distributed heating, thereby keeping the disc isothermal. It could facilitate the transport of heat directly, thereby eradicating temperature gradients. Alternatively, as suggested by Schekochihin *et al.* (2010), it could distort the magnetic field $\delta \boldsymbol{b} \sim 1$ to minimise the parallel ion temperature gradient thereby switching itself off. In magnetized plasmas on fluid scales, such behaviour has been found for the fluid instability, the HBI (Bogdanović *et al.*, 2009; Parrish & Quataert, 2008).

What all this means for the magnetic field structure is entirely unclear too. How a turbulent dynamo might operate in such a plasma remains a completely open problem. Schekochihin & Cowley (2006) have made a speculative attempt to leapfrog the detailed microphysical derivations and model the large-scale dynamics based on the idea that microscale instabilities would always isotropize pressure towards marginal stability values. This led to a rather dramatic conclusion that the ICM might support self-accelerating, explosive dynamos. While this conclusion remains to be tested by more rigorous analytical approaches, it does illustrate the general conjecture that plasma instabilities are likely to result in radical changes to, rather than merely small corrections to, the large-scale dynamics of cosmic plasmas.

One thing is clear: On the basis of our findings and the literature cited in this thesis, the default assumption should be that magnetized plasmas are categorically different to their unmagnetized counterparts (and also ubiquitous). Filling in the missing pieces represented by the crude multi-scale picture of Figure 1.2 constitutes an important and well posed scientific problem for which we now reiterate what we think are potentially fruitful lines of attack.

First, we suggest a suite of global and local nonlinear simulations to investigate the magnetized MRI. Prescriptions for handling the firehose and GTI could come from the gyroviscous corrections found in chapter 3 and the mirror could, if feasible, be corrected by the FLR term from linear theory or simply left as it

is. It would be especially interesting to include a viscous heating term too as per the discussion above. Second, the development of a transport theory for the mirror and oblique firehose is absolutely imperative (see section 3.8). Until such theories are developed any magnetized plasma theory that constrains the pressure anisotropy to the marginal stability boundary *by fiat*, will be introducing an arbitrary step. Both projects would contribute significantly to our understanding of astrophysical plasma dynamics.

4.2 Summary

The principal topic of this thesis has been the evolution and nature of two particular magnetized plasma instabilities and, where relevant, their effect on transport. These instabilities are the MRI and the firehose instability.

In chapter 1 we explained how magnetized plasmas differ from unmagnetized plasmas and neutral fluids, and therefore why they require a separate treatment. We introduced the basic formalism to do this and showed, assuming the cyclotron frequency and Larmor radius are the smallest parameters in the system, that the pressure tensor is naturally anisotropic. The same analysis showed that this tensor can be naturally decomposed into gyrophase-dependent and gyrophase-independent terms, and we explained the role each component was to have for the rest of our work. For the former, which constitutes the pressure anisotropy, we provided a physical description. The theory in this chapter laid the groundwork from which the next two chapters followed.

In chapter 2 we considered the global linear stability of a magnetized, collisional plasma (the pressure anisotropy was described by the Braginskii viscosity) in the presence of a galactic shear flow and a variety of equilibrium magnetic field configurations. We treated the system as a two parameter problem in the magnetic field strength, and S_B a dimensionless combination of the collision frequency, rotation rate and magnetic field strength that is large when magnetized effects are important and small when they are not. We found a global version of the MRI in the presence of Braginskii viscosity, and showed its growth rate and the scale of the most unstable mode varies as a function of both parameters. Moti-

vated, in part, by understanding the existence of turbulence in quiescent regions of the ISM, we considered three galactically relevant background magnetic field configurations: purely azimuthal, purely vertical and slightly pitched. We found that the first two cases are singular limits in which the effects of the Braginskii viscosity are stabilising *for all modes* (whch is in disagreement with local analysis). In particular, we found numerically that for a vertical field the growth rate varies $\propto 1/(S_B B^2) = \text{Re}$ for small values of the Reynolds number. This was in agreement with the accompanying global asymptotic analysis. In the pitched field case we found that instead of the Braginskii viscosity being a stabilising influence it leads to an enhanced growth rate. In the limit $S_B \gg 1$ the magnetized MRI tended to a value $2\sqrt{2}$ times faster than its unmagnetized counterpart. In the weak magnetic field regime we determined (numerically and asymptotically) the scaling of its (purely real) growth rate $\simeq \sqrt{2}(1 - 2^{1/4}/3 \, S_B^{-1/2})$ and the Alfvén frequency at which this most unstable mode occurs $\propto S_B^{-1/4}$. For finite magnetic field strengths we found these modes became over-stable and the frequency of the travelling wave component also increases with the S_B and, in the limit $S_B \gg 1$ it can be up to an order of magnitude greater than the unmagnetized over-stability that also occurs for finite magnetic field strengths. We also provided a physical explanation of this behaviour, compared our results to local analysis and discussed some implications of our results for modelling magnetized accretion discs.

In chapter 3 we considered the local evolution of the firehose instability that is driven by the pressure anisotropy that naturally arises when the magnetic field strength decreases. We showed that in the long-wavelength limit (e.g. lowest order Braginskii theory) the governing equations are ill-posed as a result of the instability. Generally, and in the specific context of the ICM of galaxy clusters, we argued that the instability can dramatically affect the large-scale ($\gg \lambda_{\text{mfp}}$) dynamics. We argued that its nonlinear evolution should drive pressure anisotropies towards marginal stability values, controlled by the plasma beta β_i. As such, we developed a nonlinear theory for the instability in an first-principles kinetic calculation for the parallel ($k_\perp = 0$) firehose in a high-beta plasma. We used a particular physical asymptotic ordering to determine the pressure anisotropy, and therefore close our equations. We obtained a single nonlinear equation for

the firehose turbulence. (The lengthy details of this derivation were relegated to Appendices B and C). In the nonlinear regime, both analytical theory and the numerical solution show that the instability leads to secular ($\propto t$) growth of magnetic fluctuations. The fluctuations develop a $k_{\parallel}^{-3}$ spectrum, extending from scales somewhat larger than ρ_i to the maximum scale that grows secularly with time ($\propto t^{1/2}$); the relative pressure anisotropy tends to the marginal value $-2/\beta_i$. When a parallel ion heat flux is present, the parallel firehose instability mutates into the GTI, which continues to be unstable up to values of pressure anisotropy that can be positive and are limited by the magnitude of the heat flux. Its nonlinear evolution also involves secular growth of the magnetic energy, but the fluctuation spectrum is eventually dominated by modes around a maximal scale $\sim \rho_i l_T / \lambda_{\mathrm{mfp}}$, where l_T is the typical scale of the parallel temperature variation. Implications for momentum and heat transport were discussed, as were the implications for the solar wind and, our principle example, galaxy clusters.

Throughout we have attempted to highlight areas where our results are related to other magnetized plasma phenomena and in this chapter we presented a highly speculative account of how the two main processes we consider in this thesis could interact.

We hope that our findings have provided some insight, if not sparked an interest, in magnetized plasma physics.

Part V

Appendices

Appendix A

Gyrophase dependent pressure

Following Hazeltine & Meiss (2003) and Schekochihin *et al.* (2010) we determine **G**, the gyrophase dependent part of $\mathbf{P}_s^{(1)} = \int \mathrm{d}^3 \boldsymbol{v} \boldsymbol{v} \boldsymbol{v} f_s^{(1)}$.

The results in this section are entirely general in the sense that they do not depend on the species type, and therefore we suppress the species subscript on all quantities barring the distribution function, $f_s^{(0)}, f_s^{(1)}$.

Using suffix notation we can write the **T** that appears in the gyrophase dependent part of $\boldsymbol{vv}$, equation (1.23), as

$$T_{ij} = \frac{1}{4} M_{ijkl} v_k v_l, \tag{A.1}$$

where

$$M_{ijkl} = (\delta_{ik} + 3 b_i b_k)\epsilon_{jln} b_n + \epsilon_{iln} b_n (\delta_{jk} + 3 b_j b_k). \tag{A.2}$$

Substituting this expression for T_{ij} into equation (1.28) and integrating by parts yields

$$
\begin{aligned}
G_{ij} &= -\frac{M_{ijkl}}{4} \int \mathrm{d}^3 \boldsymbol{v} v_k v_l \frac{\partial f_s^{(1)}}{\partial \varphi} \\
&= -\frac{M_{ijkl}}{4\Omega} \int \mathrm{d}^3 \boldsymbol{v} v_k v_l \left[\frac{\mathrm{d} f_s^{(0)}}{\mathrm{d} t} + \boldsymbol{v} \cdot \boldsymbol{\nabla} f_s^{(0)} - \boldsymbol{v} \cdot \nabla \boldsymbol{u} \cdot \frac{\partial f_s^{(0)}}{\partial \boldsymbol{v}} - C[f_s^{(0)}] \right],
\end{aligned}
\tag{A.3}
$$

where we have substituted in equation (1.21) for $\partial f_s^{(1)}/\partial\varphi$ in the second line and eliminated the term proportional to $\boldsymbol{a}$ after integration by parts and the use of $\int\mathrm{d}^3\boldsymbol{v}\,\boldsymbol{v}f_s^{(0)}=0$ by definition of the peculiar velocity. The full expression for $\mathbf{G}_s$ is therefore

$$
G_{ij} = -\frac{M_{ijkl}}{4\Omega}\left[\frac{\mathrm{d}P_{kl}^{(0)}}{\mathrm{d}t} + \nabla_m Q_{mkl}^{(0)} + \right.
$$
$$
\left. \left(\delta_{mn}P_{kl}^{(0)} + \delta_{kn}P_{ml}^{(0)} + \delta_{ln}P_{mk}^{(0)}\right)\nabla_m u_n - C_{kl}^{(0)}\right] \quad \text{(A.4)}
$$

where $C_{kl}^{(0)} = m\int\mathrm{d}^3\boldsymbol{v}\,v_k v_l C[f_s^{(0)}]$ and $Q_{mkl}^{(0)} = m\int\mathrm{d}^3\boldsymbol{v}\,v_m v_k v_l f_s^{(0)}$. Determining their specific form relies on knowing that $f_s^{(0)}$ is gyrotropic and so the φ component of the velocity space integral acts only on $v_i, v_i v_j$ and $v_i v_j v_k$. Performing these integrals yields

$$
\langle v_i \rangle = v_\parallel b_i,
$$
$$
\langle v_i v_j \rangle = v_\parallel^2 b_i b_j + \frac{v_\perp^2}{2}(\delta_{ij} - b_i b_j),
$$
$$
\langle v_i v_j v_k \rangle = v_\parallel^3 b_i b_j b_k + v_\parallel\frac{v_\perp^2}{2}\left[(\delta_{ij}-b_i b_j)b_k + (\delta_{ik}-b_i b_k)b_j + (\delta_{jl}-b_j b_l)b_i\right],
$$

where we denote the gyroaveraging operation $(1/2\pi)\int_0^{2\pi}$ by angle brackets. Combining M_{ijkl} with these quantities yields, eventually, the following expressions for the pressure and collisional terms in the square bracket of equation (A.4):

$$
M_{ijkl}P_{kl}^{(0)}\nabla_m u_k = M_{ijkl}C_{kl}^{(0)} = 0, \quad \text{(A.5)}
$$
$$
M_{ijkl}\frac{\mathrm{d}P_{kl}^{(0)}}{\mathrm{d}t} = -4(p_\perp^{(0)} - p_\parallel^{(0)})\left(\boldsymbol{b}\frac{\mathrm{d}\boldsymbol{b}}{\mathrm{d}t}\times\boldsymbol{b} + \frac{\mathrm{d}\boldsymbol{b}}{\mathrm{d}t}\times\boldsymbol{bb}\right), \quad \text{(A.6)}
$$
$$
M_{ijkl}P_{ml}\nabla_m u_k = -p_\perp^{(0)}\left[\boldsymbol{b}\times(\nabla\boldsymbol{u})\cdot(\mathbf{I}+3\boldsymbol{bb}) - (\mathbf{I}+3\boldsymbol{bb})\cdot(\nabla\boldsymbol{u})^{\mathrm{T}}\times\boldsymbol{b}\right], \quad \text{(A.7)}
$$
$$
M_{ijkl}P_{mk}\nabla_m u_l = -p_\perp^{(0)}\left[\boldsymbol{b}\times(\nabla\boldsymbol{u})^{\mathrm{T}}\cdot(\mathbf{I}+3\boldsymbol{bb}) - (\mathbf{I}+3\boldsymbol{bb})\cdot(\nabla\boldsymbol{u})\times\boldsymbol{b}\right]
$$
$$
- 4(p_\perp - p_\parallel)\left[\boldsymbol{b}(\boldsymbol{b}\cdot\nabla\boldsymbol{u}\times\boldsymbol{b}) + (\boldsymbol{b}\cdot\nabla\boldsymbol{u}\times\boldsymbol{b})\boldsymbol{b}\right]. \quad \text{(A.8)}
$$

Also,

$$
Q_{mkl} = q_\perp^{(0)}(b_m\delta_{kl} + \delta_{mk}b_l + \delta_{ml}b_k) - (3q_\perp^{(0)} - q_\parallel^{(0)})b_m b_k b_l, \quad \text{(A.9)}
$$

from which it follows

$$M_{ijkl}\nabla_m Q_{mkl}^{(0)} = (\mathbf{I} + 3\boldsymbol{bb}) \cdot \mathbf{V} \times \boldsymbol{b} - \boldsymbol{b} \times \mathbf{V} \cdot (\mathbf{I} + 3\boldsymbol{bb})$$
$$- 4(3q_\perp - q_\parallel)\left[\boldsymbol{b}(\boldsymbol{b} \cdot \nabla\boldsymbol{b} \times \boldsymbol{b}) + (\boldsymbol{b} \times \boldsymbol{b} \cdot \nabla\boldsymbol{b})\boldsymbol{b}\right], \quad (A.10)$$

where $\mathbf{V} = \nabla\boldsymbol{q}_\perp^{(0)} + (\nabla\boldsymbol{q}_\perp^{(0)})^{\mathrm{T}}$. Now substituting equations (A.5)-(A.10) into equation (A.4) and simplifying leads to our final expressions, equations (1.28)-(1.30).

Appendix B

Kinetic theory: Electrons

B.0.1 Mass-ratio ordering

The kinetic equation (1.2) for electrons is (recall that $\boldsymbol{v}$ is the peculiar velocity)

$$
\frac{\mathrm{d}f_e}{\mathrm{d}t_e} + \boldsymbol{v}\cdot\boldsymbol{\nabla}f_e - \left[\frac{e}{m_e}\left(\boldsymbol{L}_e + \frac{\boldsymbol{v}\times\boldsymbol{B}}{c}\right) + \frac{\mathrm{d}\boldsymbol{u}_e}{\mathrm{d}t_e} + \boldsymbol{v}\cdot\boldsymbol{\nabla}\boldsymbol{u}_e\right]\cdot\frac{\partial f_e}{\partial\boldsymbol{v}} = C[f_e],
$$
$$
1 \qquad \left(\frac{m_e}{m_i}\right)^{-\frac{1}{2}} \qquad \left(\frac{m_e}{m_i}\right)^{-\frac{1}{2}} \quad \left(\frac{m_e}{m_i}\right)^{-1} \quad \left(\frac{m_e}{m_i}\right)^{\frac{1}{2}} \qquad 1 \qquad\qquad \left(\frac{m_e}{m_i}\right)^{-\frac{1}{2}}
$$
$$
\text{(B.1)}
$$

where $\boldsymbol{L}_e = \boldsymbol{E} + \boldsymbol{u}_e\times\boldsymbol{B}/c$ (we use this notation sparingly) and $\mathrm{d}/\mathrm{d}t_e = \partial/\partial t + \boldsymbol{u}_e \cdot \nabla$ is the convective derivative with respect to the electron flow. We have labelled all terms in equation (B.1) according to their ordering in powers of $(m_e/m_i)^{1/2}$, while taking $T_e \sim T_i$ as per equation (1.14). The ordering has been done relative to $kv_{\mathrm{th},i}f_e$ and we have assumed

$$
\frac{\partial}{\partial t} \sim \omega \sim kv_{\mathrm{th},i}, \quad \boldsymbol{\nabla} \sim k \sim \rho_i^{-1} \sim \left(\frac{m_e}{m_i}\right)^{1/2}\frac{eB}{m_e c\, v_{\mathrm{th},e}}, \quad \boldsymbol{u}_e \sim v_{\mathrm{th},i}, \qquad \text{(B.2)}
$$

$$
\boldsymbol{v} \sim v_{\mathrm{th},e} \sim \left(\frac{m_e}{m_i}\right)^{-1/2} v_{\mathrm{th},i}, \quad \boldsymbol{E} \sim \frac{\boldsymbol{u}_e\times\boldsymbol{B}}{c}, \quad \nu_i \sim \omega \sim \left(\frac{m_e}{m_i}\right)^{1/2}\nu_e. \quad \text{(B.3)}
$$

We stress that these are formal orderings with respect to the mass-ratio expansion, not statements about the exact size of various quantities and their derivatives: thus, some of the quantities ordered as unity within the mass-ratio expan-

sion (e.g., $k\rho_i$ or $\boldsymbol{u}_e/v_{\text{th},i}$) will be ordered small in the subsidiary ϵ expansion to be used in solving the ion kinetics (see section 3.3.2).

We now expand the electron distribution function in powers of $(m_e/m_i)^{1/2}$: $f_e = f_e^{(0)} + f_e^{(1)} + \cdots$. (This is not be confused with the notationally identical expansion of section 1.4.1 where the small parameter was proportional to Ω_s). It turns out that we can learn all we need to know from just the two lowest orders in the expansion of equation (B.1). Note that we do not expand any of the fields — exact $\boldsymbol{E}$ and $\boldsymbol{B}$ are kept.

B.0.2   Order $(m_e/m_i)^{-1}$: gyrotropic electrons

To this order, equation (B.1) is

$$-\frac{e}{m_e}\frac{\boldsymbol{v}\times\boldsymbol{B}}{c}\cdot\frac{\partial f_e^{(0)}}{\partial\boldsymbol{v}} = -\Omega_e\frac{\partial f_e^{(0)}}{\partial\vartheta} = 0. \tag{B.4}$$

(Recall $\Omega_e = -eB/m_e c$ and ϑ is the gyroangle variable). Thus, in this order, we have learned that the lowest-order electron distribution function is gyrotropic.

B.0.3   Order $(m_e/m_i)^{-1/2}$: Maxwellian electrons

To this order, equation (B.1) is

$$\boldsymbol{v}\cdot\boldsymbol{\nabla}f_e^{(0)} - \frac{e}{m_e}\left(\boldsymbol{E} + \frac{\boldsymbol{u}_e\times\boldsymbol{B}}{c}\right)\cdot\frac{\partial f_e^{(0)}}{\partial\boldsymbol{v}} - \Omega_e\frac{\partial f_e^{(1)}}{\partial\vartheta} = C[f_e^{(0)}]. \tag{B.5}$$

Let us multiply this equation by $1 + \ln f_e^{(0)}$ and integrate over the entire phase space. This gives

$$\int\int \mathrm{d}^3\boldsymbol{r}\mathrm{d}^3\boldsymbol{v}\, C[f_e^{(0)}]\ln f_e^{(0)} = 0 \tag{B.6}$$

because the left-hand side of equation (B.5) is an exact divergence in the phase space. Let us recall that, according to the Boltzmann (1872) H-theorem,

$$\frac{\mathrm{d}}{\mathrm{d}t}\int\int \mathrm{d}^3\boldsymbol{r}\mathrm{d}^3\boldsymbol{v}\, f_e\ln f_e = \int\int \mathrm{d}^3\boldsymbol{r}\mathrm{d}^3\boldsymbol{v}\, C[f_e]\ln f_e \leq 0, \tag{B.7}$$

where the inequality becomes equality only for a local Maxwellian distribution (the proof for plasmas can be found in, e.g., Chapman & Cowling 1970; Hazeltine & Meiss 2003). Therefore, equation (B.6) implies that $f_e^{(0)}$ is a local Maxwellian:

$$f_e^{(0)} = \frac{n_e}{\left(\pi v_{\mathrm{th},e}^2\right)^{3/2}} e^{-v^2/v_{\mathrm{th},e}^2}, \tag{B.8}$$

Since v is peculiar velocity, the mean flow $\boldsymbol{u}_e$ has already been accounted for. Note that the perturbation expansion of f_e can always be constructed in such a way that n_e and T_e in equation (B.8) are the exact density and temperature of the electron distribution.

B.0.4 Isothermal electrons

More can be learned about the electrons without going to higher orders. Let us now substitute the expression (B.8) for $f_e^{(0)}$ into equation (B.5) and gyroaverage this equation, $(1/2\pi) \int \mathrm{d}\vartheta$, to eliminate the term containing $f_e^{(1)}$:

$$v_\| \boldsymbol{b}\cdot\boldsymbol{\nabla} f_e^{(0)} + \frac{e}{m_e} E_\| \frac{2v_\|}{v_{\mathrm{th},e}^2} f_e^{(0)} = \left[\frac{\boldsymbol{b}\cdot\boldsymbol{\nabla} n_e}{n_e} + \left(\frac{v^2}{v_{\mathrm{th},e}^2} - \frac{3}{2} \right) \frac{\boldsymbol{b}\cdot\boldsymbol{\nabla} T_e}{T_e} + \frac{eE_\|}{T_e} \right] v_\| f_e^{(0)} = 0, \tag{B.9}$$

where $E_\| = \boldsymbol{E}\cdot\boldsymbol{b}$. Since equation (B.9) must hold for all v, it follows from it that

$$E_\| = -\frac{T_e \boldsymbol{b}\cdot\boldsymbol{\nabla} n_e}{en_e}, \tag{B.10}$$

$$\boldsymbol{b}\cdot\boldsymbol{\nabla} T_e = 0. \tag{B.11}$$

The second equation means that electrons (to lowest order) are isothermal along the magnetic-field lines $\sim \lambda_{\mathrm{mfp}}(m_i/m_e)^{1/2}$. For our fiducial ICM parameters, we have $\lambda_{\mathrm{mfp}}(m_i/m_e)^{1/2} \sim 6\times 10^{21}$ cm, which is larger than the scale l of the motions that have the highest rate of strain (see section 3.2.1). For turbulent plasmas, this implies globally isothermal electrons ($T_e = \mathrm{const}$) because the field lines are stochastic. We will adopt this assumption of globally isothermal electrons in all our calculations.

B.0.5 Generalised Ohm's law

Let us again go back to equation (B.5), multiply it by $m_e \boldsymbol{v}$ and integrate over the velocity space. The result is the electron momentum equation to lowest order in the mass-ratio expansion:

$$en_e \left(\boldsymbol{E} + \frac{\boldsymbol{u}_e \times \boldsymbol{B}}{c} \right) = -\boldsymbol{\nabla} \cdot \int \mathrm{d}^3 \boldsymbol{v} m_e \boldsymbol{v}\boldsymbol{v} f_e^{(0)} = -\boldsymbol{\nabla} p_e = -T_e \boldsymbol{\nabla} n_e, \quad \text{(B.12)}$$

where the electron pressure is isotropic because the distribution is Maxwellian, $p_e = n_e T_e$, and the gradient only affects n_e because $T_e = const$ (section B.0.4). Note that equation (B.10) is simply the parallel part of equation (B.12). Equation (B.12) is the generalised Ohm's law, equation (3.30). We have thus arrived at the starting point of the derivation in section 3.3.1.

Appendix C

Kinetic theory: Ions

C.0.6   Ordering

The kinetic equation (1.2) for ions is

$$
\frac{\mathrm{d}f_i}{\mathrm{d}t_i} + \boldsymbol{v} \cdot \boldsymbol{\nabla} f_i + \left[\frac{Ze}{m_i} \left(\boldsymbol{L}_i + \frac{\boldsymbol{v} \times \boldsymbol{B}}{c} \right) - \frac{\mathrm{d}\boldsymbol{u}_i}{\mathrm{d}t_i} - \boldsymbol{v} \cdot \boldsymbol{\nabla} \boldsymbol{u}_i \right] \cdot \frac{\partial f_i}{\partial \boldsymbol{v}} = C[f_i],
$$

Equil.	ϵ^3	ϵ^2	ϵ^2	ϵ^{-1}	ϵ^4	ϵ^3	ϵ
Pert.	ϵ^2	ϵ	ϵ	1	ϵ^3	ϵ^2	ϵ^2

$$\text{(C.1)}$$

where $\boldsymbol{L}_i = \boldsymbol{E} + \boldsymbol{u}_i \times \boldsymbol{B}/c$ and $\mathrm{d}/\mathrm{d}t_i = \partial/\partial t + \boldsymbol{u}_i \cdot \nabla$ is the convective derivative with respect to the ion flow. We have labeled all terms according to their ordering in powers of ϵ. The ordering has been done relative to $k_\parallel v_{\mathrm{th},i} f_i$ using the assumptions explained in section 3.3.2. The first row of orderings in equation (C.1) applies to the equilibrium (lowest-order) quantities and their gradients. The second row gives the lowest order in which perturbed quantities appear in each term of the kinetic equation.

C.0.7   Expansion of the Lorentz force

We require an explanation of the ordering and the expansion of the Lorentz force. The Lorentz force is given in terms of n_i and $\boldsymbol{B}$ by eliminating the ion

flow. Expanding this equation in ϵ, we have to three lowest orders

$$\frac{Ze}{m_i}\boldsymbol{L}_i = -\underbrace{\frac{ZT_e\boldsymbol{\nabla}n_{1i}}{m_i\left(n_{0i}+n_{1i}+n_{2i}\right)}}_{\epsilon} - \underbrace{\frac{ZT_e\boldsymbol{\nabla}\left(n_{0i}+n_{2i}\right)}{m_i\left(n_{0i}+n_{1i}\right)}}_{\epsilon^2} - \underbrace{\frac{ZT_e\boldsymbol{\nabla}n_{3i}}{m_in_{0i}}}_{\epsilon^3} + \underbrace{v_A^2\nabla_\parallel\frac{\boldsymbol{B}_1^\perp}{B_0}}_{\epsilon^3},$$

$$\tag{C.2}$$

where we have used $B_1^\parallel = 0$ (see equation (3.50)). The ordering of the Lorentz force in equation (C.1) follows from equation (C.2). Note that, in order to keep ϵ^3 precision, we have to keep perturbed densities in the denominators of the first two terms on the right-hand side. However, as promised in section 3.3.3, we will see in section C.0.11 that $n_{1i} = 0$, so the contributions to the Lorentz force will start at order ϵ^2 and equation (C.2) will simplify to read

$$\frac{Ze}{m_i}\boldsymbol{L}_i = -\frac{ZT_e\boldsymbol{\nabla}\left(n_{0i}+n_{2i}\right)}{m_in_{0i}} - \frac{ZT_e\boldsymbol{\nabla}n_{3i}}{m_in_{0i}} + v_A^2\nabla_\parallel\frac{\boldsymbol{B}_1^\perp}{B_0} + \cdots \tag{C.3}$$

In section C.0.14, we will find that $n_{2i} = 0$ as well.

C.0.8   Order ϵ^{-1}: gyrotropic equilibrium

We now proceed to expand the ion kinetic equation (C.1). To lowest order, ϵ^{-1}, we get (cf. section B.0.2)

$$\frac{Ze}{m_i}\frac{\boldsymbol{v}\times\boldsymbol{B}_0}{c}\cdot\frac{\partial f_{0i}}{\partial\boldsymbol{v}} = -\Omega_i\frac{\partial f_{0i}}{\partial\vartheta} = 0. \tag{C.4}$$

Thus, the ion equilibrium distribution is gyrotropic. We will express the fact that f_{0i} is independent of the gyroangle ϑ by writing f_{0i} as a function of two velocity variables, $v = |\boldsymbol{v}|$ and $v_\parallel = \boldsymbol{v}\cdot\boldsymbol{b}_0$. In the derivation that follows these variables are more convenient than the perhaps more intuitive pair $(v_\perp, v_\parallel)$. Thus,

$$f_{0i} = f_{0i}(t, \boldsymbol{r}, v, v_\parallel). \tag{C.5}$$

Hence follows an identity that will be useful shortly both for f_{0i} and other gyrotropic functions:

$$\frac{\partial f_{0i}}{\partial \boldsymbol{v}} = \frac{\boldsymbol{v}}{v}\left(\frac{\partial f_{0i}}{\partial v}\right)_{v_{\parallel}} + \boldsymbol{b}_0 \left(\frac{\partial f_{0i}}{\partial v_{\parallel}}\right)_{v}. \tag{C.6}$$

C.0.9 Order ϵ^0

In the next order, equation (C.1) is

$$\frac{Ze}{m_i}\frac{\boldsymbol{v} \times \boldsymbol{B}_1^{\perp}}{c} \cdot \frac{\partial f_{0i}}{\partial \boldsymbol{v}} - \Omega_i \frac{\partial f_{1i}}{\partial \vartheta} = 0, \tag{C.7}$$

where we have again used $(Ze/m_i c)(\boldsymbol{v} \times \boldsymbol{B}_0) \cdot \partial/\partial \boldsymbol{v} = -\Omega_i \partial/\partial \vartheta$. Using equation (C.6), we get

$$\frac{\partial f_{1i}}{\partial \vartheta} = \frac{1}{\Omega_i}\frac{Ze}{m_i}\frac{\boldsymbol{v} \times \boldsymbol{B}_1^{\perp}}{c} \cdot \boldsymbol{b}_0 \left(\frac{\partial f_{0i}}{\partial v_{\parallel}}\right)_{v} = (\boldsymbol{b}_0 \times \boldsymbol{v}_{\perp}) \cdot \frac{\boldsymbol{B}_1^{\perp}}{B_0}\left(\frac{\partial f_{0i}}{\partial v_{\parallel}}\right)_{v}. \tag{C.8}$$

Noticing that $\boldsymbol{b}_0 \times \boldsymbol{v}_{\perp} = \partial \boldsymbol{v}_{\perp}/\partial \vartheta$, we integrate this equation:

$$f_{1i} = \boldsymbol{v}_{\perp} \cdot \frac{\boldsymbol{B}_1^{\perp}}{B_0}\left(\frac{\partial f_{0i}}{\partial v_{\parallel}}\right)_{v} + g_{1i}(t, \boldsymbol{r}, v, v_{\parallel}), \tag{C.9}$$

where g_{1i} is an arbitrary function (the gyrotropic part of the first-order perturbed distribution).

Thus, all we have learned at this order is the gyroangle dependence of f_{1i}. This will be a general feature of our expansion: since the gyroangle derivative in equation (C.1) is the lowest-order term, what we learn about each perturbed distribution function f_{1i}, f_{2i}, f_{3i}, ..., at the lowest order in which it first appears will always be its dependence on ϑ.

C.0.10   Order ϵ^1: Maxwellian equilibrium

At this order, equation (C.1) is

$$\boldsymbol{v}\cdot\boldsymbol{\nabla}f_{1i}+\frac{Ze}{m_i}\left(\boldsymbol{E}+\frac{\boldsymbol{u}_i\times\boldsymbol{B}}{c}\right)_1\cdot\frac{\partial f_{0i}}{\partial\boldsymbol{v}}-\Omega_i\frac{\partial f_{2i}}{\partial\vartheta}+\underbrace{\frac{Ze}{m_i}\frac{\boldsymbol{v}\times\boldsymbol{B}_1^{\perp}}{c}\cdot\frac{\partial f_{1i}}{\partial\boldsymbol{v}}}_{I_1}=C[f_{0i}], \quad\text{(C.10)}$$

where, using equation (C.9) and other tricks already employed in the two previous sections, we can express the last term on the left-hand side of equation (C.10) as follows

$$I_1=\Omega_i\left(\boldsymbol{b}_0\times\boldsymbol{v}_{\perp}\right)\cdot\frac{\boldsymbol{B}_1^{\perp}}{B_0}\left[\boldsymbol{v}_{\perp}\cdot\frac{\boldsymbol{B}_1^{\perp}}{B_0}\left(\frac{\partial^2 f_{0i}}{\partial v_{\parallel}^2}\right)_v+\left(\frac{\partial g_{1i}}{\partial v_{\parallel}}\right)_v\right], \quad\text{(C.11)}$$

$$=\Omega_i\frac{\partial}{\partial\vartheta}\left[\frac{1}{2}\left(\boldsymbol{v}_{\perp}\cdot\frac{\boldsymbol{B}_1^{\perp}}{B_0}\right)^2\left(\frac{\partial^2 f_{0i}}{\partial v_{\parallel}^2}\right)_v+\boldsymbol{v}_{\perp}\cdot\frac{\boldsymbol{B}_1^{\perp}}{B_0}\left(\frac{\partial g_{1i}}{\partial v_{\parallel}}\right)_v\right]. \quad\text{(C.12)}$$

Collisions have made their first appearance at this order and we can now prove that f_{0i} is a Maxwellian. The proof is similar to the one for electrons in section B.0.3: we multiply equation (C.10) by $1+\ln f_{0i}$ and integrate over the entire phase space. All terms on the left-hand side vanish because, to the order at which we are computing them, they are all full derivatives with respect to the phase-space variables. Thus,

$$\int\int \mathrm{d}^3\boldsymbol{r}\mathrm{d}^3\boldsymbol{v}C[f_{0i}]\ln f_{0i}=0 \quad\Rightarrow\quad f_{0i}=\frac{n_{0i}}{\left(\pi v_{\text{th},i}^2\right)^{3/2}}e^{-v^2/v_{\text{th},i}^2}, \quad\text{(C.13)}$$

is a Maxwellian.

C.0.11   Order ϵ^1 continued: more information about f_{1i}

The fact that f_{0i} is a Maxwellian allows us to uncover three important additional pieces of information. First, from equation (C.9), we learn that f_{1i} is gyrotropic:

$$f_{1i}=g_{1i}(t,\boldsymbol{r},v,v_{\parallel}). \quad\text{(C.14)}$$

Second, we can now prove that $n_{1i} = 0$, as promised in sections 3.3.3 and C.0.7. Using equations (C.12) and (C.13) in equation (C.10), gyroaveraging this equation, $(1/2\pi) \int d\vartheta$, and substituting for the Lorentz force the lowest-order expression from equation (C.2), we get

$$v_\parallel \left(\nabla_\parallel f_{1i} + \frac{ZT_e}{T_{0i}} \frac{\nabla_\parallel n_{1i}}{n_{0i}} f_{0i} \right) = 0 \quad \Rightarrow \quad \left(1 + \frac{ZT_e}{T_{0i}} \right) \nabla_\parallel n_{1i} = 0, \qquad \text{(C.15)}$$

where the second equation has been obtained by cancelling $v_\parallel$ in the first equation and integrating it over velocities. We have used the shorthand $\nabla_\parallel = \boldsymbol{b}_0 \cdot \boldsymbol{\nabla}$, which henceforth will be employed wherever fast parallel variation of the perturbed quantities is involved (for slow parallel gradients, we will continue writing $\boldsymbol{b}_0 \cdot \boldsymbol{\nabla}$ explicitly to emphasize that $\boldsymbol{b}_0$ is curved on the large scales). Equation (C.15) implies that we may set

$$n_{1i} = 0 \qquad \text{(C.16)}$$

(q.e.d.; see equation (3.53)) and absorb whatever slow-varying density perturbation may arise into n_{0i}. After eliminating n_{1i} from equation (C.15), we get

$$\nabla_\parallel f_{1i} = 0, \qquad \text{(C.17)}$$

so f_{1i} has no small-scale spatial variation at all. Note that this confirms equation (3.55), which was derived from the ion momentum equation in the ϵ^1 order (i.e., it is the velocity moment of equation (C.10)) and restricted the fast spatial variation of the first-order pressure tensor. Equation (C.3) is also now confirmed.

C.0.12 Order ϵ^1 continued: gyroangle dependence of f_{2i}

Finally, we go back to equation (C.10) to determine the gyroangle dependence of f_{2i}. Since f_{1i} does not have a small-scale part, the first two terms drop out. Using the fact that f_{0i} is a Maxwellian and equation (C.12), we integrate equation (C.10) with respect to the gyroangle and get

$$f_{2i} = \boldsymbol{v}_\perp \cdot \frac{\boldsymbol{B}_1^\perp}{B_0} \left(\frac{\partial f_{1i}}{\partial v_\parallel} \right)_v + g_{2i}(t, \boldsymbol{r}, v, v_\parallel), \qquad \text{(C.18)}$$

where g_{2i} is the gyrotropic part of f_{2i} (so far arbitrary).

C.0.13 Order ϵ^2: role of equilibrium density and temperature gradients

At this order, equation (C.1) becomes, upon substitution of the Maxwellian f_{0i} and the lowest-order (ϵ^2) expression for the Lorentz force from equation (C.3)

$$\frac{\partial f_{1i}}{\partial t} + \boldsymbol{v} \cdot \boldsymbol{\nabla} f_{0i} + v_\parallel \nabla_\parallel f_{2i} + \frac{ZT_e}{T_{0i}} \frac{\boldsymbol{v} \cdot \boldsymbol{\nabla} n_{0i} + v_\parallel \nabla_\parallel n_{2i}}{n_{0i}} f_{0i} - \Omega_i \frac{\partial f_{3i}}{\partial \vartheta}$$

$$+ \underbrace{\frac{Ze}{m_i}\left(\frac{\boldsymbol{v} \times \boldsymbol{B_2}}{c} \cdot \frac{\partial f_{1i}}{\partial \boldsymbol{v}} + \frac{\boldsymbol{v} \times \boldsymbol{B_1^\perp}}{c} \cdot \frac{\partial f_{2i}}{\partial \boldsymbol{v}}\right) + \frac{2v_\parallel \left(\nabla_\parallel \boldsymbol{u_{1i}^\perp}\right) \cdot \boldsymbol{v_\perp}}{v_{\text{th},i}^2} f_{0i}}_{I_2} = C[f_{1i}],$$

(C.19)

where we have explicitly enforced the assumption that perturbed quantities have no fast perpendicular spatial dependence. Analogously to equation (C.12), upon using equations (C.14) and (C.18) and noticing that $\boldsymbol{v_\perp} = -\partial(\boldsymbol{b_0} \times \boldsymbol{v})/\partial\vartheta$, we find that the last two terms on the left-hand side of equation (C.19) are a full gyroangle derivative:

$$I_2 = \Omega_i \frac{\partial}{\partial \vartheta}\left[\boldsymbol{v_\perp} \cdot \frac{\boldsymbol{B_2^\perp}}{B_0}\left(\frac{\partial f_{1i}}{\partial v_\parallel}\right)_v + \frac{1}{2}\left(\boldsymbol{v_\perp} \cdot \frac{\boldsymbol{B_1^\perp}}{B_0}\right)^2 \left(\frac{\partial^2 f_{1i}}{\partial v_\parallel^2}\right)_v\right.$$

$$\left. + \boldsymbol{v_\perp} \cdot \frac{\boldsymbol{B_1^\perp}}{B_0}\left(\frac{\partial g_{2i}}{\partial v_\parallel}\right)_v - \frac{2v_\parallel \nabla_\parallel \boldsymbol{u_{1i}^\perp}}{v_{\text{th},i}^2} \cdot \frac{\boldsymbol{b_0} \times \boldsymbol{v_\perp}}{\Omega_i} f_{0i}\right]. \quad (C.20)$$

In view of equation (C.20) and of the gyroangle independence of f_{1i} (equation (C.14)), the gyroaverage of equation (C.19) is

$$\frac{\partial f_{1i}}{\partial t} + v_\parallel\left[\boldsymbol{b_0} \cdot \boldsymbol{\nabla} f_{0i} + \nabla_\parallel g_{2i} + \frac{ZT_e}{T_{0i}} \frac{\boldsymbol{b_0} \cdot \boldsymbol{\nabla} n_{0i} + \nabla_\parallel n_{2i}}{n_{0i}} f_{0i}\right] = C[f_{1i}]. \quad (C.21)$$

Since f_{1i} has no fast spatial gradients (equation (C.17)), averaging equation (C.21) over small scales gives

$$\frac{\partial f_{1i}}{\partial t} + v_\parallel\left[\boldsymbol{b_0} \cdot \boldsymbol{\nabla} f_{0i} + \frac{ZT_e}{T_{0i}} \frac{\boldsymbol{b_0} \cdot \boldsymbol{\nabla} n_{0i}}{n_{0i}} f_{0i}\right] = C[f_{1i}]. \quad (C.22)$$

This equation determines f_{1i} purely in terms of the equilibrium density and temperature gradients. Since the time variation of the equilibrium is slow, it is clear that f_{1i} will converge to a steady solution after a few collision times. Then $\partial f_{1i}/\partial t$ in equation (C.22) can be neglected and the solution obtained by inverting the linearised collision operator. Since we are not interested in exact collisional transport coefficients here, instead of the full Landau collision operator, we will use a very simple model one — the Lorentz pitch-angle scattering operator (see, e.g., Helander & Sigmar, 2002), so equation (C.22) becomes in steady state

$$
C[f_{1i}] = \nu_i \frac{\partial}{\partial \xi} \frac{1-\xi^2}{2} \frac{\partial f_{1i}}{\partial \xi} = \xi v \left[\left(1 + \frac{ZT_e}{T_{0i}} \right) \frac{\boldsymbol{b}_0 \cdot \boldsymbol{\nabla} n_{0i}}{n_{0i}} + \left(\frac{v^2}{v_{\text{th},i}^2} - \frac{3}{2} \right) \frac{\boldsymbol{b}_0 \cdot \boldsymbol{\nabla} T_{0i}}{T_{0i}} \right] f_{0i},
$$
(C.23)

where $\xi = v_\parallel/v$ and, once again, the dependency of ν_i on v has been suppressed for simplicity. The solution of equation (C.23) that satisfies equation (C.16) is

$$
\begin{aligned}
f_{1i} &= -\frac{v_\parallel}{\nu_i} \left[\left(1 + \frac{ZT_e}{T_{0i}} \right) \frac{\boldsymbol{b}_0 \cdot \boldsymbol{\nabla} n_{0i}}{n_{0i}} + \left(\frac{v^2}{v_{\text{th},i}^2} - \frac{3}{2} \right) \frac{\boldsymbol{b}_0 \cdot \boldsymbol{\nabla} T_{0i}}{T_{0i}} \right] f_{0i} \\
&= -\frac{v_\parallel}{\nu_i} \left(\frac{v^2}{v_{\text{th},i}^2} - \frac{5}{2} \right) \frac{\boldsymbol{b}_0 \cdot \boldsymbol{\nabla} T_{0i}}{T_{0i}} f_{0i}.
\end{aligned}
$$
(C.24)

The second, simplified, expression above is obtained by noticing that the temperature and density gradients are, in fact, related by the equilibrium pressure balance, equation (3.57), which was obtained in section 3.3.3 from the ion momentum equation in the ϵ^2 order. It is easily recovered by taking the velocity moment of equation (C.19) and averaging out the small scales. Since f_{0i} is a Maxwellian, the pressure balance takes the form (previewed in footnote 5, chapter 3)

$$
\left(1 + \frac{ZT_e}{T_{0i}} \right) \frac{\boldsymbol{\nabla} n_{0i}}{n_{0i}} + \frac{\boldsymbol{\nabla} T_{0i}}{T_{0i}} = 0,
$$
(C.25)

whence immediately follows the final expression for f_{1i} in equation (C.24).

Let us note two useful properties of the solution (C.24). First, f_{1i} makes no

contribution to the pressure tensor:

$$\mathbf{P}_{1i} = m_i \int \mathrm{d}^3\boldsymbol{v} \, \boldsymbol{v}\boldsymbol{v} f_{1i} = 0, \tag{C.26}$$

a result we promised in section 3.3.3 (equation (3.55)). Second, the derivative of f_{1i} with respect to $v_\parallel$ is isotropic:

$$\left(\frac{\partial f_{1i}}{\partial v_\parallel} \right)_v = -\frac{1}{\nu_i} \left(\frac{v^2}{v_{\mathrm{th},i}^2} - \frac{5}{2} \right) \frac{\boldsymbol{b}_0 \cdot \boldsymbol{\nabla} T_{0i}}{T_{0i}} f_{0i}, \qquad \left(\frac{\partial^2 f_{1i}}{\partial v_\parallel^2} \right)_v = 0, \tag{C.27}$$

which leads to vanishing of one of the terms in equation (C.20).

We will see in Appendix C.0.17 that f_{1i} encodes the ion collisional heat flux (equation (C.24) is the standard form of the appropriate contribution to the perturbed distribution function; see, e.g., equation (D16) of Schekochihin *et al.* 2009). We will carry the ion-temperature-gradient effect contained in f_{1i} through to the end of this calculation because it will interesting and instructive to see how contributions from the ion heat flux arise in the problem. However, this is not the main effect we are after and an impatient reader attempting to follow this derivation may find the following simplification useful. If one assumes by fiat that $\boldsymbol{\nabla} T_{0i} = 0$, then $\boldsymbol{\nabla} n_{0i} = 0$ as well (from equation (C.25)) and in all the calculations that follow one may set $f_{1i} = 0$ and $f_{0i} = \mathrm{const}$, which substantially reduces the amount of algebra.

C.0.14   Order ϵ^2 continued: more information about f_{2i}

Staying at this order, we can learn more about f_{2i} and f_{3i}. Subtracting equation (C.22) from equation (C.21), we get

$$v_\parallel \left(\nabla_\parallel g_{2i} + \frac{ZT_e}{T_{0i}} \frac{\nabla_\parallel n_{2i}}{n_{0i}} f_{0i} \right) = 0 \quad \Rightarrow \quad \left(1 + \frac{ZT_e}{T_{0i}} \right) \nabla_\parallel n_{2i} = 0, \tag{C.28}$$

analogously to equation (C.15). We have used the fact that, as follows from equation (C.18), $n_{2i} = \int \mathrm{d}^3\boldsymbol{v} f_{2i} = \int \mathrm{d}^3\boldsymbol{v} g_{2i}$. Similarly to the argument in section

C.0.11, this implies that n_{2i} has no fast spatial variation and so we can set

$$n_{2i} = 0. \tag{C.29}$$

Equation (C.28) then implies

$$\nabla_\parallel g_{2i} = 0, \tag{C.30}$$

i.e., g_{2i} has no small-scale spatial dependence. Since the first term in equation (C.18) does not contribute to the second-order pressure tensor (because the derivative of f_{1i} is a function of v only), we have

$$\mathbf{P}_{2i} = m_i \int \mathrm{d}^3\boldsymbol{v}\, \boldsymbol{v}\boldsymbol{v}\, g_{2i}, \tag{C.31}$$

and so, in view of equation (C.30), $\mathbf{P}_{2i}$ has no small-scale dependence. This confirms equation (3.58), derived in section 3.3.3 from the ion momentum equation. Note that the tensor $\mathbf{P}_{2i}$ will be needed in the large-scale momentum equation (3.62). It will contain the lowest-order pressure anisotropy.

C.0.15 Order ϵ^2 continued: gyroangle dependence of f_{3i}

Subtracting equation (C.21) from equation (C.19) and using equation (C.18), we get

$$\Omega_i \frac{\partial f_{3i}}{\partial \vartheta} = I_2 + \boldsymbol{v}_\perp \cdot \left[\boldsymbol{\nabla} f_{0i} + \frac{ZT_e}{T_{0i}} \frac{\boldsymbol{\nabla} n_{0i}}{n_{0i}} f_{0i} \right] + \frac{v_\parallel \left(\nabla_\parallel \boldsymbol{B}_1^\perp \right) \cdot \boldsymbol{v}_\perp}{B_0} \left(\frac{\partial f_{1i}}{\partial v_\parallel} \right)_v, \tag{C.32}$$

where I_2 is given by equation (C.20) (note that the second derivative of f_{1i} vanishes there; see equation (C.27)). Using again the fact that $\boldsymbol{v}_\perp = -\partial(\boldsymbol{b}_0 \times \boldsymbol{v}_\perp)/\partial\vartheta$, we integrate equation (C.32) and get

$$f_{3i} = -\frac{\boldsymbol{b}_0 \times \boldsymbol{v}_\perp}{\Omega_i} \cdot \left[\frac{2v_\parallel \nabla_\parallel \boldsymbol{u}_{1i}^\perp}{v_{\mathrm{th},i}^2} f_{0i} + \frac{v_\parallel \nabla_\parallel \boldsymbol{B}_1^\perp}{B_0} \left(\frac{\partial f_{1i}}{\partial v_\parallel} \right)_v + \left(\frac{v^2}{v_{\mathrm{th},i}^2} - \frac{5}{2} \right) \frac{\boldsymbol{\nabla} T_{0i}}{T_{0i}} f_{0i} \right]$$
$$+ \boldsymbol{v}_\perp \cdot \left[\frac{\boldsymbol{B}_2^\perp}{B_0} \left(\frac{\partial f_{1i}}{\partial v_\parallel} \right)_v + \frac{\boldsymbol{B}_1^\perp}{B_0} \left(\frac{\partial g_{2i}}{\partial v_\parallel} \right)_v \right] + g_{3i}(t, \boldsymbol{r}, v, v_\parallel), \tag{C.33}$$

where g_{3i} is the gyrotropic part of f_{3i} (so far arbitrary) and we have used equation (C.25) to simplify the terms that contain equilibrium gradients.

We will see in section C.0.20 that we do not need to know either g_{3i} or $\boldsymbol{B}_2$ in order to calculate the third-order ion pressure tensor $\mathbf{P}_{3i}$ and close the ion momentum equation (3.59) for the firehose perturbations. The only remaining quantity we do need is g_{2i} — we will now derive the equation for it by going to next order in the ϵ expansion.

C.0.16   Order ϵ^3

At this order, equation (C.1) is, upon substitution of the Maxwellian f_{0i}, gyrotropic f_{1i}, and equation (C.3) for the Lorentz force,

$$
\frac{\mathrm{d}f_{0i}}{\mathrm{d}t_{0i}} + \frac{\mathrm{d}f_{2i}}{\mathrm{d}t_{0i}} + \boldsymbol{v} \cdot \boldsymbol{\nabla} f_{1i} + v_\parallel \nabla_\parallel f_{3i} + \left(\frac{ZT_e}{T_{0i}} \frac{v_\parallel \nabla_\parallel n_{3i}}{n_{0i}} - \frac{2}{\beta_i} \frac{(\nabla_\parallel \boldsymbol{B}_1^\perp) \cdot \boldsymbol{v}_\perp}{B_0} \right) f_{0i}
$$

$$
- \Omega_i \frac{\partial f_{4i}}{\partial \vartheta} + \frac{Ze}{m_i} \underbrace{\left[\frac{\boldsymbol{v} \times \boldsymbol{B}_1^\perp}{c} \cdot \frac{\partial f_{3i}}{\partial \boldsymbol{v}} + \frac{\boldsymbol{v} \times \boldsymbol{B}_2}{c} \cdot \frac{\partial f_{2i}}{\partial \boldsymbol{v}} + \frac{\boldsymbol{v} \times \boldsymbol{B}_3}{c} \cdot \boldsymbol{b}_0 \left(\frac{\partial f_{1i}}{\partial v_\parallel} \right)_v \right]}_{I_3}
$$

$$
- \frac{ZT_e}{m_i} \frac{\boldsymbol{\nabla} n_{0i}}{n_{0i}} \cdot \left[\frac{\boldsymbol{v}}{v} \left(\frac{\partial f_{1i}}{\partial v} \right)_{v_\parallel} + \boldsymbol{b}_0 \left(\frac{\partial f_{1i}}{\partial v_\parallel} \right)_v \right] + \frac{2\boldsymbol{vv} : \boldsymbol{\nabla} (\boldsymbol{u}_{0i} + \boldsymbol{u}_{2i})}{v_{\mathrm{th},i}^2} f_{0i}
$$

$$
+ \frac{\mathrm{d}\boldsymbol{u}_{1i}^\perp}{\mathrm{d}t_{0i}} \cdot \frac{2\boldsymbol{v}_\perp}{v_{\mathrm{th},i}^2} f_{0i} - v_\parallel (\nabla_\parallel \boldsymbol{u}_{1i}^\perp) \cdot \frac{\boldsymbol{v}_\perp}{v} \left(\frac{\partial f_{1i}}{\partial v} \right)_{v_\parallel} = C[f_{2i}] + C[f_{1i}, f_{1i}],
$$

$$
\tag{C.34}
$$

where $\mathrm{d}/\mathrm{d}t_{0i} = \partial/\partial t + \boldsymbol{u}_{0i} \cdot \boldsymbol{\nabla}$ is the convective derivative (with respect to the large-scale flow). Note that $\boldsymbol{\nabla} f_{1i}$ in the above equation is with respect to slow spatial variation. Note also that the collision operator at this order has two parts: the linearised operator describing interaction of f_{2i} with the Maxwellian equilibrium f_{0i} and the nonlinear operator, denoted $C[f_{1i}, f_{1i}]$, describing interaction of f_{1i} with itself.

We will only ever need the gyroaverage of equation (C.34). Many terms then vanish or simplify. What happens is mostly straightforward: the gyroaverages of

$\partial/\partial\vartheta$ are zero, the gyroaverages of the velocities are done using the identities

$$\langle \boldsymbol{v} \rangle = v_{\parallel}\boldsymbol{b}_0, \quad \langle \boldsymbol{v}\boldsymbol{v} \rangle = \frac{v_{\perp}^2}{2}\left(\mathbf{I} - \boldsymbol{b}_0\boldsymbol{b}_0\right) + v_{\parallel}^2\boldsymbol{b}_0\boldsymbol{b}_0 \qquad (C.35)$$

(as before angle brackets denote $(1/2\pi)\int \mathrm{d}\vartheta$). There are a few terms that are perhaps not obvious and so require explanation.

The first is essentially a variation on equations (1.37) and (1.38). To recap; we showed above that f_{1i} is a function of v, $v_{\parallel}$, and $\boldsymbol{r}$. However, the spatial gradient here is still taken at constant $\boldsymbol{v}$. Since one of the new velocity variables $v_{\parallel} = \boldsymbol{v} \cdot \boldsymbol{b}_0$ is a function of $\boldsymbol{v}$ and $\boldsymbol{r}$, we have

$$\boldsymbol{v} \cdot \left(\boldsymbol{\nabla} f_{1i}\right)_{\boldsymbol{v}} = \boldsymbol{v} \cdot \left(\boldsymbol{\nabla} f_{1i}\right)_{v,v_{\parallel}} + \left(\boldsymbol{v}\boldsymbol{v} : \boldsymbol{\nabla}\boldsymbol{b}_0\right)\left(\frac{\partial f_{1i}}{\partial v_{\parallel}}\right)_v, \qquad (C.36)$$

and so

$$\left\langle \boldsymbol{v} \cdot \left(\boldsymbol{\nabla} f_{1i}\right)_{\boldsymbol{v}} \right\rangle = v_{\parallel}\boldsymbol{b}_0 \cdot \boldsymbol{\nabla} f_{1i} + \left(\boldsymbol{\nabla} \cdot \boldsymbol{b}_0\right)\frac{v_{\perp}^2}{2}\left(\frac{\partial f_{1i}}{\partial v_{\parallel}}\right)_v. \qquad (C.37)$$

In the final expression, $\boldsymbol{\nabla} f_{1i}$ is now understood to be at constant v and $v_{\parallel}$. Since $\boldsymbol{\nabla} \cdot \boldsymbol{b}_0 = -\left(\boldsymbol{b}_0 \cdot \boldsymbol{\nabla} B_0\right)/B_0$, the additional term that has emerged is readily interpreted as the mirror force associated with the large-scale variation of the magnetic field.

Now let us turn to the two terms in equation (C.34) denoted by I_3: the second of these terms gives

$$\left\langle \frac{Ze}{m_i}\frac{\boldsymbol{v} \times \boldsymbol{B}_2}{c} \cdot \frac{\partial f_{2i}}{\partial \boldsymbol{v}} \right\rangle = \left\langle \frac{Ze}{m_i}\frac{\boldsymbol{v} \times \boldsymbol{B}_2}{c} \cdot \left[\frac{\boldsymbol{B}_1^{\perp}}{B_0}\left(\frac{\partial f_{1i}}{\partial v_{\parallel}}\right)_v + \boldsymbol{b}_0\left(\frac{\partial g_{2i}}{\partial v_{\parallel}}\right)_v\right]\right\rangle \qquad (C.38)$$

$$= \Omega_i v_{\parallel}\left(\boldsymbol{b}_0 \times \frac{\boldsymbol{B}_2^{\perp}}{B_0}\right) \cdot \frac{\boldsymbol{B}_1^{\perp}}{B_0}\left(\frac{\partial f_{1i}}{\partial v_{\parallel}}\right)_v, \qquad (C.39)$$

where we have used equation (C.18) and the fact that $\left(\partial f_{1i}/\partial v_{\parallel}\right)_v$ only depends

on v (equation (C.27)); the first term, upon substitution of equation (C.33), gives

$$
\left\langle \frac{Ze}{m_i} \frac{\boldsymbol{v} \times \boldsymbol{B}_1^\perp}{c} \cdot \frac{\partial f_{3i}}{\partial \boldsymbol{v}} \right\rangle =
$$
$$
\left\langle \frac{Ze}{m_i} \frac{\boldsymbol{v} \times \boldsymbol{B}_1^\perp}{c} \cdot \left\{ \frac{\boldsymbol{B}_2^\perp}{B_0} \left(\frac{\partial f_{1i}}{\partial v_\parallel} \right)_v + \boldsymbol{b}_0 \, \boldsymbol{v}_\perp \cdot \frac{\boldsymbol{B}_1^\perp}{B_0} \left(\frac{\partial^2 g_{2i}}{\partial v_\parallel^2} \right)_v + \frac{\boldsymbol{b}_0}{\Omega_i} \times \right. \right.
$$
$$
\left[\frac{2 v_\parallel \nabla_\parallel \boldsymbol{u}_{1i}^\perp}{v_{\text{th},i}^2} f_{0i} + \frac{v_\parallel \nabla_\parallel \boldsymbol{B}_1^\perp}{B_0} \left(\frac{\partial f_{1i}}{\partial v_\parallel} \right)_v + \left(\frac{v^2}{v_{\text{th},i}^2} - \frac{5}{2} \right) \frac{\boldsymbol{\nabla} T_{0i}}{T_{0i}} f_{0i} \right]
$$
$$
\left. \left. - \boldsymbol{b}_0 \frac{\boldsymbol{b}_0 \times \boldsymbol{v}_\perp}{\Omega_i} \cdot \left[\frac{2 \nabla_\parallel \boldsymbol{u}_{1i}^\perp}{v_{\text{th},i}^2} f_{0i} + \frac{\nabla_\parallel \boldsymbol{B}_1^\perp}{B_0} \left(\frac{\partial f_{1i}}{\partial v_\parallel} \right)_v \right] + \boldsymbol{b}_0 \left(\frac{\partial g_{3i}}{\partial v_\parallel} \right)_v \right\} \right\rangle \quad \text{(C.40)}
$$

which becomes

$$
\left\langle \frac{Ze}{m_i} \frac{\boldsymbol{v} \times \boldsymbol{B}_1^\perp}{c} \cdot \frac{\partial f_{3i}}{\partial \boldsymbol{v}} \right\rangle =
$$
$$
\Omega_i v_\parallel \left(\boldsymbol{b}_0 \times \frac{\boldsymbol{B}_1^\perp}{B_0} \right) \cdot \frac{\boldsymbol{B}_2^\perp}{B_0} \left(\frac{\partial f_{1i}}{\partial v_\parallel} \right)_v + v_\parallel \left(\boldsymbol{b}_0 \times \frac{\boldsymbol{B}_1^\perp}{B_0} \right) \cdot \left\{ \boldsymbol{b}_0 \times \right.
$$
$$
\left. \left[\frac{2 v_\parallel \nabla_\parallel \boldsymbol{u}_{1i}^\perp}{v_{\text{th},i}^2} f_{0i} + \frac{v_\parallel \nabla_\parallel \boldsymbol{B}_1^\perp}{B_0} \left(\frac{\partial f_{1i}}{\partial v_\parallel} \right)_v + \left(\frac{v^2}{v_{\text{th},i}^2} - \frac{5}{2} \right) \frac{\boldsymbol{\nabla} T_{0i}}{T_{0i}} f_{0i} \right] \right\}
$$
$$
- \frac{\boldsymbol{B}_1^\perp}{B_0} \cdot \left\langle (\boldsymbol{b}_0 \times \boldsymbol{v}_\perp)(\boldsymbol{b}_0 \times \boldsymbol{v}_\perp) \right\rangle \cdot \left[\frac{2 \nabla_\parallel \boldsymbol{u}_{1i}^\perp}{v_{\text{th},i}^2} f_{0i} + \frac{\nabla_\parallel \boldsymbol{B}_1^\perp}{B_0} \left(\frac{\partial f_{1i}}{\partial v_\parallel} \right)_v \right]. \quad \text{(C.41)}
$$

The first term in equation (C.41) exactly cancels when equation (C.39) is added to it. Simplifying the double vector product in the second term and noticing that the gyroaverage in the third term is equal to $(v_\perp^2/2)\,(\mathsf{I} - \boldsymbol{b}_0 \boldsymbol{b}_0)$, we have

$$
\langle I_3 \rangle = \frac{\boldsymbol{B}_1^\perp}{B_0} \cdot \left\{ \left(v_\parallel^2 - \frac{v_\perp^2}{2} \right) \left[\frac{2 \nabla_\parallel \boldsymbol{u}_{1i}^\perp}{v_{\text{th},i}^2} f_{0i} + \frac{\nabla_\parallel \boldsymbol{B}_1^\perp}{B_0} \left(\frac{\partial f_{1i}}{\partial v_\parallel} \right)_v \right] \right.
$$
$$
\left. + v_\parallel \left(\frac{v^2}{v_{\text{th},i}^2} - \frac{5}{2} \right) \frac{\boldsymbol{\nabla} T_{0i}}{T_{0i}} f_{0i} \right\}
$$
$$
= \frac{2 v_\parallel^2 - v_\perp^2}{v_{\text{th},i}^2} \left[\frac{1}{2} \frac{\mathrm{d}}{\mathrm{d}t} \frac{|\boldsymbol{B}_1^\perp|^2}{B_0^2} f_{0i} + \frac{v_{\text{th},i}^2}{4} \frac{\nabla_\parallel |\boldsymbol{B}_1^\perp|^2}{B_0^2} \left(\frac{\partial f_{1i}}{\partial v_\parallel} \right)_v \right]
$$
$$
+ v_\parallel \left(\frac{v^2}{v_{\text{th},i}^2} - \frac{5}{2} \right) \frac{\boldsymbol{B}_1^\perp}{B_0} \cdot \frac{\boldsymbol{\nabla} T_{0i}}{T_{0i}} f_{0i}, \quad \text{(C.42)}
$$

where we have used the perturbed induction equation (3.51) to express $\nabla_\parallel \boldsymbol{u}_{1i}^\perp$ in terms of $\boldsymbol{B}_1^\perp$. Finally, the gyroaverage of equation (C.34) is

$$
\begin{aligned}
&\frac{\mathrm{d}f_{0i}}{\mathrm{d}t} + \frac{\partial g_{2i}}{\partial t} + v_\parallel \left(\boldsymbol{b}_0 \cdot \boldsymbol{\nabla} f_{1i} + \nabla_\parallel g_{3i} \right) + (\boldsymbol{\nabla} \cdot \boldsymbol{b}_0) \frac{v_\perp^2}{2} \left(\frac{\partial f_{1i}}{\partial v_\parallel} \right)_v + \frac{ZT_e}{T_{0i}} \frac{v_\parallel \nabla_\parallel n_{3i}}{n_{0i}} f_{0i} \\
&+ \langle I_3 \rangle + \left[\frac{2v_\parallel^2 - v_\perp^2}{v_{\mathrm{th},i}^2} \boldsymbol{b}_0 \boldsymbol{b}_0 : \boldsymbol{\nabla} (\boldsymbol{u}_{0i} + \boldsymbol{u}_{2i}) + \frac{v_\perp^2}{v_{\mathrm{th},i}^2} \boldsymbol{\nabla} \cdot (\boldsymbol{u}_{0i} + \boldsymbol{u}_{2i}) \right] f_{0i} \\
&- \frac{ZT_e}{m_i} \frac{\boldsymbol{b}_0 \cdot \boldsymbol{\nabla} n_{0i}}{n_{0i}} \left[\frac{v_\parallel}{v} \left(\frac{\partial f_{1i}}{\partial v} \right)_{v_\parallel} + \left(\frac{\partial f_{1i}}{\partial v_\parallel} \right)_v \right] = C[g_{2i}] + C[f_{1i}, f_{1i}], \quad \text{(C.43)}
\end{aligned}
$$

where $\langle I_3 \rangle$ is given by equation (C.42). Note that g_{2i} does not have fast spatial variation (equation (C.30)), so, to the order we are keeping, $\mathrm{d}g_{2i}/\mathrm{d}t = \partial g_{2i}/\partial t$. The next step is to average this equation over small scales: again many terms vanish (in particular, all terms where the fast-varying perturbed quantities enter linearly) and we get

$$
\begin{aligned}
&\frac{\mathrm{d}f_{0i}}{\mathrm{d}t} + \frac{\partial g_{2i}}{\partial t} + v_\parallel \boldsymbol{b}_0 \cdot \boldsymbol{\nabla} f_{1i} + (\boldsymbol{\nabla} \cdot \boldsymbol{b}_0) \frac{v_\perp^2}{2} \left(\frac{\partial f_{1i}}{\partial v_\parallel} \right)_v - \frac{ZT_e}{m_i} \frac{\boldsymbol{b}_0 \cdot \boldsymbol{\nabla} n_{0i}}{n_{0i}} \boldsymbol{b}_0 \cdot \frac{\partial f_{1i}}{\partial \boldsymbol{v}} \\
&+ \left[\frac{2v_\parallel^2 - v_\perp^2}{v_{\mathrm{th},i}^2} \left(\boldsymbol{b}_0 \boldsymbol{b}_0 : \boldsymbol{\nabla} \boldsymbol{u}_{0i} + \frac{1}{2} \frac{\partial}{\partial t} \overline{\frac{|\boldsymbol{B}_1^\perp|^2}{B_0^2}} \right) + \frac{v_\perp^2}{v_{\mathrm{th},i}^2} \boldsymbol{\nabla} \cdot \boldsymbol{u}_{0i} \right] f_{0i} \\
&\hspace{6cm} = C[g_{2i}] + C[f_{1i}, f_{1i}], \quad \text{(C.44)}
\end{aligned}
$$

where the overline denotes the small-scale average and the derivatives of f_{1i} have been written in a compact form that will prove useful momentarily. Remarkably, the contribution of the perturbations has survived in equation (C.44) in the form of a single quadratic term — in section C.0.18, we will see that it gives rise to precisely the nonlinear feedback on the pressure anisotropy that was anticipated qualitatively in section 3.2.3.

By averaging out the gyroangle- and small-scale-dependent parts of the third-order kinetic equation (C.34), we have eliminated f_{4i}, g_{3i}, $\boldsymbol{B}_2$, $\boldsymbol{B}_3$, and $\boldsymbol{u}_{2i}$, which are unknown and potentially very cumbersome to calculate. As we are about to see, in order to calculate the ion pressure tensor to the relevant orders, we do not, in fact, need to know any of these quantities, so we will neither have to revisit the unaveraged equations (C.34) or (C.43) or go to higher orders in the ϵ expansion

of equation (C.1). Equation (C.44) determines g_{2i}, which is all that we require to calculate $\mathbf{P}_{2i}$ (section C.0.18) and $\mathbf{P}_{3i}$ (section C.0.20). Knowing these tensors will then allow us to close the ion momentum equations describing the plasma motion at large (equation (3.62)) and small (equation (3.59)) scales.

C.0.17   Order ϵ^3 continued: transport equations

Since g_{2i} is gyrotropic, the tensor $\mathbf{P}_{2i}$ is diagonal:

$$\mathbf{P}_{2i} = p_{2i}^\perp (\mathbf{I} - \boldsymbol{b}_0\boldsymbol{b}_0) + p_{2i}^\| \boldsymbol{b}_0\boldsymbol{b}_0 = p_{2i}\mathbf{I} + (p_{2i}^\perp - p_{2i}^\|) \left(\frac{1}{3}\mathbf{I} - \boldsymbol{b}_0\boldsymbol{b}_0 \right), \qquad \text{(C.45)}$$

where the scalar pressures are

$$p_{2i}^\perp = \int \mathrm{d}^3\boldsymbol{v}\, \frac{m_i v_\perp^2}{2}\, g_{2i}, \quad p_{2i}^\| = \int \mathrm{d}^3\boldsymbol{v}\, m_i v_\|^2 g_{2i}, \quad p_{2i} = \frac{2}{3}\, p_{2i}^\perp + \frac{1}{3}\, p_{2i}^\|. \quad \text{(C.46)}$$

Then the ion momentum equation (3.62) becomes[1]

$$m_i n_{0i} \frac{\mathrm{d}\boldsymbol{u}_{0i}}{\mathrm{d}t} = -\boldsymbol{\nabla}\tilde{\Pi} + \boldsymbol{\nabla} \cdot \left[\boldsymbol{b}_0\boldsymbol{b}_0 \left(p_{2i}^\perp - p_{2i}^\| + \frac{B_0^2}{4\pi} \right) \right], \qquad \text{(C.47)}$$

where $\tilde{\Pi} = p_{2i} + (p_{2i}^\perp - p_{2i}^\|)/3 + B_0^2/8\pi$ and we have recovered the familiar momentum equation in the long-wavelength limit (equation (3.18)). Let us first explain how p_{2i} (or, equivalently, $\tilde{\Pi}$) is determined and then calculate the pressure anisotropy $p_{2i}^\perp - p_{2i}^\|$ (section C.0.18).

First, let us integrate equation (C.44) over velocities. Since $\int \mathrm{d}^3\boldsymbol{v}\, g_{2i} = 0$ and $\int \mathrm{d}^3\boldsymbol{v}\, v_\| f_{1i} = 0$, we get

$$\frac{\mathrm{d}n_{0i}}{\mathrm{d}t} = -n_{0i}\boldsymbol{\nabla} \cdot \boldsymbol{u}_{0i}, \qquad \text{(C.48)}$$

an unsurprising result (the continuity equation was already obtained in section 3.3.4; see equation (3.61)). Now multiply equation (C.44) by $m_i v^2/3$ and integrate

---

[1]Formally, this equation is the result of taking the velocity moment of the kinetic equation (C.1) at the order ϵ^4. We do not write explicitly equation (C.1) at this order because it is not needed for anything except the momentum equation, the form of which we already know.

over velocities:

$$\frac{\mathrm{d}p_{0i}}{\mathrm{d}t} + \frac{\partial p_{2i}}{\partial t} = -\frac{2}{3} \boldsymbol{\nabla} \cdot \left(\boldsymbol{b}_0 q_{1i}\right) - \frac{5}{3} p_{0i} \boldsymbol{\nabla} \cdot \boldsymbol{u}_{0i}, \tag{C.49}$$

where $p_{0i} = n_{0i} T_{0i}$ and the parallel collisional heat flux is, using equation (C.24),[2]

$$q_{1i} = \int \mathrm{d}^3 \boldsymbol{v} \, \frac{m_i v^2 v_\parallel}{2} f_{1i} = -\int \mathrm{d}^3 \boldsymbol{v} \, \frac{m_i v^2 v_\parallel^2}{2\nu_i} \left(\frac{v^2}{v_{\mathrm{th},i}^2} - \frac{5}{2}\right) f_{0i} \, \frac{\boldsymbol{b}_0 \cdot \boldsymbol{\nabla} T_{0i}}{T_{0i}}$$

$$= -\frac{5}{4} \, n_{0i} \, \frac{v_{\mathrm{th},i}^2}{\nu_i} \, \boldsymbol{b}_0 \cdot \boldsymbol{\nabla} T_{0i}. \tag{C.50}$$

The heat flux term in equation (C.49) arises from the third and fourth terms on the left-hand side of equation (C.44) (in the fourth term, write $v_\perp^2 = v^2 - v_\parallel^2$ and integrate by parts with respect to $v_\parallel$ at constant v).

Since formally all terms in equation (C.49) except the one involving p_{2i} have slow time dependence, we may assume that so does p_{2i} and, therefore, $\partial p_{2i}/\partial t$ can be dropped from this equation (this can be formalised via averaging over short timescales). Using now equations (C.48) and (C.50), we can rewrite equation (C.49) as an evolution equation for the equilibrium temperature:

$$n_{0i} \frac{\mathrm{d}T_{0i}}{\mathrm{d}t} = \boldsymbol{\nabla} \cdot (n_{0i} \kappa_i \boldsymbol{b}_0 \boldsymbol{b}_0 \cdot \boldsymbol{\nabla} T_{0i}) - \frac{2}{3} \, n_{0i} T_{0i} \boldsymbol{\nabla} \cdot \boldsymbol{u}_{0i}, \quad \kappa_i = \frac{5}{6} \frac{v_{\mathrm{th},i}^2}{\nu_i}, \tag{C.51}$$

where κ_i is the ion thermal conductivity. The first term on the right-hand side represents collisional heat transport, the second compressional heating.

Equations (C.48) and (C.51) evolve n_{0i} and T_{0i}. However, the equilibrium density and temperature can only change in such a way that pressure balance, equation (C.25), is maintained. This means that if we know the spatial distribution of T_{0i}, we also know that of n_{0i}, or vice versa. Compressive motions will develop to make the density and temperature distributions adjust to each other and preserve the pressure balance. These motions must be consistent with the momentum equation (C.47) and the isotropic pressure perturbation p_{2i} will adjust to make

---

[2]Since we used a very simplified collision operator in our calculation of f_{1i} in section C.0.13, the numerical prefactor in the expression for the heat flux should not be regarded as quantitatively correct. This is not a problem for our purposes. The same caveat applies to equation (C.54) and equation (C.64).

it so. Thus, if we provide the expression for the pressure anisotropy $p_{2i}^\perp - p_{2i}^\parallel$, the other 5 equilibrium quantities — $\boldsymbol{u}_{0i}$, n_{0i}, T_{0i}, p_{2i}, and $\boldsymbol{B}_0$ — are determined by the closed set of 5 equations:[3] momentum equation (C.47), continuity equation (C.48), heat conduction equation (C.51), pressure balance equation (C.25), and induction equation (3.60).

C.0.18   Order ϵ^3 continued: pressure anisotropy

In order to calculate the pressure anisotropy $p_{2i}^\perp - p_{2i}^\parallel$, we multiply equation (C.44) by $m_i(v_\perp^2 - 2v_\parallel^2)/2$ and integrate over velocities. All isotropic terms vanish, as does the term containing $\partial f_{1i}/\partial \boldsymbol{v}$, which generally cannot contribute to pressure (after integration by parts, it is zero because $\int \mathrm{d}^3\boldsymbol{v}\, \boldsymbol{v} f_{1i} = 0$). The result is

$$\frac{\partial}{\partial t}\left(p_{2i}^\perp - p_{2i}^\parallel\right) = 3p_{0i}\left(\boldsymbol{b}_0\boldsymbol{b}_0 : \boldsymbol{\nabla}\boldsymbol{u}_{0i} - \frac{1}{3}\boldsymbol{\nabla}\cdot\boldsymbol{u}_{0i} + \frac{1}{2}\frac{\partial}{\partial t}\frac{\overline{|\boldsymbol{B}_1^\perp|^2}}{B_0^2}\right)$$
$$- \boldsymbol{\nabla}\cdot\left[\boldsymbol{b}_0(q_{1i}^\perp - q_{1i}^\parallel)\right] - 3q_{1i}^\perp\boldsymbol{\nabla}\cdot\boldsymbol{b}_0 - 3\nu_i(p_{2i}^\perp - p_{2i}^\parallel), \quad \text{(C.52)}$$

where $q_{1i}^\perp$ and $q_{1i}^\parallel$ are parallel fluxes of perpendicular and parallel heat, respectively: using equation (C.24),

$$q_{1i}^\perp = \int \mathrm{d}^3\boldsymbol{v}\,\frac{m_i v_\perp^2 v_\parallel}{2}\,f_{1i} = -\frac{1}{2}\,n_{0i}\,\frac{v_{\mathrm{th},i}^2}{\nu_i}\,\boldsymbol{b}_0\cdot\boldsymbol{\nabla}T_{0i}, \qquad\qquad \text{(C.53)}$$

$$q_{1i}^\parallel = \int \mathrm{d}^3\boldsymbol{v}\,m_i v_\parallel^3\,f_{1i}, = -\frac{3}{2}\,n_{0i}\,\frac{v_{\mathrm{th},i}^2}{\nu_i}\,\boldsymbol{b}_0\cdot\boldsymbol{\nabla}T_{0i}, \qquad\qquad \text{(C.54)}$$

and we note that $q_{1i}^\perp + q_{1i}^\parallel/2 = q_{1i}$ (see equation (C.50)). To work out the collision term in equation (C.52), we have again resorted to brutal simplification by using the Lorentz operator (see equation (C.23)) and dropping the nonlinear collision term $C[f_{1i}, f_{1i}]$ in equation (C.44) (the consequences of retaining this term, which are mostly small and irrelevant for our purposes, have been explored by Catto &

---

[3]If, as discussed in section C.0.13, one takes the easy option and assumes $\boldsymbol{\nabla}T_{0i} = 0$ and $\boldsymbol{\nabla}n_{0i} = 0$, then no equations are needed for the constant density and temperature, while p_{2i} in equation (C.47) is determined by the incompressibility condition $\boldsymbol{\nabla}\cdot\boldsymbol{u}_{0i} = 0$ (which follows from equation (C.48) with $n_{0i} = \text{const}$).

Simakov 2004). The solution of equation (C.52) is

$$\Delta(t) \equiv \frac{p_{2i}^{\perp} - p_{2i}^{\parallel}}{p_{0i}} \tag{C.55}$$

$$= \Delta_0 + \frac{3}{2} \int_0^t \mathrm{d}t' e^{-3\nu_i(t-t')} \frac{\partial}{\partial t'} \overline{\frac{|\boldsymbol{B}_1^{\perp}(t')|^2}{B_0^2}}, \tag{C.56}$$

where Δ_0 is the part of the anisotropy due to the large-scale dynamics:

$$\Delta_0 = \frac{1}{\nu_i} \left\{ \boldsymbol{b}_0 \boldsymbol{b}_0 : \boldsymbol{\nabla} \boldsymbol{u}_{0i} - \frac{1}{3} \boldsymbol{\nabla} \cdot \boldsymbol{u}_{0i} - \frac{\boldsymbol{\nabla} \cdot \left[\boldsymbol{b}_0 (q_{1i}^{\perp} - q_{1i}^{\parallel}) \right] + 3q_{1i}^{\perp} \boldsymbol{\nabla} \cdot \boldsymbol{b}_0}{3p_{0i}} \right\} \tag{C.57}$$

and we have assumed $\Delta(0) = \Delta_0$. The first two terms in equation (C.57) are the well known collisional contributions to the pressure anisotropy calculated by Braginskii (1965). The heat-flux terms did not occur in Braginskii's calculation because they were small in his assumed sonic-flow ordering ($\boldsymbol{u}_{0i} \sim v_{\mathrm{th},i}$). They occur here because our ordering is subsonic ($\boldsymbol{u}_{0i} \sim \epsilon v_{\mathrm{th},i}$; see equation (3.43)) — that heat fluxes appear in the pressure tensor under such assumptions is also a known fact (Mikhailovskii & Tsypin, 1971, 1984; Catto & Simakov, 2004). The new, nonlinear part of the anisotropy is the second term in equation (C.56), which is due to the firehose fluctuations. This result was predicted on heuristic grounds in section 3.2.3.

Equation (C.56) completes the set of transport equations derived in section C.0.17, but we still need to calculate $\overline{|\boldsymbol{B}_1^{\perp}|^2}$. This is done via equations (3.51) and (3.59). The third-order pressure term in the latter equation will be calculated in section C.0.20.

C.0.19   CGL equations with nonlinear feedback

It is certainly useful to compare what we have found to the modified CGL equations found in chapter 1. They were the conceptual starting point for our work. Let us first recall that the induction equation (3.60) implies

$$\frac{1}{B_0} \frac{\mathrm{d}B_0}{\mathrm{d}t} = \boldsymbol{b}_0 \boldsymbol{b}_0 : \boldsymbol{\nabla} \boldsymbol{u}_{0i} - \boldsymbol{\nabla} \cdot \boldsymbol{u}_{0i}. \tag{C.58}$$

Using equation (C.48) for $\boldsymbol{\nabla} \cdot \boldsymbol{u}_{0i}$, we may, therefore, rewrite equation (C.52) as follows

$$
\begin{aligned}
\frac{\partial}{\partial t} \left(p_{2i}^\perp - p_{2i}^\| \right) = 3 p_{0i} &\left(\frac{1}{\overline{\overline{B}}} \frac{\mathrm{d}\overline{B}}{\mathrm{d}t} - \frac{2}{3} \frac{1}{n_{0i}} \frac{\mathrm{d}n_{0i}}{\mathrm{d}t} \right) \\
&- \boldsymbol{\nabla} \cdot \left[\boldsymbol{b}_0 (q_{1i}^\perp - q_{1i}^\|) \right] - 3 q_{1i}^\perp \boldsymbol{\nabla} \cdot \boldsymbol{b}_0 - 3 \nu_i (p_{2i}^\perp - p_{2i}^\|), \quad \text{(C.59)}
\end{aligned}
$$

where $\overline{B}$ includes both the large-scale magnetic field B_0 and the averaged firehose fluctuations (see equation (3.24)). This is the same as equation (1.44). Equivalently, we can combine equations (C.49) and (C.59), we get

$$
\frac{\mathrm{d}}{\mathrm{d}t} \ln \frac{p_i^\perp}{n_{0i}\overline{B}} = -\frac{\boldsymbol{\nabla} \cdot \left(\boldsymbol{b}_0 q_{1i}^\perp \right) + q_{1i}^\perp \boldsymbol{\nabla} \cdot \boldsymbol{b}_0}{p_{0i}} - \nu_i \frac{p_i^\perp - p_i^\|}{p_{0i}}, \qquad \text{(C.60)}
$$

$$
\frac{\mathrm{d}}{\mathrm{d}t} \ln \frac{p_i^\| \overline{B}^2}{n_{0i}^3} = -\frac{\boldsymbol{\nabla} \cdot \left(\boldsymbol{b}_0 q_{1i}^\| \right) - 2 q_{1i}^\perp \boldsymbol{\nabla} \cdot \boldsymbol{b}_0}{p_{0i}} - 2\nu_i \frac{p_i^\| - p_i^\perp}{p_{0i}}. \qquad \text{(C.61)}
$$

These are equations (1.39) and (1.40), the original equations of Chew *et al.* (1956) (without neglecting the heat fluxes or collisions). They are also the equations that form the basis for recent numerical studies by Sharma *et al.* (2006, 2007) of the effects of pressure anisotropies as related to the MRI. We have derived, from first-principles, the equations we started with chapter 1. We might have guessed these would emerge exactly, but this had to be demonstrated rather than assumed.

As pointed out in Sharma *et al.* (2006), equation (C.60) can be rewritten in a form that makes explicit the conservation of the first adiabatic invariant (including by the heat-flux terms):

$$
\frac{\partial}{\partial t} \frac{p_i^\perp}{\overline{B}} + \boldsymbol{\nabla} \cdot \left(\frac{p_i^\perp}{\overline{B}} \boldsymbol{u}_{0i} + \boldsymbol{b}_0 \frac{q_{1i}^\perp}{\overline{B}} \right) = -\nu_i \frac{p_i^\perp - p_i^\|}{p_{0i}}. \qquad \text{(C.62)}
$$

The nonlinear feedback in equations (C.60)-(C.61) is provided by the small-scale magnetic fluctuations in $\overline{B}$. Sharma *et al.* (2006, 2007) do not have the small-scale fluctuations and model their effect by introducing strong effective damping terms in equations (C.60)-(C.61) that limit the pressure anisotropies to the marginal state of the plasma instabilities. The calculation carried out here attempts to derive this feedback from first principles.

C.0.20   Pressure tensor for the firehose turbulence

In order to close the small-scale momentum equation (3.59), we must calculate the divergence of the third-order ion-pressure tensor or, more precisely, the perpendicular part thereof: since the fast spatial variation is only in the parallel direction, we have, from equation (C.33)

$$
\begin{aligned}
(\boldsymbol{\nabla} \cdot \mathbf{P}_{3i})_\perp &= \nabla_\parallel \int \mathrm{d}^3\boldsymbol{v}\, m_i v_\parallel \boldsymbol{v}_\perp f_{3i} \\
&= \nabla_\parallel \int \mathrm{d}^3\boldsymbol{v}\, \frac{m_i v_\perp^2}{2} \left\{ v_\parallel \left(\frac{\partial g_{2i}}{\partial v_\parallel} \right)_v \frac{\boldsymbol{B}_1^\perp}{B_0} \right. \\
&\quad \left. + v_\parallel^2 \frac{\boldsymbol{b}_0}{\Omega_i} \times \left[\frac{2\nabla_\parallel \boldsymbol{u}_{1i}^\perp}{v_{\mathrm{th},i}^2} f_{0i} + \frac{\nabla_\parallel \boldsymbol{B}_1^\perp}{B_0} \left(\frac{\partial f_{1i}}{\partial v_\parallel} \right)_v \right] \right\} \\
&= -\nabla_\parallel \left\{ (p_{2i}^\perp - p_{2i}^\parallel) \frac{\boldsymbol{B}_1^\perp}{B_0} \right. \\
&\quad \left. + \frac{1}{\Omega_i} \left[p_{0i} \nabla_\parallel \boldsymbol{u}_{1i}^\perp - (2q_{1i}^\perp - q_{1i}^\parallel) \frac{\nabla_\parallel \boldsymbol{B}_1^\perp}{B_0} \right] \times \boldsymbol{b}_0 \right\}, \quad (C.63)
\end{aligned}
$$

where the last formula was obtained via integration by parts with respect to $v_\parallel$ (at constant v). Note that the terms in equation (C.33) containing $\boldsymbol{B}_2$ and g_{3i} do not contribute, so, as announced at the end of section C.0.16, we do not need to compute these quantities. The pressure anisotropy $p_{2i}^\perp - p_{2i}^\parallel$ is given by equation (C.56) and the heat fluxes $q_{1i}^\perp$ and $q_{1i}^\parallel$ by equation (C.54), whence[4]

$$
\Gamma_T \equiv \frac{2q_{1i}^\perp - q_{1i}^\parallel}{p_{0i} v_{\mathrm{th},i}} = \frac{1}{2} \frac{v_{\mathrm{th},i}}{\nu_i} \frac{\boldsymbol{b}_0 \cdot \boldsymbol{\nabla} T_{0i}}{T_{0i}}. \tag{C.64}
$$

The second term in equation (C.63) is recognizable as the collision-independent "gyroviscosity" (Braginskii, 1965) and the third term as the collisional heat-flux contribution to it that arises for subsonic flows (Mikhailovskii & Tsypin, 1971, 1984; Catto & Simakov, 2004). It is the gyroviscous term that will limit the range of wavenumbers susceptible to the firehose instability (see section 3.4.2), while the heat-flux term will lead to substantial modifications of the firehose turbulence

---

[4]As explained in footnote 2, the numerical prefactor here should not be taken literally because we have used a very simplified collision operator. The correct prefactors can be found, e.g., in Catto & Simakov (2004).

and even give rise to an additional source of unstable behaviour (the gyrothermal instability; see section 3.5).

Appendix D

Commonly used symbols

Throughout a subscript $s = i, e$ denotes ions or electrons (except for c_s as stated below). A numbered subscript or parenthetical superscript usually denotes a term an asymptotic series, e.g. f_2. However, in chapter 2, a subscript is the order (or branch index) of the mode. A linearly perturbed quantity is prefaced by the symbol δ and an equilibrium quantity is usually subscripted with a "0". In other contexts δ is also a small expansion parameter. The symbols $\parallel$ and $\perp$ denote the "orientation" of the associated quantity with respect to the magnetic field and an over-line denotes a spatial average e.g. $\overline{B}$ (in chapter 3 it is an average over scales less than λ_{mfp}).

Vectors & Tensors	Expression
$\boldsymbol{a}$	Particle force (see equation (1.2))
$\boldsymbol{b}$	Magnetic field unit vector
$\boldsymbol{B}$	Magnetic field (in chapter 2 it is also the Alfvén speed)
$\boldsymbol{E}$	Electric field
$\boldsymbol{j}$	Current
$\boldsymbol{q}_{\parallel}, \boldsymbol{q}_{\perp}$	Heat flux (parallel, perpendicular)
$\boldsymbol{u}$	Fluid velocity
$\mathbf{P}$	Pressure tensor
$\mathbf{D}$	Deviatoric stress tensor
$\mathbf{I}$	Identity
$\mathbf{G}$	Gyrophase dependent component of the pressure tensor

Roman symbols	Expression
c_s	Sound speed (subscript indicates "sound" not species)
f_s	Number density distribution function
k	wavenumber
K	Modified Bessel function (second kind)
$\mathcal{M}$	Mach number
m_s	Mass
n_s	Number density
n	Mode index (chapter 2 only)
$v_{\mathrm{th},s}$	Thermal speed
v_A	Alfvén speed
$p, p_{\parallel}, p_{\perp}$	Isotropic pressure (total, parallel, perpendicular)
r	Radius (cylindrical polar coordinates)
Re	Reynolds number
S_B	Measure of Braginskii viscosity (see equation (2.17))
t	Time
T	Temperature
$v, v_{\parallel}, v_{\perp}$	Particle velocity variable (total, parallel, perpendicular)
v_n	Order of the modified Bessel function (second kind)
w	Argument coefficient of the modified Bessel function (second kind)
z	Vertical direction (in chapter 3 it is aligned with $\boldsymbol{b}$)

Greek symbols	Expression
Ω_s	Cyclotron frequency
$\hat{\Omega}$	Galactic rotation frequency
β	Plasma beta
Δ	Pressure anisotropy (without a subscript read ions)
γ	Growth rate (general field)
Γ_T	Magnitude of the parallel heat flux
λ_{mfp}	Inter-particle mean free path
μ_{B}	Coefficient of the Braginskii viscosity
ν_s	Collision frequency
ω	Frequency (general field)
σ	Alfvén frequency
ϕ	Azimuthal angle (cylindrical polar coordinates)
ρ_s	Larmor radius
θ	Pitch angle: $\arctan(B_z/B_\phi)$
ϑ	Gyrophase angle

Bibliography

Abel, IG, Barnes, M., Cowley, SC, Dorland, W. & Schekochihin, AA 2008 Linearized model fokker–planck collision operators for gyrokinetic simulations. i. theory. *Physics of Plasmas* **15**, 122509.

Abramowitz, Milton & Stegun, Irene A. 1964 *Handbook of Mathematical Functions*, ninth dover printing, tenth gpo printing edn. New York: Dover.

Bahcall, N.A. 2000 Clusters and cosmology. *Physics Reports* **333**, 233–244.

Balbus, S. A. 2000 Stability, Instability, and "Backward" Transport in Stratified Fluids. *ApJ* **534**, 420–427.

Balbus, S. A. 2001 Convective and Rotational Stability of a Dilute Plasma. *ApJ* **562**, 909–917.

Balbus, S. A. 2003 Enhanced Angular Momentum Transport in Accretion Disks. *ARA&A* **41**, 555–597.

Balbus, S. A. 2004 Viscous Shear Instability in Weakly Magnetized, Dilute Plasmas. *ApJ* **616**, 857–864.

Balbus, S. A. & Hawley, J. F. 1991 A powerful local shear instability in weakly magnetized disks. I - Linear analysis. II - Nonlinear evolution. *ApJ* **376**, 214–233.

Balbus, S. A. & Hawley, J. F. 1992 Is the Oort A-value a universal growth rate limit for accretion disk shear instabilities? *ApJ* **392**, 662–666.

Balbus, S. A. & Hawley, J. F. 1998 Instability, turbulence, and enhanced transport in accretion disks. *Reviews of Modern Physics* **70**, 1–53.

Balbus, S. A. & Reynolds, C. S. 2008 Regulation of Thermal Conductivity in Hot Galaxy Clusters by MHD Turbulence. *ApJ Letters* **681**, L65–L68.

Balbus, S. A. & Terquem, C. 2001 Linear Analysis of the Hall Effect in Protostellar Disks. *ApJ* **552**, 235–247.

Bale, SD, Kasper, JC, Howes, GG, Quataert, E., Salem, C. & Sundkvist, D. 2009 Magnetic fluctuation power near proton temperature anisotropy instability thresholds in the solar wind. *Physical review letters* **103** (21), 211101.

Beck, R., Brandenburg, A., Moss, D., Shukurov, A. & Sokoloff, D. 1996 Galactic Magnetism: Recent Developments and Perspectives. *ARA&A* **34**, 155–206.

Binney, J. & Tremaine, S. 1988 *Galactic dynamics*. Princeton Univ Pr.

Blaes, O. M. & Balbus, S. A. 1994 Local shear instabilities in weakly ionized, weakly magnetized disks. *ApJ* **421**, 163–177.

Bogdanović, T., Reynolds, C. S., Balbus, S. A. & Parrish, I. J. 2009 Simulations of Magnetohydrodynamics Instabilities in Intracluster Medium Including Anisotropic Thermal Conduction. *ApJ* **704**, 211–225.

Boltzmann, L. 1872 Transport Processes in a Plasma. *Sitsungsber. Akad. Wiss. Wien* **66**, 275.

Braginskii, S. I. 1965 Transport Processes in a Plasma. *Reviews of Plasma Physics* **1**, 205.

Brandenburg, A. & Nordlund, A. 2009 Astrophysical turbulence. *ArXiv e-prints* .

Brandenburg, A. & Subramanian, K. 2005 Astrophysical magnetic fields and nonlinear dynamo theory. *Phys. Rep.* **417**, 1–209.

Brush, S.G. 1976 *The Kind of Motion We Call Heat: Statistical physics and irreversible processes*. North-Holland Pub. Co.

CARILLI, CL & TAYLOR, GB 2002 Cluster magnetic fields. *Annual Review of Astronomy and Astrophysics* **40** (1), 319–348.

CATTO, P. J. & SIMAKOV, A. N. 2004 A drift ordered short mean free path description for magnetized plasma allowing strong spatial anisotropy. *Physics of Plasmas* **11**, 90–102.

CHANDRAN, B. D. G. & COWLEY, S. C. 1998 Thermal Conduction in a Tangled Magnetic Field. *Physical Review Letters* **80**, 3077–3080.

CHANDRASEKHAR, S. 1960 The Stability of Non-Dissipative Couette Flow in Hydromagnetics. *Proceedings of the National Academy of Science* **46**, 253–257.

CHANDRASEKHAR, S. 1961 *Hydrodynamic and hydromagnetic stability*. Clarendon Press, Oxford.

CHANDRASEKHAR, S., KAUFMAN, AN & WATSON, KM 1958 The stability of the pinch. *Proceedings of the Royal Society of London. Series A, Mathematical and Physical Sciences* pp. 435–455.

CHAPMAN, S. & COWLING, T. G. 1970 *The mathematical theory of non-uniform gases*.

CHEW, G. F., GOLDBERGER, M. L. & LOW, F. E. 1956 The Boltzmann Equation and the One-Fluid Hydromagnetic Equations in the Absence of Particle Collisions. *Royal Society of London Proceedings Series A* **236**, 112–118.

CHURAZOV, E., FORMAN, W., JONES, C. & SUNYAEV, R. 2004 B öringer h., 2004. *MNRAS* **347**, 29.

COCHRAN, J. A 1965 The Zeros of Hankel Functions as Functions of Their Order. *Numerische Mathematik* **7**, 238–250.

COPPINS, M. 1988 Ideal magnetohydrodynamic linear instabilities in the Z-pinch. *Plasma Physics and Controlled Fusion* **30**, 201–216.

CURRY, C. & PUDRITZ, R. E. 1995 On the Global Stability of Magnetized Accretion Disks. II. Vertical and Azimuthal Magnetic Fields. *ApJ* **453**, 697.

Curry, C., Pudritz, R. E. & Sutherland, P. G. 1994 On the global stability of magnetized accretion disks. 1: Axisymmetric modes. *ApJ* **434**, 206–220.

David, LP, Nulsen, PEJ, McNamara, BR, Forman, W., Jones, C., Ponman, T., Robertson, B. & Wise, M. 2001 A high-resolution study of the hydra a cluster with chandra. *The Astrophysical Journal* **557**, 546.

Davidson, R.C. & Völk, H.J. 1968 Macroscopic quasilinear theory of the garden-hose instability. *Physics of Fluids* **11**, 2259.

Dellar 2010 Image credit paul dellar. http://people.maths.ox.ac.uk/dellar/.

Dennis, T.J. & Chandran, B.D.G. 2005 Turbulent heating of galaxy-cluster plasmas. *The Astrophysical Journal* **622**, 205.

Devlen, E. & Pekünlü, E. R. 2010 Finite Larmor radius effects on weakly magnetized, dilute plasmas. *MNRAS* **404**, 830–836.

Dubrulle, B. & Knobloch, E. 1993 On instabilities in magnetized accretion disks. *A&A* **274**, 667.

Dudson, B. D., Ben Ayed, N., Kirk, A., Wilson, H. R., Counsell, G., Xu, X., Umansky, M., Snyder, P. B., LLoyd, B. & the MAST team 2008 Experiments and simulation of edge turbulence and filaments in MAST. *Plasma Physics and Controlled Fusion* **50** (12), 124012.

Dziourkevitch, N., Elstner, D. & Rüdiger, G. 2004 Interstellar turbulence driven by the magnetorotational instability. *A&A* **423**, L29–L32.

Ensslin, T. & Vogt, C. 2006 Magnetic turbulence in cool cores of galaxy clusters. *A&A* **453**, 447.

Fabian, AC, Reynolds, CS, Taylor, GB & Dunn, RJH 2005 On viscosity, conduction and sound waves in the intracluster medium. *Monthly Notices of the Royal Astronomical Society* **363** (3), 891–896.

FABIAN, AC, SANDERS, JS, ALLEN, SW, CRAWFORD, CS, IWASAWA, K., JOHNSTONE, RM, SCHMIDT, RW & TAYLOR, GB 2003*a* A deep chandra observation of the perseus cluster: shocks and ripples. *Monthly Notices of the Royal Astronomical Society* **344** (3), L43–L47.

FABIAN, AC, SANDERS, JS, CRAWFORD, CS, CONSELICE, CJ, GALLAGHER III, JS & WYSE, RFG 2003*b* The relationship between the optical hα filaments and the x-ray emission in the core of the perseus cluster. *Monthly Notices of the Royal Astronomical Society* **344** (3), L48–L52.

FABIAN, AC, SANDERS, J.S., TAYLOR, GB, ALLEN, SW, CRAWFORD, CS, JOHNSTONE, RM & IWASAWA, K. 2006 A very deep chandra observation of the perseus cluster: shocks, ripples and conduction. *Monthly Notices of the Royal Astronomical Society* **366** (2), 417–428.

FABIAN, A. C. 1994 Cooling Flows in Clusters of Galaxies. *ARA&A* **32**, 277–318.

FERRARO, N. M. 2007 Finite Larmor Radius Effects on the Magnetorotational Instability. *ApJ* **662**, 512–516.

FERREIRA, E. M & SESMA, J. 1970 Zeros of the Modified Hankel Function. *Numer. Math* **16**, 278–284.

FERREIRA, E. M. & SESMA, J. 2008 Zeros of the Macdonald function of complex order. *Journal of Computational and Applied Mathematics* **211**, 223–231.

FERRIÈRE, K. M. 2001 The interstellar environment of our galaxy. *Reviews of Modern Physics* **73**, 1031–1066.

FURUKAWA, M., YOSHIDA, Z., HIROTA, M. & KRISHAN, V. 2007 Irregular Singularity of the Magnetorotational Instability in a Keplerian Disk. *ApJ* **659**, 1496–1504.

GAMMIE, C. F. & BALBUS, S. A. 1994 Quasi-Global Linear Analysis of a Magnetized Disc. *MNRAS* **270**, 138.

GARY, S.P. & FELDMAN, WC 1978 A second-order theory for k b electromagnetic instabilities. *Physics of Fluids* **21**, 72.

GARY, S.P., LI, H., OŔOURKE, S. & WINSKE, D. 1998 Proton resonant firehose instability: Temperature anisotropy and fluctuating field constraints. *Journal of Geophysical Research* **103** (A7), 14567.

GARY, S.P., SKOUG, R.M., STEINBERG, J.T. & SMITH, C.W. 2001 Proton temperature anisotropy constraint in the solar wind: Ace observations. *Geophysical Research Letters* **28** (14), 2759–2762.

GOLDREICH, P. & LYNDEN-BELL, D. 1965 I. Gravitational stability of uniformly rotating disks. *MNRAS* **130**, 97.

GOODMAN, J. & XU, G. 1994 Parasitic instabilities in magnetized, differentially rotating disks. *The Astrophysical Journal* **432**, 213–223.

GOVONI, F. 2006 Observations of magnetic fields in regular and irregular clusters. *Astronomische Nachrichten* **327** (5-6), 539–544.

GUAN, X., GAMMIE, C.F., SIMON, J.B. & JOHNSON, B.M. 2009 Locality of mhd turbulence in isothermal disks. *The Astrophysical Journal* **694**, 1010.

GURNETT, D.A. & BHATTACHARJEE, A. 2005 *Introduction to plasma physics: with space and laboratory applications*. Cambridge Univ Pr.

HALL, AN 1981 The firehose instability in interstellar space. *Monthly Notices of the Royal Astronomical Society* **195**, 685–696.

HALL, AN & SCIAMA, DW 1979 The angular broadening of compact radio sources observed through ionized gas in a rich cluster of galaxies. *Astrophysical Journal* **228**, L15–L18.

HASEGAWA, A. 1969 Drift mirror instability in the magnetosphere. *Physics of Fluids* **12**, 2642.

HAZELTINE, RD & MEISS, JD 2003 *Plasma confinement*. Dover Pubns.

HELANDER, P. & SIGMAR, D. J. 2002 *Collisional transport in magnetized plasmas*.

HELLINGER, P. 2007 Comment on the linear mirror instability near the threshold. *Physics of plasmas* **14** (8), 82105–82105.

HELLINGER, P. & MATSUMOTO, H. 2000 New kinetic instability: Oblique alfvén fire hose. *Journal of geophysical research* **105**, 10.

HELLINGER, P. & MATSUMOTO, H. 2001 Nonlinear competition between the whistler and alfvén fire hoses. *Journal of Geophysical Research* **106**, 13215–13218.

HORTON, W., XU, BY & WONG, HV 2004a Firehose driven magnetic fluctuations in the magnetosphere (doi 10.1029/2003gl018309). *GEOPHYSICAL RESEARCH LETTERS* **31** (6), 6807–6807.

HORTON, W., XU, BY, WONG, HV & VAN DAM, JW 2004b Nonlinear dynamics of the firehose instability in a magnetic dipole geotail (doi 10.1029/2003ja010288). *JOURNAL OF GEOPHYSICAL RESEARCH-ALL SERIES-* **109** (1), 9216–9216.

HOWES, G. G., COWLEY, S. C., DORLAND, W., HAMMETT, G. W., QUATAERT, E. & SCHEKOCHIHIN, A. A. 2006 Astrophysical Gyrokinetics: Basic Equations and Linear Theory. *ApJ* **651**, 590–614.

ISLAM, T. & BALBUS, S. 2005 Dynamics of the Magnetoviscous Instability. *ApJ* **633**, 328–333.

KASPER, J.C., LAZARUS, A.J. & GARY, S.P. 2002 Wind/swe observations of firehose constraint on solar wind proton temperature anisotropy. *Geophysical Research Letters* **29** (17), 20–1.

KENNEL, CF & SAGDEEV, RZ 1967 Collisionless shock waves in high beta plasma 1 and 2. *J Geophys Res* **72**, 3303–3326.

KERSALÉ, E., HUGHES, D. W., OGILVIE, G. I., TOBIAS, S. M. & WEISS, N. O. 2004 Global Magnetorotational Instability with Inflow. I. Linear Theory and the Role of Boundary Conditions. *ApJ* **602**, 892–903.

KIM, W.-T., OSTRIKER, E. C. & STONE, J. M. 2003 Magnetorotationally Driven Galactic Turbulence and the Formation of Giant Molecular Clouds. *ApJ* **599**, 1157–1172.

KIRK, A., WILSON, H. R., AKERS, R., CONWAY, N. J., COUNSELL, G. F., COWLEY, S. C., DOWLING, J., DUDSON, B., FIELD, A., LOTT, F., LLOYD, B., MARTIN, R., MEYER, H., PRICE, M., TAYLOR, D., WALSH, M. & THE MAST TEAM 2005 Structure of ELMs in MAST and the implications for energy deposition. *Plasma Physics and Controlled Fusion* **47**, 315–333.

KITCHATINOV, L. L. & RÜDIGER, G. 2004 Seed fields for galactic dynamos by the magnetorotational instability. *A&A* **424**, 565–570.

KNOBLOCH, E. 1992 On the stability of magnetized accretion discs. *MNRAS* **255**, 25P–28P.

KULSRUD, R.M. 1962 *Rendiconti della Scuola Internatzionale di Fiscia "Enrico FermI", Course XXV*. Academic Press, New York.

KULSRUD, R. M. 1983 MHD description of plasma. In *Basic Plasma Physics: Selected Chapters, Handbook of Plasma Physics, Volume 1* (ed. A. A. Galeev & R. N. Sudan), p. 1.

KULSRUD, R. M. 1999 A Critical Review of Galactic Dynamos. *ARA&A* **37**, 37–64.

KULSRUD, R. M. 2005 *Plasma physics for astrophysics*. Princeton University Press, N.J.

KUNZ, MW, SCHEKOCHIHIN, AA, COWLEY, SC, BINNEY, JJ & SANDERS, JS 2010 A thermally stable heating mechanism for the intracluster medium: turbulence, magnetic fields and plasma instabilities. *Arxiv preprint arXiv:1003.2719* .

KUNZ, M. W. & BALBUS, S. A. 2004 Ambipolar diffusion in the magnetorotational instability. *MNRAS* **348**, 355–360.

LAGANA, T.F., ANDRADE-SANTOS, F. & NETO, G.B.L. 2009 Spiral-like structure in nearby clusters of galaxies. *Arxiv preprint arXiv:0911.3785* .

LIFSHITZ, EM, LANDAU, LD & PITAEVSKII, LP 1984 *Electrodynamics of continuous media*. Pergamon Press.

LYUTIKOV, M. 2007 Dissipation in Intercluster Plasma. *ApJ Letters* **668**, L1–L4.

MAHAJAN, S. M. & KRISHAN, V. 2008 Existence of the Magnetorotational Instability. *ApJ* **682**, 602–607.

MALYSHKIN, L. M. & KULSRUD, R. M. 2002 Magnetized Turbulent Dynamo in Protogalaxies. In *Bulletin of the American Astronomical Society*, , vol. 34, p. 1194.

MARKEVITCH, M., MAZZOTTA, P., VIKHLININ, A., BURKE, D., BUTT, Y., DAVID, L., DONNELLY, H., FORMAN, WR, HARRIS, D., KIM, D.W. *et al.* 2003 Chandra temperature map of a754 and constraints on thermal conduction. *The Astrophysical Journal Letters* **586**, L19.

MARKEVITCH, M. & VIKHLININ, A. 2007 Shocks and cold fronts in galaxy clusters. *Physics Reports* **443** (1), 1–53.

MATTEINI, L., LANDI, S., HELLINGER, P., PANTELLINI, F., MAKSIMOVIC, M., VELLI, M., GOLDSTEIN, B.E. & MARSCH, E. 2007 Evolution of the solar wind proton temperature anisotropy from 0.3 to 2.5 au. *Geophysical Research Letters* **34** (20), L20105.

MATTEINI, L., LANDI, S., HELLINGER, P. & VELLI, M. 2006 Parallel proton fire hose instability in the expanding solar wind: Hybrid simulations (doi 10.1029/2006ja011667). *JOURNAL OF GEOPHYSICAL RESEARCH-ALL SERIES-* **111** (A10), 10101.

MESTEL, L. 1963 On the galactic law of rotation. *MNRAS* **126**, 553.

MICHAEL, D. H. 1954 The stability of an incompressible electrically conducting fluid rotating about an axis when current flows parallel to the axis. *Mathematika* **1**, 45–50.

MIKHAILOVSKII, A. B., LOMINADZE, J. G., CHURIKOV, A. P., EROKHIN, N. N., PUSTOVITOV, V. D. & KONOVALOV, S. V. 2008 Axisymmetric magnetorotational instability in ideal and viscous laboratory plasmas. *Plasma Physics Reports* **34**, 837–846.

MIKHAILOVSKII, A. B. & TSYPIN, V. S. 1971 Transport equations and gradient instabilities in a high pressure collisional plasma. *Plasma Physics* **13**, 785–798.

MIKHAILOVSKII, A. B. & TSYPIN, V. S. 1984 Plasma drift equilibrium (gyration) in toroidal systems with complex magnetic-field geometry. *Tech. Rep.*.

MILLION, E.T. & ALLEN, S.W. 2009 *MNRAS* **399** (1307).

MOFFATT, HK 1978 *Field Generation in Electrically Conducting Fluids*. Cambridge University Press, Cambridge, London, New York, Melbourne.

NARAYAN, R. & MEDVEDEV, M.V. 2001 Thermal conduction in clusters of galaxies. *The Astrophysical Journal Letters* **562**, L129.

OGILVIE, G. I. 1998 Waves and instabilities in a differentially rotating disc containing a poloidal magnetic field. *MNRAS* **297**, 291–314.

OGILVIE, G. I. & PRINGLE, J. E. 1996 The non-axisymmetric instability of a cylindrical shear flow containing an azimuthal magnetic field. *MNRAS* **279**, 152–164.

PARKER, EN 1958 Dynamical instability in an anisotropic ionized gas of low density. *Physical Review* **109** (6), 1874–1876.

PARRISH, I.J. & QUATAERT, E. 2008 Nonlinear simulations of the heat-flux-driven buoyancy instability and its implications for galaxy clusters. *The Astrophysical Journal Letters* **677**, L9.

PARRISH, I.J., QUATAERT, E. & SHARMA, P. 2010 Turbulence in galaxy cluster cores: a key to cluster bimodality? *The Astrophysical Journal Letters* **712**, L194.

PARRISH, I. J., STONE, J. M. & LEMASTER, N. 2008 The Magnetothermal Instability in the Intracluster Medium. *ApJ* **688**, 905–917.

Pessah, M. E. & Chan, C.-k. 2008 Viscous, Resistive Magnetorotational Modes. *ApJ* **684**, 498–514.

Peterson, J.R. & Fabian, AC 2006 X-ray spectroscopy of cooling clusters. *Physics Reports* **427** (1), 1–39.

Peterson, J. R. & Fabian, A. C. 2006 X-ray spectroscopy of cooling clusters. *Phys. Rep.* **427**, 1–39.

Piffaretti, R., Jetzer, P., Kaastra, JS & Tamura, T. 2005 Temperature and entropy profiles of nearby cooling flow clusters observed with xmm-newton. *A&A* **433**, 101–111.

Pino, J. & Mahajan, S. M. 2008 Global Axisymmetric Magnetorotational Instability with Density Gradients. *ApJ* **678**, 1223–1229.

Piontek, R. A. & Ostriker, E. C. 2005 Saturated-State Turbulence and Structure from Thermal and Magnetorotational Instability in the ISM: Three-dimensional Numerical Simulations. *ApJ* **629**, 849–864.

Piontek, R. A. & Ostriker, E. C. 2007 ISM turbulence driven by the magnetorotational instability. In *IAU Symposium* (ed. B. G. Elmegreen & J. Palous), *IAU Symposium*, vol. 237, pp. 65–69.

Quataert, E. 2008 Buoyancy Instabilities in Weakly Magnetized Low-Collisionality Plasmas. *ApJ* **673**, 758–762.

Quataert, E., Dorland, W. & Hammett, G. W. 2002 The Magnetorotational Instability in a Collisionless Plasma. *ApJ* **577**, 524–533.

Quest, KB & Shapiro, VD 1996 Evolution of the fire-hose instability: Linear theory and wave-wave coupling. *Journal of Geophysical Research* **101** (A11), 24457.

Rayleigh, Lord 1916 *Proc. Royal Soc. A* **93**, 148–154.

Reale, F. & Peres, G. 2000 TRACE-derived Temperature and Emission Measure Profiles along Long-lived Coronal Loops: The Role of Filamentation. *ApJ Letters* **528**, L45–L48.

Reale, F., Peres, G., Serio, S., Betta, R. M., DeLuca, E. E. & Golub, L. 2000 A Brightening Coronal Loop Observed by TRACE. II. Loop Modeling and Constraints on Heating. *ApJ* **535**, 423–437.

Rebusco, P., Churazov, E., Böhringer, H. & Forman, W. 2006 Effect of turbulent diffusion on iron abundance profiles. *Monthly Notices of the Royal Astronomical Society* **372** (4), 1840–1850.

Rebusco, P., Churazov, E., Sunyaev, R., Böhringer, H. & Forman, W. 2008 Width of x-ray lines as a diagnostic of gas motions in cooling flows. *Monthly Notices of the Royal Astronomical Society* **384** (4), 1511–1518.

Regev, O. & Umurhan, O. M. 2008 On the viability of the shearing box approximation for numerical studies of MHD turbulence in accretion disks. *A&A* **481**, 21–32.

Rincon, F., Schekochihin, A. A. & Cowley, S. C. 2010 *MNRAS - in preparation* .

Rosenbluth, MN 1956 Los alamos scientific laboratory report. *LA-2030 In the text* .

Rosin, M. S., Schekochihin, A. A. & Mestel, A. J. 2010a *In preparation, MNRAS* .

Rosin, M. S., Schekochihin, A. A., Rincon, F. & Cowley, S. C. 2010b A nonlinear theory of the parallel firehose and gyrothermal instabilities in a weakly collisional plasma. *ArXiv e-print: http://adsabs.harvard.edu/abs/2010arXiv1002.4017R* .

Rubin, V. C. & Ford, Jr., W. K. 1970 Rotation of the Andromeda Nebula from a Spectroscopic Survey of Emission Regions. *ApJ* **159**, 379.

Sanders, JS & Fabian, AC 2008 Sound waves in the intracluster medium of the centaurus cluster. *Monthly Notices of the Royal Astronomical Society: Letters* **390** (1), L93–L97.

SANDERS, JS, FABIAN, AC & SMITH, RK 2010*a* Constraints on turbulent velocity broadening for a sample of clusters, groups and elliptical galaxies using xmm-newton. *Arxiv preprint arXiv:1008.3500* .

SANDERS, JS, FABIAN, AC, SMITH, RK & PETERSON, JR 2010*b* A direct limit on the turbulent velocity of the intracluster medium in the core of abell 1835 from xmm–newton. *Monthly Notices of the Royal Astronomical Society: Letters* **402** (1), L11–L15.

SARAZIN, C.L. 2003 Hot plasma in clusters of galaxies, the largest objects in the universe. *Physics of Plasmas* **10**, 1992.

SCHEKOCHIHIN, A. A. & COWLEY, S. C. 2006 Turbulence, magnetic fields, and plasma physics in clusters of galaxies. *Physics of Plasmas* **13** (5), 056501–+.

SCHEKOCHIHIN, A. A. & COWLEY, S. C. 2007 *Turbulence and Magnetic Fields in Astrophysical Plasmas*, p. 85. Springer.

SCHEKOCHIHIN, A. A., COWLEY, S. C., DORLAND, W., HAMMETT, G. W., HOWES, G. G., QUATAERT, E. & TATSUNO, T. 2009 Astrophysical Gyrokinetics: Kinetic and Fluid Turbulent Cascades in Magnetized Weakly Collisional Plasmas. *ApJ* **182**, 310–377.

SCHEKOCHIHIN, A. A., COWLEY, S. C., KULSRUD, R. M., HAMMETT, G. W. & SHARMA, P. 2005 Plasma Instabilities and Magnetic Field Growth in Clusters of Galaxies. *ApJ* **629**, 139–142.

SCHEKOCHIHIN, A. A., COWLEY, S. C., KULSRUD, R. M., ROSIN, M. S. & HEINEMANN, T. 2008 Nonlinear Growth of Firehose and Mirror Fluctuations in Astrophysical Plasmas. *Physical Review Letters* **100** (8), 081301.

SCHEKOCHIHIN, A. A., COWLEY, S. C., RINCON, F. & ROSIN, M. S. 2010 Magnetofluid dynamics of magnetized cosmic plasma: firehose and gyrothermal instabilities. *MNRAS* p. 484.

SCHUECKER, P., FINOGUENOV, A., MINIATI, F., BÖHRINGER, H. & BRIEL, U., G. 2004 2004 *A&A* **426**, 387.

Sellwood, J. A. & Balbus, S. A. 1999 Differential Rotation and Turbulence in Extended H I Disks. *ApJ* **511**, 660–665.

Shakura, N. I. & Sunyaev, R. A. 1973 Black holes in binary systems. Observational appearance. *A&A* **24**, 337–355.

Shapiro, V.D. & Schevchenko, V.I. 1964 *JETP* **18**, 1109.

Sharma, P., Chandran, B.D.G., Quataert, E. & Parrish, I.J. 2009 Buoyancy instabilities in galaxy clusters. *The Astrophysical Journal* **699**, 348.

Sharma, P., Hammett, G. W. & Quataert, E. 2003 Transition from Collisionless to Collisional Magnetorotational Instability. *ApJ* **596**, 1121–1130.

Sharma, P., Hammett, G. W., Quataert, E. & Stone, J. M. 2006 Shearing Box Simulations of the MRI in a Collisionless Plasma. *ApJ* **637**, 952–967.

Sharma, P., Quataert, E., Hammett, G. W. & Stone, J. M. 2007 Electron Heating in Hot Accretion Flows. *ApJ* **667**, 714–723.

Sharma, P., Quataert, E. & Stone, J.M. 2008 Spherical accretion with anisotropic thermal conduction. *Monthly Notices of the Royal Astronomical Society* **389** (4), 1815–1827.

Shukurov, A., Subramanian, K. & Haugen, N. E. L. 2006 The origin and evolution of cluster magnetism. *Astronomische Nachrichten* **327**, 583–586.

Simionescu, A., Böhringer, H., Brüggen, M. & Finoguenov, A. 2007 The gaseous atmosphere of m87 seen with xmm-newton. *Heating versus Cooling in Galaxies and Clusters of Galaxies* pp. 87–89.

Skinner, M. A. & Ostriker, E. C. 2010 The Athena Astrophysical Magnetohydrodynamics Code in Cylindrical Geometry. *ApJ* **188**, 290–311.

Snyder, P. B., Hammett, G. W. & Dorland, W. 1997 Landau fluid models of collisionless magnetohydrodynamics. *Physics of Plasmas* **4**, 3974–3985.

Sofue, Y. & Rubin, V. 2001 Rotation Curves of Spiral Galaxies. *ARA&A* **39**, 137–174.

Southwood, D.J. & Kivelson, M.G. 1993 Mirror instability, 1, physical mechanism of linear instability. *JOURNAL OF GEOPHYSICAL RESEARCH-ALL SERIES-* **98**, 9181–9181.

Spitzer, L. 1962 *Physics of Fully Ionized Gases*.

Stone, J.M., Gardiner, T.A., Teuben, P., Hawley, J.F. & Simon, J.B. 2008 Athena: a new code for astrophysical mhd. *Astrophysical Journal Supplement* **178** (1), 137–177.

Tamburro, D., Rix, H.-W., Leroy, A. K., Low, M.-M. M., Walter, F., Kennicutt, R. C., Brinks, E. & de Blok, W. J. G. 2009 What is Driving the H I Velocity Dispersion? *ApJ* **137**, 4424–4435.

TRACE 2000 Transition region and coronal explorer: Coronal loop: Ar9154 in 171 angstrom. http://trace.lmsal.com/POD/TRACEpodoverview.html.

Umurhan, O. M. & Regev, O. 2004 Hydrodynamic stability of rotationally supported flows: Linear and nonlinear 2D shearing box results. *A&A* **427**, 855–872.

Vedenov, AA & Sagdeev, RZ 1958 Some properties of the plasma with anisotropic distribution of the velocities of ions in the magnetic field. In *Sov Phys Dokl*, , vol. 3, p. 278.

Velikhov, E. P. 1959 *JETP* **36**, 1398.

Vikhlinin, A., Markevitch, M., Murray, SS, Jones, C., Forman, W. & Speybroeck, L.V. 2005 Chandra temperature profiles for a sample of nearby relaxed galaxy clusters. *The Astrophysical Journal* **628**, 655.

Vogt, C. & Ensslin, T. 2005 A bayesian view on faraday rotation maps - seeing that magnetic power spectra in galaxy clusters. *A&A* **434**, 67–76.

Voigt, LM & Fabian, AC 2004 Thermal conduction and reduced cooling flows in galaxy clusters. *Monthly Notices of the Royal Astronomical Society* **347** (4), 1130–1149.

WANG, P. & ABEL, T. 2009 Magnetohydrodynamic Simulations of Disk Galaxy Formation: The Magnetization of the Cold and Warm Medium. *ApJ* **696**, 96–109.

WATSON, G. N. 1944 *A Treatise on the Theory of Bessel Functions*, second ed. edn. Cambridge: Cambridge University Press.

WICKS, RT, HORBURY, TS, CHEN, CHK & SCHEKOCHIHIN, AA 2010 Power and spectral index anisotropy of the entire inertial range of turbulence in the fast solar wind. *Arxiv preprint arXiv:1002.2096* .

YOON, P.H., WU, CS & DE ASSIS, AS 1993 Effect of finite ion gyroradius on the fire-hose instability in a high beta plasma. *Physics of Fluids B: Plasma Physics* **5**, 1971.

ZAKAMSKA, N.L. & NARAYAN, R. 2003 Models of galaxy clusters with thermal conduction. *The Astrophysical Journal* **582**, 162.